INDENTATION CONTACT MECHANICS

– Micro/Nano Physics of Materials –

(REVISED EDITION)

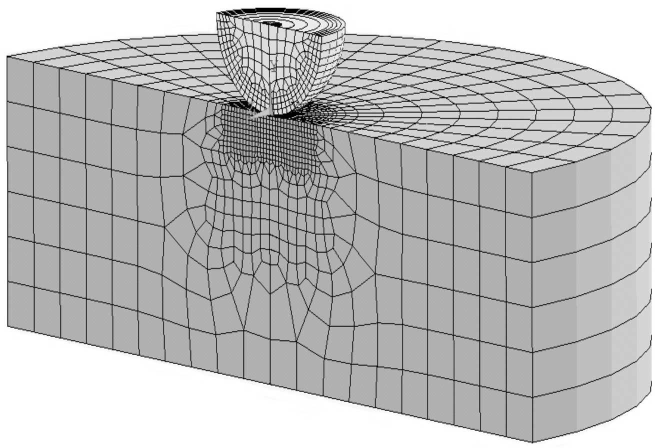

Mototsugu Sakai

Preface

This textbook is intended to make considerations on the continuum mechanics of indentation contact in micro/nano-scales, experimental details for measuring/analyzing mechanical properties (elastic, plastic, elastoplastic, and viscoelastic properties), instrumented indentation apparatuses, and on the materials physics in micro/nano-regimes that makes a great contribution to developing various types of engineering materials and composites through designing their microstructures.

The contact hardness has been conventionally defined as a mean contact pressure calculated from the applied indentation load. The most widely utilized and well-known hardness number is the Vickers hardness; this hardness number is determined by pressing a Vickers indenter (a tetrahedral pyramidal diamond tip) on a material, and then by calculating the apparent contact pressure from the indentation load divided by the total contact area of the residual impression. Besides the Vickers indenter, depending on the tip-geometry of indenter, various types of indenters including Berkovich (trigonal pyramid), Brinell (sphere), and Rockwell (cone with a rounded-tip) indenters have also been widely acknowledged.

The history of the concept, test procedure, and the physics of contact hardness number date back to the mid-19th century, in which the hardness number was defined as the indentation load divided by *the total contact area* of residual impression. However, on the basis of the experimental results for spherical indentation on various metallic alloys along with the considerations on the geometrical similarity of indentation contact, in 1908, E. Meyer proposed the concept of "contact hardness, the Meyer hardness H_{M}" as a mean contact pressure defined by the applied load divided by *the projected contact area* of residual impression. The Meyer hardness of *very ductile* materials is closely related to the yield strength Y via the relation of $H_{\mathrm{M}} = cY$ with the constraint factor c. In 1920s, C. Prandtle examined the constraint factor in relation to the plastic flow beneath a two-dimensional flat punch, and then R. Hill extended his considerations to what is now known as the slip-line field theory, leading to the c-value of 2.57. Based on their extensive as well as intensive research activities, the Meyer hardness H_{M} has long been recognized as a "measure of the yield strength Y" of ductile metals. Since the mid-20th, the engineering of organic polymers as well as of ceramic materials has significantly been progressed. Due to a significant elastic deformation of these engineering materials, their Meyer hardness numbers are by no means the measure of yield strength; the Meyer hardness is given by a function of the elastic modulus (Young's modulus E) and the yield strength Y. Thorough understanding of the materials physics of Meyer hardness will be given in this textbook for the materials including perfectly elastic, elastoplastic, fully plastic, as well as time-dependent viscoelastic materials.

In 1881, H. Hertz, 24 years old at that time, published a classic paper, *On the contact of elastic solids*, in which he made theoretical considerations on the contact pressure distributions of spherical solids in order to understand the optical interference fringe patterns at contact. This paper founded the present contact mechanics as the "Hertzian contact theory". Four years after his paper, in 1885, J. Boussinesq made a classical approach to finding the elastic stresses and their spatial distributions induced by arbitrary surface tractions on the basis of potential theory. Though the Boussinesq's theoretical framework included the Hertzian contact problem as a specific case, its analytical solution was first derived by A.E.H. Love in 1930s, and then by I.N. Sneddon in 1960s by applying the Hankel transforms to the Airy's/Love's stress functions, having led to the basis of the present elastic theory for conical/pyramidal indentation contact problems.

The classic book, "Contact Mechanics", published by K.L Johnson in 1985, encompasses various types of contact problems in a systematic manner, including the Hertzian contact problems on the basis of *continuum mechanics*, but not deeply discussing the *materials physics*. Accordingly, none of considerations were made on the materials physics of elastoplastic/viscoelastic deformation and flow induced by indentation contact. On the other hand, D. Tabor, through his book "Hardness of Metals" published in 1951, discussed in an intensive manner the correlation between the elastoplastic characteristics of metals and their indentation contact behavior, while no discussions were made for the contact behavior of organic polymers and engineering ceramic materials in micro/nano-regimes, due to the significant development of these engineering materials that has been made after the publication of his textbook.

In 1980's, several types of conventional instrumented indentation apparatuses came onto the market. These apparatuses can measure the indentation load P and the associated penetration depth h in micro/nano-scales but cannot determine the *indentation contact-area under the applied load*. This incapability of the contact-area determination in experiments is fatal, since none of material characteristics (elastic modulus, yield strength, any of viscoelastic functions, etc.) cannot be obtained in a quantitative manner without the experimental information on the *in-situ contact-area*. We have to make several undesirable approximations/assumptions prior to estimating the contact-area in these conventional instrumented indentation apparatuses in order to determine the material characteristics.

Due to the axisymmetric nature of indentation, we need the information not only on the deformation along the loading direction, i.e., the penetration depth, but also on the deformation perpendicular to the loading axis, i.e., the contact area, in order to describe the indentation-induced surface deformation and flow. Accordingly, the quantitative information on the indentation contact-area is very essential in determining any of material characteristics. To overcome these difficulties included in the present conventional instrumented indentation systems, an *instrumented indentation microscope*, as a new generation of instrumented indentation apparatuses, was design and fabricated by T. Miyajima and M. Sakai in 2003. This indentation microscope can determine in experiment the indentation contact-area along with the load and the depth of penetration. Furthermore, once we utilized the indentation microscope, we can readily determine the elastic/elastoplastic material characteristics, as well as quantitatively analyze any-types of viscoelastic functions by conducting computer-assisted indentation tests for the applied load, depth of penetration, as well as the applied contact area as functions of time.

Up to the present date, have not been published none of the appropriate textbooks that deal with the micro-nano materials physics based on the continuum mechanics of indentation contact. Throughout this textbook, therefore, the author intends to discuss the materials physics as well as the detailed considerations on the testing apparatuses, quantitative analyses of experimental data, etc. on the basis of continuum mechanics of indentation contact. In the first several chapters, the continuum mechanics of indentation contact will be given, and then in the subsequent chapters, discussed will be the micro-nano materials characteristics (elastic, elastoplastic, viscoelastic properties) of several types of engineering materials by the use of the experimental data obtained with the conventional indentation apparatus as well as the instrumented indentation microscope. Intensive considerations on the finite element analyses will also be given that are definitely invaluable for the considerations on the materials physics of engineering materials with complicated microstructures such as film/substrate laminates.

The author acknowledges the collaborations of his research stuffs and students in The Toyohashi University of Technology. Without their contributions, the author cannot complete this textbook. In particular, the author appreciates the great contribution of Dr. T. Miyajima (National Institute of Advanced Industrial Science and Technology (AIST)) who successfully designed and fabricated the world's first instrumented indentation microscope. As will be repeatedly emphasized in this book, the quantitative determination of the contact area by the use of the instrumented indentation microscope is very essential in experiments for determining the micro-nano material characteristics without making any of undesirable assumption and approximation. The potentials of the instrumented indentation microscope will play an extremely significant role in establishing the theoretical as well as experimental frameworks of indentation contact mechanics.

M. Sakai

(Revised in January, 2020)

CONTENTS

List of Symbols

A	Contact area of indentation
A_{proj}	Projected area of residual impression
A_{e}	Elastic contact area
A_{p}	Plastic contact area
$A_{\mathrm{ve}}(t)$	Viscoelastic contact area
a_{H}	Contact radius of homogeneous body
a	Indentation contact radius
B	Indenter's shape factor defined in Eq. (3.34)
C_{f}	Frame compliance of indentation apparatus
C_{g} ; C_{e}	Glass compliance; equilibrium compliance
$C_{\mathrm{creep}}(t)$, $C'_{\mathrm{creep}}(t)$, $C'(t)$	Creep compliance functions
$C^*(p)$	Carson transform of creep compliance defined by $p\overline{C}(p)$
c	Indenter's shape factor defined in Eq. (3.34)
c	Constraint factor defined in Eq. (5.7)
E ; E'	Elastic modulus (Young's modulus)
E_{g} ; E_{e}	Glass modulus, equilibrium modulus
E_{M}	Elastic modulus of Maxwell's spring
E_{V}	Elastic modulus of Voigt's spring
$E_{\mathrm{relax}}(t)$, $E'_{\mathrm{relax}}(t)$, $E(t)$	Relaxation moduli
$\overline{E}(p)$	Laplace transform of relaxation modulus
$E^*(p)$	Carson transform of relaxation modulus; $p\overline{E}(p)$
E'_{eff}	Effective elastic modulus of laminate composite
e	Bulk strain defined in Eq. (2.16)
G	Shear modulus; elastic modulus in shear
$G_{\mathrm{relax}}(t)$	Relaxation modulus in shear
FEA, FEM	Finite Element Analysis, Finite Element Method
g	Area index of cone/pyramid indenter defined by $A = gh^2$
HTT	Hear-treatment-temperature
$H(\tau)$	Relaxation time spectrum
H_{M}	Meyer hardness
h, $h_{\max}$, $h(t)$	Penetration depths of indentation
h_{c}	Contact depth of penetration
h_{r}	Depth of residual impression
$J_n(x)$	Bessel function of the first kind of order n
$J_{\mathrm{creep}}(t)$	Creep function in shear
K	Bulk modulus
k	Critical yield stress in shear (Eq. (4.2))
k_h	Indentation loading coefficient defined in Eq. (3.33)
k_{e}, k_{p}, k_{ep}	Loading coefficients (slopes of P - h^2 linear plots) of cone/pyramid indentation
k_1	Slope of P - h^2 loading linear plot (loading coefficient)
k_2	Slope of P - h^2 unloading linear plot (unloading coefficient)
$L(\tau)$	Retardation time spectrum
M	Unloading stiffness
P, $P(t)$	Indentation load
PI	Plastic strain (plastic index) defined by $\varepsilon_{\mathrm{I}}E'/cY$
$p(r)$	Distribution of indentation contact pressure
p_{C}, p_{F}, p_{S}	Coefficients of contact pressure distribution define in Eqs. (8.1) - (8.3)
p_{m}	Mean contact pressure of indentation ; $P/\pi a^2$
p_0	Maximum contact pressure of spherical indentation ; $(3/2)\,p_{\mathrm{m}}$
R	Radius of spherical indenter
S_{obs}	Unloading stiffness

T_g Glass transition temperature

T Absolute temperature

t, t' Time

t_f Film thickness of laminate

U Density of strain energy defined in Eq. (4.6)

U_T, U_e, U_r

Energies defined in Eqs. (5.19) - (5.21) for characterizing P - h hysteresis curve

$u(t)$ Heaviside step function

V, V_e, V_p

Indentation-induced excluded volumes defined in Eq. (5.12)

WOI Work-of-Indentation defined in Eq. (5.24)

Y Yield stress (Yield strength)

β Inclined face-angle of cone/pyramid indenter

β_c Inclined face-angle of cone indenter

$\chi(t)$ Sneddon's function defined in Eq. (3.4)

Δ Laplace operator (Laplacian) defined in Eq. (2.3)

ΔG Change in Gibbs free energy

ΔH Change in enthalpy

ΔS Change in entropy

$\delta(t)$ Dirac's delta function

ε_R, $(\varepsilon_p)_R$ Representative strains of work-hardening materials

ε_I Indentation strain

ε_{IY} Threshold indentation strain for plastic deformation

ε_i Normal strain

$\varepsilon(t)$ Viscoelastic strain

$\bar{\varepsilon}(p)$ Laplace transform of $\varepsilon(t)$

$\varphi(r,z)$ Airy's stress function; Love's stress function

$\varphi_n{}^H(\zeta,z)$ Hankel transform of $\varphi(r,z)$ defined in Eq. (2.23)

γ $(a/a_H)_h$

γ, γ_{EP} Surface energy

γ_{ij} Shear strain

η, η_c, $\eta_c(t)$ Relative contact-depth of penetration defined by h_c/h

η_e η -value of elastic body

η_p η -value of fully plastic body

η Shear viscosity in steady-state

κ Bulk compliance, $1/K$

λ, λ_{EP} Adhesion toughness

ν, $\nu(t)$ Poisson's ratios

ρ Non-dimensional radius; r/a

Σ Sum of normal stresses define in Eq. (2.3)

σ_i Normal stress

$\sigma(t)$ Time-dependent stress of viscoelastic body

$\bar{\sigma}(p)$ Laplace transform of $\sigma(t)$

τ Relaxation time

τ_M Relaxation time of Maxwell model

τ_Z Relaxation time of Zener model

τ_{ij} Shear stress

ξ Non-dimensional thickness of coating defined by t_f/a

ξ_r Non-dimensional depth of residual impression defined by h_r/h_{max} or h_r/h

GENERAL CONCEPT OF DEFORMATION −STRAIN AND STRESS−

CHAPTER 1

Indentation contact mechanics is a field of the science and engineering of continuum mechanics that focuses on several types of contact problems. Very complicated is the mechanical field of the contacting area that is formed between two of the continuum bodies with different mechanical properties. Accordingly, we are sometimes facing to numbers of mathematical difficulties in describing the mechanical field of this contacting area. In applying the general stress/strain analysis to the indentation contact mechanics, therefore, it will be appropriate to make mathematical formulations for describing the mechanical equilibrium and the constitutive equations. This is the objective of the present chapter **[1.1-1.3]**.

The definition and the quantitative expression for the deformation of a solid body are given in this chapter. If all points within the body experience the same displacement, the body moves as a rigid translation, being not stretched or deformed internally. Under the applied load, the body must experience different displacements for strain to occur. Consider the deformations shown in Fig. 1.1, where the deformations are depicted in two-dimensional plane, for simplicity. Suppose two points A and B initially separated by a small distance of dx. These points are experiencing translational motion along the x-axis. The displacements at point A and B are u_{A} and $u_{\mathrm{B}}\left(=u_{\mathrm{A}}+\delta\right)$, respectively. Accordingly, by the use of Taylor expansion around the point A, the differential motion (the net displacement; i.e., elongation) δ is then

$$\begin{aligned}\delta &= u_{\mathrm{B}} - u_{\mathrm{A}} \\ &= \left(u_{\mathrm{A}} + \frac{\partial u}{\partial x}dx\right) - u_{\mathrm{A}} = \frac{\partial u}{\partial x}dx\end{aligned}$$

The x-component of strain as the differential displacement per unit length, i.e., the strain for elongation is then defined by

$$\varepsilon_x = \frac{\delta}{dx} = \frac{\partial u}{\partial x} \tag{1.1}$$

Hence, the strain is a displacement gradient. Applying similar arguments

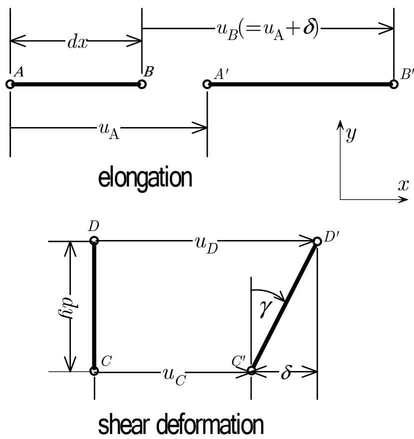

Figure 1.1 Elongation (incremental deformation) and shear deformation in two-dimensional space

[1.1] S.P. Timoshenko, J.N. Goodier, "Theory of Elasticity", McGraw-Hill (1970)
[1.2] I.H. Shames, F.A. Cozzarelli, "Elastic and Inelastic Stress Analysis", Prentice Hall (1992)
[1.3] D. Roylance, "Mechanics of Materials", John Wiley & Sons (1996)

to the differential motions in the y - and z - directions, the y - and z - components of normal strains are given by

$$\varepsilon_y = \frac{\partial v}{\partial y} \qquad \varepsilon_z = \frac{\partial w}{\partial z} \tag{1.2}$$

where v and w are, respectively, the displacements in y - and z - directions.

Elongation or compression is always associated with the change in the normal separation of atomic planes of the body deformed, while shear distortion results in relative sliding of these atomic planes, but no changes occur in their normal direction. The vertical line element CD having the length of dy in y-direction is experienced with the shear displacement of δ to the horizontal direction (x-direction), and tilted to the line element C'D' with the shear angle γ, as depicted in Fig. 1.1;

$$\delta = u_{\mathrm{D}} - u_{\mathrm{C}} = \left(u_{\mathrm{C}} + \frac{\partial u}{\partial y} dy \right) - u_{\mathrm{C}} = \frac{\partial u}{\partial y} dy$$

The shear strain in y -direction is thus defined by the displacement gradient of shear, $\partial u / \partial y (= \tan \gamma)$;

$$\gamma (\approx \tan \gamma) = \frac{\delta}{dy} = \frac{\partial u}{\partial y}$$

In addition to the shear displacement of u along the x -direction, there exists the coupled shear displacement of v to the y-direction. This is a requisite for prohibiting the rotation of this two-dimensional xy -plane in mechanical equilibrium, resulting in the shear strain of $\partial v/\partial x$. Accordingly, a general formula for shear strain in the xy-plane is given by

$$\gamma_{xy} = \frac{\partial u}{\partial y} + \frac{\partial v}{\partial x} \tag{1.3}$$

In a similar way, the shear strains in yz- and zx-planes are described, respectively, by

$$\gamma_{yz} = \frac{\partial v}{\partial z} + \frac{\partial w}{\partial y} \tag{1.4}$$

$$\gamma_{zx} = \frac{\partial w}{\partial x} + \frac{\partial u}{\partial z} \tag{1.5}$$

Since these six strains [the normal strains of ($\varepsilon_x, \varepsilon_y, \varepsilon_z$), and the shear strains of ($\gamma_{xy}, \gamma_{yz}, \gamma_{zx}$)] are written in terms of only three displacements

(u, v, w), they cannot be specified arbitrarily; there must exist some correlations (compatibility equations) among these six strains. These compatibility relations stand for the physics that any adjacent two points in the continuum are neither overlapped nor cracked in between during the deformation. Equations (1.1) - (1.3) are rewritten with

$$\frac{\partial^2 \varepsilon_x}{\partial y^2} = \frac{\partial^3 u}{\partial x \partial y^2} \qquad \frac{\partial^2 \varepsilon_y}{\partial x^2} = \frac{\partial^3 v}{\partial x^2 \partial y} \qquad \frac{\partial^2 \gamma_{xy}}{\partial x \partial y} = \frac{\partial^3 u}{\partial x \partial y^2} + \frac{\partial^3 v}{\partial x^2 \partial y},$$

resulting in

$$\frac{\partial^2 \varepsilon_x}{\partial y^2} + \frac{\partial^2 \varepsilon_y}{\partial x^2} = \frac{\partial^2 \gamma_{xy}}{\partial x \partial y}$$

Similarly, using the following four equations

$$\frac{\partial^2 \varepsilon_x}{\partial y \partial z} = \frac{\partial^3 u}{\partial x \partial y \partial z} \qquad \frac{\partial \gamma_{yz}}{\partial x} = \frac{\partial^2 v}{\partial x \partial z} + \frac{\partial^2 w}{\partial x \partial y}$$

$$\frac{\partial \gamma_{zx}}{\partial y} = \frac{\partial^2 u}{\partial y \partial z} + \frac{\partial^2 w}{\partial x \partial y} \qquad \frac{\partial \gamma_{xy}}{\partial z} = \frac{\partial^2 u}{\partial y \partial z} + \frac{\partial^2 v}{\partial x \partial z}$$

we have

$$2\frac{\partial^2 \varepsilon_x}{\partial y \partial z} = \frac{\partial}{\partial x}\left(-\frac{\partial \gamma_{yz}}{\partial x} + \frac{\partial \gamma_{zx}}{\partial y} + \frac{\partial \gamma_{xy}}{\partial z} \right)$$

Applying a similar differential operation to the other strain components, the following Saint Venant's compatibility equations are finally obtained:

$$\begin{aligned}
&\frac{\partial^2 \varepsilon_x}{\partial y^2} + \frac{\partial^2 \varepsilon_y}{\partial x^2} = \frac{\partial^2 \gamma_{xy}}{\partial x \partial y} \qquad 2\frac{\partial^2 \varepsilon_x}{\partial y \partial z} = \frac{\partial}{\partial x}\left(-\frac{\partial \gamma_{yz}}{\partial x} + \frac{\partial \gamma_{zx}}{\partial y} + \frac{\partial \gamma_{xy}}{\partial z} \right) \\
&\frac{\partial^2 \varepsilon_y}{\partial z^2} + \frac{\partial^2 \varepsilon_z}{\partial y^2} = \frac{\partial^2 \gamma_{yz}}{\partial y \partial z} \qquad 2\frac{\partial^2 \varepsilon_y}{\partial x \partial z} = \frac{\partial}{\partial y}\left(\frac{\partial \gamma_{yz}}{\partial x} - \frac{\partial \gamma_{zx}}{\partial y} + \frac{\partial \gamma_{xy}}{\partial z} \right) \\
&\frac{\partial^2 \varepsilon_z}{\partial x^2} + \frac{\partial^2 \varepsilon_x}{\partial z^2} = \frac{\partial^2 \gamma_{zx}}{\partial x \partial z} \qquad 2\frac{\partial^2 \varepsilon_z}{\partial x \partial y} = \frac{\partial}{\partial z}\left(\frac{\partial \gamma_{yz}}{\partial x} + \frac{\partial \gamma_{zx}}{\partial y} - \frac{\partial \gamma_{xy}}{\partial z} \right)
\end{aligned} \tag{1.6}$$

These compatibility equations along with the equations for mechanical equilibrium, the details of which are given below, play an important role in deriving the bi-harmonic equation that describes the mechanical responses of the continuum body under a given boundary condition.

Suppose a continuum body in mechanical equilibrium under several arbitrary tractions and displacement constraints acting on the boundary surfaces. These boundary tractions and constraints induce internal strains and forces (stresses) in the continuum body as the requisites for mechanical equilibrium. Consider now an infinitesimal rectangular parallelepiped embedded in this continuum. Choose the *x*-, *y*-, and *z*-axes so as to be parallel to the edges of this rectangular parallelepiped, as shown in Fig. 1.2. The normal stresses σ_x, σ_y, and σ_z are defined as the normal forces acting *on* the *x*-, *y*-, and *z*-unit planes with their normal vectors directed to *x*-, *y*-, and *z*-coordinates, respectively. The shear stresses (τ_{xy}, τ_{xz}), (τ_{yx}, τ_{yz}), and (τ_{zx}, τ_{zy}) are the shear forces acting *in* these *x*-, *y*-, and *z*-unit planes; the first subscript identifies the respective unit planes *in* which the stress acts, while the second subscript identifies the coordinate direction of the stress itself; τ_{xy} is the shear stress acting *in* the *x*-plane and directing to the *y*-coordinate, by way of example.

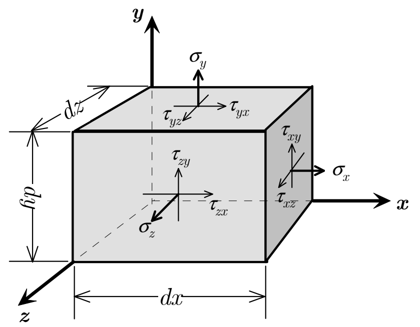

Figure 1.2 Stress components in three dimensions acting on/in the respective surfaces of a rectangular parallelepiped in a continuum

The parallelepiped shown in Fig. 1.2 neither rotate nor translate, because it is embedded in a continuum with mechanical equilibrium. This fact implies that there exist momentum balances around the *x*-, *y*-, and *z*-axes, resulting in the following symmetric relations of shear stresses;

$$\begin{aligned} \tau_{xy} &= \tau_{yx} \\ \tau_{yz} &= \tau_{zy} \\ \tau_{zx} &= \tau_{xz} \end{aligned} \tag{1.7}$$

Furthermore, the following force-balance must be satisfied along the *x*-axis

$$\begin{aligned} &\left(\sigma_x + \frac{\partial \sigma_x}{\partial x} dx\right) dydz - \sigma_x dydz \\ &\quad + \left(\tau_{yx} + \frac{\partial \tau_{yx}}{\partial y} dy\right) dzdx - \tau_{yx} dzdx \\ &\quad + \left(\tau_{zx} + \frac{\partial \tau_{zx}}{\partial z} dz\right) dxdy - \tau_{zx} dxdy \\ &\quad + Xdxdydz = 0, \end{aligned}$$

resulting in the following equilibrium equation along the *x*-axis:

$$\frac{\partial \sigma_x}{dx} + \frac{\partial \tau_{xy}}{dy} + \frac{\partial \tau_{xz}}{dz} + X = 0 \tag{1.8a}$$

where X stands for the *x*-directed body force (gravitational force, centrifugal force, etc.) acting on the continuum body. In a similar way to the *x*-axis, we have the following mechanical equilibrium equations for the *y*-, and *z*-axes, as well:

$$\frac{\partial \tau_{yx}}{dx} + \frac{\partial \sigma_y}{dy} + \frac{\partial \tau_{yz}}{dz} + Y = 0 \quad (1.8b)$$

$$\frac{\partial \tau_{zx}}{dx} + \frac{\partial \tau_{zy}}{dy} + \frac{\partial \sigma_z}{dz} + Z = 0 \quad (1.8c)$$

where Y and Z are the body forces directing to the y- and the z-coordinates, respectively.

The mechanical field induced by indentation loading/unloading processes is, in general, axisymmetric along the penetration axis. This fact implies that the axisymmetric cylindrical coordinates (r, θ, z) depicted in Fig. 1.3 might be much more appropriate than the Cartesian (x, y, z)-coordinate for representing the indentation-induced contact field, compatibility relations, and the mechanical equilibrium equations. In Fig. 1.3, the r-, θ-, and the z-axes represent, respectively, the radial, azimuthal, and the vertical coordinates. In the indentation contact mechanics, the vertical coordinate (the z-axis) is to the direction of indentation penetration. The respective components of the displacement in this coordinate system are denoted by u_r, u_θ, and u_z. The three-dimensional strains in the cylindrical coordinate system are;

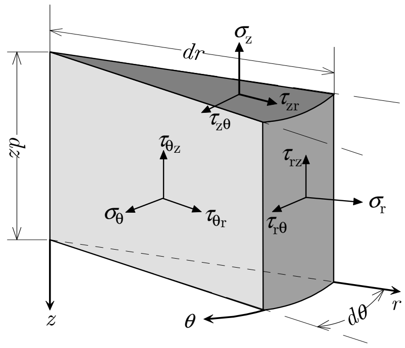

Figure 1.3 Three dimensional stresses in the cylindrical coordinate system

$$\begin{aligned}
\varepsilon_r &= \frac{\partial u_r}{\partial r} \\
\varepsilon_\theta &= \frac{1}{r}\frac{\partial u_\theta}{\partial \theta} + \frac{u_r}{r} \\
\varepsilon_z &= \frac{\partial u_z}{\partial z} \\
\gamma_{r\theta} &= \frac{\partial u_\theta}{\partial r} + \frac{1}{r}\frac{\partial u_r}{\partial \theta} - \frac{u_\theta}{r} \\
\gamma_{\theta z} &= \frac{\partial u_\theta}{\partial z} + \frac{1}{r}\frac{\partial u_z}{\partial \theta} \\
\gamma_{zr} &= \frac{\partial u_r}{\partial z} + \frac{\partial u_z}{\partial r}
\end{aligned} \quad (1.9)$$

The Saint Venant's compatibility equations, i.e., Eq. (1.6) in (x, y, z)-Cartesian coordinate system, are rewritten with the following expressions in (r, θ, z)-cylindrical coordinate system:

$$\frac{1}{r}\frac{\partial^2\varepsilon_r}{\partial\theta^2}+\frac{\partial}{\partial r}\left\{r\frac{\partial\varepsilon_\theta}{\partial r}-\left(\varepsilon_r-\varepsilon_\theta\right)\right\}=\frac{\partial}{\partial\theta}\left(\frac{\partial\gamma_{r\theta}}{\partial r}+\frac{\gamma_{r\theta}}{r}\right)$$
$$\frac{1}{r^2}\frac{\partial^2\varepsilon_z}{\partial\theta^2}+\frac{\partial^2\varepsilon_\theta}{\partial z^2}+\frac{1}{r}\frac{\partial\varepsilon_z}{\partial r}=\frac{1}{r}\frac{\partial}{\partial z}\left(\frac{\partial\gamma_{\theta z}}{\partial\theta}+\gamma_{rz}\right)$$
$$\frac{\partial^2\varepsilon_z}{\partial r^2}+\frac{\partial^2\varepsilon_r}{\partial z^2}=\frac{\partial^2\gamma_{rz}}{\partial r\partial z}$$
$$\frac{2}{r}\frac{\partial^2\varepsilon_r}{\partial\theta\partial z}=\frac{1}{r}\frac{\partial}{\partial r}\left(r\frac{\partial\gamma_{r\theta}}{\partial z}-\gamma_{\theta z}\right)+\frac{\partial}{\partial r}\left(\frac{1}{r}\frac{\partial\gamma_{rz}}{\partial\theta}-\frac{\partial\gamma_{\theta z}}{\partial r}\right)+\frac{1}{r}\frac{\partial\gamma_{r\theta}}{\partial z}+\frac{\gamma_{\theta z}}{r^2}$$
$$2\frac{\partial}{\partial z}\left(\frac{\partial\varepsilon_\theta}{\partial r}-\frac{\varepsilon_r-\varepsilon_\theta}{r}\right)=\frac{1}{r}\frac{\partial}{\partial\theta}\left(\frac{\partial\gamma_{\theta z}}{\partial r}-\frac{1}{r}\frac{\partial\gamma_{rz}}{\partial\theta}+\frac{\partial\gamma_{r\theta}}{\partial z}\right)+\frac{1}{r^2}\frac{\partial\gamma_{\theta z}}{\partial\theta}$$
$$\frac{2}{r}\frac{\partial}{\partial\theta}\left(\frac{\partial\varepsilon_z}{\partial r}-\frac{\varepsilon_z}{r}\right)=\frac{\partial}{\partial z}\left(\frac{\partial\gamma_{\theta z}}{\partial r}+\frac{1}{r}\frac{\partial\gamma_{rz}}{\partial\theta}-\frac{\partial\gamma_{r\theta}}{\partial z}-\frac{\gamma_{\theta z}}{r}\right)$$
$$(1.10)$$

The mechanical equilibrium equations in the cylindrical coordinate system, that are corresponding to Eqs. (1.8a) - (1.8c) in the Cartesian system, are given in Eq. (1.11) in terms of the *R*-, Θ-, and *Z*-body forces;

$$\begin{aligned}&\frac{\sigma_r-\sigma_\theta}{r}+\frac{\partial\sigma_r}{\partial r}+\frac{1}{r}\frac{\partial\tau_{\theta r}}{\partial\theta}+\frac{\partial\tau_{zr}}{\partial z}+R=0\\&\frac{2\tau_{\theta r}}{r}+\frac{\partial\tau_{\theta r}}{\partial r}+\frac{1}{r}\frac{\partial\sigma_\theta}{\partial\theta}+\frac{\partial\tau_{z\theta}}{\partial z}+\Theta=0\\&\frac{\tau_{zr}}{r}+\frac{\partial\tau_{zr}}{\partial r}+\frac{1}{r}\frac{\partial\tau_{z\theta}}{\partial\theta}+\frac{\partial\sigma_z}{\partial z}+Z=0\end{aligned}\qquad(1.11)$$

The details for the derivation of Eqs. (1.9) - (1.11) are given in APPENDIX A.

CONTINUUM MECHANICS OF PERFECTLY ELASTIC BODY

CHAPTER 2

2.1 CONSTITUTIVE EQUATION

In the second-half of 17th century, Robert Hook made measuring small changes in the length of a long wire under various loads. He observed the fact that the load P and its resulting elongation δ were related linearly as long as the loads were sufficiently small. Furthermore, he observed the fact that the wire recovered to the original length after unloading. This relation has been generally known as the Hook's law, and can be written by

$$P = k\delta$$

where the constant of proportionality k is referred to as the *stiffness* or the *spring constant* having the unit of N/m. He also recognized that k is not a material characteristic parameter, depending on the specimen shape as well as on the dimension.

A century afterword from the experiment of R. Hook, Thomas Young introduced a useful way to adjusting the stiffness so as to be *a characteristic material property* by introducing the concept of tensile stress σ defined as the load per unit cross-sectional area combined to the concept of tensile strain ε as the deformation per unit length of the test specimen. In terms of the stress and the strain, the Hook's law is written by

$$\sigma = E\varepsilon$$

The constant of proportionality E in this linear law is referred to as the Young's modulus or the modulus of elasticity, one of the most important mechanical characteristics of an elastic material. It has the same unit as stress, Pa.

In general, a somewhat subtle contraction in the radial direction is observed, when a load is applied to an elastic rod in its axial direction, just as stretching a rubber band to make it longer in on direction makes it thinner in the other direction. This lateral contraction accompanying a longitudinal extension is called the *Poisson's effect*, after the French mathematician, Simeon Denis Poisson. The Poisson's effect is resulted from the natural law of isometric deformation, i.e., no changes in volume after deformation. The Poisson's ratio is a material characteristic property defined as

$$\nu = \frac{-\varepsilon_{\text{radial}}}{\varepsilon_{\text{axial}}},$$

where the minus sign accounts for the sign change between the radial and axial strains; due to the Poisson's effect, $\varepsilon_{\text{axial}} > 0$ results in $\varepsilon_{\text{radial}} < 0$.

The three-dimensional expression for the constitutive equations of an elastic body is given in Eq. (2.1) in terms of the Young's modulus *E* and the Poisson's ratio ν;

$$\begin{aligned} \varepsilon_x &= \frac{1}{E}\left[\sigma_x - \nu\left(\sigma_y + \sigma_z\right)\right] \\ \varepsilon_y &= \frac{1}{E}\left[\sigma_y - \nu\left(\sigma_z + \sigma_x\right)\right] \\ \varepsilon_z &= \frac{1}{E}\left[\sigma_z - \nu\left(\sigma_x + \sigma_y\right)\right] \\ \gamma_{xy} &= \frac{\tau_{xy}}{G} \quad \gamma_{yz} = \frac{\tau_{yz}}{G} \quad \gamma_{zx} = \frac{\tau_{zx}}{G} \end{aligned} \tag{2.1}$$

where the shear modulus *G* as the elastic modulus for shear deformation is related to the Young's modulus *E* via the Poisson's ratio ν in the following equation

$$G = \frac{E}{2(1+\nu)} \tag{2.2}$$

Combining the Saint Venant's compatibility (Eq. (1.6)), mechanical equilibrium equation (Eq. (1.8)), and the constitutive equation (Eq. (2.1)) for elastic body leads to the following Beltrami-Michell compatibility relations:

$$\begin{aligned} &(1+\nu)\Delta\sigma_x + \frac{\partial^2\Sigma}{\partial x^2} = 0 \quad (1+\nu)\Delta\tau_{xy} + \frac{\partial^2\Sigma}{\partial x \partial y} = 0 \\ &(1+\nu)\Delta\sigma_y + \frac{\partial^2\Sigma}{\partial y^2} = 0 \quad (1+\nu)\Delta\tau_{yz} + \frac{\partial^2\Sigma}{\partial y \partial z} = 0 \\ &(1+\nu)\Delta\sigma_z + \frac{\partial^2\Sigma}{\partial z^2} = 0 \quad (1+\nu)\Delta\tau_{zx} + \frac{\partial^2\Sigma}{\partial z \partial x} = 0 \end{aligned} \tag{2.3}$$

In Eq. (2.3), Δ is the Laplace operator (so called Laplacian) that is defined by $\Delta = \partial^2/\partial x^2 + \partial^2/\partial y^2 + \partial^2/\partial z^2$, and Σ stands for the sum of normal stresses, $\Sigma = \sigma_x + \sigma_y + \sigma_z$. In general, mathematically very cumbersome procedures are required in solving the Beltrami-Michell equations under a given boundary condition. However, as the details will be discussed in the following section, the analytical solution of the Beltrami-Michell equations can be rather easily obtained in the states of *plane-strain* and of *axial symmetry*. In Sec. 2.2, the elastic theory of two-dimensional plane-strain problems is given, and then followed by the considerations on the elastic indentation contact mechanics in Sec. 2.3 as axisymmetric problems.

2.2 PLANE-STRAIN PROBLEMS

Let us consider the plane strain problems where the displacement w in the z-direction is zero, i.e., $w = 0$, and the displacements u and v in the x- and y-directions are respectively independent of the z-coordinate **[1.1-1.3]**. Substituting these plane-strain conditions into Eqs. (1.2), (1.4), and (1.5) leads to the following expressions for the normal and shear strains:

$$\begin{aligned}&\varepsilon_z = \gamma_{zx} = \gamma_{zy} = 0\\ &\varepsilon_x = \frac{\partial u}{\partial x} \qquad \varepsilon_y = \frac{\partial v}{\partial y} \qquad \gamma_{xy} = \frac{\partial u}{\partial y} + \frac{\partial v}{\partial x}\end{aligned} \tag{2.4}$$

Furthermore, by substituting Eq. (2.4) into the Saint Venant's compatibility relation of Eq. (1.6), we have the following simple expression that holds among the normal and shear strains:

$$\frac{\partial^2 \varepsilon_x}{\partial y^2} + \frac{\partial^2 \varepsilon_y}{\partial x^2} = \frac{\partial^2 \gamma_{xy}}{\partial x \partial y} \tag{2.5}$$

In plane-strain problems, the equilibrium equations, Eqs. (1.8a) and (1.8b), reduce to

$$\frac{\partial \sigma_x}{\partial x} + \frac{\partial \tau_{xy}}{\partial y} = 0 \tag{2.6a}$$

$$\frac{\partial \tau_{yx}}{\partial x} + \frac{\partial \sigma_y}{\partial y} = 0 \tag{2.6 b}$$

$$\tau_{xy} = \tau_{yx} \qquad \tau_{yz} = 0 = \tau_{zx} \tag{2.6 c}$$

where the body forces of X and Y are assumed to be zero for simplicity. On the other hand, by substituting the relation of $\varepsilon_z = 0$ into Eq. (2.1), the constitutive equation of an elastic body in plane-strain is given as

$$
\begin{aligned}
&\varepsilon_x = \frac{1}{E'}\left(\sigma_x - \nu'\sigma_y\right) \\
&\varepsilon_y = \frac{1}{E'}\left(\sigma_y - \nu'\sigma_x\right) \\
&\varepsilon_z = 0 \\
&\gamma_{xy} = \frac{\tau_{xy}}{G} \qquad \gamma_{yz} = 0 = \gamma_{zx}
\end{aligned}
\tag{2.7}
$$

In Eq. (2.7), the elastic modulus E' and the Poisson's ratio ν' in "plane-strain" are defined by $E' = E\big/\left(1-\nu^2\right)$ and $\nu' = \nu\big/\left(1-\nu\right)$, respectively.

The Saint Venant equation (Eq. (2.5)) in plane-strain state represents the compatibility among the strains, while the compatibility among the stresses, i.e., the Beltrami-Michell compatibility of elastic body, can be given by substituting Eq. (2.7) (the constitutive relations of perfectly elastic body in plane-strain) into Eq. (2.5);

$$
\frac{\partial^2}{\partial y^2}\left(\sigma_x - \nu'\sigma_y\right) + \frac{\partial^2}{\partial x^2}\left(\sigma_y - \nu'\sigma_x\right) = 2\left(1+\nu'\right)\frac{\partial^2 \tau_{xy}}{\partial x \partial y}
\tag{2.8}
$$

Differentiating the equilibrium equations, Eqs. (2.6a) and (2.6b), with *x* and *y* results in the following relation

$$
2\frac{\partial^2 \tau_{xy}}{\partial x \partial y} = -\frac{\partial^2 \sigma_x}{\partial x^2} - \frac{\partial^2 \sigma_y}{\partial y^2}
$$

and then substituting it into the Beltrami-Michell compatibility (Eq. (2.8)) finally leads to the following Laplace equation

$$
\left(\frac{\partial^2}{\partial x^2} + \frac{\partial^2}{\partial y^2}\right)\left(\sigma_x + \sigma_y\right) = 0
\tag{2.9a}
$$

Eq. (2.9a) is alternatively written by

$$
\Delta\left(\sigma_x + \sigma_y\right) = 0
\tag{2.9b}
$$

using the Laplace operator (Laplacian)

$$
\Delta = \frac{\partial^2}{\partial x^2} + \frac{\partial^2}{\partial y^2}.
$$

The solution of Laplace equation is referred to as the harmonic function. Equation (2.9) encompasses all the requisites included in the compatibility relation (Eq. (2.5)), equilibrium equation (Eq. (2.6), as well as the elastic constitutive equation (Eq. (2.7)). Accordingly, under the given boundary conditions applied to Eq. (2.9), we can solve any of plane-strain problems of elastic bodies.

G.B. Airy showed that if one introduces a stress function $\varphi(x, y)$ such that

$$\sigma_x = \frac{\partial^2 \varphi}{\partial y^2} \qquad \sigma_y = \frac{\partial^2 \varphi}{\partial x^2} \qquad \tau_{xy} = -\frac{\partial^2 \varphi}{\partial x \partial y}, \tag{2.10}$$

the equilibrium equations (Eqs. (2.6a) and (2.6b)) are automatically and reciprocally satisfied. We have the following forth-order differential equation of the stress function $\varphi(x, y)$ by substituting Eq. (2.10) into Eq. (2.9);

$$\begin{aligned} &\frac{\partial^4 \varphi}{\partial x^4} + 2\frac{\partial^4 \varphi}{\partial x^2 \partial y^2} + \frac{\partial^4 \varphi}{\partial y^4} \\ &= \Delta \cdot \Delta \varphi \\ &= 0 \end{aligned} \tag{2.11}$$

The stress function φ is, therefore, also called the bi-harmonic function since Eq. (2.11) is the Laplace equation of $\Delta\varphi$. Accordingly, the stresses and strains in elastic problems under any boundary conditions in two-dimensional plane-strain state can be found in a quantitative manner by substituting the solution φ of Eq. (2.11) into Eq. (2.10), and then into Eq. (2.7).

2.3 AXISYMMETRIC PROBLEMS

The axisymmetric problems along the penetration axis (z-axis) of indentation are independent of the azimuthal coordinate θ, and are appropriately represented as the three-dimensional problems in cylindrical coordinate. Equation (1.9) in axisymmetric problems is, therefore, recast into

$$\begin{aligned} &\varepsilon_r = \frac{\partial u_r}{\partial r} \qquad \varepsilon_\theta = \frac{u_r}{r} \qquad \varepsilon_z = \frac{\partial u_z}{\partial z} \\ &\gamma_{r\theta} = 0 \qquad \gamma_{\theta z} = 0 \qquad \gamma_{zr} = \frac{\partial u_r}{\partial z} + \frac{\partial u_z}{\partial r} \end{aligned} \tag{2.12}$$

Furthermore, applying Eq. (2.12) to the Saint Venant's compatibility (Eq. (1.10)) leads to the following axisymmetric compatibility expressions:

$$
\begin{aligned}
&\frac{\partial}{\partial r}\left\{r\frac{\partial \varepsilon_\theta}{\partial r}-(\varepsilon_r-\varepsilon_\theta)\right\}=0\\
&\frac{\partial^2\varepsilon_\theta}{\partial z^2}+\frac{1}{r}\frac{\partial \varepsilon_z}{\partial r}=\frac{1}{r}\frac{\partial \gamma_{rz}}{\partial z}\\
&\frac{\partial^2\varepsilon_z}{\partial r^2}+\frac{\partial^2\varepsilon_r}{\partial z^2}=\frac{\partial^2\gamma_{rz}}{\partial r\partial z}\\
&\frac{\partial}{\partial z}\left(\frac{\partial \varepsilon_\theta}{\partial r}-\frac{\varepsilon_r-\varepsilon_\theta}{r}\right)=0
\end{aligned}
\tag{2.13}
$$

On the other hand, the axisymmetric expressions of the equilibrium equation (Eq. (1.11)) are given by

$$
\frac{\sigma_r-\sigma_\theta}{r}+\frac{\partial \sigma_r}{\partial r}+\frac{\partial \tau_{zr}}{\partial z}=0 \tag{2.14a}
$$

$$
\frac{\tau_{zr}}{r}+\frac{\partial \tau_{zr}}{\partial r}+\frac{\partial \sigma_z}{\partial z}=0 \tag{2.14b}
$$

$$
\tau_{r\theta}=0=\tau_{z\theta} \quad , \tag{2.14c}
$$

where we assume that the body forces (R , Θ , Z) in Eq. (1.11) are all zero for simplicity.

The constitutive equations for perfectly elastic body ((Eq. (2.1)) in the Cartesian (x, y, z) coordinate turn to the following equations of axisymmetric problems in the cylindrical coordinate;

$$
\begin{aligned}
&\varepsilon_r=\frac{1}{E}\left[\sigma_r-\nu(\sigma_\theta+\sigma_z)\right]\\
&\varepsilon_\theta=\frac{1}{E}\left[\sigma_\theta-\nu(\sigma_z+\sigma_r)\right]\\
&\varepsilon_z=\frac{1}{E}\left[\sigma_z-\nu(\sigma_r+\sigma_\theta)\right]\\
&\gamma_{r\theta}=0 \qquad \gamma_{\theta z}=0 \qquad \gamma_{zr}=\frac{\tau_{zr}}{G}
\end{aligned}
\tag{2.15a}
$$

The conjugate expressions of Eq. (2.15a) in terms of strain and displacement are

$$
\begin{aligned}
&\sigma_r=\lambda e+2G\varepsilon_r=\lambda e+2G\frac{\partial u_r}{\partial r}\\
&\sigma_\theta=\lambda e+2G\varepsilon_\theta=\lambda e+2G\frac{u_r}{r}\\
&\sigma_z=\lambda e+2G\varepsilon_z=\lambda e+2G\frac{\partial u_z}{\partial z}\\
&\tau_{r\theta}=0 \qquad \tau_{\theta z}=0 \qquad \tau_{zr}=G\gamma_{zr}=G\left(\frac{\partial u_r}{\partial z}+\frac{\partial u_z}{\partial r}\right)
\end{aligned}
\tag{2.15b}
$$

In Eq. (2.15b), the volumetric strain e and the Lame constant λ are respectively defined by

$$
\begin{aligned}
e &= \varepsilon_r + \varepsilon_\theta + \varepsilon_z \\
&= \frac{\partial u_r}{\partial r} + \frac{u_r}{r} + \frac{\partial u_z}{\partial z} \\
\lambda &= \frac{\nu}{(1+\nu)(1-2\nu)} E
\end{aligned}
\tag{2.16}
$$

Combining Eqs. (2.14) – (2.16) with Eq. (2.13) results in the following Beltrami-Michell compatibility in axisymmetric problems;

$$
\begin{aligned}
&\Delta\sigma_r - \frac{2}{r^2}(\sigma_r - \sigma_\theta) + \frac{1}{1+\nu}\frac{\partial^2 \Sigma}{\partial r^2} = 0 \\
&\Delta\sigma_\theta - \frac{2}{r^2}(\sigma_\theta - \sigma_r) + \frac{1}{1+\nu}\frac{\partial \Sigma}{r \partial r} = 0 \\
&\Delta\sigma_z + \frac{1}{1+\nu}\frac{\partial^2 \Sigma}{\partial z^2} = 0 \\
&\Delta\tau_{rz} - \frac{1}{r^2}\tau_{rz} + \frac{1}{1+\nu}\frac{\partial^2 \Sigma}{\partial r \partial z} = 0
\end{aligned}
\tag{2.17}
$$

where Σ represents the sum of normal stresses, $\Sigma = \sigma_r + \sigma_\theta + \sigma_z$, while the Laplace operator Δ in axisymmetric cylindrical coordinate is written by

$$
\begin{aligned}
\Delta &= \frac{\partial^2}{\partial r^2} + \frac{1}{r}\frac{\partial}{\partial r} + \frac{\partial^2}{\partial z^2} \\
&= \frac{1}{r}\frac{\partial}{\partial r}\left(r\frac{\partial}{\partial r}\right) + \frac{\partial^2}{\partial z^2}
\end{aligned}
\tag{2.18}
$$

We have introduced the Airy's stress function in Eq. (2.10) that enables the quantitative description of two-dimensional plane-strain problems via the bi-harmonic equation (Eq. (2.11)). In a similar way to the plane-strain problem, we introduce the Love's stress function φ for three-dimensional axisymmetric elastic problems to represent the stress components in cylindrical coordinate;

$$\sigma_r = \frac{\partial}{\partial z}\left(\nu\Delta\varphi - \frac{\partial^2\varphi}{\partial r^2}\right)$$
$$\sigma_\theta = \frac{\partial}{\partial z}\left(\nu\Delta\varphi - \frac{1}{r}\frac{\partial\varphi}{\partial r}\right)$$
$$\sigma_z = \frac{\partial}{\partial z}\left((2-\nu)\Delta\varphi - \frac{\partial^2\varphi}{\partial z^2}\right) \tag{2.19}$$
$$\tau_{rz} = \frac{\partial}{\partial r}\left((1-\nu)\Delta\varphi - \frac{\partial^2\varphi}{\partial z^2}\right)$$

Furthermore, once we assume that the stress function φ is the solution of the following bi-harmonic equation

$$\Delta \cdot \Delta\varphi = 0\ , \tag{2.20}$$

not only Eq. (2.14a) but also Eq. (2.14b) are automatically satisfied. In addition to these facts, by the use of Eqs. (2.15), (2.16), and (2.19) combined with the relations of $u_r = r\varepsilon_\theta$, and $u_z = \int \varepsilon_z dz$, the displacements u_r and u_z are easily written in terms of the stress function φ, as follows;

$$2Gu_r = -\frac{\partial^2\varphi}{\partial r \partial z}$$
$$2Gu_z = 2(1-\nu)\Delta\varphi - \frac{\partial^2\varphi}{\partial z^2} \tag{2.21}$$

One can therefore quantitatively describe the stress-strain fields of the axisymmetric problem of any perfectly elastic body in cylindrical coordinate by substituting the stress function φ (the solution of the biharmonic equation, Eq. (2.20)) into Eq. (2.19) combined with Eq. (2.15a).

2.4 SOLUTION OF BI-HARMONIC EQUATION IN AXISYMMETRIC PROBLEMS - APPLICATION OF HANKEL TRANSFORM -

As mentioned in the preceding section, in order to find the stress function φ for elastic problems, we need to solve the bi-harmonic equation, Eq. (2.11) or Eq. (2.20), under a given boundary condition. In the second half of 19th century to the beginning of 20th century, some of physicists and mathematicians have contended with solving the bi-harmonic equation under the specific boundary conditions by the uses of polynomial equations and/or Fourier series. In general, the theories of complex functions have been widely applied to solving the bi-harmonic equation in the Cartesian (x , y) coordinate. On the other hand, in the cylindrical coordinate that is more appropriate for describing the indentation contact problems, it has been well-known that the use of the Bessel function-based Hankel transform is effective and useful for solving the harmonic/bi-harmonic equations. We will discuss in this section the application of Hankel transform to the bi-harmonic equation (Eq. (2.20)) for axisymmetric indentation contact problems of elastic body **[2.1-2.2]**.

In cylindrical coordinate system, the application of the method of separation variables to the axisymmetric Laplace equation $\Delta\varphi(r,z)=0$ leads to the ordinary differential equation with the variable *r* or *z*, and then the resultant equation with the variable *r* forms the first-kind Bessel differential equation. On the other hand, the Hankel-transform integral includes the Bessel function as its integral kernel. This is the reason why we can easily find the solution of the harmonic or the bi-harmonic equation via the Hankel transform. The details of Bessel function are given in Appendix B at the back of this book.

The Bessel function $J_n(x)$ of the first kind of order *n* is defined as the solution of the following differential equation;

$$\frac{d^2 J_n(x)}{dx^2}+\frac{1}{x}\frac{dJ_n(x)}{dx}+\left(1-\frac{n^2}{x^2}\right)J_n(x)=0 \qquad (2.22)$$

The Hankel transform of the stress function $\varphi(r,z)$ is defined in Eq. (2.23) using the Bessel function of order *n* as the kernel of the following transform integral;

[2.1] I.N. Sneddon, “Fourier Transforms”, McGraw-Hill (1951)
[2.2] D. Maugis, “Contact, Adhesion and Rupture of Elastic Solids”, Springer (2000)

$$\varphi_n^{\mathrm{H}}(\xi,z)=\int_0^\infty r\varphi(r,z)J_n(\xi r)dr\ , \tag{2.23}$$

while its inverse is written by

$$\varphi(r,z)=\int_0^\infty \xi\varphi_n^{\mathrm{H}}(\xi,z)J_n(\xi r)d\xi \tag{2.24}$$

Let us now consider the zero-order Hankel transform of $\Delta\varphi$;

$$\begin{aligned} I &= \int_0^\infty r\Delta\varphi(r,z)J_0(\xi r)dr \\ &= \int_0^\infty \frac{\partial}{\partial r}\left(r\frac{\partial\varphi}{\partial r}\right)J_0(\xi r)dr+\frac{\partial^2}{\partial z^2}\int_0^\infty r\varphi J_0(\xi r)dr \end{aligned}$$

where Δ is the Laplacian operator (refer to Eq. (2.18)), and φ means the Love's stress function. Applying the partial integration twice to the first term of the right-hand side of the above equation, and then using the zero-order Bessel differential equation ($n=0$ in Eq. (2.22)), we have

$$\frac{d^2\left[J_0(\xi r)\right]}{d(\xi r)^2}+\frac{1}{\xi r}\frac{d\left[J_0(\xi r)\right]}{d(\xi r)}+J_0(\xi r)=0\ ,$$

and then finally obtain the following result of the integral I ;

$$\begin{aligned} I &= \int_0^\infty r\Delta\varphi(r,z)J_0(\xi r)dr \\ &= \left(\frac{d^2}{dz^2}-\xi^2\right)\int_0^\infty r\varphi J_0(\xi r)dr \\ &= \left(\frac{d^2}{dz^2}-\xi^2\right)\varphi_0^{\mathrm{H}}(\xi,z) \end{aligned} \tag{2.25}$$

where use has been made of the mechanical requirement that the stress function φ and its spatial gradient $d\varphi/dr$ always diminish with $r\to\infty$. Replacing the stress function φ with $\varphi\equiv\Delta\varphi$ in Eq. (2.25), and repeating the same mathematical operations used in deriving Eq. (2.25), we finally have the Hankel transform of the *bi-harmonic equation*, as follows;

$$\left(\frac{d^2}{dz^2}-\xi^2\right)\left(\frac{d^2}{dz^2}-\xi^2\right)\varphi_0^{\mathrm{H}}(\xi,z)=0 \tag{2.26}$$

Accordingly, one can get the solution $\varphi_0^{\mathrm{H}}(\xi,z)$ of bi-harmonic equation by solving the fourth-order ordinary differential equation, Eq. (2.26), and then the application of *inverse Hankel transform* to $\varphi_0^{\mathrm{H}}(\xi,z)$ finally results in the stress function $\varphi(r,z)$ of the bi-harmonic equation (Eq.

(2.20)). In other words, we can say that the Hankel transform of bi-harmonic function $\varphi(r,z)$ satisfies the fourth-order ordinary differential equation, Eq. (2.26). Accordingly, once we notice the fact that the characteristic (auxiliary) fourth-order polynomial equation (Eq. (2.26)) has the multiple roots of $\pm\xi$, it is rather easy to solve Eq. (2.26), resulting in the following general solution;

$$\varphi_0^{\mathrm{H}}(\xi,z) = (A + B\xi z)e^{-\xi z} + (C + D\xi z)e^{\xi z}, \qquad (2.27)$$

in which the integral constants *A*, *B*, *C* and *D* will be finally fixed under the given boundary conditions.

Let us now derive the analytical expressions for the stresses and the strains in terms of $\varphi_0^{\mathrm{H}}(\xi,z)$. These expressions will play some of important roles in the elastic theory of indentation contact mechanics, the details of which will soon be given in the following sections. The order-zero Hankel transform of $\Delta\varphi$ is given in Eq. (2.25), and the first order Hankel transform of the derivative $d\varphi/dr$ is reduced to the order-zero Hankel transform of φ, as follows (refer to Appendix B),

$$\int_0^\infty r\left(d\varphi/dr\right)J_1(\xi r)\,dr = -\xi\int_0^\infty r\varphi J_0(\xi r)dr$$

Using these facts combined with the Hankel transform of Eq. (2.21) and its inverse, we finally describe the displacements, u_r and u_z, *in the real space* through using the stress function $\varphi_0^{\mathrm{H}}(\xi,z)$ *in the Hankel-space*;

$$2Gu_r = \int_0^\infty \xi^2 \frac{d\varphi_0^{\mathrm{H}}}{dz} J_1(\xi r)\,d\xi \qquad (2.28)$$

$$2Gu_z = \int_0^\infty \xi\left[(1-2\nu)\frac{d^2\varphi_0^{\mathrm{H}}}{dz^2} - 2(1-\nu)\xi^2\varphi_0^{\mathrm{H}}\right]J_0(\xi r)\,d\xi \qquad (2.29)$$

In a similar manner to the above considerations, by applying the Hankel-transform operations to Eq. (2.19), we can uniquely express the stress components, σ_r, σ_θ, σ_z, and τ_{rz} by the use of $\varphi_0^{\mathrm{H}}(\xi,z)$, as follows;

$$\sigma_r = \int_0^\infty \xi \left[\nu \frac{d^3 \varphi_0^{\mathrm{H}}}{dz^3} + (1-\nu)\xi^2 \frac{d\varphi_0^{\mathrm{H}}}{dz} \right] J_0(\xi r)\, d\xi \\ -\frac{1}{r}\int_0^\infty \xi^2 \frac{d\varphi_0^{\mathrm{H}}}{dz} J_1(\xi r)\, d\xi \tag{2.30}$$

$$\sigma_\theta = \nu \int_0^\infty \xi \left[\frac{d^3 \varphi_0^{\mathrm{H}}}{dz^3} - \xi^2 \frac{d\varphi_0^{\mathrm{H}}}{dz} \right] J_0(\xi r)\, d\xi \\ +\frac{1}{r}\int_0^\infty \xi^2 \frac{d\varphi_0^{\mathrm{H}}}{dz} J_1(\xi r)\, d\xi \tag{2.31}$$

$$\sigma_z = \int_0^\infty \xi \left[(1-\nu) \frac{d^3 \varphi_0^{\mathrm{H}}}{dz^3} - (2-\nu)\xi^2 \frac{d\varphi_0^{\mathrm{H}}}{dz} \right] J_0(\xi r)\, d\xi \tag{2.32}$$

$$\tau_{rz} = \int_0^\infty \xi^2 \left[\nu \frac{d^2 \varphi_0^{\mathrm{H}}}{dz^2} + (1-\nu)\xi^2 \varphi_0^{\mathrm{H}} \right] J_1(\xi r)\, d\xi \tag{2.33}$$

Equations (2.28) - (2.33) will play an important role in describing the indentation load P vs. the penetration depth h relation (P - h relation) for axisymmetric indentation problems (cylindrical punch, spherical/conical indentation), the details of which will be given in the subsequent chapter for perfectly elastic body.

INDENTATION CONTACT MECHANICS OF PERFECTLY ELASTIC BODY

CHAPTER 3

The tip-geometry of the conventional indenter includes sphere (Brinell indenter), cone with rounded tip (Rockwell indenter), and pyramid (Vickers tetrahedral indenter; Berkovich trihedral indenter). These indenters have been utilized in experiments for determining not only the contact hardness, but also other mechanical properties. One can estimate/determine the mechanical characteristics of the material tested through analyzing the indentation load P vs. penetration depth h relation, i.e., P-h relation. It will be readily expected that the P-h relation is highly dependent on the tip-geometry of indenter. We will discuss in this chapter the elastic indentation contact mechanics of the axisymmetric indenter with an arbitrary tip-geometry **[2-2]**.

A schematic contact view is depicted in Fig. 3.1 for an axisymmetric indenter with arbitrary tip-geometry that is pressed onto an elastic half-space with the indentation load of P (the contact friction between the indenter and the surface of elastic body is assumed to be zero for simplicity). The geometrical parameters of indentation are: the penetration depth h, contact depth h_c, contact radius a, and the surface displacement $u_z(r,0)$ of contact plane at the location r from the penetration-axis (z-axis). The boundary conditions at the free surface (z=0) are given by

$$\begin{aligned} &u_z(\rho,0) = h - f(\rho); \quad 0 \le \rho \le 1 \\ &\sigma_z(\rho,0) = 0; \qquad\qquad \rho > 1 \\ &\tau_{rz}(r,0) = 0 \end{aligned} \tag{3.1}$$

where $\rho = r/a$ is the non-dimensional radius normalized with the contact radius a, and $f(\rho)$ is the shape-function of the axisymmetric indenter defined with $f(0) = 0$. The first relation in Eq. (3.1) describes the surface displacement within the contact area ($0 \le \rho \le 1$), the second means the free surface with no stresses along the z-direction outside the contact area ($\rho > 1$), and the third relation represents the frictionless contact.

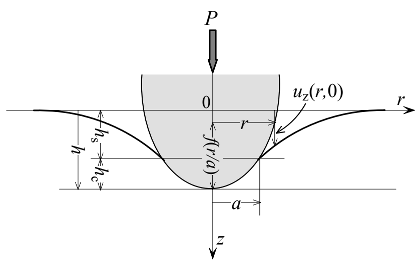

Figure3.1 The surface deformation $f(r/a)$ of elastic half-space for an axisymmetric indentation contact.

All of the stresses at the locations far away of the contact area ($r \to \infty$) must be zero. This fact implies that the Hankel transform of the bi-harmonic stress function $\varphi_0^{\mathrm{H}}(\xi,z)$ given in Eq. (2.27) must be finite in the region of $\xi \to \infty$, leading to the following formula;

$$\varphi_0^{\mathrm{H}}(\xi,z) = (A + B\xi z)e^{-\xi z} \tag{2.27a}$$

Substituting the frictionless boundary condition $\tau_{rz}(r,0) = 0$ into Eq. (2.33) results in

$$(1-\nu)\xi^2\varphi_0^{\mathrm{H}}(\xi,0) + \nu\left(\frac{d^2\varphi_0^{\mathrm{H}}}{dz^2}\right)_{z=0} = 0\,,$$

and then combining Eq. (2.27a) with the above relation leads to $A = 2\nu B$. Accordingly, the Hankel transform of the bi-harmonic stress function $\varphi_0^{\mathrm{H}}(\xi,z)$ is represented with

$$\varphi_0^{\mathrm{H}}(\xi,z) = B(2\nu + \xi z)e^{-\xi z} \tag{3.2}$$

Furthermore, Eqs. (2.29) and (2.32) combined with the boundary conditions of Eq. (3.1) finally fix the unknown integral constant B as follows;

$$B = -\frac{E'a}{2\xi^3}\int_0^1 \chi(t)\cos(a\xi t)\,dt \tag{3.3}$$

in which E' denotes the plane-strain elastic modulus, $E' = E/(1-\nu^2)$. The Sneddon's function $\chi(t)$ in Eq. (3.3) is defined by

$$\chi(t) = \frac{2}{\pi}\left(h - t\int_0^t \frac{f'(x)}{\sqrt{t^2 - x^2}}\,dx\right) \tag{3.4}$$

in terms of the shape-function of indenter $f(r)$ and the penetration depth h. We, therefore, finally obtain the analytical expression of $\varphi_0^{\mathrm{H}}(\xi,z)$;

$$\varphi_0^{\mathrm{H}}(\xi,z) = -(2\nu + \xi z)e^{-\xi z}\frac{E'a}{2\xi^3}\int_0^1 \chi(t)\cos(a\xi t)dt \tag{3.5}$$

by substituting Eq. (3.3) into Eq. (3.2). Equation (3.5) makes it possible for us to quantitatively describe the surface deformation and the stresses of elastic half-space for an arbitrary axisymmetric indentation contact (see Fig. 3.1) through the uses of Eqs. (2.28) - (2.33).

Let us start discussing the indentation load P vs. the penetration depth h relationship, i.e., P - h relationship, in terms of $\varphi_0^{\mathrm{H}}(\xi,z)$ (Eq. (3.5)). Substituting Eqs. (3.4) and (3.5) into Eq. (2.32) and using the fact that the indentation load P is described by $P = -2\pi\int_0^a r\sigma_z(r,0)dr$ in terms of the contact pressure $\sigma_z(r,0)$ within the contact area $(r \le a)$, we finally have the following P - h relation;

$$P = 2aE'\left[h - \int_0^1 \frac{xf(x)}{\sqrt{1-x^2}}dx\right] \tag{3.6}$$

Furthermore, combining Eq. (3.5) with Eq. (2.32) results in the contact pressure $\sigma_z(\rho,0)$ within the contact area ($\rho < 1$) as follows;

$$\sigma_z(\rho,0) = -\frac{E'}{2a}\left[\frac{\chi(1)}{\sqrt{1-\rho^2}} - \int_\rho^1 \frac{\chi'(t)dt}{\sqrt{t^2-\rho^2}}\right] \tag{3.7}$$

On the other hand, by substituting Eq. (3.5) into Eq. (2.29), the displacement $u_z(\rho,0)$ along the z-direction, i.e., the displacement along the loading direction of the free-surface outside the contact zone ($\rho > 1$) is written by

$$\begin{aligned} u_z(\rho,0) &= \int_0^1 \frac{\chi(t)dt}{\sqrt{\rho^2-t^2}} \\ &= \chi(1)\sin^{-1}\frac{1}{\rho} - \int_0^1 \chi'(t)\sin^{-1}\frac{t}{\rho}dt \end{aligned} \tag{3.8}$$

Based on the preceding considerations on the indentation contact mechanics of elastic body for an axisymmetric indenter with arbitrary tip-geometry of $f(r)$, let us discuss the elastic contact mechanics for the flat-punch, sphere, as well as the cone indentation in what follows.

3.1 FLAT-ENDED CYLINDRICAL PUNCH

In Fig 3.2, depicted is the deformation of the indented elastic half-space for a flat-ended cylindrical punch with the radius of a_0. The indenter's tip-geometry is denoted by $f(\rho)$;

$$f(\rho) = 0; \quad 0 \le \rho \le 1$$

where $\rho(= r/a_0)$ is the non-dimensional radius normalized with the radius a_0. Equation (3.6) combined with this tip-geometry function reduces to the following simple P-h relation, since the integral in the right-hand side of Eq. (3.6) turns to zero;

$$P = 2a_0E'h \tag{3.9}$$

Equation (3.9) means that the indentation load P linearly increases with

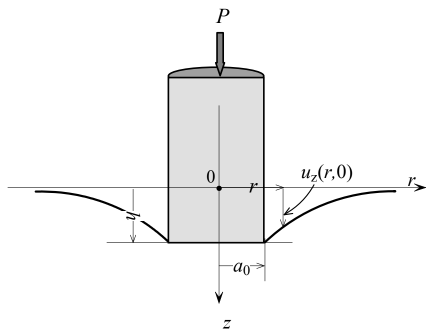

Figure 3.2 The surface-displacement of an elastic half-space indented by a flat-ended cylindrical punch

the increase in the penetration depth h, and the slope of this linear relation gives the Young's modulus E' of the elastic body indented. In addition to this fact, noticing the expression of $\chi(t) = 2h/\pi$ in Eq. (3.4), the contact stresses $\sigma_z(\rho,0)$ within the contact zone ($0 \le \rho \le 1$) is written as

$$\frac{\sigma_z(\rho,0)}{p_m} = -\frac{1}{2}\frac{1}{\sqrt{1-\rho^2}}; \quad 0 \le \rho < 1 \tag{3.10}$$

by the uses of Eqs. (3.7) and (3.9) combined with the mean contact pressure $p_{\mathrm{m}}\left(= P/\pi a_0^{\,2}\right)$. Equation (3.10) implies that the contact pressure $p(r)\left(\equiv -\sigma_z(\rho,0)\right)$ has its minimum value at the center of contact ($\rho = 0$), and then increases monotonically with the increase in ρ to infinity at the edge of the flat-punch, i.e., at $\rho = 1$.

On the other hand, the displacement $u_z(r,0)$ of the free surface outside the contact zone ($\rho \ge 1$), namely the sink-in of the free-surface, is described by

$$\begin{aligned} u_z(\rho,0) &= \frac{2h}{\pi}\sin^{-1}\frac{1}{\rho} \\ &= \frac{1}{\pi E'}\frac{P}{a_0}\sin^{-1}\frac{1}{\rho} \end{aligned} \tag{3.11}$$

where use has been made of the relations $\chi'(t) = 0$ and $\chi(1) = 2h/\pi$ in Eq. (3.8).

3.2 SPHERICAL INDENTER (HERTZIAN CONTACT)

The displacement of the surface of an elastic half-space contacted with a spherical indenter (radius *R*) is shown in Fig. 3.3, where the shape function $f(\rho)$ of spherical indenter is given by

$$\begin{aligned} f(\rho) &= R - \sqrt{R^2 - a^2\rho^2} \\ &\approx \frac{1}{2}\frac{a^2}{R}\rho^2; \quad a \ll R \end{aligned} \tag{3.12}$$

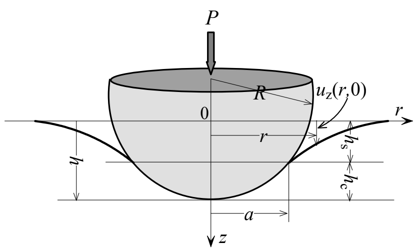

Figure 3.3 The surface-displacement of an elastic half-space indented by a sphere (Hertzian contact)

We will assume $a \ll R$ in the following considerations for simplicity. In fact, it is well known that the approximation given in Eq. (3.12) is sufficient enough for describing the experimental results in the region of $a \le 0.4R$. Hence, by applying the approximation $f(\rho) \approx \left(a^2\rho^2/2R\right)$ to Eq. (3.4), we have the following Sneddon's function $\chi(t)$;

$$\chi(t) = \frac{2}{\pi}\left[h - \frac{a^2}{R}t^2\right] \tag{3.13}$$

Furthermore, the substitutions of Eq. (3.12) into Eq. (3.6) and of Eq. (3.13) into Eq. (3.7) lead to the following P - h relation along with the contact stress distribution $\sigma_z(\rho,0)$ of spherical indentation;

$$P = 2aE'\left(h - \frac{1}{3}\frac{a^2}{R}\right) \tag{3.14}$$

$$\sigma_z(\rho,0) = -\frac{E'}{2a}\left[\frac{\chi(1)}{\sqrt{1-\rho^2}} + \frac{4a^2}{\pi R}\sqrt{1-\rho^2}\right]; \quad 0 \le \rho \le 1 \tag{3.15}$$

As has been mentioned in the preceding section, the contact stress $\sigma_z(\rho,0)$ of cylindrical flat-punch changes in a discontinuous manner at the contact periphery, i.e. $\sigma_z(\rho,0) \uparrow -\infty$ at $\rho = 1-\varepsilon\ (\varepsilon \downarrow 0)$ and $\sigma_z(\rho,0) \equiv 0$ at $\rho = 1+\varepsilon\ (\varepsilon \downarrow 0)$. This discontinuity in the contact stress is resulted from the discontinuous flexion of the contact surface at $\rho = 1$, as depicted in Fig. 3.2, while the free surface of sphere-indented elastic body changes continuously from the indented area to the outside of the contact, as shown in Fig. 3.3. In addition to this fact, when we notice the fact that the surface free-energy, i.e. the surface tension, is negligibly small in the indentation contact of an elastic body having higher elastic modulus (refer to Chapter 8), the contact stress $\sigma_z(\rho,0)$ at the contact boundary [$\rho = 1-\varepsilon \quad (\varepsilon \downarrow 0)$] is required to coincide with the stress $\sigma_z(\rho,0) = 0(\rho \ge 1)$ of the free surface outside the contact zone, leading to

$$\chi(1) = 0 \tag{3.16}$$

in Eq. (3.15). The contact radius a and the contact load P in Hertzian contact problems, therefore, are expressed in terms of the penetration depth h, as follows

$$a = \sqrt{R}h^{1/2} \tag{3.17}$$

$$P = \frac{4}{3}E'\sqrt{R}h^{3/2} \tag{3.18}$$

where uses have been made of Eqs. (3.13) and (3.14). Equation (3.18) means that the indentation load P increases linearly with the increase in the penetration depth $h^{3/2}$, and the slope of this linear line gives the elastic modulus E' of the elastic body indented. Furthermore, combining

Eqs. (3.15), (3.17), and (3.18), the contact stress distribution $\sigma_z(\rho,0)$ is written by

$$\frac{\sigma_z(\rho,0)}{p_{\mathrm{m}}} = -\frac{3}{2}\sqrt{1-\rho^2}\,; \quad 0 \le \rho \le 1 \tag{3.19a}$$

or

$$\frac{\sigma_z(\rho,0)}{p_0} = -\sqrt{1-\rho^2}\,; \quad 0 \le \rho \le 1 \tag{3.19b}$$

in which $p_{\mathrm{m}} = P/\left(\pi a^2\right)$ and $p_0 = (3/2)p_{\mathrm{m}}$ are the mean and the maximum contact pressures, respectively.

Equation (3.8) combined with Eq. (3.13) describes the sink-in profile $u_z(\rho,0)$ of the free-surface outside the contacted area ($\rho > 1$);

$$\begin{aligned} u_z(\rho,0) &= \frac{a^2}{\pi R\rho^2}\left[\left(2-\rho^2\right)\sin^{-1}\frac{1}{\rho} + \sqrt{\rho^2-1}\right] \\ &= \frac{h}{\pi\rho^2}\left[\left(2-\rho^2\right)\sin^{-1}\frac{1}{\rho} + \sqrt{\rho^2-1}\right]; \quad \rho \ge 1 \end{aligned} \tag{3.20}$$

The sink-in depth h_{s} at the contact periphery (see Fig. 3.3) is $h_{\mathrm{s}}\left(= u_z\left(1,0\right)\right) = h/2$ that is obtained by substituting $\rho = 1$ into Eq. (3.20), resulting in the contact depth $h_{\mathrm{c}} = h/2$. The relative contact depth $\eta_{\mathrm{c}}\left(= h_{\mathrm{c}}/h\right)$ for Hertzian contact is, therefore,

$$\eta_{\mathrm{c}}\left(\equiv \frac{h_{\mathrm{c}}}{h}\right) = \frac{1}{2} \tag{3.21}$$

that is independent of the penetration depth *h*.

3.3 CONICAL INDENTER

The surface deformation of an elastic half-space indented by a cone with its inclined face-angle of β is shown in Fig. 3.4. The shape function of the indenter is described by

$$f(\rho) = a\rho\tan\beta \tag{3.22}$$

The Sneddon's function $\chi(t)$ in Eq. (3.4) combined with Eq. (3.22) is given by

$$\begin{aligned} \chi(t) &= \frac{2}{\pi}\left(h - ta\tan\beta\int_0^t \frac{1}{\sqrt{t^2-x^2}}dx\right) \\ &= \frac{2h}{\pi} - ta\tan\beta \end{aligned} \tag{3.23}$$

When we notice the fact that the boundary value of

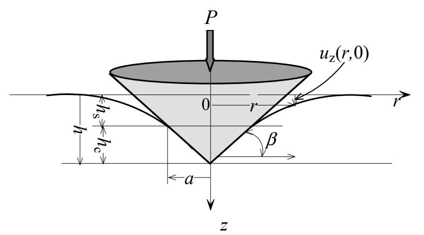

Figure 3.4 The surface displacement of an elastic half-space contacted with a conical indenter

$\chi(1) = 2h / \pi - a \tan \beta$ must satisfy the physical requirement of $\chi(1) = 0$ at the contact periphery like as Eq. (3.16) for the Hertzian contact, we finally obtain the following relationship between the contact radius *a* and the depth of penetration *h*;

$$a = \frac{2\cot\beta}{\pi} h \tag{3.24}$$

Furthermore, conducting similar mathematical operations that we made in the Hertzian contact problem, we have the following key results for conical indentation contact;

$$P = \frac{2\cot\beta}{\pi} E' h^2 \tag{3.25}$$

$$\frac{\sigma_z(\rho,0)}{p_{\mathrm{m}}} = -\cosh^{-1}\frac{1}{\rho}; \quad 0 < \rho \le 1 \tag{3.26}$$

$$u_z(\rho,0) = \frac{2h}{\pi}\left[\sin^{-1}\frac{1}{\rho} - \rho + \sqrt{\rho^2 - 1}\right]; \quad \rho \ge 1 \tag{3.27}$$

Equation (3.25) means that the indentation load P increases linearly with the increase in the penetration depth h^2, and the slope of this linear line gives the elastic modulus E' of the body indented. Substitution of $\rho = 1$ into Eq. (3.27) leads to the contact depth $h_{\mathrm{c}}\left[\equiv u_z(1,0)\right]$, and then yields the relative contact depth $\eta_{\mathrm{c}}\left(= h_{\mathrm{c}}/h\right)$ as follows;

$$\eta_{\mathrm{c}}\left(\equiv \frac{h_{\mathrm{c}}}{h}\right) = \frac{2}{\pi} \tag{3.28}$$

As in the case of spherical indentation contact, for the conical indentation contact as well, the relative contact depth η_{c} is always *independent of the total penetration depth* h. We show in Figs. 3.5 and 3.6 the tip-geometry dependence of the normalized contact stress distribution $\sigma_z(\rho,0)/p_{\mathrm{m}}; \rho \le 1$ and the normalized surface displacement $u_z(\rho,0)/h; \rho \ge 1$ plotted against the normalized contact radius $\rho(\equiv r/a)$ for the flat-punch, sphere, and the cone indentations, respectively.

In the preceding considerations, the experimentally observable relations, i.e. the indentation load *P* vs. the penetration depth *h* relations, have been given in Eqs. (3.9), (3.18), and (3.25) for the respective indenter's tip-geometries. These P - h relations are essential in

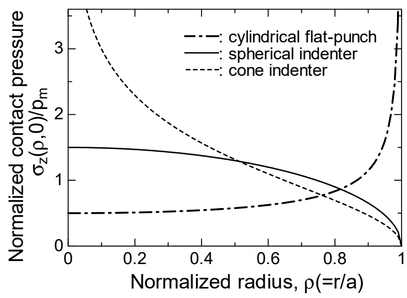

Figure 3.5 Normalized contact stress distributions for flat-ended cylindrical punch, spherical, and conical indenters

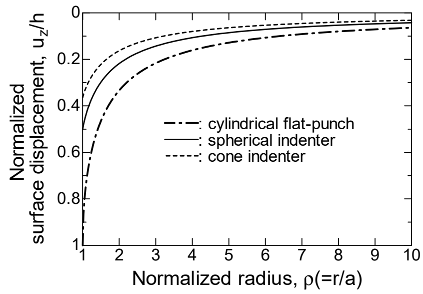

Figure 3.6 Normalized surface deformations (sink-in profiles) of elastic half-space indented by flat-ended cylindrical punch, spherical, and conical indenters

experimentally determining the plane-strain elastic modulus E' of the tested body. It must be noticed in this context that both Eq. (3.18) ($P \propto h^{3/2}$) and Eq. (3.25) ($P \propto h^2$) of spherical/conical indentations do not satisfy the *linear* P - h relationship although the body tested is *perfectly elastic*. However, once we introduce the following *indentation strain* ε_{I}, we have the generalized Hook's law of $p_{\mathrm{m}} = E'\varepsilon_{\mathrm{I}}$ through using the mean contact pressure $p_{\mathrm{m}} \left(= P/\pi a^2\right)$, where the indentation strain ε_{I} is defined as follows;

Flat-ended cylindrical punch:

$$\varepsilon_{\mathrm{I}} = \frac{2}{\pi}\left(\frac{h}{a_0}\right) \tag{3.29}$$

Spherical indenter：

$$\varepsilon_{\mathrm{I}} = \frac{4}{3\pi}\left(\frac{a}{R}\right)\left(= \frac{4}{3\pi}\sqrt{\frac{h}{R}}\right) \tag{3.30}$$

Conical indenter:

$$\varepsilon_{\mathrm{I}} = \frac{\tan\beta}{2} \tag{3.31}$$

It must be noticed in these equations that the indentation strain ε_{I} of *conical indenter* is independent of the penetration depth h, not like the flat-punch and the spherical indenter. This fact is resulted from the *geometrical similarity* of the conical indenter, i.e., the contact radius a linearly changes with the penetration depth h as shown in Eq. (3.24). The geometrical similarity of cone/pyramid indenters is, therefore, very essential in quantitatively as well as easily determining the material characteristics not only in elastic but also in elastoplastic/viscoelastic regimes. This is the reason why the cone/pyramid indenters have long been conventionally utilized in the history of indentation contact mechanics.

As mentioned in the preceding considerations, we have the linear relation between the mean contact pressure $p_{\mathrm{m}} \left(= P/\pi a^2\right)$ and the indentation strain ε_{I};

$$p_{\mathrm{m}} \left(= P/\pi a^2\right) = E'\varepsilon_{\mathrm{I}} \tag{3.32}$$

This simple linear relation implies the fact that *the indentation contact* *area $A(=\pi a^2)$ plays a very essential role in the indentation contact mechanics not only in the elastic but also in the elastoplastic/ viscoelastic regimes, as well. We will discuss/emphasize in the following chapters that the in-situ measurement of the contact area A along with the indentation load P is a very essential requisite for quantitatively determining the material characteristics in the elastic/elastoplastic/ viscoelastic indentation tests.*

Among the indentation contact responses for various types of tip-geometry of the indenters discussed in Sec. 3.1-3.3, the most essential ones are the $P-h$, $a-h$, and the $a-P$ relations;

$$P = k_h E' h^n \tag{3.33}$$

$$\begin{aligned} a\left(\equiv \sqrt{A/\pi}\right) &= Bh^{n-1} \\ &= cP^{(n-1)/n} \end{aligned} \tag{3.34}$$

The parameters denoted in these equations are listed in Table 3.1.

Table 3.1 List of indentation contact parameters

	flat-ended cylindrical punch	spherical indenter	conical indenter
$f(\rho)$	0	$\left(a^2/2R\right)\rho^2$	$a\rho\tan\beta$
$\sigma_z(\rho,0)/p_m$	$-1/2\sqrt{1-\rho^2}$	$-3\sqrt{1-\rho^2}/2$	$-\cosh^{-1}(1/\rho)$
n	1	$3/2$	2
k_h	$2a_0$	$4\sqrt{R}/3$	$2\cot\beta/\pi$
B	a_0	$\sqrt{R}$	$2\cot\beta/\pi$
c	a_0	$\left(3/4E'\right)^{1/3} R^{1/3}$	$\sqrt{2\cot\beta/\pi E'}$
h_c/h	1	$1/2$	$2/\pi$
ε_I	$2h/\pi a_0$	$(4/3\pi)\sqrt{h/R}$	$\tan\beta/2$

* $\rho = r/a$

ONSET OF PLASTIC YIELD AND INDENTATION CONTACT PROBLEMS

CHAPTER 4

Engineering materials including metals and ceramics deform in elastic manners under minute strain. The mechanical work for inducing elastic deformation of these materials leads to the increase in the Gibbs free energy ΔG through the increase in the enthalpy ΔH via the reversible deformation of the inter-atomic separation of these materials. On the other hand, the external work applied to organic polymers/rubbers is stored by the increase in $\Delta G(\approx -T\Delta S)$ through the decrease in the entropy $\Delta S(<0)$ of polymeric chains. Accordingly, the elastic deformation of the former materials is referred to as the enthalpic elasticity, while the latter is named as the entropic elasticity. Once the loads or the constrained displacements of these elastic bodies are taken away, the deformation instantly as well as reversibly disappears, and the body recovers to its original shape and size. **[1.2, 1.3]**

Elasticity is, therefore, the characteristic material property of immediate recovery of deformation upon unloading, while there exists the elastic limit, at which the material experiences a permanent deformation (plastic flow) that is not lost on unloading. This is the beginning of plastic yielding process, in which the shear slip of atomic or molecular planes causes atoms/molecules to move to their new equilibrium positions. The stress-strain curve (S-S curve) of a rod undertaken with a simple tension or compression is schematically depicted in Fig. 4.1. There is a specific stress Y at which the S-S curve becomes nonlinear. This specific stress Y is referred to as the yield stress (or yielding stress, yielding strength), and defines the elastic limit, beyond which the deformation becomes elastoplastic, meaning that the deformation includes not only elastic deformation but also plastic flow as well;

$$\sigma \geq Y \tag{4.1}$$

Equation (4.1) expresses the criterion for the onset of plastic yield for tension/compression. A complete unload from an elastoplastic S-S state results in a finite residual strain ε_p as shown in Fig. 4.1. The residual strain ε_p represents the plastic flow that is induced during loading in the

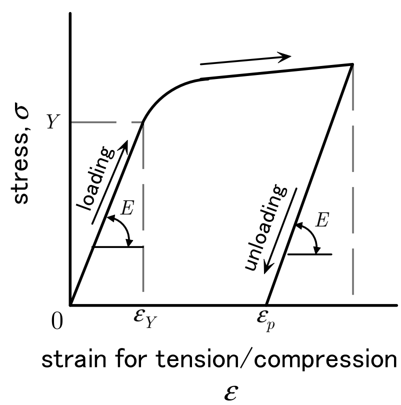

Figure 4.1 Stress-strain curve of a rod undertaken with a simple tension or compression, indicating the onset of plastic yielding at the yield stress Y

plastic region exceeding the elastic limit.

Let us now scrutinize the *microscopic processes for the onset of plastic yield of a metallic single crystal* as a representative of elastoplastic body. Not only normal but also shear deformations are imposed in the three-dimensional crystal under externally applied loads, as mentioned in Chap. 1. Among these deformations, shear deformation contributes to the relative slips of crystalline planes. If the shear deformation is small enough, the relative slips are mechanically reversible, leading to the elastic shear deformation that is dictated by the shear modulus G. However, once the imposed shear stress τ crosses over the characteristic value of k termed the yield stress in shear, these shear slips become irreversible, and lead to the onset of plastic yield. The criterion for the onset of plastic yield in shear, therefore, is written by

$$\tau \geq k \tag{4.2}$$

The criterion for the onset of plastic yield under multi-axial S-S states is rather complicated not like the simple tension/compression or the shear deformation given in Eq. (4.1) or Eq. (4.2); the details will be given in the following considerations.

4.1 MAXIMUM SHEAR STRESS CRITERION -TRESCA CRITERION-

In a simple tension test of a rod with its axial stress σ, the maximum resolved shear stress $\tau_{\max}$ appears on the plane tilted at 45° to the applied axial stress, leading to the correlation of $\tau_{\max} = \sigma/2$. Accordingly, the maximum shear stress criterion, i.e., the Tresca criterion, leads to the following formula;

$$\max\{\sigma\} \geq 2k = Y \tag{4.3}$$

In more general three-dimensional S-S state, the Tresca criterion can be written as follows;

$$\max\{|\sigma_1 - \sigma_2|, |\sigma_2 - \sigma_3|, |\sigma_3 - \sigma_1|\} \geq 2k = Y \tag{4.4}$$

where σ_1, σ_2, and σ_3 stand for the principal stresses. In three dimensions, as shown in Figs. 1.2 and 1.3, not only normal stresses σ_i but also shear stresses τ_{ij} exist on an arbitrary plane. However, as shown in Fig. 4.2, we can find a specific orientation of the coordinate system such that no shear stresses appear, leaving only normal stresses in its three orthogonal directions. The 1-, 2-, and 3-coordinate axes are termed the *principal axes*, and the planes normal to these axes are named as the *principal planes*. *No shear stresses exist on these principal planes* except the normal stresses that are termed the principal stresses of σ_1, σ_2, and σ_3, respectively. In Fig. 4.2, the shear stress τ on the plane encompassed by the white broken lines is induced by the combined normal stresses of σ_1 and σ_2, the maximum shear stress $\tau_{\max}$ of which is written by $\tau_{\max} = |\sigma_1 - \sigma_2|/2$ through a similar consideration made in Eq. (4.3). The Tresca criterion for the onset of plastic yield is, therefore, given by

$$\max\{|\sigma_1 - \sigma_2|\} \geq 2k = Y \tag{4.5}$$

Equation (4.4) is the more generalized extension of Eq. (4.5) in the three-dimensional S-S state.

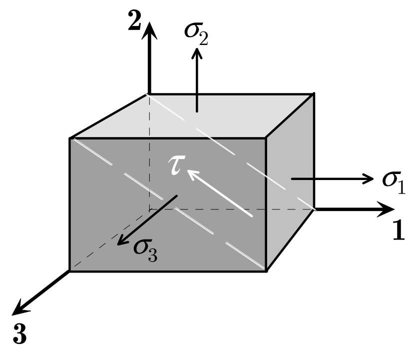

Figure 4.2 Principal axes and principal stresses

4.2 MAXIMUM SHEAR STRAIN ENERGY CRITERION -VON MISES CRITERION-

The Tresca criterion is convenient for using it in practical plastic analyses, but a somewhat better fit to experimental data of ductile metals can often be obtained from the von Mises criterion, on which the onset of plastic yield is dictated with *shear strain energy*. The elastic *strain energy density* U stored in a unit cube (see Fig. 1.2 with $dx = dy = dz = 1$) under a three-dimensional S-S state is given by

$$U = (1/2)(\sigma_x\varepsilon_x + \sigma_y\varepsilon_y + \sigma_z\varepsilon_z + \tau_{xy}\gamma_{xy} + \tau_{yz}\gamma_{yz} + \tau_{zx}\gamma_{zx})$$

having the physical dimension of J/m^3. Applying the elastic constitutive equation, Eq. (2.1), to the above formula of strain energy density, we finally have the following expressions of U in terms of only the stress components:

$$
\begin{aligned}
U &= \frac{1}{2E}\left\{\sigma_x{}^2 + \sigma_y{}^2 + \sigma_z{}^2 - 2\nu\left(\sigma_x\sigma_y + \sigma_y\sigma_z + \sigma_z\sigma_x\right)\right\} \\
&\qquad + \frac{1}{2G}\left(\tau_{xy}^2 + \tau_{yz}^2 + \tau_{zx}^2\right) \\
&= \frac{1}{2K}\sigma_{\mathrm{m}}^2 + \frac{1+\nu}{6E}\left\{\left(\sigma_x - \sigma_y\right)^2 + \left(\sigma_y - \sigma_z\right)^2 + \left(\sigma_z - \sigma_x\right)^2\right\} \\
&\qquad + \frac{1}{2G}\left(\tau_{xy}^2 + \tau_{yz}^2 + \tau_{zx}^2\right)
\end{aligned}
\tag{4.6}
$$

In Eq. (4.6), K stands for the bulk modulus that is related to the Young's modulus with $K = E/\left[3(1-2\nu)\right]$, and the mean normal stress σ_{m} is defined by $\sigma_{\mathrm{m}} = \left(\sigma_x + \sigma_y + \sigma_z\right)/3$. The first term of the right-hand side of the second equation in Eq. (4.6) means the strain energy density associated with volumetric change, and the second and the third terms represent the shear strain energy density U_{S}. As mentioned in the preceding considerations and in Fig. 4.2, when we choose the x -、 y-, and Z -axes as their principal axes, the shear stress components τ_{xy}, τ_{yz}, and τ_{zx} all diminish, then the shear strain energy density U_{S} can be described by the use of the principal stresses of σ_1, σ_2, and σ_3, as follows;

$$
U_{\mathrm{S}} = \frac{1+\nu}{6E}\left\{\left(\sigma_1 - \sigma_2\right)^2 + \left(\sigma_2 - \sigma_3\right)^2 + \left(\sigma_3 - \sigma_1\right)^2\right\} \tag{4.7}
$$

As an example, when a rod yields at $\sigma_1 = Y$ and $\sigma_2 = 0 = \sigma_3$ in a simple tension test, Eq. (4.7) gives $U_{\mathrm{S}}(\text{Tension}) = (1+\nu)Y^2/3E$. On the other hand, in a pure shear test, the onset of plastic yield occurs at $\sigma_1 = -\sigma_2 = k$, and $\sigma_3 = 0$, then Eq. (4.7) results in $U_{\mathrm{S}}(\text{PureShear}) = (1+\nu)k^2/E$ (notice that the mean normal stress $\sigma_m = \left(\sigma_1 + \sigma_2 + \sigma_3\right)/3$ turns to zero in pure shear, leading to the presence of only shear deformations in the body tested). At the onset of plastic yield, the *critical* strain energy densities both in the simple tension and the pure shear tests must agree with each other, i.e., $U_{\mathrm{S}}(\text{Tension}) = U_{\mathrm{S}}(\text{PureShear})$, resulting in the relationship of $Y = \sqrt{3}k$ for the von Mises criterion. These *critical* strain energy densities are also supposed to be equal to Eq. (4.7) in the von Mises criterion, and thus we finally have the following general expression for the onset of plastic yield;

$$\frac{1}{2}\left\{(\sigma_1-\sigma_2)^2+(\sigma_2-\sigma_3)^2+(\sigma_3-\sigma_1)^2\right\}\geq Y^2=3k^2 \quad (4.8)$$

Note that this result of $k = Y/\sqrt{3}$ is somewhat different from the Tresca criterion with $k = Y/2$.

4.3 ONSET OF PLASTIC YIELD UNDER SHERICAL INDENTATION CONTACT

Let us consider the plastic yield induced beneath the contact surface of spherical indentation **[4.1]**. The onset of plastic yield will appear along the penetration axis. i.e., *z*-axis ($\rho = 0$), since the principal stresses $\sigma_1(=\sigma_r)$, $\sigma_2(=\sigma_\theta)$, and $\sigma_3(=\sigma_z)$ have their maximum values on the *z*-axis for spherical indentation contact in an elastic half-space (see Sec. 3.2). These principal stresses are given in the following equations by the uses of Eqs. (2.30) - (2.32), (3.5), and (3.13);

$$\frac{\sigma_r}{p_0}\left(\equiv\frac{\sigma_\theta}{p_0}\right)=-(1+\nu)\left(1-\varsigma\tan^{-1}\frac{1}{\varsigma}\right)+\frac{1}{2\left(1+\varsigma^2\right)} \quad (4.9)$$

$$\frac{\sigma_z}{p_0}=-\frac{1}{1+\varsigma^2} \quad (4.10)$$

where p_0 is the maximum contact pressure defined in Eq. (3.19b), and $\varsigma = z/a$ is the non-dimensional *z*-coordinate normalized with the contact radius *a*. Furthermore, the maximum shear stress $\tau_{\max}(=|\sigma_r-\sigma_z|/2)$ (see Eq. (4.5)) is written by

$$\begin{aligned}\frac{\tau_{\max}}{p_0}&=\frac{|\sigma_r-\sigma_z|}{2p_0}\\ &=\frac{1}{2}\left|-(1+\nu)\left(1-\varsigma\tan^{-1}\frac{1}{\varsigma}\right)+\frac{3}{2\left(1+\varsigma^2\right)}\right|\end{aligned} \quad (4.11)$$

in which uses have been made of the relations of Eqs. (4.9) and (4.10). The analytical result of $\tau_{\max}/p_0$ vs. $\varsigma(=z/a)$ relation is plotted in Fig. 4.3 for the Poisson's ratio of $\nu = 0.3$ as an example. Figure 4.3 actually shows that the shear stress attains its maximum value of $\tau_{\max} = 0.31p_0$ at $z = 0.48a$ along the *z*-axis. Accordingly, the

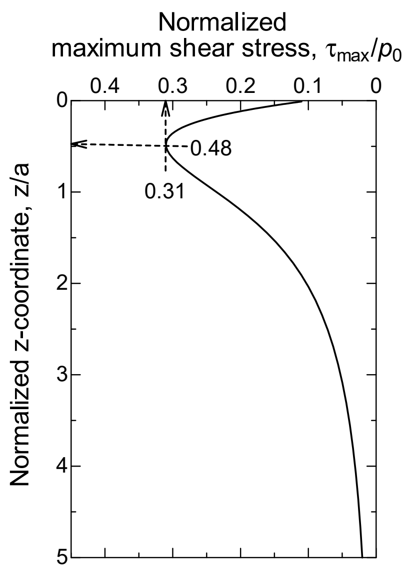

Figure 4.3 Distribution of the maximum shear stress (Eq. (4.11)) along the penetration axis

[4.1] K.L. Johnson, "Contact Mechanics", Cambridge University Press (1985) maximum contact pressure $p_0 \left(\equiv 3p_{\mathrm{m}}/2\right)$ as the threshold for the onset of plastic yield is

$$p_0 \geq 3.2k = 1.6Y , \tag{4.12}$$

for the Tresca criterion ($2\tau_{\max}\left(\equiv \max\left\{\left|\sigma_1 - \sigma_2\right|\right\}\right) \geq 2k = Y$),

and

$$p_0 \geq 2.8k = 1.6Y \tag{4.13}$$

for the Von Mises criterion ($2\tau_{\max}\left(\equiv \max\left\{\left|\sigma_1 - \sigma_2\right|\right\}\right) \geq \sqrt{3}k = Y$).

The preceding considerations combined with the relations of $p_0 = \left(3/2\right) p_{\mathrm{m}}$, $p_{\mathrm{m}} = P/\pi a^2$, Eq. (3.17) and Eq. (3.18), therefore, finally give the threshold Hertzian contact load P_{Y} for the onset of plastic yield;

$$P_{\mathrm{Y}} = \left(1.6\right)^3 \frac{\pi^3 R^2}{6} \frac{Y^3}{E'^2} , \tag{4.14}$$

meaning that the resistance to the plastic flow increases with the increase in Y^3/E'^2 for spherical indentation contact (Hertzian contact). Namely, Eq. (4.14) implies that the elastoplastic body with a larger yield stress and a smaller elastic modulus resists to the onset of plastic flow under Hertzian indentation contact.

Figure 4.4 (the numerical result of finite element analysis (FEA), the details of which will be given in Chap. 10) demonstrates the plastic core beneath the contact surface induced at the threshold Hertzian contact load P_Y . As actually predicted in Eq. (4.11) and in Fig. 4.3, the plastic core appears at the location of z=0.48a that is clearly seen in Fig. 4.4.

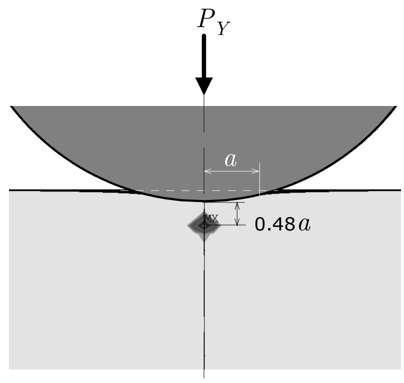

Figure 4.4 A plastic core appears at the location of z=0.48a beneath the contact surface under spherical indentation (FEA-based numerical result with von Mises criterion)

ELASTOPLASTIC INDENTATION CONTACT MECHANICS

CHAPTER 5

5.1 MATERIALS PHYSICS OF THE MEYER HARDNESS

The science and engineering of contact plasticity significantly evolved with the invention of steam locomotives in the second half of 19th century, where the plastic contact deformation induced between the rail and the wheel was very critical. In the beginning of 20th century, the concept and the test methods of indentation hardness were proposed for characterizing the plasticity of metallic materials. The well-known test methods of indentation hardness include "Brinell test" (Johan August Brinell, 1900) and "Vickers test" (Vickers Ltd., 1925). In these tests, the hardness H is defined as the indentation load P divided by the *total contact area* S of the *residual impression*;

$$H = \frac{P}{S}$$

The details for various types of indentation hardness test are given in the Japanese Industrial Standards (JIS) **[5.1]**.

The physics of indentation contact hardness as a material characteristic parameter was first examined by E. Meyer in 1908. He defined the Meyer hardness H_M as the indentation load P divided by the *projected contact area* A_{proj} of *residual impression*;

$$H_M = \frac{P}{A_{proj}} \tag{5.1a}$$

He emphasized the importance of *projected contact area* in determining the contact hardness through the theoretical considerations on the mechanical processes of spherical/conical indentation. In ductile metals, the projected contact area A *at the maximum indentation load* approximately equals its projected contact area of the residual impression A_{proj}, i.e. $A \cong A_{proj}$, because the *elastic recovery in unloading* is negligibly small. However, in ceramics and organic polymers, due to a significant elastic recovery of contact impression during indentation unloading, there always exists the relation of $A > A_{proj}$. Accordingly, when we want not only to measure the plasticity, but also to characterize the elasticity in an indentation contact test, the use of contact area A_{proj}

[5.1] Examples;

JIS Z2243, "Brinell Hardness Test" (2008)

JIS Z2244, "Vickers Hardness Test" (2009)

JIS Z2245, "Rockwell Hardness Test" (2011)

JIS Z2246, "Shore Hardness Test" (2000)

of the residual impression we get it after a complete elastic recovery is inappropriate. *In-situ measurement* of the projected contact area A *at the indentation load* P is very essential in characterizing the elasticity/plasticity of the material indented. In this text, therefore, we redefine the Meyer hardness H_M by the use of the projected contact area A at the indentation load P, as follows;

$$H_M = \frac{P}{A} \tag{5.1b}$$

We use Eq. (5.1b) as the definition of the Meyer hardness, since the projected contact area A *under load* is very essential for understanding the materials physics of indentation contact mechanics, the details of which will be discussed in the following chapters. However, upon using the conventional instrumented indentation apparatuses, it is impossible in experiments for us to determine the projected contact area A *under load*, though these apparatuses are capable of determining the penetration depth h in relation to the associated indentation load P. This fact implies that we cannot determine in *a quantitative manner* not only the Meyer hardness, but also the material characteristics (elastic modulus, yield stress, viscoelastic functions, etc.) on the conventional indentation apparatuses. We have to circumvent this difficulty through making an appropriate approximation/assumption to estimate A from the observed P - h relation prior to determining the material characteristics. The *instrumented indentation microscope* has been designed to overcome this essential difficulty in conventional instrumented indentation testing. The indentation microscope enables in-situ measurement of the projected contact area A in relation to the applied indentation load P. The details (the concept/principle of measurement, the mechanical structure of the apparatus, experimental procedure for determining material characteristics, etc.) of the indentation microscope will be given in Sec. 11.3.

Let us first consider the Meyer hardness of a *perfectly elastic body*. The Meyer hardness of an elastic body is related to its elastic modulus E' via Eq. (5.2) combined with Eq. (3.32);

$$H_M \left(= \frac{P}{A_e} \right) = \varepsilon_I E' \tag{5.2}$$

where A_e stands for the projected contact area created at the indentation load P (the subject index "e" means "elastic"), and ε_{I} is the indentation strain that has been defined in Eqs. (3.29) - (3.31). As emphasized in Chap. 3, the indentation strain ε_{I} depends not only on the tip-geometry of the indenter, but also on the depth of penetration for flat-ended cylinder and sphere. Once we apply Eqs. (3.29) - (3.31) to Eq. (5.2), the H_{M} vs. E' relations for the respective tip-geometries of indentation are given as follows;

Flat-ended cylindrical punch:

$$H_{\mathrm{M}} = \frac{2}{\sqrt{\pi A_0}} h \cdot E' \tag{5.3}$$

Spherical indenter: $$H_{\mathrm{M}} = \frac{4}{3\pi^{3/2} R} \sqrt{A_{\mathrm{e}}} \cdot E' \tag{5.4}$$

Conical indenter: $$H_{\mathrm{M}} = \frac{\tan\beta}{2} \cdot E' \tag{5.5}$$

The Meyer hardness of flat-ended cylindrical punch exhibits a linear increase with the increase in the penetration depth h, i.e., $H_{\mathrm{M}} \propto h$, due to the invariance of the contact area A_0. In spherical indentation, on the other hand, the Meyer hardness depends on the square root of the projected contact area or the square root of the penetration, i.e., $H_{\mathrm{M}} \propto \sqrt{A_{\mathrm{e}}} \big/ R \propto \sqrt{h/R}$. In contrast to the tip-geometries of these indenters, the Meyer hardness of *conical indentation*, however, is *independent of the depth of penetration*, *resulting in a constant value of the hardness that is proportional to the elastic nodulus* E'. This fact is very essential in characterizing the mechanical characteristics from the Meyer hardness observed in experiments. The geometrical similarity of the cone indentation (the linear relation between the penetration depth and the contact radius; $a \propto h$ as shown in Eq. (3.24)) actually results in the Myer hardness that is *independent of the depth of indentation penetration*. In the history of indentation contact mechanics, this geometrical similarity of indentation yields the reason why the cone indenter (Rockwell indenter) and the pyramid indenters (Vickers indenter, Berkovich indenter) have long been utilized as the standard test methods for determining the contact hardness numbers.

Let us now consider the elastic limit and the onset of plastic yield that appears when the indentation strain ε_{I} increases to its threshold value of $\varepsilon_{\mathrm{IY}}$ (see Fig. 4.1). The indentation strain ε_{I} increases with the increase in the penetration depth h of a flat-ended cylindrical punch or a spherical indenter. It is also possible for us to increase ε_{I} by the use of a spherical indenter with smaller radius R, or a conical indenter with larger inclined face angle β. When ε_{I} reaches to it threshold value of $\varepsilon_{\mathrm{IY}}$, the plastic core appears beneath the contact surface, as shown in Fig. 4.4 for a spherical indentation by way of example. The Meyer hardness at the threshold strain $\varepsilon_{\mathrm{IY}}$ is given by

$$H_{\mathrm{M}}\left(=\varepsilon_{\mathrm{IY}} E'\right) \approx Y, \tag{5.6}$$

as has been suggested both in the Tresca and in the von Mises criteria (see Eqs. (4.12) and (4.13)). In other words, the plastic yield is resulted in when the *elastic* Meyer hardness $\varepsilon_{\mathrm{I}} E'$ (Eq. (5.2)) increases up to the yield stress Y.

Most of *ductile materials* fall into the category of *perfectly plastic body* (*fully plastic body*), once the plasticity overwhelms the elasticity in the indentation-induced deformation. The Meyer hardness of a *fully plastic body* is independent of the indentation strain ε_{I}, and described by

$$H_{\mathrm{M}}\left(=\frac{P}{A_{\mathrm{p}}}\right)=cY \tag{5.7}$$

in which A_{p} means the projected contact area of indentation (the subject index "p" stands for plasticity). The major of plastic deformation induced beneath the indentation contact surface is accommodated in the elastic field surrounding the plastic core of indentation. However, when the plastic deformation becomes so significant that the surrounding elastic field becomes insufficient for accommodating this plastic deformation, the excess of the in-surface plastic deformation flows out to the free surface, resulting in the indentation pile-up. On the other hand, the surface energy (i.e., the surface tension) of the free surface constrains this plastic flow-out. The constraint factor c in Eq. (5.7) thus describes the constraint resistance to the plastic flow-out. The constraint factor c is not only dependent on the tip-geometry of the indenter used, but also on the contact friction. The experimental results along with the FEM-based numerical analyses suggest that the constraint factor c ranges from 2.5

to 3.5, i.e., $2.5 \le c \le 3.5$ **[4.1]**.

The elastoplastic deformation induced with indentation contact can therefore be divided into the following three regions **[4.1]**:

$H_M < Y$:	elastic region	(5.8a)
$Y \le H_M < cY$:	elastoplastic region	(5.8b)
$H_M \approx cY$:	fully plastic region	(5.8c)

Since the Meyer hardness is described by $H_M = \varepsilon_I E'$ (see Eq. (5.2)) in the elastic region ($H_M/Y < 1$), Eq. (5.8a) can be rewritten with

$$\frac{\varepsilon_I E'}{Y} < 1 \tag{5.9}$$

$$\varepsilon_I = \frac{2}{\pi}\frac{h}{a_0} \quad ; \text{flat-ended cylindrical punch}$$

$$\varepsilon_I = \frac{4}{3\pi}\frac{a}{R} \quad ; \text{spherical indenter}$$

$$\varepsilon_I = \frac{\tan\beta}{2} \quad ; \text{conical/pyramidal indenter}$$

Namely, the deformation of an *elastoplastic* body having the elastic modulus of E' and the yield stress of Y is always *perfectly elastic* when the indentation strain ε_I applied to the body satisfies $\varepsilon_I E'/Y < 1$ (elastic region). *Accordingly, in the elastic region, the Meyer hardness is a material characteristic parameter for representing the elastic modulus* E', i.e., $H_M = \varepsilon_I E'$. On the other hand, *the Meyer hardness represents the yield stress* Y*, i.e.,* $H_M = cY$ *in the fully plastic region* ($\varepsilon_I E'/Y > 20$), *while in the elastoplastic region* ($1 < \varepsilon_I E'/Y < 20$)*, it is an elastoplastic parameter given as a function of* E' *and* Y*, the details of which will be given in the followings.*

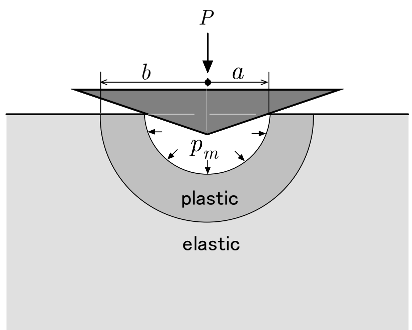

Figure 5.1 Cavity model of an elastoplastic indentation contact by a cone; the model comprises a hemi-spherical cavity of radius a with internal hydrostatic contact pressure $p_m\left(=P/\pi a^2\right)$. The cavity is surrounded by a plastic core with radius b embedded in an elastic half-space

(1) Cavity model [4.1]

Figure 5.1 shows the cavity model of the Meyer hardness, where a cone indenter with the inclined face angle β (see Fig. 3.4) is pressed onto the free surface of an elastoplastic half-space with the elastic modulus E' and the yield stress Y. The cavity model comprises (i) a hemi-spherical cavity of radius a with the internal hydrostatic contact pressure, $p_m\left(=P/\pi a^2\right)$, (ii) a plastic core ($a < r \le b$) with radius b surrounding the cavity, which is embedded in (iii) an elastic half-space ($r > b$). The

volume of the cavity ($\equiv (2\pi/3)a^3$) stands for the excluded volume of indentation. The materials (atoms and molecules) thus excluded from the cavity is assumed to be accommodated in the elastic half-space through the plastic core. In the cavity model, therefore, the indentation contact mechanics is simply reduced to the elastoplastic continuum mechanics of a semi-infinite elastic half-space with a surface cavity of radius *a* that is surrounded by a plastic core of radius *b*, where the cavity is subjected to the hydrostatic pressure of p_m. The cavity model finally gives the following formula for the Meyer hardness,
$H_{\mathrm{M}}(\equiv p_{\mathrm{m}}) = P/\pi a^2$ **[4.1]**:

$$\frac{H_{\mathrm{M}}}{Y} = \frac{2}{3}\left[2 + \ln\left(\frac{(1+\nu)}{3}\varepsilon_{\mathrm{I}}\frac{E'}{Y} + \frac{2(1-2\nu)}{3(1-\nu)}\right)\right] \qquad (5.10a)$$

Equation (5.10a) is simply rewritten by

$$\frac{H_{\mathrm{M}}}{Y} = \frac{2}{3}\left[2 + \ln\left(\frac{1}{2}\varepsilon_{\mathrm{I}}\frac{E'}{Y}\right)\right] \qquad (5.10b)$$

for incompressible elastoplastic body with $\nu = 1/2$. It must be noticed that the cavity model can describe the indentation contact behavior *only in the elastoplastic region* (Eq. (5.8b)). The model neither can be applied to the elastic region (Eq. (5.8a)), nor to the fully plastic region (Eq. (5.8c)). In the subsequent section, we will introduce a unified theory that is fully capable of describing the Meyer hardness from the perfectly elastic to the fully plastic regions.

(2) Unified theory of the Meyer hardness:
The additivity principle of the excluded volume of indentation

The theory describes the Meyer hardness H_{M} in terms of the elastic modulus E' and the yield stress Y as a function of the tip-geometry of indentation in *a unified manner* that encompasses the elastoplastic Meyer hardness ranging from perfectly elastic to fully plastic indentation contacts. Since the theory is based on a phenomenological principle, i.e., a thermodynamic principle, any of elastoplastic models can be adopted. In this textbook, we apply an energy-based consideration to the preceding cavity model. Let us consider the virtual increment of the Gibbs free energy δG that is associated with the virtual increment of the excluded volume δV under the virtual increment of the contact pressure from $p_m\left(\equiv P / \pi a^2\right)$ to $p_m + \delta p$ acting on the internal surface of the cavity. The increment of the free energy, i.e., the externally applied work $\delta W\left(\equiv \delta G\right)$ is, therefore, given by

$$\delta W\left(\equiv p_{\mathrm{m}}\delta V\right) = p_{\mathrm{m}}\delta V_{\mathrm{e}} + p_{\mathrm{m}}\delta V_{\mathrm{p}} \tag{5.11}$$

where the higher-order term of $\delta p \cdot \delta V$ is assumed to be negligibly small. In Eq. (5.11), δV_{e} and δV_{p} are the volumetric increments associated with the elastic and plastic indentation deformations, respectively. The first term ($p_{\mathrm{m}}\delta V_{\mathrm{e}}$) in the right-hand side of Eq. (5.11) stands for the elastic stored energy, and the second term ($p_{\mathrm{m}}\delta V_{\mathrm{p}}$) is the energy dissipation associated with plastic flow.

Equation (5.11) is thus rewritten by $\delta V = \delta V_{\mathrm{e}} + \delta V_{\mathrm{p}}$, and then finally we have *the additivity principle of excluded volume of indentation* as follows;

$$V = V_{\mathrm{e}} + V_{\mathrm{p}} \tag{5.12}$$

Let us consider the alternative expression of this additivity principle in terms of the contact area *A*. Since the excluded volume *V* is related to the contact area *A* via $V = \left(\tan\beta / 3\sqrt{\pi}\right) \cdot A^{3/2}$ for cone/pyramid indentation (inclined face-angle of β), and to $V = \left(1/6\pi R\right) \cdot A^2$ ($a/R \ll 1$) for spherical indentation (radius of *R*), there exists the relation of $V \propto A^m$ ($m = 3/2$ for cone/pyramid indenter; $m = 2$ for spherical indenter). The additivity principle of the excluded volume, therefore, finally results in the following formula of the contact area A;

$$A^m = A_{\mathrm{e}}^{\,m} + A_{\mathrm{p}}^{\,m} \tag{5.13a}$$

or

$$\frac{A_{\mathrm{p}}}{A} = \left[\frac{\left(A_{\mathrm{p}} / A_{\mathrm{e}}\right)^m}{1 + \left(A_{\mathrm{p}} / A_{\mathrm{e}}\right)^m}\right]^{1/m} \tag{5.13b}$$

In these equations, A is the contact area of an *elastoplastic body* (elastic modulus E' and yield stress Y) generated by the indentation load of P. A_{e} and A_{p} are, respectively, the contact areas of a *perfectly elastic* *body* with the elastic modulus E' and of a *fully plastic body* with the yield stress of Y; *both are created by the same indentation load* P *and the same tip-geometry of the indenter applied to the elastoplastic body*. Substituting $A = P/H_M$ (Eq. (5.1b)), $A_e = P/\varepsilon_I E'$ (Eq. (5.2)), and $A_p = P/cY$ (Eq. (5.7)) into Eq. (5.13b), we can express the elastoplastic Meyer hardness H_M in terms of the elastic modulus E' and the yield stress Y, as follows;

$$\frac{H_M}{cY} = \left[\frac{\left(\frac{\varepsilon_I E'}{cY}\right)^m}{1 + \left(\frac{\varepsilon_I E'}{cY}\right)^m} \right]^{1/m} \tag{5.14}$$

$m = 3/2$; conical indenter

$m = 2$; spherical indenter

It should be emphasized that Eq. (5.13b) is equivalent to Eq. (5.14), though these equations are expressed in somewhat different ways. Equation (5.13b) plays an important role in determining the elastoplastic material characteristics, once we directly measure the P - A relation in experiments by the use of the "instrumented indentation microscope" (refer to the details in Chap. 11). The elastoplastic parameter $\varepsilon_I E'/cY (\equiv A_p/A_e)$ in Eq. (5.14) represents the relative ratio of plastic to elastic deformation, namely, describes the amount of plastic deformation relative to the elastic deformation. In this text book, therefore, we define it as the <u>*plastic index, PI*</u> ; $PI = \varepsilon_I E'/cY$.

The comparison between the cavity model (Eqs. (5.10a), (5.10b)) and the unified theory of volumetric additivity (Eqs. (5.13b), (5.14)) is shown in Fig. 5.2. As emphasized in the preceding considerations, the cavity model is applicable only in the elastoplastic region, while the additivity principle analytically predicts the elastic/plastic indentation contact encompassing the all ranges from perfectly elastic to fully plastic deformation. As recognized in Fig. 5.2 and in Eq. (5.14), the elastoplastic contact behavior depends not only on the elastoplastic characteristics E'/cY, but also on the tip-geometry of the indenter used (spherical, conical indenters, etc.) via ε_I. The elastoplastic contact

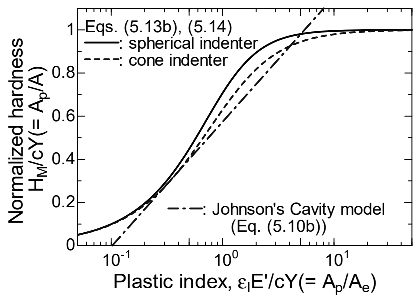

Figure 5.2 The relation between the normalized hardness and the plastic index. The unified theory of volumetric additivity (Eqs. (5.13b) and (5.14)) is given by the solid (spherical indentation) and the broken (conical indentation) lines. The Johnson's cavity model (Eq. (5.10)) is given by the dashed-dotted line.

behavior is, therefore, classified in terms of the plastic index *PI*, as follows;

perfectly elastic region:	$PI<0.2$	sphere; cone
elastoplastic region:	$0.4 \le PI<8$	sphere
	$0.4 \le PI<20$	cone
fully plastic region:	$PI \ge 8$	sphere
	$PI \ge 20$	cone

The validity and the reliability are scrutinized in Fig. 5.3 for the additivity principle of the excluded volume of indentation, where the analytical predictions of the volumetric additivity principle (the solid and the broken lines) are compared with the finite-element-based numerical results (the triangles and circles). As clearly seen in Fig. 5.3, *the analytical results based on the principle of volumetric additivity faithfully as well as precisely predict the FEA-based numerical results not only for spherical but also for conical indentation contacts*.

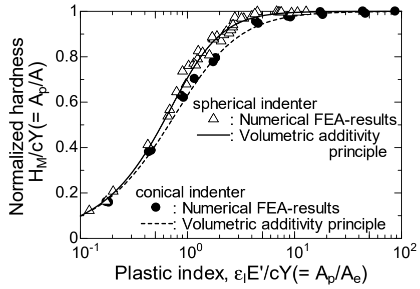

Figure 5.3 Normalized Meyer hardness vs. plastic index plots in spherical and conical indentation contacts: The solid and the broken lines are the analytical predictions (Eqs. (5.13b) and (5.14)) of the volumetric additivity principle; the symbols (triangles△ and circles●) are the finite-element-based numerical results

(3) Elastoplastic deformation and flow of cone/pyramid indentation

As mentioned in the preceding sections, due to the geometrical similarity of cone/pyramid indentation, the Meyer hardness is independent of the penetration depth, leading to the relation of $P = H_M \cdot A \propto a^2 \propto h^2$. Accordingly, it will be easily expected in cone/pyramid indentation that the indentation load P is proportional to the square of penetration depth h^2, i.e., the indentation load linearly increases with the increase in h^2. Figure 5.4 shows the numerical results of finite element analysis (FEA); the P - h^2 hysteresis relations are demonstrated for the perfectly elastic (*PI* (= $\varepsilon_I E'/cY$)=0.05) , elastoplastic (*PI*=1.0), and the fully plastic (*PI*=20) bodies in their loading/unloading cycles of the Vickers/Berkovich equivalent cone indentation. In all ranges of the perfectly elastic to the fully plastic indentation contact, the loading P - h^2 relations (the solid lines) are linear. It should be noticed, as shown in Fig. 5.4, that the subsequent unloading P - h^2 relations (the broken lines) are also linear; the loading linear P - h^2 line coincides with the subsequent unloading linear lines for the perfectly elastic body with *PI*=0.05. The slopes of

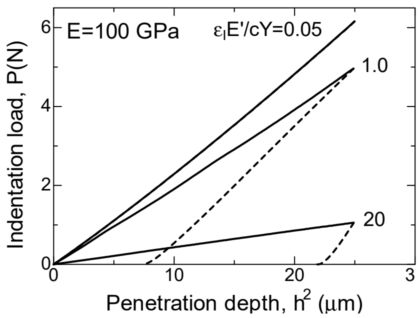

Figure 5.4 P - h^2 hysteresis relations of the elastic (*PI*=0.05), elastoplastic (*PI*=1.0), and the fully plastic bodies (*PI*=20) in their loading/unloading cycles of the Vickers/Berkovich equivalent cone (FEA-based numerical results). The solid and the broken lines indicate the loading and the subsequent unloading P - h^2 relations, respectively.

loading/unloading P - h^2 linear relations are intimately related to the material characteristic parameters of the Meyer hardness H_M, elastic modulus E', and the yield stress Y, the details of which will be given in the subsequent chapters.

Outside the contact area of indentation, the free-surface of an *elastic* half space always sinks-in along with the penetration, i.e., $\eta_c(\equiv h_c/h)<1$. As discussed in Chap. 3, $\eta_c(\equiv h_c/h)=1/2$ for spherical indentation, and $\eta_c(\equiv h_c/h)=2/\pi$ for conical indentation (refer to Figs. 3.3 and 3.4; Eqs. (3.21) and (3.28), and Table 3.1). On the other hand, due to a significant plastic deformation of *elastoplastic* indentation contact (*PI*>0.4), the indentation-displaced molecules/atoms beneath the contact area flow out to the free-surface, resulting in a pile-up outside the contact area, i.e., $\eta_c(\equiv h_c/h)>1$. The FEA-based numerical results of the relative contact depth h_c/h *under load* are plotted against the plastic index $PI(\equiv\varepsilon_I E'/cY)$ in Fig. 5.5 for the Vickers/Berkovich equivalent cone, where the transition from sinking-in to piling-up occurs at about *PI*=6. Figure 5.6 shows the side views of the surface profiles outside the contact area of the equivalent cone at the penetration depth of *h*=5μm *under load* (the right-hand half in Fig. 5.6), and the profiles of residual impression *after unloading* (the left-hand half in Fig. 5.6); the profiles are of *PI*=0.318, 3.18, and 31.8, respectively. As well recognized in Fig. 5.6, in the elasticity-dominant region of *PI*<3, the elastic recovery along the penetration axis is very significant in unloading. Furthermore, it should be noticed that the threshold value of plastic index *PI* at the sink-in/pile-up crossover is about *PI*=6 *under load* in Fig. 5.5, while it is about *PI*=3 after unload shown in the left-hand half of Fig. 5.6; this significant discrepancy is resulted from the *enhanced pile-up associated with the elastic recovery in unloading.*

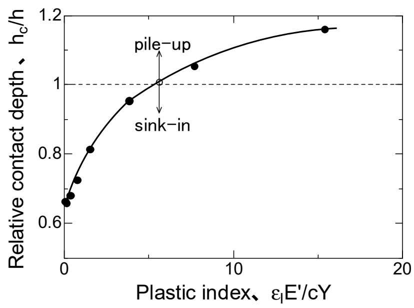

Figure 5.5 Relative contact depth h_c/h *under load* is plotted against the plastic index *PI* (FEA-based numerical results). The profile of the free surface outside the contact area undergoes the transition from sinking-in ($h_c/h<1$) to piling-up ($h_c/h>1$) with the increase in the plastic index (FEA-based numerical results)

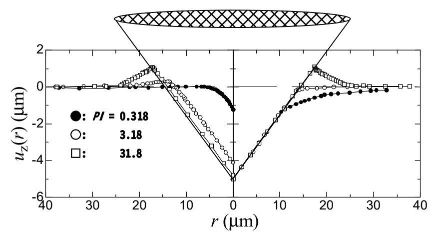

Figure 5.6 The side views of the surface profiles outside the contact area of the Vickers/Berkovich equivalent cone for the elastoplastic bodies with three different values of the plastic index $PI=\varepsilon_I E'/cY$. The right-hand half is the side views at the penetration depth *h*=5μm, and the left-hand half is the profiles of residual impressions after unload

******* Tip-Geometries of Vickers/Berkovich Indenters *******

The Vickers indenter was designed to circumvent the inconvenience of the Brinell's spherical indenter, the hardness of which is always dependent on the penetration depth. As shown in Fig. 5.7, the inclined face-angle of the Vickers indenter is designed to be $\beta = 22.0^\circ$, being consistent to the including face-angle of sphere at $a/R = 0.375$ of the standard Brinell hardness test condition. On the other hand, the geometry of the trigonal Berkovich indenter is designed with the inclined face angle of $\beta = 24.7^\circ$, resulting in the same excluded volume of the Vickers indentation. A *conical indenter* having the inclined face-angle of $\beta = 19.7^\circ$ is called as the *Vickers/Berkovich equivalent cone*, the excluded volume of which coincides with that of Vickers/Berkovich indenters. The details of the equivalent cone will be given in Chap. 11

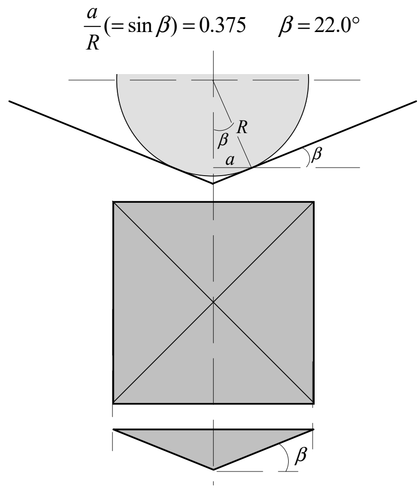

Figure 5.7 Tip-geometry of the Vickers indenter designed to be consistent with the Brinell indenter

5.2 THE *P-h* LOADING/UNLOADING HYSTERESIS CURVE OF CONICAL INDENTATION

The P - h relationship of a *perfectly elastic body* ($PI < 0.2$) for conical indentation contact is given in the following equation by substituting the elastic contact area $A_e = \pi(\eta_e \cot\beta)^2 h^2$ into Eq. (5.2);

$$P(\equiv \varepsilon_I E' A_e) = k_e h^2$$
$$k_e = \left(\pi \eta_e^2 \cot^2 \beta\right) \varepsilon_I E' \tag{5.15}$$

in which $\eta_e (\equiv h_c/h) = 2/\pi$ is the relative contact depth of the elastic body.

For a *fully plastic body* ($PI \geq 20$), on the other hand, Eq. (5.7) leads to the following P - h relationship;

$$P(\equiv cYA_p) = k_p h^2$$
$$k_p = \left(\pi \eta_p^2 \cot^2 \beta\right) cY \tag{5.16}$$

In Eq. (5.16), η_p denotes the relative contact depth h_c/h of a fully plastic body, the value of which is $\eta_p \approx 1.2$ as shown in Fig. 5.5. The P - h relation of an *elastoplastic body* with its plastic index *PI* ranging from 0.2 to 20 is given in Eq. (5.17) in terms of the Meyer hardness H_M ;

$$P(\equiv H_M A) = k_{ep} h^2$$
$$k_{ep} = \left(\pi \eta_{ep}^2 \cot^2 \beta\right) H_M \tag{5.17}$$

In Eq. (5.17), the subscript "ep" stands for "elastoplastic", and the relative contact depth η_{ep} changes in the range of $2/\pi < \eta_{ep} < 1.2$, depending on the plastic index *PI* (refer to Fig. 5.4).

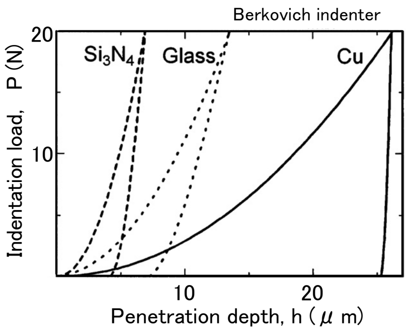

Figure 5.8 The P - h loading-unloading hysteresis curves of three engineering materials with different elastoplastic behavior (Berkovich indentation)

Figure 5.8 shows the loading-unloading P - h hysteresis curves (Berkovich indentation) of silicon nitride ceramic (Si_3N_4), soda-lime glass (Glass), and metallic copper (Cu) as the representatives of engineering materials exhibiting various elastoplastic behaviors, i.e., having the different PI -values.

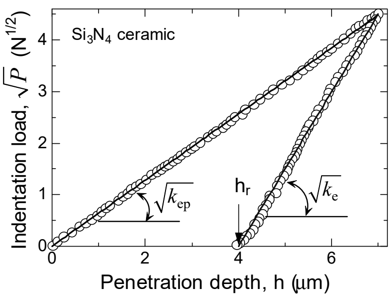

Figure 5.9 The loading-unloading $\sqrt{P}$ - h linear plot of Si_3N_4 ceramic, the P - h hysteresis of which is plotted in Fig. 5.8

The loading-unloading $\sqrt{P}$ - h linear hysteresis is plotted in Fig. 5.9 of the Si_3N_4 ceramic that has been demonstrated in Fig. 5.8. The considerations on Fig. 5.4 combined with Eqs. (5.15) – (5.17) lead to the relation of $P \propto h^2$ or $\sqrt{P} \propto h$ both in the loading and in the unloading processes due to the geometrical similarity of cone/pyramid indentation.

The indentation loading process is described by Eq. (5.17), and the subsequent unloading process is well approximated by

$$P\left(\equiv \varepsilon_{\mathrm{I}} E' A_{\mathrm{e}}\right) = k_{\mathrm{e}}\left(h - h_{\mathrm{r}}\right)^2 \qquad (5.18)$$
$$k_{\mathrm{e}} = \left(\pi \eta_{\mathrm{e}}^2 \cot^2 \beta\right) \varepsilon_{\mathrm{I}} E'$$

like as Eq. 5.15 for the P - h relation of perfectly elastic body since the unloading process of any elastoplastic body is essentially resulted from the *elastic recovery* of the indentation contact impression. In Eq. (5.18) and in Fig. 5.9, h_{r} denotes the residual depths of contact impression formed after a complete unload.

The subsequent unloading P - h^2 linear line of a *perfectly elastic body* overlaps with the preceding loading P - h^2 line (refer to the P - h^2 loading-unloading relations for *PI* =0.05 in Fig. 5.5), resulting in none of P - h hysteresis phenomenon. This fact implies that the external work applied to the system is completely released during the elastic recovery in unloading. The change of Gibbs free energy ΔG of the system, therefore, is zero in this loading-unloading mechanical cycle. In contrast to the elastic indentation process, the hysteresis loop areas enclosed with the loading and the unloading curves demonstrated in Figs. 5.5, 5.8, and 5.9 stand for the plastic energy that dissipates to the outside of the system as a heat flux during indentation loading-unloading mechanical cycle (note: the hysteresis loop energy may partly include the elastic strain energy stored in the field surrounding the residual impression).

The energy diagram associated with the indentation loading- unloading processes of an elastoplastic body is depicted in Fig. 5.10. The external work U_{T} applied to the system in the loading process up to its maximum indentation load $P_{\max}$ is described by

$$U_{\mathrm{T}} = U_{\mathrm{r}} + U_{\mathrm{e}} \qquad (5.19)$$

as a sum of the loop energy (the plastic energy dissipation) U_{r} and the elastic strain energy U_{e}. Using Eqs. (5.17) and (5.18), we finally have the following expressions for the energies of U_{T} and U_{e};

$$U_{\mathrm{T}} = \int_0^{h_{\max}} P dh = \frac{k_{\mathrm{ep}}}{3} h_{\max}{}^3 \qquad (5.20)$$

$$U_{\mathrm{e}} = \int_{h_{\mathrm{r}}}^{h_{\max}} P dh = \frac{k_{\mathrm{e}}}{3} h_{\max}{}^3 \left(1 - \xi_{\mathrm{r}}\right)^3 \qquad (5.21)$$

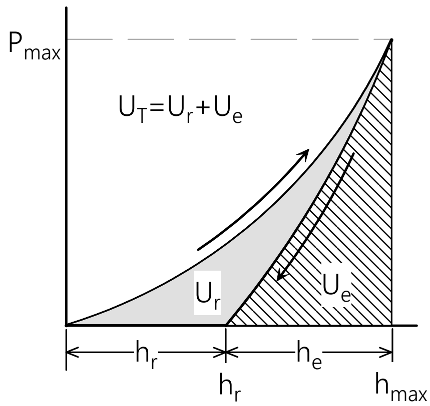

Figure 5.10 Energy diagram for the indentation loading- unloading process.

where ξ_r means the relative residual depth defined by $\xi_r = h_r / h_{max}$. The plastic energy dissipation U_r is, therefore, related to the externally applied work U_T as follows;

$$U_r \left(\equiv U_T - U_e \right) = \xi_r U_T \tag{5.22}$$

In the derivation of Eq. (5.22), we have utilized the compatibility relation of $k_{ep} h_{max}{}^2 = k_e \left(h_{max} - h_r \right)^2$, or $k_{ep} / k_e = \left(1 - \xi_r \right)^2$, due to the fact that the loading curve crosses the unloading curve at the coordinate of (h_{max}, P_{max}).

(1) Work-of-Indentation, *WOI*

The *work-of- indentation WOI* is defined as the externally applied work to create a unit volume of residual impression;

$$WOI = \frac{U_r}{V_r} \tag{5.23}$$

where V_r means the volume of residual impression. Substituting Eqs. (5.17), (5.20), and (5.22) into Eq. (5.23) and noticing the approximations of $V_{max} \approx \left(\pi \cot^2 \beta / 3 \right) h_{max}{}^3$ and $V_r \approx \xi_r V_{max}$ finally give the following important conclusion that *the work-of-indentation WOI is equivalent to the Meyer hardness*:

$$\begin{aligned} WOI & \left(\equiv U_r / V_r \equiv U_T / V_{max} \right) \\ & = H_M \end{aligned} \tag{5.24}$$

In other words, the Meyer hardness H_M that has been historically defined as the indentation load divided by the contact area $H_M = P / A$ (see Eq. (5.1b)) is re-defined in this context as *the plastic energy dissipation to create a unit volume of residual impression* U_r / V_r, or *the externally applied work to create an indentation-excluded unit volume* U_T / V_{max}.

The one-to-one correlation between the Meyer hardness H_M and the work-of-indentation WOI is shown in Fig. 5.11 for the elastoplastic materials having their material characteristics of the elastic modulus $E = 10$ GPa, and the yield stresses ranging $0.1\text{GPa} \le Y \le 3\text{GPa}$, all being the numerical results examined in a finite element analysis (FEA).

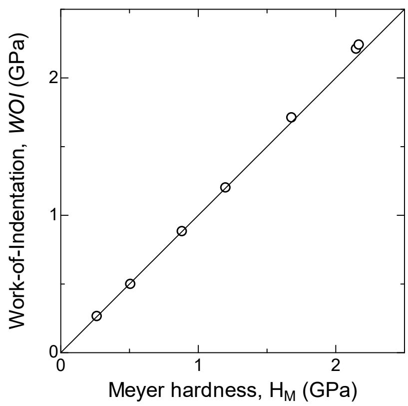

Figure 5.11 One-to-one correlation between H_M and WOI of the elastoplastic materials having the elastic modulus of $E = 10$ GPa and the yield stress ranging $0.1\text{GPa} \le Y \le 3\text{GPa}$ (FEA-based numerical results)

(2) Correlation between the loop energy U_r and the yield stress cY

As discussed in the preceding section, the loop energy U_r of an elastoplastic body defined by the area enclosed by the indentation loading-unloading hysteresis curve stands for the heat dissipation associated with the *plastic flow* in the indentation contact process. Accordingly, the *elastoplastic* loop energy U_r will nearly equal the plastic energy dissipation U_p of a *fully plastic body* having the same yield stress Y as that of the elastoplastic body, where the plastic energy dissipation U_p can be given through integrating the *P* - *h* relation of Eq. (5.16);

$$U_p\left(\equiv\int_0^{h_p} P dh\right)=\frac{k_p}{3}h_p^{\,3} \tag{5.25}$$

The elastoplastic and the fully plastic loop energies U_r and U_p are depicted in Fig. 5.12 for comparison. As shown in the figure, the relations of $U_r \approx U_p$ and $h_p \approx h_r$ exist *under the same maximum indentation load*, since both of the elastoplastic and the fully plastic bodies have *the same yield stress* Y, resulting in the following unique expression that correlates the elastoplastic loop energy U_r with the yield stress Y through the following linear relation of U_r vs. $P^{3/2}$;

$$U_r\left(\approx U_p\right)=\frac{P^{3/2}}{3\sqrt{k_p}}=\frac{\tan\beta}{3\eta_p\sqrt{\pi}}\frac{P^{3/2}}{\sqrt{cY}} \tag{5.26}$$

We can, therefore, determine the yield stress cY from the slope of the observed linear U_r vs. $P^{3/2}$ plot as well demonstrated in Fig. 5.13 for the several engineering materials (Vickers indentation) **[5.2]**.

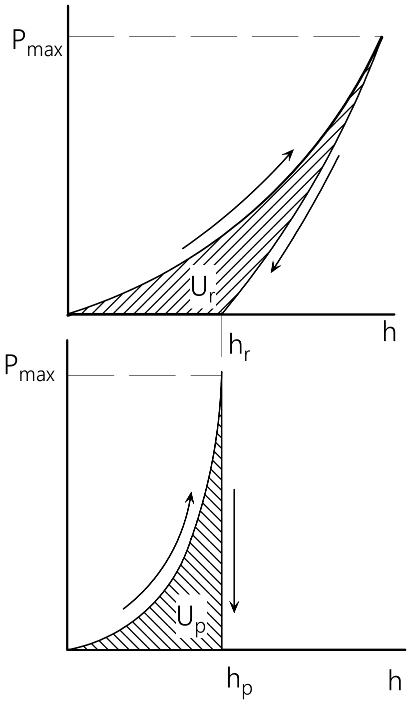

Figure 5.12 The loop energy U_r of an elastoplastic body and the plastic energy dissipation U_p of a fully plastic body, both having the same value of the yield stress Y. There exist the approximations $U_r \approx U_p$ and $h_p \approx h_r$ under the same maximum indentation load of P_{max}

[5.2] M. Sakai, *Acta Metall. Mater.*, **41**, 1751 (1993)

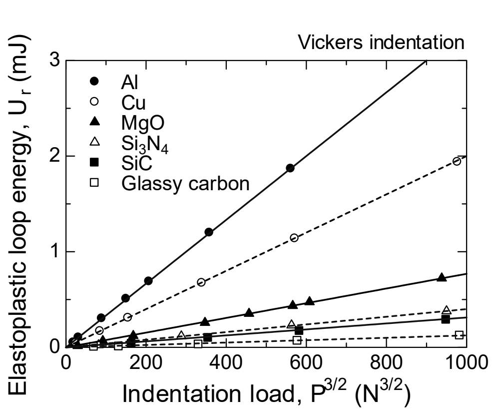

Figure 5.13 U_r - $P^{3/2}$ linear plots (Vickers indentation test results). These linear plots are, respectively, for metallic aluminum, metallic copper, magnesium oxide, silicon nitride, silicon carbide, and for glass-like carbon, from the top to the bottom. The slope of the respective linear plot gives the yield stress cY (see Eq. 5.26)

LINEAR VISCOELASTIC FORMULATION *CHAPTER* 6

6.1 GLASS TRANSITION BEHAVIOR AND VISCOELASTIC RESPONCE

(1) Glass Transition Behavior [6.1, 6.2]

The mechanical responses of elastic and elastoplastic bodies are independent of the time as well as of the rate of deformation/load applied to the system. These mechanical responses instantaneously onset once the stress/strain is applied to the system. Furthermore, the system does not show the time-dependent relaxation phenomena and the creep deformation against a stepwise application of stress/strain. On the other hand, amorphous materials including organic polymers, inorganic glasses, etc., exhibit time/rate-dependent mechanical responses at temperatures above their glass transition point. These materials fall into the group of *viscoelastic materials*.

The volumetric change of an amorphous body is shown in Fig. 6.1 against the temperature in comparison to that of a polycrystalline body such as a metallic body. Most of liquids including molten metals show a discrete change in their volumes at their freezing point (crystalline point) associated with cooling, and turn to the crystals, as shown in Fig. 6.1. Since this volumetric change goes through a *thermodynamically equilibrium process*, the resultant crystal reversibly turns to liquid at the melting point (T_m) with a discrete volumetric dilation on heating. On the other hand, molten organic polymers and inorganic glasses change to glass-like amorphous solids in their cooling processes through the glass transition region without any discrete volumetric changes, as shown in Fig. 6.1, where the glass-transition temperature (glass-transition point) T_g as a material characteristic temperature is defined at the intercepting temperature between the liquid and the solid lines with the associated upper- and lower-temperatures, T_U and T_L, respectively. The glass-transition behavior is *thermodynamically irreversible*, resulting in these characteristic temperatures of T_g, T_U, and T_L dependent on the cooling/heating rate; these temperatures shift to lower for larger the cooling rate, and vice versa.

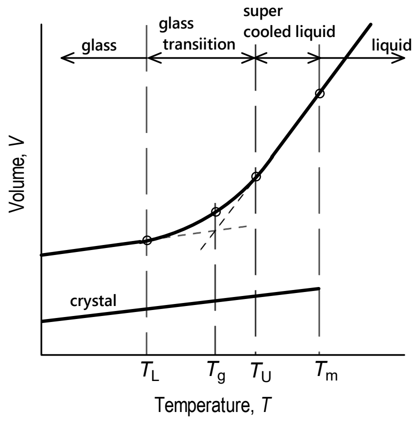

Figure 6.1 Volumetric changes of crystalline and amorphous bodies in the cooling/heating cycle, and their characteristic temperatures of T_L, T_g, T_U, and T_m.

[6.1] E.J. Donth, "The Glass Transition: Relaxation Dynamics in Liquids and Distorted Materials", Springer (2001)
[6.2] G.W. Scherer, "Relaxation in Glass and Composites", John Wiley (1986)

(2) Viscoelastic Models: Maxwell Liquid and Zener Solid

As mentioned in the preceding section, the mechanical responses of amorphous bodies are time/rate-dependent viscoelastic. The Maxwell model and the Zener model shown in Fig. 6.2 are the most common for describing in a phenomenological manner the viscoelastic behaviors of amorphous bodies in its glass-transition region. The Maxwell model comprises a Hookean spring (the elastic modulus E_M) and a Newtonian dashpot (the viscosity η) connected in series. The spring visualizes the elastic deformation, while the dashpot represents the viscous flow. The Maxwell model is the simplest for describing a *viscoelastic liquid*. On the other hand, the simplest models for representing *viscoelastic solids* include the Zener models of I and II. The Zener model I comprises a Voigt model placed in series with a Hookean spring (the elastic modulus E_g), where the Voigt model is given by a parallel combination of a spring (the elastic modulus E_V) and a dashpot (the viscosity η). The parallel combination of a Maxwell model and a Hookean spring (the elastic modulus E_e) leads to the Zener model II **[1.3]**.

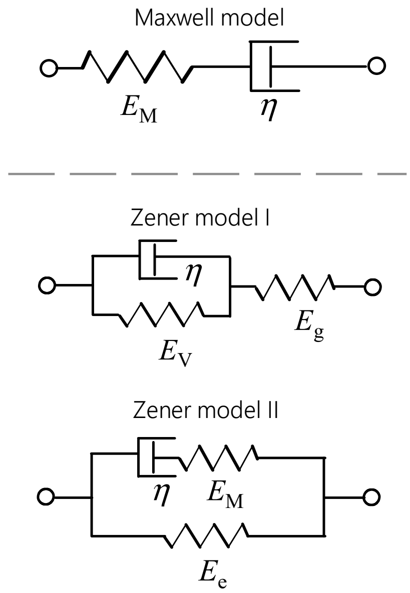

Figure 6.2 The Maxwell model to represent a *viscoelastic liquid* and the Zener models for describing *viscoelastic solids*

The mechanical response of a Hookean spring is given by

$$\sigma = E\varepsilon$$

In a dashpot, the stress produces not a strain ε but a strain rate $d\varepsilon/dt$ as follows:

$$\sigma = \eta \frac{d\varepsilon}{dt}$$

In many of the following considerations, it will be convenient to introduce the ratio of viscosity η (Pa•s) to stiffness E (Pa);

$$\tau = \frac{\eta}{E}$$

The unit of τ is time (s), and it will be seen that this characteristic time plays an important role in describing the material's viscoelastic response; τ is referred to as the relaxation time in stress relaxation phenomena, and as the retardation time in creep deformation.

The mechanical responses of the viscoelastic liquid/solid models shown in Fig. 6.2 are generally described with the following linear first-order differential equation;

$$a_0\varepsilon + a_1\frac{d\varepsilon}{dt} = b_0\sigma + b_1\frac{d\sigma}{dt} \qquad (6.1)$$

in which the coefficients are

$$\begin{aligned} a_0 &= 0 \\ a_1 &= 1 \\ b_0 &= 1/\eta \left(= 1/\tau_{\mathrm{M}} E_{\mathrm{M}}\right) \\ b_1 &= 1/E_{\mathrm{M}} \end{aligned} \tag{6.2a}$$

for the Maxwell model,

$$\begin{aligned} a_0 &= E_{\mathrm{V}}/\eta \left(= 1/\tau_{\mathrm{V}}\right) \\ a_1 &= 1 \\ b_0 &= \left(E_{\mathrm{g}}/E_{\mathrm{V}} + 1\right)/\tau_{\mathrm{V}} E_{\mathrm{g}} \\ b_1 &= 1/E_{\mathrm{g}} \end{aligned} \tag{6.2b}$$

for the Zener I model, and

$$\begin{aligned} a_0 &= E_{\mathrm{e}}/\left[\tau_{\mathrm{M}}\left(E_{\mathrm{e}} + E_{\mathrm{M}}\right)\right] \\ a_1 &= 1 \\ b_0 &= 1/\left[\tau_{\mathrm{M}}\left(E_{\mathrm{e}} + E_{\mathrm{M}}\right)\right] \\ b_1 &= 1/\left(E_{\mathrm{e}} + E_{\mathrm{M}}\right) \end{aligned} \tag{6.2c}$$

for the Zener II model. The Zener I model with $E_{\mathrm{V}} = 0$ and $E_{\mathrm{g}} = E_{\mathrm{M}}$, or the Zener II model with $E_{\mathrm{e}} = 0$ is reduced to the Maxwell model. In Eqs. (6.1) - (6.2c), the subscript "g" of E_{g}, and "e" of E_{e} stand for the "glassy modulus" and the "equilibrium modulus", respectively.

The Laplace transform is very effective in solving linear differential equations like as Eq. (6.1), the mathematical details of which are given in APPENDIX C. The Laplace transform of *a function* $f(t)$ in the time-space of $t \geq 0$ is denoted here as $\mathcal{L} f(t) \left(\equiv \overline{f}(p)\right)$, and is defined by

$$\mathcal{L} f(t) = \overline{f}(p) = \int_0^{\infty} f(t) e^{-pt} dt$$

where *p* is a nonnegative real parameter with the unit of inverse time (1/s) termed the *transform parameter*. Applying Laplace transform to both sides of Eq. (6.1) turns the differential equation to the following algebraic equation;

$$\overline{\sigma}(p) = E^*(p)\overline{\varepsilon}(p) \tag{6.3a}$$

where $E^*(p)$ is referred to as the *pseudo elastic modulus* define by

$$E^*(p) = \frac{a_0 + a_1 p}{b_0 + b_1 p} \tag{6.4}$$

By way of example, the pseudo elastic modulus $E^*(p)$ of the viscoelastic Maxwell liquid is written by

$$E^*(p) = p \cdot \frac{E_{\mathrm{M}}}{p + \dfrac{1}{\tau_{\mathrm{M}}}} \tag{6.5a}$$

through substituting Eq. (6.2a) into Eq. (6.4). In a similar mathematical substitution of Eq. (6.2b) or Eq. (6.2c) into Eq. (6.4), we finally have

$$E^*(p) = E_{\mathrm{g}} \left(\frac{1}{\tau_{\mathrm{V}}} \frac{1}{p + \dfrac{1}{\tau_{\mathrm{Z}}}} + \frac{p}{p + \dfrac{1}{\tau_{\mathrm{Z}}}} \right) \tag{6.5b}$$

$$\tau_{\mathrm{Z}} = \left(E_{\mathrm{e}} / E_{\mathrm{g}} \right) \tau_{\mathrm{V}}\,; \quad 1/E_{\mathrm{e}} = 1/E_{\mathrm{g}} + 1/E_{\mathrm{V}}$$

for the Zener I viscoelastic solid, and

$$E^*(p) = E_{\mathrm{g}} \left(\frac{E_{\mathrm{e}}/E_{\mathrm{g}}}{\tau_{\mathrm{M}}} \frac{1}{p + \dfrac{1}{\tau_{\mathrm{M}}}} + \frac{p}{p + \dfrac{1}{\tau_{\mathrm{M}}}} \right) \tag{6.5c}$$

$$E_{\mathrm{g}} = E_{\mathrm{e}} + E_{\mathrm{M}}$$

for the Zener II viscoelastic solid.

As readily seen in Eqs. (6.5b) and (6.5c), their mathematical expressions are formally the same, though the respective coefficients describing their $E^*(p)$-values are different. As a matter of fact, both of the models I and II coincide with each other, and their viscoelastic responses become equivalent when we substitute the relations of $E_{\mathrm{e}}/E_{\mathrm{g}} = \tau_{\mathrm{M}}/\tau_{\mathrm{V}}$ and $\tau_{\mathrm{M}} = \tau_{\mathrm{Z}}$ into the Model II.

The mathematically conjugated formula of Eq. (6.3a)

$$\bar{\varepsilon}(p) = C^*(p)\bar{\sigma}(p) \tag{6.3b}$$

defines the *pseudo compliance* $C^*(p)$ that is related to $E^*(p)$ with $C^*(p) = 1/E^*(p)$. As shown in Eqs. (6.3a) and (6.3b), it will be worthy of note that *the formulas of* ***linear viscoelastic*** *constitutive equations* $\bar{\sigma}(p) = E^*(p)\bar{\varepsilon}(p)$ *and* $\bar{\varepsilon}(p) = C^*(p)\bar{\sigma}(p)$ *in the Laplace space are equivalent to those of* ***linear elastic*** *constitutive equations* $\sigma = E\varepsilon$ *and* $\varepsilon = C\sigma$ *in the real space. Furthermore, there exists one-to-one correspondence of* $C = 1/E$ *and* $C^*(p) = 1/E^*(p)$ *in the real and the Laplace spaces. This one-to-one correspondence is named as "****The Elastic-Viscoelastic Correspondence Principle****"* **[1.2, 1.3]**, *playing an*

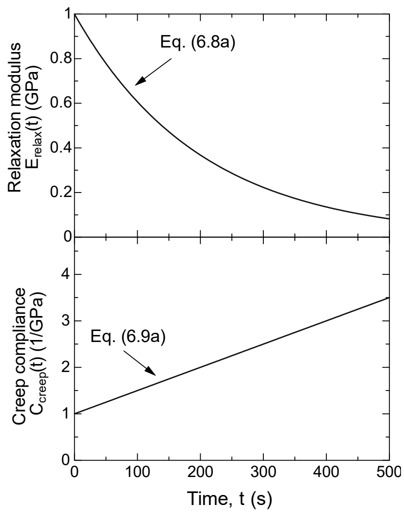

Figure 6.3 Relaxation modulus and creep compliance (Maxwell model): $E_{\mathrm{M}}\left(\equiv E_{\mathrm{g}}\right) = 1\ \mathrm{GPa}$, $\tau_{\mathrm{M}} = 200\ \mathrm{s}$, $\eta\left(\equiv \tau_{\mathrm{M}} \cdot E_{\mathrm{M}}\right) = 200\ \mathrm{GPa{\cdot}s}$

essential role in formulating the viscoelastic indentation contact mechanics, the details of which will be discussed in the later chapters.

Let us now consider; (i) the stress relaxation under stepwise strain and (ii) the creep deformation for stepwise loading in order to make further understanding the viscoelastic responses of the Maxwell liquid and the Zener II solid.

(i) Stress relaxation under stepwise strain

The stepwise application of a constant value of strain ε_0 to the system can be mathematically made by

$$\varepsilon(t) = \varepsilon_0 u(t), \qquad u(t) = \begin{cases} 0, & t < 0 \\ 1, & t \geq 0 \end{cases} \tag{6.6}$$

using the Heaviside step function $u(t)$. Accordingly, substituting the Laplace transform of Eq. (6.6), i.e., $\bar{\varepsilon}(p) = \varepsilon_0/p$ (refer to APPENDIX C) into Eq. (6.3a) leads to the following viscoelastic constitutive equation in the Laplace space;

$$\begin{aligned} \bar{\sigma}(p) &= \left[E^*(p)/p\right]\varepsilon_0 \\ &= \bar{E}_{\mathrm{relax}}(p) \cdot \varepsilon_0 \end{aligned} \tag{6.7}$$

$\bar{E}_{\mathrm{relax}}(p)$ represents the relaxation modulus $E_{\mathrm{relax}}(t)\left[\equiv \sigma(t)/\varepsilon_0\right]$ in the Laplace space, relating to the pseudo modulus $E^*(p)$ with $\bar{E}_{\mathrm{relax}}(p) = E^*(p)/p$, and then through the inverse of Laplace transforms of Eq. (6.5a) (Maxwell model) and Eq. (6.5c) (Zener II model) (refer to APPENDIX C), we finally have the following relaxation moduli in the real space;

[Maxwell liquid]

$$\begin{aligned} \frac{\sigma(t)}{\varepsilon_0} &= E_{\mathrm{relax}}(t) = E_{\mathrm{M}} \exp\left(\frac{-t}{\tau_{\mathrm{M}}}\right) \\ E_{\mathrm{g}} &= E_{\mathrm{M}} \end{aligned} \tag{6.8a}$$

[Zener II solid]

$$\begin{aligned} \frac{\sigma(t)}{\varepsilon_0} &= E_{\mathrm{relax}}(t) = E_{\mathrm{e}} + \left(E_{\mathrm{g}} - E_{\mathrm{e}}\right) \exp\left(\frac{-t}{\tau_{\mathrm{M}}}\right) \\ E_{\mathrm{g}} &= E_{\mathrm{e}} + E_{\mathrm{M}} \end{aligned} \tag{6.8b}$$

(ii) Creep deformation for stepwise loading

Using the Heaviside step function $u(t)$, we readily describe the stepwise application of a constant stress σ_0 to the system with $\sigma(t) = \sigma_0 u(t)$, and then the substitution of its Laplace transform of $\bar{\sigma}(p) = \sigma_0/p$ into Eq. (6.3b) combined with the creep function of $C_{\text{creep}}(t)[\equiv \varepsilon(t)/\sigma_0]$ results in the pseudo compliance of $C^*(p)[\equiv 1/E^*(p)] = p\bar{C}_{\text{creep}}(p)$ with $\bar{C}_{\text{creep}}(p)(\equiv \bar{\varepsilon}(p)/\sigma_0)$. The creep functions $C_{\text{creep}}(t)$ of the Maxwell and the Zener II models in their real spaces are, therefore via the inverse Laplace transform, finally written with

[Maxwell liquid]

$$\frac{\varepsilon(t)}{\sigma_0} = C_{\text{creep}}(t) = \frac{1}{E_{\text{M}}} + \frac{t}{\eta} \tag{6.9a}$$

[Zener II solid]

$$\frac{\varepsilon(t)}{\sigma_0} = C_{\text{creep}}(t)$$

$$= \frac{1}{E_{\text{g}}} + \left(\frac{1}{E_{\text{e}}} - \frac{1}{E_{\text{g}}}\right)\left[1 - \exp\left(\frac{-t}{\tau_{\text{Z}}}\right)\right] \tag{6.9b}$$

$$E_{\text{g}} = E_{\text{e}} + E_{\text{M}}$$

$$\tau_{\text{Z}} = (1 + E_{\text{M}}/E_{\text{e}})\tau_{\text{M}}$$

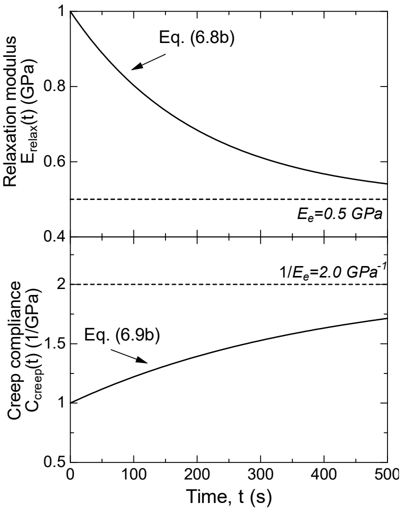

Figure 6.4 Relaxation modulus and creep compliance (Zener II model): $E_{\text{M}} = 0.5\,\text{GPa}$、 $E_{\text{e}} = 0.5\,\text{GPa}$、 $E_{\text{g}}(= E_{\text{M}} + E_{\text{e}}) = 1.0\,\text{GPa}$ $\tau_{\text{M}} = 200\,\text{s}$、 $\tau_{\text{Z}}(\equiv E_{\text{g}}\tau_{\text{M}}/E_{\text{e}}) = 400\text{s}$

It must be noticed in the Zener viscoelastic solid that the relaxation time τ_{M} in Eq. (6.8b) for stress relaxation is always smaller than the retardation time τ_{Z} in Eq. (6.9b) for creep deformation; $\tau_{\text{Z}}[\equiv (1 + E_{\text{M}}/E_{\text{e}})\tau_{\text{M}}] > \tau_{\text{M}}$. This fact indicates that *the creep deformation always proceeds in a more sluggish manner than the stress relaxation* (see Fig. 6.4).

The specific discrepancies in their viscoelastic responses observed in the Maxwell liquid and the Zener solid are graphically compared in Figs. 6.3 and 6.4. The viscoelastic *liquid* exhibits a complete stress relaxation in time ($E_{\text{relax}}(t) \downarrow 0$), while the induced stress of the viscoelastic *solid* relaxes to a finite value of its equilibrium modulus ($E_{\text{relax}}(t) \downarrow E_{\text{e}}$).

6.2 DIFFERENTIAL FORM OF VISCOELASTIC CONSTITUTIVE EQUATION -WIECHERT MODEL-

We cannot describe the time-dependent viscoelastic responses with a *single* value of the relaxation/retardation time τ for most of engineering materials including organic polymers, being required to use the *multiple* characteristic times or the relaxation/retardation time spectrum.

The Wiechert model is shown in Fig. 6.5 that is an extended Zener II model; a parallel combination of the multiple Maxwell models having the specific relaxation time $\tau_i\left(\equiv \eta_i/E_i\right)\left(i=1,2,3\cdots\right)$ and an elastic spring with the equilibrium elastic modulus of E_{e}. The stress $\sigma(t)$ applied to the model is, therefore, the sum of the stress $\sigma_i\left(t\right)$ on the *i*-th Maxwell element and on the equilibrium spring $\sigma_{\mathrm{e}}\left(t\right)$, as follows;

$$\sigma(t)=\sigma_{\mathrm{e}}(t)+\sum_i \sigma_i(t) \tag{6.10}$$

Due to the parallel combination of each element, the strain $\varepsilon(t)$ of the model equals to the strain of each element, that is, $\varepsilon(t)=\varepsilon_i\left(t\right)$, leading to the following constitutive relations;

$$\begin{aligned}&\sigma_{\mathrm{e}}(t)=E_{\mathrm{e}}\varepsilon(t)\\&\frac{d\varepsilon(t)}{dt}=\frac{1}{E_i}\frac{d\sigma_i(t)}{dt}+\frac{\sigma_i(t)}{\eta_i}\end{aligned} \tag{6.11}$$

The Laplace transforms of Eqs. (6.10) and (6.11) result in Eq. (6.3a), where the pseudo modulus $E^*(p)$ is written with

$$\begin{aligned}E^*(p)&=p\bar{E}_{\mathrm{relax}}(p)\\&=p\left(\frac{E_{\mathrm{e}}}{p}+\sum_i\frac{E_i}{p+\dfrac{1}{\tau_i}}\right)\end{aligned} \tag{6.12}$$

The relaxation modulus in the Laplace space is, therefore, given by

$$\bar{E}_{\mathrm{relax}}(p)=\frac{E_{\mathrm{e}}}{p}+\sum_i\frac{E_i}{p+\dfrac{1}{\tau_i}}$$

Applying the inverse Laplace transform to Eq. (6.12), the stress relaxation modulus $E_{\mathrm{relax}}(t)$ of the Wiechert model as the generalized expression for

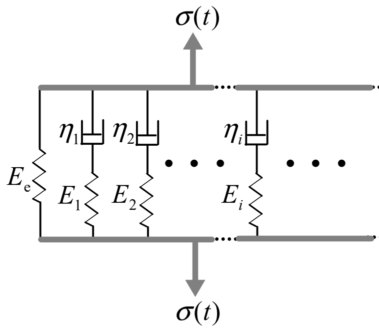

Figure 6.5 Wiechert model comprising the Maxwell models with various values of the relaxation times

$\tau_i\left(\equiv \eta_i/E_i\right)\left(i=1,2,3\cdots\right)$
and the equilibrium spring E_{e} in a parallel combination.

Eqs. (6.8a) and (6.8b) is given by

$$E_{\text{relax}}(t) = E_{\text{e}} + \sum_i E_i \exp\left(\frac{-t}{\tau_i}\right) \tag{6.13}$$

in which the model with $E_{\text{e}} = 0$ stands for the viscoelastic *liquid* as a specific of the Wiechert model. Since the viscoelastic constitutive equations that we have considered in this section are based on the differential equations of Eqs. (6.1) and (6.11), these equations are referred to as the "*differential type of viscoelastic constitutive equation*".

As has been discussed in this section, the generalized linear viscoelastic constitutive equations in the Laplace space are written by

$$\begin{aligned}\bar{\sigma}(p) &= p\bar{E}_{\text{relax}}(p)\bar{\varepsilon}(p) \\ &= E^* \cdot \bar{\varepsilon}(p)\end{aligned} \tag{6.14}$$

The inverse Laplace transform of Eq. (6.14), thus, leads to the following viscoelastic constitutive equation in its real space (see APENDIX C);

$$\sigma(t) = \int_0^t E_{\text{relax}}(t-t')\frac{d\varepsilon(t')}{dt'}dt' \tag{6.15}$$

In deriving Eq. (6.15), we have used the fundamental formulas of Laplace transform;

$$\mathcal{L}\left[d\varepsilon(t)/dt\right] = p\bar{\varepsilon}(p) - \varepsilon(0^-)$$

with $\varepsilon(0^-) = 0$, and

$$\mathcal{L}\left[\int_0^t f(t-t')g(t')dt'\right] = \bar{f}(p)\bar{g}(p)$$

The fact that none of external strains are applied to the system in past times ($\varepsilon(t') = 0$; $t' < 0$) gives the initial condition of $\varepsilon(0^-) = 0$. In a similar way, by the use of the creep function $C_{\text{creep}}(t)$ instead of using the relaxation modulus $E_{\text{relax}}(t)$, the following linear viscoelastic constitutive equation is also given;

$$\varepsilon(t) = \int_0^t C_{\text{creep}}(t-t')\frac{d\sigma(t')}{dt'}dt' \tag{6.16}$$

Accordingly, when we compare the Laplace transform of Eq. (6.16)

$$\begin{aligned}\bar{\varepsilon}(p) &= p \cdot \bar{C}_{\text{creep}}(p)\bar{\sigma}(p) \\ &= C^*(p)\bar{\sigma}(p)\end{aligned} \tag{6.17}$$

with Eq. (6.14), we can find the following essential relationship between the relaxation modulus $E_{\text{relax}}(t)$ and the creep compliance $C_{\text{creep}}(t)$ in the Laplace space as follows;

$$\begin{aligned} &p^2 \bar{E}_{\text{relax}}(p)\bar{C}_{\text{creep}}(p) = \\ &\quad = E^*_{\text{relax}}(p) \cdot C^*_{\text{creep}}(p) = 1 \end{aligned} \tag{6.18}$$

Furthermore, the inverse Laplace transform of Eq. (6.18) leads to the following relation in the real space;

$$\int_0^t E_{\text{relax}}(t-t')C_{\text{creep}}(t')dt' = t \tag{6.19}$$

Due to the integral expressions of the constitutive equations given in Eq. (6.15) and (6.16), they are referred to as the *integral type of viscoelastic constitutive equation*. The *differential type* and the *integral type* of the linear viscoelastic constitutive equations we discussed in this section are *mathematically equivalent*. However, the integral equation is more universal and more extensive in applying it to describing the viscoelastic behavior of engineering materials, since the integral constitutive equation is described in terms of the *generic* viscoelastic function of $E_{\text{relax}}(t)$ or $C_{\text{creep}}(t)$ instead of using the *specific* mechanical combination of Hookean springs and Newtonian dashpots in the differential equation.

6.3. INTEGRAL FORM OF VISCOELASTIC CONSTITUTIVE EQUATION – BOLTZMANN'S HEREDITARY INTEGRAL –

An elastic body responds in an instantaneous manner to the mechanical stimulus such as the stress/strain externally applied, as repeatedly mentioned in the preceding sections. In other word, it recovers in an instantaneous manner to the original state once the applied stimulus is taken away. On the other hand, as seen in the time-dependent phenomena of stress relaxation and creep deformation of a viscoelastic body, the mechanical history *in past time* t' has an affect on the stress/strain state that we observe at the present time t. Due to the fact that the past memory remains in the present mechanical state of viscoelastic body, it is referred to as the *memory material*; the rheological functions such as the relaxation modulus $E_{\text{relax}}(t)$ and the creep function $C_{\text{creep}}(t)$ are, therefore, often called as the memory functions.

The Boltzmann's convolution integral (the Boltzmann's hereditary integral) forms the basis of the linear viscoelastic theory **[1.2, 1.3]**. Suppose a strain $\varepsilon(t')$ at the past time t' as a mechanical stimulus, and the induced stress $\sigma(t')$ as its linear response. In such a way, we denote the induced stresses $\sigma(t_1)$ and $\sigma(t_2)$ for the applied strains of $\varepsilon(t_1)$ and $\varepsilon(t_2)$ at the past times of $t'=t_1$ and $t'=t_2$ ($t_1<t_2<t$), respectively. The Boltzmann's convolution principle supports the assumption that the stress $\sigma(t)$ observed at the present time $t'=t$ is described with the convolution of the respective stresses $\sigma(t_1)$ and $\sigma(t_2)$;

$$\sigma(t)=\sigma(t-t_1)+\sigma(t-t_2)$$

for the total strain $\varepsilon(t)=\varepsilon(t_1)+\varepsilon(t_2)$ having been applied to the system at the present time. Namely, the Boltzmann's principle indicates that the stress (or strain) observed at the present time can be described with the convolution (i.e., the sum) of the respective stresses (or strains) induced at past times. A schematic of the Boltzmann's hereditary principle is depicted in Fig. 6.6 for an arbitrary strain history. As demonstrated in the figure, the stress $\sigma(t)$ we are observing at the present time t is given by

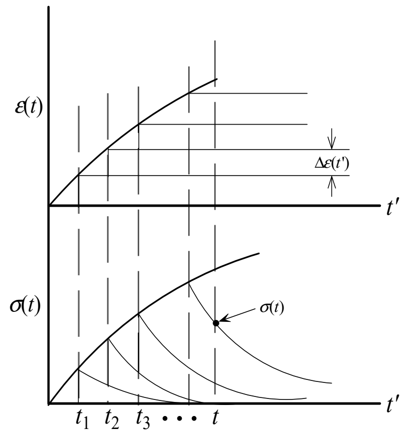

Figure 6.6 Boltzmann's hereditary principle. The stress $\sigma(t_i)$ induced by a stepwise strain at the past time $t'=t_i$ dictates the stress $\sigma(t)$ at the present time t in a hereditary as well as a convolutional manner

$$\sigma(t)=\sum_i E_{\text{relax}}(t-t_i)\Delta\varepsilon(t_i) \tag{6.20}$$

in terms of the stepwise strain $\Delta\varepsilon(t_i)$ applied to the system at the past time t_i via the stress relaxation modulus $E_{\text{relax}}(t)$ as its memory function. Equation (6.20) turns to its integral form;

$$\sigma(t)=\int_0^t E_{\text{relax}}(t-t')\frac{d\varepsilon(t')}{dt'}dt' \tag{6.15}$$

by replacing the stepwise strain in Eq. (6.20) with $\Delta\varepsilon(t_i)=[d\varepsilon(t')/dt']dt'$. By the use of the creep function $C_{\text{creep}}(t)$ as the memory function in the Boltzmann's hereditary integral, in a similar way, we derive Eq. (6.16);

$$\varepsilon(t)=\int_0^t C_{\text{creep}}(t-t')\frac{d\sigma(t')}{dt'}dt' \tag{6.16}$$

In the mathematical framework of Laplace transform, the so-called *Carson transform* is defined by;

$$f^*(p)=p\bar{f}(p)=p\int_0^\infty f(t)e^{-pt}dt \tag{6.21}$$

as a specific type of Laplace transform. Accordingly, as mentioned above, the pseudo elastic modulus $E^*(p)$ and the pseudo compliance $C^*(p)$ are, respectively, the Carson transforms of $E_{\mathrm{relax}}(t)$ and $C_{\mathrm{creep}}(t)$;

$$\begin{aligned} E^*(p) &= p\bar{E}_{\mathrm{relax}}(p) \\ C^*(p) &= p\bar{C}_{\mathrm{creep}}(p) \end{aligned} \tag{6.22}$$

with the simple interrelation of $E^*(p) \cdot C^*(p) = 1$ that is the one-to-one corresponding relation of $E \cdot C = 1$ for a perfectly elastic body, as discussed in the preceding section (see Eq. (6.18)). In other word, *the Carson transform of a viscoelastic constitutive equation yields the corresponding perfectly elastic constitutive equation*. This one-to-one correspondence leads to the most essential principle, i.e., **the elastic-viscoelastic correspondence principle***; the very complicated time-dependent viscoelastic problems are simply reduced to the perfectly elastic problems through Carson transform*; an example will be demonstrated in the following section.

6.4 TIME-DEPENDENT POISSON'S RATIO IN VISCOELASTIC DEFORMATION

The Poisson's ratio is also time-dependent in a viscoelastic regime, leading to somewhat complicated mechanical analysis **[1.3]**. To circumvent this difficulty, a simple shear test has widely been utilized in the conventional rheological tests, due to the iso-volumetric deformation/flow under shear, i.e., no need of the considerations on the Poisson's effect. This is the reason why we have long been making use of the relaxation shear modulus $G_{\mathrm{relax}}(t)$ and the shear creep compliance function $J_{\mathrm{creep}}(t)$ in most of rheological tests and analyses. However, the mechanical processes of indentation contact are always as well as inevitably associated with the volumetric change of the material indented. The time-dependent viscoelastic Poisson's ratio $\nu(t)$, therefore, significantly affects the indentation contact mechanics through its effect on the elastic moduli $E_{\mathrm{relax}}(t)$ and $E'_{\mathrm{relax}}(t)$. As an appropriate example of the application of Carson transform combined with *the elastic-viscoelastic corresponding principle* to the viscoelastic deformation and flow, we will discuss in this section the time-dependent Poisson's effect on the viscoelastic functions.

The Young's modulus E, shear modulus G, bulk modulus K and the Poisson's ratio ν of a perfectly elastic body are correlated to each other through the following equations **[1.2]**;

$$\nu = \frac{3K - 2G}{6K + 2G} = \frac{3 - 2\kappa G}{6 + 2\kappa G} \tag{6.23a}$$

$$E = 2(1 + \nu)G \tag{6.24a}$$

$$E'\left(\equiv \frac{E}{1-\nu^2}\right) = \frac{2G}{1-\nu} \tag{6.25a}$$

In Eq. (6.23a), the bulk modulus K is defined by $p = K(\Delta V/V)$ in terms of the volumetric strain $\Delta V/V$ under hydrostatic pressure p, and the bulk compliance κ is defined as the inverse of bulk modulus, i.e., $\kappa = 1/K$. Since the bulk compliance of incompressible body is zero, i.e., $\kappa = 0$, Eqs. (6.23a), (6.24a), and (6.25a) lead to the well-known relations of $\nu = 1/2$, $E = 3G$, and $E' = 4G$.

In linear viscoelastic bodies, once we apply the elastic-viscoelastic correspondence principle combined with the Carson transform to their time dependent viscoelastic moduli of $E(t)$, $G(t)$, and $\nu(t)$ through the formulas of Eqs. (6.23a), (6.24a), and (6.25a), we have the following relations in the Laplace space;

$$\nu^* = \frac{3K^* - 2G^*}{6K^* + 2G^*} = \frac{3 - 2\kappa^* G^*}{6 + 2\kappa^* G^*} \tag{6.23b}$$

$$E^* = 2(1 + \nu^*)G^* \tag{6.24b}$$

$$E'^*\left(\equiv \frac{E^*}{1-\nu^{*2}}\right) = \frac{2G^*}{1-\nu^*} \tag{6.25b}$$

Suppose a model viscoelastic *solid* having the following shear modulus with a single relaxation time τ_0;

$$G(t) = G_e + (G_g - G_e)\exp\left(-\frac{t}{\tau_0}\right) \tag{6.26}$$

where $G_g\,(= G(0))$ is the glassy modulus (instantaneous modulus) and $G_e\,(= G(\infty))$ stands for the equilibrium modulus; substituting $G_e = 0$ in Eq. (6.26) turns the model to a viscoelastic *liquid*, so-called the

Maxwell model. Since the time-dependent nature of the bulk compliance $\kappa(t)$ is very minor when we compare it to other viscoelastic functions **[1.3]**, the bulk compliance is, in the present context, assumed to be time-independent, i.e., $\kappa(t) = \kappa_0$ (a constant value), making the subsequent mathematical operations/procedures rather simple and compact.

Substituting the Carson transform G^* of Eq. (6.26) into Eqs. (6.23b) – (6.25b), and then making their inverse Laplace transform, we finally have the following viscoelastic functions in the real space;

$$\frac{E(t)}{2(1+\nu_g)G_g} = \left(1 - \frac{3R}{2(1+\nu_g)(1+\gamma R)}\right)\exp\left(-t/\tau_1\right) + \frac{3R}{2(1+\nu_g)(1+\gamma R)} \tag{6.27}$$

$$\nu(t) = \frac{1}{2} - \left(\frac{1-2\nu_g}{2}\right)\left[\frac{E(t)}{2(1+\nu_g)G_g}\right] \tag{6.28}$$

and

$$\frac{E'(t)}{2G_g/1-\nu_g} = 2(1-\nu_g)\frac{1+\gamma R}{1+4\gamma R}R + \frac{(1-\nu_g)}{2}(1-R)\exp\left(-t/\tau_0\right) + \frac{(1+\nu_g)}{2}\frac{1-R}{1+4\gamma R}\exp\left(-t/\tau_2\right) \tag{6.29}$$

The characteristic relaxation times τ_1 and τ_2 in these equations are described in terms of the shear relaxation time τ_0 through the following equations;

$$\tau_1 = \frac{3}{2(1+\nu_g)}\frac{1}{1+\gamma R}\tau_0 \tag{6.30}$$

$$\tau_2 = \frac{1+4\gamma}{1+4\gamma R}\tau_0 \tag{6.31}$$

in which ν_g means the glassy (instantaneous) Poisson's ratio defined as $\nu_g = \nu(0)$; R and γ are, respectively, defined by $R = G_e/G_g$, $\gamma = (1-2\nu_g)/\left[2(1+\nu_g)\right]$; the R-value, therefore, becomes zero in viscoelastic *liquid* ($G_e = 0$). The characteristic relaxation time τ_1 dictates the relaxation behavior of the present viscoelastic model through

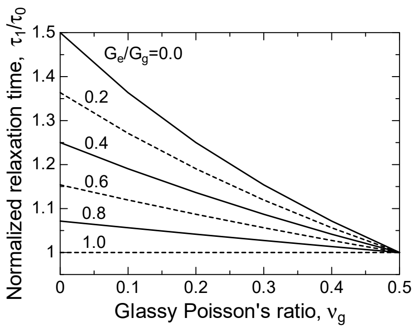

Figure 6.7 The characteristic relaxation time τ_1 (Eq. (6.30)) that dictates the time-dependent natures of $E(t)$ and $\nu(t)$. Notice that there exists the relation of $\tau_1 \geq \tau_0$

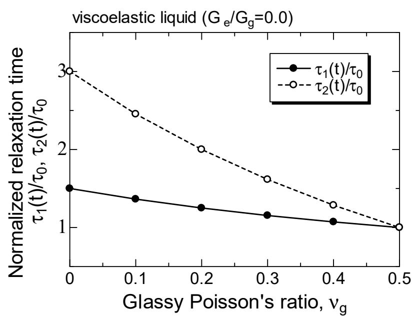

Figure 6.8 Characteristic relaxation times of τ_1 and τ_2 plotted against the glassy Poison's ratio ν_g (refer to Eqs. (6.30) and (6.31))

$E(t)$ (see Eq. (6.27)) and the time-dependent $\nu(t)$ (see Eq. (6.28)). As well demonstrated in Fig. 6.7, it should be noticed that the relaxation time τ_1 is always larger than the shear relaxation modulus τ_0, i.e., $\tau_1 \geq \tau_0$, leading to a more sluggish relaxation of $E(t)$ than the shear relaxation $G(t)$. On the other hand, the relaxation behavior of $E'(t)$ (see Eq. (6.29)) is described via the twin characteristic times of τ_0 and τ_2 with $\tau_2 \geq \tau_0$; Figure 6.8 shows the interrelation between these characteristic relaxation times and the glassy Poisson's ratio ν_g of viscoelastic liquids, indicating the relations of $\tau_2 > \tau_1$ for arbitrary values of $0 \leq \nu_g < 1/2$. Furthermore, it should be noticed that these characteristic relaxation times agree with each other, i.e., $\tau_1 = \tau_0 = \tau_2$, for the *incompressible* viscoelastic body with $\nu_g = 1/2$. The relaxation behaviors of $E(t)$ and $E'(t)$ are plotted in Fig. 6.9 in comparison to the shear relaxation of $G(t)$ for the viscoelastic liquid ($\nu_g = 0.3$, $\tau_0 = 200$ s). Due to the fact of $\tau_0 \leq \tau_1 \leq \tau_2$, the relaxation behaviors are progressively more sluggish in the order of $G(t)$, $E(t)$, and then $E'(t)$. The time-dependent nature of the viscoelastic Poisson's ratio $\nu(t)$ is shown in Fig. 6.10 for the viscoelastic bodies ($\nu_g = 0.1$, $\tau_0 = 200$ s) with various values of G_e/G_g. As readily seen in Eq. (6.28), the time-dependent nature of $\nu(t)$ stems from the relaxation modulus $E(t)$, resulting in its monotonic increase with time: Figure 6.10 demonstrates the time-dependent Poisson's ratio $\nu(t)$ of the viscoelastic bodies, where the Poisson's ratio of *viscoelastic liquid* ($G_e/G_g = 0$) converges to $\nu(t) = 1/2$ with time, i.e., $\lim_{t\to\infty} \nu(t) = 1/2$, implying that the liquid turns to an incompressible fluid in time.

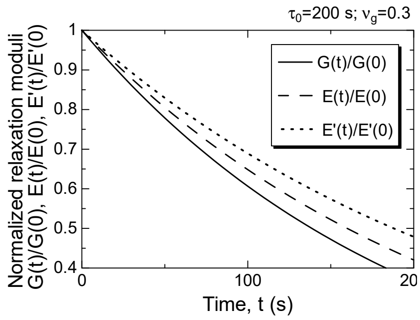

Figure 6.9 The stress relaxation moduli $G(t)$, $E(t)$, and $E'(t)$. Due to the fact of $\tau_0 \leq \tau_1 \leq \tau_2$, their relaxations become progressively more sluggish in the order of $G(t)$, $E(t)$, and $E'(t)$

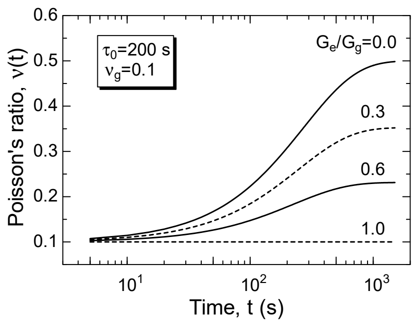

Figure 6.10 Time-dependent viscoelastic Poisson's ratio

VISCOELASTIC INDENTATION CONTACT MECHANICS

CHAPTER 7

7.1 MATHEMATICAL FORMULATION

We can readily make a mathematical formulation of *viscoelastic indentation contact mechanics* through the "elastic-viscoelastic correspondence principle" applied to the *elastic indentation contact mechanics*. Namely, the elastic theory of indentation contact mechanics we developed in Chapter 3 is readily extended to the corresponding viscoelastic theory via the Laplace transform and its inversion (see Chapter 6) **[7.1-7.5]**. The constitutive equation of the elastic indentation contact given in Eq. (3.32) is rewritten in terms of the indentation load P and the contact area $A(=\pi a^2)$, as follows;

$$P = \left(E'\varepsilon_{\mathrm{I}}\right) A \tag{3.32'}$$

Once we apply the elastic-viscoelastic correspondence principle to Eq. (3.32'), the following constitutive equations of viscoelastic indentation contact are obtained;

$$\begin{aligned} P(t) &= \int_0^t E'_{\mathrm{relax}}(t-t') \frac{d\left[\varepsilon_{\mathrm{I}}(t') \cdot A(t')\right]}{dt'} dt' \\ \varepsilon_{\mathrm{I}}(t) \cdot A(t) &= \int_0^t C'_{\mathrm{creep}}(t-t') \frac{d\left[P(t')\right]}{dt'} dt' \end{aligned} \tag{7.1}$$

In Eq. (7.1), $E'_{\mathrm{relax}}(t)$ stands for the plane-strain relaxation modulus defined as $E'_{\mathrm{relax}}(t) = E_{\mathrm{relax}}(t) / \left[1-\nu^2(t)\right]$. There is also a similar relation to Eq. (6.19) for the plane-strain creep function $C'_{\mathrm{creep}}(t)$

$$\int_0^t E'_{\mathrm{relax}}(t-t') C'_{\mathrm{creep}}(t') dt' = t \tag{7.2}$$

As readily expected from Eqs. (3.29) - (3.31), it must be noticed that the indentation strains $\varepsilon_{\mathrm{I}}(t)$ of flat-ended punch and spherical indenter are time-dependent in viscoelastic regime. In Tab. 7.1 listed are the viscoelastic constitutive equations for different indenter's tip geometries. As clearly seen in the table, due to the geometrical similarity of cone/pyramid indenter (including Vickers/Berkovich indenters), the indentation strain ε_{I} is dependent only on the inclined face-angle β, but not on the penetration depth, leading to the time-independent indentation strain, i.e., $\varepsilon_{\mathrm{I}}(t') = \tan\beta/2$, and making the constitutive equations very simple and compact;

[7.1] J.R.M. Radock, *Q. Appl. Math.*, **15**, 198 (1957)
[7.2] S.C. Hunter, *J. Mech. Phys. Solids,* **8**, 219 (1960)
[7.3] M. Sakai, *Phil. Mag, A*, **82[10]**, 1841 (2002)
[7.4] M. Sakai, S. Shimizu, *J. Non-Crystal. Solids,* 282, 236 (2001)
[7.5] M. Sakai, *J, Soc. Rheol. Japan*, **39(1・2)**, 7 (2011)

$$
\begin{aligned}
P(t) &= \frac{\tan\beta}{2}\int_0^t E'_{\text{relax}}(t-t')\frac{dA(t')}{dt'}dt' \\
A(t) &= 2\cot\beta\int_0^t C'_{\text{creep}}(t-t')\frac{dP(t')}{dt'}dt'
\end{aligned}
\qquad (7.3)
$$

In the following sections, using Eq. (7.3), we will discuss the viscoelastic indentation contact behaviors in the various types of tests of cone/pyramid indentation.

(i) Step-wise penetration tests

Let us discuss the indentation load relaxation for the stepwise application of a constant contact-area A_0;

$$A(t) = A_0 \cdot u(t), \qquad (7.4)$$

and the creep deformation of contact-area under the stepwise application of a constant indentation load P_0;

$$P(t) = P_0 \cdot u(t) \qquad (7.5)$$

The applications of Eqs. (7.4) and (7.5) to the right-hand side of Eqs. (7.3) combined with the relation of $du(t)/dt = \delta(t)$ ($\delta(t)$; Dirac's delta function) result in

$$
\begin{aligned}
P(t) &= \frac{\tan\beta}{2} A_0 \cdot E'_{\text{relax}}(t) \\
A(t) &= 2\cot\beta P_0 \cdot C'_{\text{creep}}(t)
\end{aligned}
\qquad (7.6)
$$

Accordingly, we can determine the relaxation modulus $E'_{\text{relax}}(t)$ and/or the creep function $C'_{\text{creep}}(t)$ through measuring the indentation load relaxation $P(t)$ and/or the creep deformation of the contact area $A(t)$. However, in the *conventional instrumented indentation apparatus*, we cannot measure the indentation contact areas not only A_0 but also $A(t)$, although it is possible for us to measure the indentation load relaxation $P(t)$ and the time-dependent penetration depth $h(t)$. We need, therefore, to use somewhat undesirable approximation/assumption to estimate $A(t)$ from the $h(t)$ observed. To circumvent this difficulty, we have to use the *instrumented indentation microscope*, the details of which will be given in the later chapter (Chapter 11).

(ii) Constant-rate of penetration tests

In the indentation tests with a constant-rate k_A of contact-area increment

$$A(t') = k_A \cdot t', \tag{7.7}$$

and with a constant-rate of loading k_P

$$P(t') = k_P \cdot t', \tag{7.8}$$

the resultant viscoelastic responses of $P(t)$ for the former, and of $A(t)$ for the latter are, respectively, described by the use of Eq. (7.3) combined with Eqs. (7.7) and (7.8), as follows;

$$\begin{aligned} P(t) &= \frac{k_A \tan\beta}{2}\int_0^t E'_{\text{relax}}(t-t')dt' \\ A(t) &= 2k_P \cot\beta \int_0^t C'_{\text{creep}}(t-t')dt' \end{aligned} \tag{7.9}$$

We can, therefore, readily determine the relaxation function $E'_{\text{relax}}(t)$ and/or the creep function $C'_{\text{creep}}(t)$ via using the time-derivative of $P(t)$ and/or $A(t)$ observed in experiments;

$$\begin{aligned} E'_{\text{relax}}(t) &= \frac{2\cot\beta}{k_A}\frac{dP(t)}{dt} \\ C'_{\text{creep}}(t) &= \frac{\tan\beta}{2k_P}\frac{dA(t)}{dt} \end{aligned} \tag{7.10}$$

In these indentation tests, in order to measure $A(t)$, *the instrumented indentation microscope* plays a very essential role (see Sec. 11.3). The details of the viscoelastic constitutive relations are listed in Tables 7.1 – 7.3 for the flat-ended cylindrical punch, spherical indenter, and the conical indenter.

Table 7.1 Integral-type viscoelastic constitutive equations for the axisymmetric indenters

Flat-ended cylindrical punch	Spherical indenter	Conical indenter
$P(t) = 2a_0 \int_0^t E'_{\text{relax}}(t-t')\frac{dh(t')}{dt'}dt'$	$P(t) = \frac{4}{3\pi^{3/2}R}\int_0^t E'_{\text{relax}}(t-t')\frac{dA^{3/2}(t')}{dt'}dt'$	$P(t) = \frac{\tan\beta}{2}\int_0^t E'_{\text{relax}}(t-t')\frac{dA(t')}{dt'}dt'$
$h(t) = \frac{1}{2a_0}\int_0^t C'_{\text{creep}}(t-t')\frac{dP(t')}{dt'}dt'$	$A^{3/2}(t) = \frac{3\pi^{3/2}R}{4}\int_0^t C'_{\text{creep}}(t-t')\frac{dP(t')}{dt'}dt'$	$A(t) = 2\cot\beta\int_0^t C'_{\text{creep}}(t-t')\frac{dP(t')}{dt'}dt'$

a_0 : radius of the cylinder $\qquad R$: radius of the sphere $\qquad \beta$: inclined face-angle of the cone

Table 7.2 Viscoelastic responses for the step-wise indentation

	Stepwise penetration to a constant contact-area A_0	Stepwise penetration to a constant load P_0
	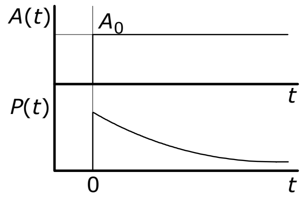	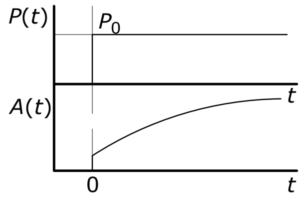
flat-ended cylinder	$P(t)=2a_0h_0E'_{\text{relax}}(t)$	$h(t)=\frac{P_0}{2a_0}C'_{\text{creep}}(t)$
spherical indenter	$P(t)=\frac{4}{3R}\left(\frac{A_0}{\pi}\right)^{3/2}E'_{\text{relax}}(t)$	$A^{3/2}(t)=\frac{3\pi^{3/2}RP_0}{4}C'_{\text{creep}}(t)$
conical indenter	$P(t)=\frac{\tan\beta}{2}A_0E'_{\text{relax}}(t)$	$A(t)=2P_0\cot\beta\cdot C'_{\text{creep}}(t)$

* Use the penetration depths of $h(t)$ and h_0 instead of the contact areas of $A(t)$ and A_0 for the flat-ended cylindrical punch

Table 7.3 Viscoelastic responses for the constant-rate indentation

	Constant-rate of contact area increment	Constant-rate of loading
	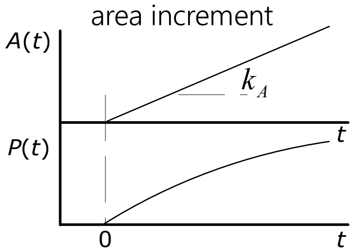	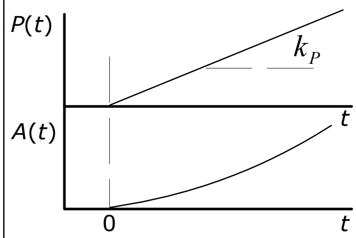
flat-ended cylinder	$\frac{dP(t)}{dt}=2a_0k_hE'_{\text{relax}}(t)$	$\frac{dh(t)}{dt}=\frac{k_P}{2a_0}C'_{\text{creep}}(t)$
spherical indenter	$\bar{P}(p)=\frac{k_A^{3/2}}{\pi R}\frac{\bar{E}'_{\text{relax}}(p)}{p^{3/2}}$	$\frac{dA^{3/2}(t)}{dt}=\frac{3\pi^{3/2}Rk_P}{4}C'_{\text{creep}}(t)$
conical indenter	$\frac{dP(t)}{dt}=\frac{k_A}{2}\tan\beta\cdot E'_{\text{relax}}(t)$	$\frac{dA(t)}{dt}=2k_P\cot\beta\cdot C'_{\text{creep}}(t)$

* Use the penetration depth of $h(t)\left(=k_h\cdot t\right)$ instead of the $A(t)\left(=k_A\cdot t\right)$ for the flat-ended cylindrical punch

7.2 VISCOELASTIC MEYER HARDNESS

The Meyer hardness H_{M} of elastic/elastoplastic bodies is time/rate-independent, and defined by the ratio of the applied indentation load P and the resultant contact area A as $H_{\mathrm{M}} = P/A$ (see Eq. (5.1b)). Accordingly, on the basis of the elastic-viscoelastic corresponding principle, when we apply the Laplace transform inversion to the transformed Meyer hardness $\overline{P} = H^*_{\mathrm{M}} \cdot \overline{A}$, we have the following formula of the viscoelastic Meyer hardness $H_{\mathrm{M}}(t)$;

$$P(t) = \int_0^t H_{\mathrm{M}}(t-t') \frac{dA(t')}{dt'} dt' \tag{7.11}$$

The viscoelastic Meyer hardness $H_{\mathrm{M}}(t)$ is, therefore, *by no means given by the indentation load* $P(t)$ *divided by the contact area* $A(t)$ *at the respective time* t ; $H_{\mathrm{M}}(t) \neq P(t)/A(t)$.

In order to understand *the physics* of viscoelastic Meyer hardness, further considerations will be made in this context for the stepwise penetration, as an example. Substituting $A(t') = A_0 \cdot u(t')$ into Eq. (7.11) and $\varepsilon_{\mathrm{I}}(t') \cdot A(t') = \varepsilon_{\mathrm{I0}} A_0 \cdot u(t')$ into Eq. (7.1), and comparing these resultant relations, we finally find the fact that *the viscoelastic Meyer hardness* $H_{\mathrm{M}}(t)$ *is equivalent to the relaxation modulus* $E'_{\mathrm{relax}}(t)$;

$$H_{\mathrm{M}}(t) = \varepsilon_{\mathrm{I0}} E'_{\mathrm{relax}}(t) \tag{7.12}$$

in which the indentation strain $\varepsilon_{\mathrm{I0}}$ (refer to Eqs. (3.29) - (3.31)) is;

flat-ended cylindrical punch:

$$\varepsilon_{\mathrm{I0}} = \frac{2}{\pi}\left(\frac{h_0}{a_0}\right) \tag{7.13a}$$

spherical indenter：

$$\varepsilon_{\mathrm{I0}} = \frac{4}{3\pi}\left(\frac{a_0}{R}\right) \tag{7.13b}$$

conical indenter:

$$\varepsilon_{\mathrm{I0}} = \frac{\tan\beta}{2} \tag{7.13c}$$

In Eq. (7.13a), h_0 is the penetration depth of the cylindrical punch (the radius of a_0). In Eq. (7.13b), a_0 is the contact radius induced by the stepwise penetration in spherical indentation. Due to the geometrical similarity of cone indentation, its indentation strain $\varepsilon_{\mathrm{I0}}$ is independent of the penetration depth applied, and described by $\varepsilon_{\mathrm{I0}} = \tan\beta/2$ in terms of the characteristic inclined face-angle β of the cone. This fact means that Eq. (7.13c) is always applicable to arbitrary depths of penetration. The equivalence of the viscoelastic Meyer hardness and the relaxation modulus is also well recognized from the fact that the viscoelastic Meyer hardness is given by $H_M(t) = P(t)/A_0$ *in terms of the indentation load relaxation* $P(t)$ observed in the indentation test of a stepwise penetration to a constant contact-area A_0.

7.3 INDENTATION CONTACT MECHANICS OF THE VISCOELASTIC MODELS

The numerical indentation contact mechanics will be discussed in this section for the Maxwell liquid and the Zener II solid ($E_M = E_e$ is assumed in Fig. 6.2 for simplicity) in the constant-rate penetration/loading tests (Eqs. (7.7) and (7.8); Table 7.3) of a conical indenter with the inclined face-angle β.

[Constant-rate penetration test]

In the constant-rate penetration test ($A(t') = k_A \cdot t'$), the viscoelastic indentation load $P(t)$) is given by the first formula of Eq. (7.9);

$$P(t) = \frac{k_A \tan\beta}{2}\int_0^t E'_{\text{relax}}(t-t')dt' \qquad (7.9a)$$

Through applying the relaxation moduli $E'_{\text{relax}}(t)$ of the Maxwell liquids (Eq. (6.8a)) and of the Zener II solid (Eq. (6.8b) with $E'_M = E'_e = E'_g/2$ for simplicity) to Eq. (7.9a), we have the following formulas of the time-dependent indentation load $P(t)$:

(i) Viscoelastic *Maxwell liquid*

$$P(t) = \frac{E'_M \tan\beta}{2}(k_A\tau_M)\left[1-\exp(-t/\tau_M)\right] \qquad (7.14)$$

(ii) Viscoelastic *Zener solid*

$$P(t) = \frac{E'_M \tan\beta}{2}(k_A\tau_M)\left[t/\tau_M + \{1-\exp(-t/\tau_M)\}\right] \qquad (7.15)$$

The normalized indentation load

$$P_N(t/\tau_M)\left[\equiv (2P(t)\cot\beta)/(k_A\tau_M \cdot E'_M)\right]$$

of Eqs. (7.14) and (7.15) are plotted in Fig. 7.1 against the normalized time t/τ_M. Figure 7.1 shows that the indentation load of the Maxwell liquid converges to $P_N(t/\tau_M) \to 1.0$ or $P(t) \to (k_A \tan\beta/2)\eta$ in the

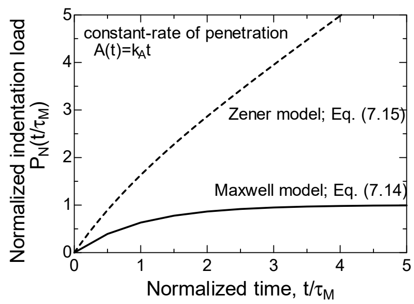

Figure 7.1 The normalized indentation load in the constant-rate of penetration test ($A(t') = k_A \cdot t'$): The solid line represents the Maxwell liquid, and the dashed line indicates the Zener solid.

long-time region of $t \gg \tau_{\mathrm{M}}$. This fact indicates that the Maxwell liquid in its steady state behaves as the Newtonian liquid with the shear viscosity η. On the other hand, as shown in Fig. 7.1 for the Zener solid, there exist a linear relation between $P_{\mathrm{N}}(t/\tau_{\mathrm{M}})$ and t/τ_{M} in the long-time region of $t \gg \tau_{\mathrm{M}}$, i.e.,

$$P_{\mathrm{N}}\left(t/\tau_{\mathrm{M}}\right) \propto t/\tau_{\mathrm{M}} \propto A(t)/k_A\tau_{\mathrm{M}}$$

or

$$P(t) \propto \left(E'_{\mathrm{e}} \tan\beta/2\right) A(t)$$

This linear relation indicates that the Zener model behaves as the perfectly elastic body with the equilibrium elastic modulus of E'_{e} in the long-time region.

[Constant-rate of indentation loading]

The time-dependent viscoelastic contact area $A(t)$ for constant-rate of indentation loading $P(t') = k_p \cdot t'$ is given by the second formula of Eq. (7.9);

$$A(t) = 2k_P \cot\beta \int_0^t C'_{\mathrm{creep}}(t-t')dt' \tag{7.9b}$$

When we apply the creep functions of the Maxwell liquids (Eq. 6.9a) and of the Zener II solid (Eq. 6.9b) to Eq. (7.9b), we have the following formulas of the time-dependent contact area $A(t)$:

(i) *Viscoelastic Maxwell liquid*

$$A(t) = \frac{2\cot\beta}{E'_{\mathrm{M}}}\left(k_P\tau_{\mathrm{M}}\right)\left[t/\tau_{\mathrm{M}} + \frac{1}{2}\left(t/\tau_{\mathrm{M}}\right)^2\right] \tag{7.16}$$

(ii) *Viscoelastic Zener solid*

$$A(t) = \frac{2\cot\beta}{E'_{\mathrm{M}}}\left(k_P\tau_{\mathrm{M}}\right)\left[t/\tau_{\mathrm{M}} - \left\{1-\exp\left(-t/\tau_{\mathrm{Z}}\right)\right\}\right]$$
$$\tau_{\mathrm{Z}} = \left(1+E_{\mathrm{M}}/E_{\mathrm{e}}\right)\tau_{\mathrm{M}} \tag{7.17}$$

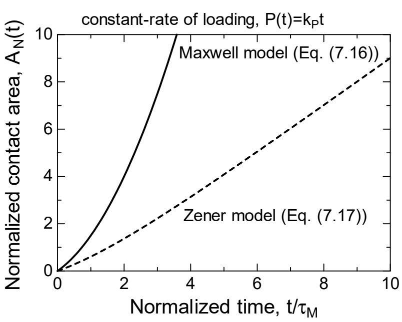

Figure 7.2 The normalized contact area in the constant-rate of loading test ($P(t') = k_P \cdot t'$): The solid line represents the Maxwell liquid, and the dashed line indicates the Zener solid.

The Zener's relaxation time τ_{Z} is given by $\tau_{\mathrm{z}} = 2\tau_{\mathrm{M}}$ because of the relation $E_{\mathrm{M}} = E_{\mathrm{e}}$ we assumed for simplicity. The normalized contact areas $A_{\mathrm{N}}\left(t/\tau_{\mathrm{M}}\right)\left[\equiv A(t)E'_{\mathrm{M}}\tan\beta/2k_P\tau_{\mathrm{M}}\right]$ of Eqs. (7.16) and (7.17) are plotted in Fig. 7.2 against the normalized time t/τ_{M}. In the long-time region of $t \gg \tau_{\mathrm{M}}$, the $A_{\mathrm{N}}(t/\tau_{\mathrm{M}})$ vs. t/τ_{M} relation of the Zener solid becomes linear with the slope of 1.0, i.e., $A_{\mathrm{N}}\left(t/\tau_{\mathrm{M}}\right) \propto t/\tau_{\mathrm{M}} = P(t)/k_P\tau_{\mathrm{M}}$, thus leading to the linear relation between the indentation load $P(t)$ and the resultant contact area $A(t)$, i.e., $P(t) \propto E'_{\mathrm{e}} \cdot A(t)$. This fact implies that the viscoelastic Zener solid behaves as a perfectly elastic body having the elastic modulus of E'_{e} in the long-time region, like as the steady-state deformation observed in the constant-rate penetration test (refer to the consideration on Eq. (7.15) and in Fig. 7.1).

We emphasized in Sec. 7.2 and in Eq. (7.11) that the viscoelastic Meyer hardness $H_{\mathrm{M}}(t)$ is by no means given by $H_{\mathrm{M}}(t) = P(t)/A(t)$ at all, but there exists an inequality relation of $H_{\mathrm{M}}(t) \neq P(t)/A(t)$. The significant discrepancies existing between the viscoelastic Meyer hardness $H_{\mathrm{M}}(t)$ (see Eq. (7.11)) and the ratio of $P(t)/A(t)$ calculated via Eqs. (7.14) – (7.17) are well demonstrated in Figs. 7.3 and 7.4 for their normalized plots; the hardness numbers of $\left[H_{\mathrm{M}}(t)\right]_{\mathrm{N}}$ and $\left[P(t)/A(t)\right]_{\mathrm{N}}$ are, respectively, defined as $H_{\mathrm{M}}(t)$ and $P(t)/A(t)$ normalized with $E'_{\mathrm{g}} \tan\beta/2$. The relaxation behaviors of the hardness number $P(t)/A(t)$ (indicated by the symbols of ○ and ● in Figs. 7.3 and 7.4) are always more sluggish than those of the Meyer hardness $H_{\mathrm{M}}(t)$ (indicated by the solid lines), leading to always larger values of $P(t)/A(t)$ than those of $H_{\mathrm{M}}(t)$. The hardness numbers both $P(t)/A(t)$ and $H_{\mathrm{M}}(t)$ of the Maxwell liquid (Fig. 7.3) progressively diminish with time, while those values of the Zener solid (Fig. 7.4) converge to a finite value of $E'_{\mathrm{e}}/E'_{\mathrm{g}} = 0.5$ in the long-time region of $t/\tau \to \infty$ (notice that we assumed $E'_{\mathrm{M}} = E'_{\mathrm{e}} = E'_{\mathrm{g}}/2$ for the model examined).

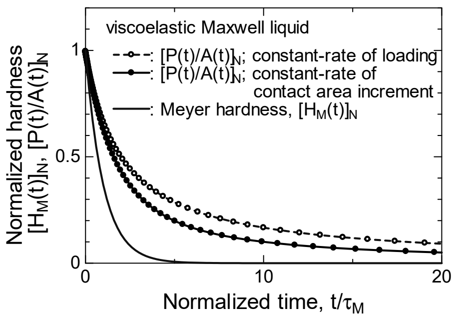

Figure 7.3 Normalized viscoelastic Meyer hardness $\left[H_{\mathrm{M}}(t)\right]_{\mathrm{N}}$, and $\left[P(t)/A(t)\right]_{\mathrm{N}}$ plotted against the normalized time of t/τ_{M} (viscoelastic Maxwell liquid)

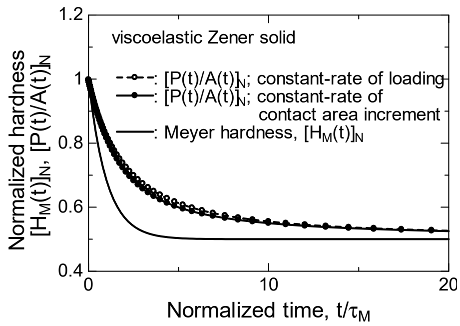

Figure 7.4 Normalized viscoelastic Meyer hardness $\left[H_{\mathrm{M}}(t)\right]_{\mathrm{N}}$, and $\left[P(t)/A(t)\right]_{\mathrm{N}}$ plotted against the normalized time of t/τ_{M} (viscoelastic Zener solid)

INDENTATION CONTACT MECHANICS OF SOFT MATTERS WITH SURFACE ADHESION

CHAPTER 8

In the preceding sections, we have discussed the elastic/elastoplastic indentation contact mechanics of engineering materials including metals and ceramics so called *the hard materials* having rather large elastic modulus of $E' \geq 100$ GPa. Due to the large elastic modulus of such hard materials, the surface adhesion, even if there exists, makes a rather minor effect on their contact behavior. In most cases, therefore, we can neglect the surface adhesion in their indentation contact mechanics. On the other hand, the elastic moduli of *soft materials* including organic polymers, biomaterials, and microbiological mediums are rather small, and fall in the range of $E' \approx 1$ kPa - 100MPa, where the surface adhesion plays an essential role in their mechanical characteristics and functions. It must be also noticed that the mechanical characteristics of most of these soft matters are time dependent viscoelastic and/or elastoplastic.

The indentation contact mechanics of *perfectly elastic bodies* with surface adhesion has well been appreciated through the JKR-theory (Johnson-Kendall-Roberts theory) (**[8.1], [8.2], [8.3]**), the details of which will be given in Section 8.1. While on the other hand, neither *theoretical considerations nor well-conducted experiments* have been conducted for *elastoplastic/viscoelastic bodies* with surface adhesion. To overcome these difficulties and issues, the considerations on FEA-based numerical indentation contact mechanics will be made in Section 8.2 for elastoplastic bodies. As to the indentation contact mechanics of time-dependent viscoelastic bodies with surface adhesion, the "elastic-viscoelastic correspondence principle" (refer to Chapters 6 and 7) will be applied to the JKR-theory in Section 8.3. The details of experimental studies of elastoplastic/viscoelastic soft matters with surface adhesion will be given in Chapter 12.

[8.1] K.L. Johnson, "Contact Mechanics", Cambridge University Press (1985)
[8.2] K.L. Johnson, K. Kendall, A.D. Roberts, "Surface energy and the contact of elastic solids", Proc. Roy. Soc. London A, 324:301-8.7(1971)
[8.3] D. Maugis, "Contact, Adhesion and Rupture of Elastic Solid", Springer (2000)

8.1 ELASTIC BODIES WITH SURFACE ADHESION - THE JKR THEORY-

The JKR theory focuses only on the contact mechanics of sphere. In this section, however, we will also discuss the JKR theory extended to the conical/pyramidal indentation contact, since the Vickers/Berkovich indentation is very conventional in the practical indentation tests.

Suppose an axisymmetric indenter with an arbitrarily shape indented onto an elastic half-space, resulting in the contact radius a and the penetration depth h under the indentation load P. The indenter will be withdrawn to the elastic body having surface adhesion, i.e., the surface adhesion induces *negative contact pressure*. This fact implies that the indentation load P at the contact radius a will be smaller than that of the elastic body without surface adhesion. The JKR theory models the surface adhesion as the *negative contact pressure acting on the cylindrical flat punch with the radius* a.

Using Eq. (3.10), the contact pressure $p(r)$ of a cylindrical flat punch having the radius a is given by

$$p_{\mathrm{F}}(r) = p_{\mathrm{F}}\left[1-\left(\frac{a}{r}\right)^{2}\right]^{-1/2}; \quad 0 \le r < a \tag{8.1}$$

where use has been made of the relation $p(r) = -\sigma_z(r)$. In Eq. (8.1), the subscript F stands for Flat punch. The coefficient of the contact pressure p_{F} must be a negative value ($p_{\mathrm{F}} < 0$) when it describes surface adhesion. In a similar way, using Eqs. (3.19) and (3.26), the contact pressure is

$$p_{\mathrm{S}}(r) = p_{\mathrm{S}}\left[1-\left(\frac{a}{r}\right)^{2}\right]^{1/2}; \quad 0 \le r < a \tag{8.2}$$

for spherical indentation, and

$$p_{\mathrm{c}}(r) = p_{\mathrm{C}} \cosh^{-1}(a/r); \quad 0 \le r < a \tag{8.3}$$

for conical indentation. In these expressions, the subscripts S and C indicate Sphere and Cone, respectively. In the JKR theory, therefore, the contact pressure distribution beneath the indenter of an elastic body with surface adhesion is described by superposing Eq. (8.1) on Eq. (8.2) or on Eq. (8.3) as follows;

Spherical indentation

$$p(r) = p_S \left[1 - \left(\frac{a}{r}\right)^2\right]^{1/2} + p_F \left[1 - \left(\frac{a}{r}\right)^2\right]^{-1/2} \qquad (8.4)$$

Conical indentation

$$p(r) = p_C \cosh^{-1}(a/r) + p_F \left[1 - \left(\frac{a}{r}\right)^2\right]^{-1/2} \qquad (8.5)$$

On the other hand, using the geometrical formula of Eq. (3.1), the contact surface profile beneath the indenter ($0 \le r \le a$) is described by

Spherical indentation

$$u_z(r) = h - \frac{r^2}{2R} \qquad (8.6)$$

Conical indentation

$$u_z(r) = h - r\tan\beta \qquad (8.7)$$

Appling the analytical procedures in Sec. 3.1 combined with Eqs. (8.1) – (8.5) to Eq. (8.6) or to Eq. (8.7), we finally have the following relations;

【**Spherical indentation**】

$$\frac{\pi p_S}{4aE'}\left(2a^2 - r^2\right) + \frac{\pi a p_F}{E'} = h - \frac{r^2}{2R} \qquad (8.8)$$

Notice the algebraic identity of Eq. (8.8) as to the variable r , then we have the following relations;

$$p_S = \frac{2aE'}{\pi R} \qquad (8.9)$$

$$h = \frac{\pi a}{2E'}\left(p_S + 2p_F\right) \qquad (8.10)$$

Furthermore, applying $P = \int_0^a p(r) 2\pi r dr$ to Eq. (8.4), the indentation load is given by

$$P = \left(\frac{2}{3}p_S + 2p_F\right)\pi a^2 \qquad (8.11)$$

【**Conical indentation**】

A similar mathematics in the preceding spherical indentation contact leads to the following relations;

$$\frac{\pi a p_C}{E'}\left(1 - \frac{2}{\pi}\frac{r}{a}\right) + \frac{\pi a p_F}{E'} = h - r\tan\beta \qquad (8.8')$$

$$p_{\mathrm{C}} = \frac{E'}{2}\tan\beta \tag{8.9'}$$

$$h = \frac{\pi a}{E'}\left(p_{\mathrm{S}} + p_{\mathrm{F}}\right) \tag{8.10'}$$

$$P = \left(p_{\mathrm{C}} + 2p_{\mathrm{F}}\right)\pi a^2 \tag{8.11'}$$

The coefficients of contact pressure distribution p_{S} and p_{C} in Eqs. (8.9) and (8.9') are, therefore, successfully related to the elastic modulus E'. It must be noticed that these coefficients of contact pressure distribution are identical to those we have already derived in Secs. 3.2 and 3.3 for the perfectly elastic body without surface adhesion. Unfortunately, however, we have failed in describing the pressure distribution coefficient p_{F} of cylindrical flat punch in terms of the surface adhesion in the preceding context. To overcome this difficulty, let us make an *energy-based consideration* on the indentation contact processes, since the surface adhesion γ (N/m) is equivalent to the *surface energy* γ (J/m^2).

In the first step of indentation contact process, suppose an axisymmetric indenter pressed onto an elastic body *without surface adhesion* to the indentation load P_1 as depicted in Fig. 8.1(a), at which the penetration depth h_1 and the contact radius a_1 are assumed to be induced. The elastic strain energy $U_1\left(=\int_0^{h_1} P dh\right)$ stored in the elastic body associated with this indentation contact process is

Spherical indentation

$$U_1 = \frac{2}{15}\frac{\pi^2 a_1^{\,3}}{E'} p_{\mathrm{S}1}^{\ 2} \tag{8.12}$$

Conical indentation

$$U_1 = \frac{\pi^2 a_1^{\,3}}{3E'} p_{\mathrm{C}1}^{\ 2}. \tag{8.13}$$

The elastic stored energy U_1 is represented by the area OABO in Fig. 8.1(a) of the P - h diagram. In Eqs. (8.12) and (8.13), $p_{\mathrm{S}1}$ and $p_{\mathrm{C}1}$ are, respectively, the contact pressure coefficients of spherical and conical indentations at the contact radius a_1; $p_{\mathrm{S}1} = 2a_1 E'/\pi R$ and $p_{\mathrm{C}1} = \left(E'/2\right)\tan\beta$. It must be noticed that $p_{\mathrm{C}1}$ is independent of the contact radius a_1 due to the geometrical similarity of conical indentation.

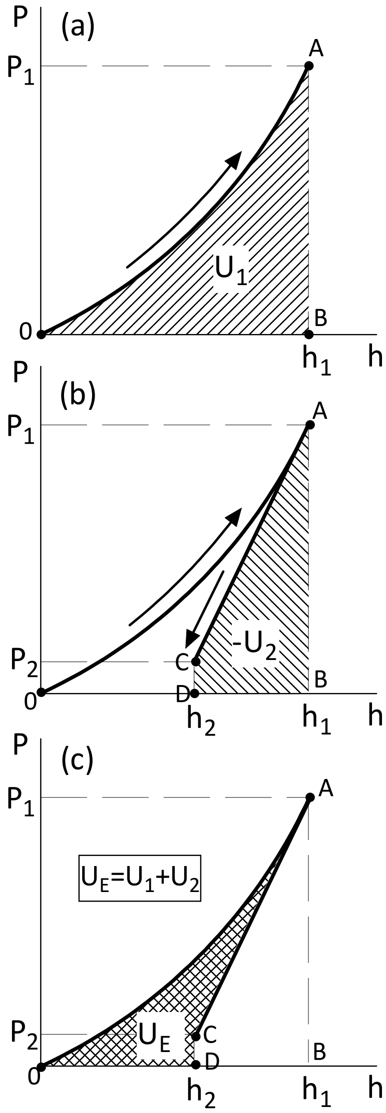

Figure 8.1 Energy-based considerations on the indentation contact processes of an elastic body with surface adhesion: (a) the indentation loading path of an elastic body without surface adhesion (the line OA), (b) the unloading path associated with the incremental increase of surface adhesion (the line AC), (c) the elastic stored energy U_{E} of the elastic body with surface adhesion at the point A

In the subsequent second step of indentation contact process, at the point A (P_1, h_1, a_1) in Fig. 8.1(b), let us consider the variation of the strain energy associated with the incremental surface adhesion from 0 to γ on the contact surface maintaining its contact area at πa_1^2. This mechanical process implies that the indenter is progressively pulled to the contact surface, resulting in unloading, as shown in Fig. 8.1(b), along the *linear* line AC, since the contact area maintains constant. The indentation contact state at the point C (P_2, h_2, a_1) is the *equilibrium state of the elastic body having the surface energy of* γ. This mechanical process along the line AC will be equivalent to *the unloading process of a flat-punch with the radius* a_1. The total energy released through this unloading process along the line AC is denoted by $U_2(<0)$, and given by the area ABDCA ($= -U_2$) in Fig. 8.1(b). The P - h unloading path along the line AC is, therefore, described by

$$
\begin{aligned}
P &= P_1 + 2\pi a_1^2 p_{\mathrm{F1}} \\
&= 2a_1 E'(h - h_1) + P_1 \qquad (8.14) \\
h &= h_1 + \frac{\pi a_1}{E'} p_{\mathrm{F1}}
\end{aligned}
$$

where use has been made of Eq. (3.9) for the indentation of a flat-punch. In Eq. (8.14), we must notice the fact that the coefficient of contact pressure distribution p_{F1} (see Eq. (8.1)) of the cylindrical flat-punch with the radius a_1 is negative *due to surface adhesion*. The indentation load P_1 at the point A is given by $P_1 = \left(2\pi a_1^2/3\right) p_{\mathrm{S1}}$ for spherical indentation, and $P_1 = \pi a_1^2 p_{\mathrm{C1}}$ for conical indentation. On the other hand, the released energy $U_2(<0)$ associated with the incremental surface adhesion is finally given by

Spherical indentation

$$
U_2 = \frac{\pi^2 a_1^3}{E'}\left(\frac{2}{3} p_{\mathrm{S1}} p_{\mathrm{F1}} + p_{\mathrm{F1}}^2\right) \qquad (8.15)
$$

Conical indentation

$$
U_2 = \frac{\pi^2 a_1^3}{E'}\left(p_{\mathrm{C1}} p_{\mathrm{F1}} + p_{\mathrm{F1}}^2\right) \qquad (8.16)
$$

through using the formula of $U_2 = \int_{h_1}^{h_2} P dh = \int_{P_1}^{P_2} P \frac{dP}{2a_1 E'} = \frac{P_2^{\,2} - P_1^{\,2}}{4a_1 E'}$.

Accordingly, when we apply an indentation load to an *elastic half-space with surface adhesion* to the contact radius of a, using Eqs. (8.12) - (8.16), the associated elastic strain energy U_{E} stored in the body (the area of ACDOA in Fig. 8.1(c)) is;

Spherical indentation

$$U_{\mathrm{E}}\left(\equiv U_1 + U_2\right) = \frac{\pi^2 a^3}{E'}\left(\frac{2}{15} p_{\mathrm{S}}^{\,2} + \frac{2}{3} p_{\mathrm{S}} p_{\mathrm{F}} + p_{\mathrm{F}}^{\,2}\right)$$

(8.17a)

or Eqs. (8.9) and (8.10) combined with Eq. (8.17a) result in

$$U_{\mathrm{E}}\left(\equiv U_1 + U_2\right) = \frac{\pi^2 a^3}{E'}\left\{\frac{1}{5}\left(\frac{aE'}{\pi R}\right)^2 - \frac{2}{3}\frac{E'^2}{\pi^2 R} h + \left(\frac{E'}{\pi a}\right)^2 h^2\right\}$$

(8.17b)

Conical indentation

$$U_{\mathrm{E}}\left(\equiv U_1 + U_2\right) = \frac{\pi^2 a^3}{E'}\left(\frac{1}{3} p_{\mathrm{C}}^{\,2} + p_{\mathrm{C}} p_{\mathrm{F}} + p_{\mathrm{F}}^{\,2}\right)$$

(8.18a)

or Eqs. (8.9') and (8.10') combined with Eq. (8.18a) lead to

$$U_{\mathrm{E}}\left(\equiv U_1 + U_2\right) = \frac{\pi^2 a^3}{E'}\left\{\frac{1}{3}\left(\frac{E'\tan\beta}{2}\right)^2 - \frac{E'^2 \tan\beta}{2\pi a} h + \left(\frac{E'}{\pi a}\right)^2 h^2\right\}$$

(8.18b)

As mentioned in the preceding considerations, in the present indentation contact problem, the adhesive surface force introduces the surface energy U_{S} which *decreases* when the surfaces come into intimately contact and *increases* when they separate. Therefore, we can write

$$U_{\mathrm{S}} = -2\gamma\pi a^2 \qquad (8.19)$$

The total energy (the Gibbs free energy) U_{T} of the present mechanical system, therefore, is given by

$$U_{\mathrm{T}} = U_{\mathrm{E}} + U_{\mathrm{S}} \qquad (8.20)$$

In the mechanical equilibrium under a fixed depth of penetration meaning none of external works, the variation of total energy associated with incremental contact radius δa results in

$$\left(\frac{\partial U_{\mathrm{T}}}{\partial a}\right)_h = 0 \qquad (8.21)$$

Substituting Eqs. (8.17) - (8.20) into Eq. (8.21) and using Eq. (8.17b) or Eq. (8.18b), we have the relation of $\left(\partial U_{\mathrm{E}}/\partial a\right)_h = \left(\pi^2 a^2/E'\right) p_{\mathrm{F}}{}^2$ both for spherical and conical indentations. We can, therefore, finally relate the pressure distribution coefficient p_{F} to the adhesive energy γ as follows;

$$p_{\mathrm{F}} = -\sqrt{\frac{4\gamma E'}{\pi a}} \qquad (8.22)$$

Once we get the analytical formulas of p_{S} (Eq. (8.9)), p_{C} (Eq. (8.9')), and p_{F} ((8.22)), substituting these coefficients into Eqs. (8.10) and (8.11), or into Eqs. (8.10') and (8.11'), we can finally describe the penetration depth h and the indentation load P in terms of the contact radius a:

Spherical indentation

$$h = \frac{a^2}{R} - 2\sqrt{\frac{\pi\gamma}{E'}}a^{1/2} \qquad (8.23)$$

$$P = \frac{4E'}{3R}a^3 - 4\sqrt{\pi\gamma E'}a^{3/2} \qquad (8.24)$$

Conical indentation

$$h = \frac{\pi \tan\beta}{2}a - 2\sqrt{\frac{\pi\gamma}{E'}}a^{1/2} \qquad (8.23')$$

$$\begin{aligned} P &= \left(\frac{E'}{2}\tan\beta\right)\pi a^2 - 4\sqrt{\pi\gamma E'}a^{3/2} \\ &= \left(\frac{E'}{2}\tan\beta\right)A - 4\sqrt{\frac{\gamma E'}{\pi^{1/2}}}A^{3/4} \end{aligned} \qquad (8.24')$$

in which $A\left(=\pi a^2\right)$ stands for the contact area. Substitution of $\gamma = 0$ into the above formulas naturally reduces them to those of purely elastic body that we have already derived in Secs. 3.2 and 3.3. The use of *the instrumented indentation microscope* (see the details in Sec. 11.3) makes us possible for determining not only the indentation load P and the penetration depth h, but also for measuring the contact radius a and the contact area A in experiment. We, therefore, readily determine in experiment the quantitative values of E' and γ without using any undesirable approximation and assumption. As readily seen in Eqs. (8.23) - (8.24'), however, the P - h relationship can only be obtained in an *implicit manner* via the contact radius a as its intermediate variable.

In order to understand the role of surface adhesion in the indentation contact mechanics, Figs 8.2(a) and 8.2(b) demonstrate the P - A relations (Eq. (8.24')) of conical indentation for the elastic bodies with surface adhesion. In Fig. 8.2(a), the linear P - A relation indicates $P = \left(E' \tan\beta/2\right) A$ of the perfectly elastic body without surface adhesion ($\gamma = 0$ N/m). As clearly seen in Fig. 8.2, with the increase in the adhesive energy γ and with the decrease in the elastic modulus E', the effect of surface adhesion on the contact behavior becomes progressively more significant, leading to the enhanced nonlinearity in their P - A relations.

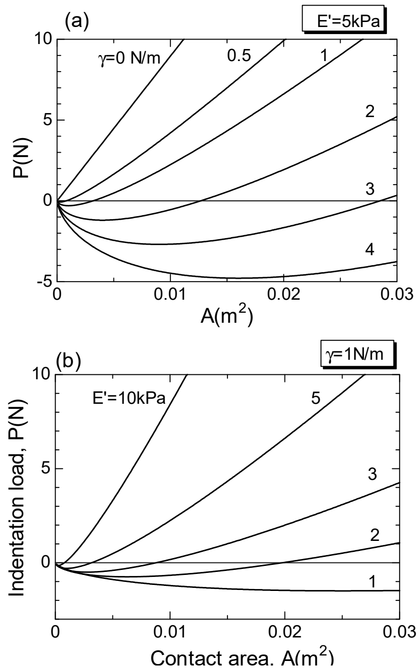

Figure 8.2 The P - A relations of conical indentation for the elastic bodies with surface adhesion:
(a) E'=5kPa; γ =0N/m～4N/m
(b) $\gamma = 1$ N/m; E' = 1kPa～10kPa

The normalized expressions of Eqs. (8.23) – (8.24') will lead us to deeper and more comprehensive understanding for the role of surface adhesion in the indentation contact mechanics. As readily seen in Fig. 8.2, since the adhesive force pulls the surface into contact, the indentation load has a minimum value of P_c at the critical contact radius a_c, i.e., $\left(dP/da\right)_{a_c} = 0$. In this textbook, we adopt a_c, P_c, and the critical penetration depth $h_c \left(= h\left(a_c\right)\right)$ as the critical parameters in normalizing Eqs. (8.23) – (8.24') (notice that we will use the absolute values of $|P_c|$ and $|h_c|$, whenever these parameters are negative). These critical parameters thus defined are summarized as follows;

Spherical indentation

$$
\begin{aligned}
a_c &= \left(\frac{9\pi\gamma R^2}{4E'}\right)^{1/3} \\
P_c &= -3\pi\gamma R \qquad\qquad (8.25) \\
h_c &= -\left(\frac{3\pi^2\gamma^2 R}{16E'^2}\right)^{1/3}
\end{aligned}
$$

Conical indentation

$$a_c = \frac{36\gamma}{\pi E' \tan^2 \beta}$$

$$P_c = -\left(\frac{6}{\pi \tan \beta}\right)^3 \frac{\gamma^2}{E'} \qquad (8.25')$$

$$h_c = \frac{6\gamma}{E' \tan \beta}$$

The normalized P - a and h - a relations thus derived in terms of these critical parameters are given by

Spherical indentation

$$P_N = a_N{}^3 - 2a_N{}^{3/2}$$
$$h_N = 3a_N{}^2 - 4a_N{}^{1/2} \qquad (8.26)$$

Conical indentation

$$P_N = 3a_N{}^2 - 4a_N{}^{3/2}$$
$$h_N = 3a_N - 2a_N{}^{1/2} \qquad (8.26')$$

where a_N, P_N, and h_N indicate, respectively, the normalized contact parameters of $a_N = a/a_c$, $P_N = P/|P_c|$, and $h_N = h/|h_c|$ (spherical indentation) or $h_N = h/h_c$ (conical indentation). On the other hand, the P_N - h_N relation is numerically given in an *implicit manner* via the contact radius a_N as its intermediate variable via Eq. (8.26) or Eq. (8.26'). These normalized expressions thus obtained are plotted in Fig. 8.3; the closed circles (●) are the normalized relations of Eq. (8.26') (conical indentation), while the open circles (○) indicate Eq. (8.26) (spherical indentation). Furthermore in Fig. 8.3, the solid lines represent the elastic body *with surface adhesion*, and the broken lines are for *without surface adhesion*. Due to the face-contact of spherical indentation while the point-contact of conical indentation in their initial stages of indentation contact, the surface adhesion makes more significant effect on the spherical indentation contact than that of conical indentation, as well recognized in Figs. 8.3(a) and 8.3(c).

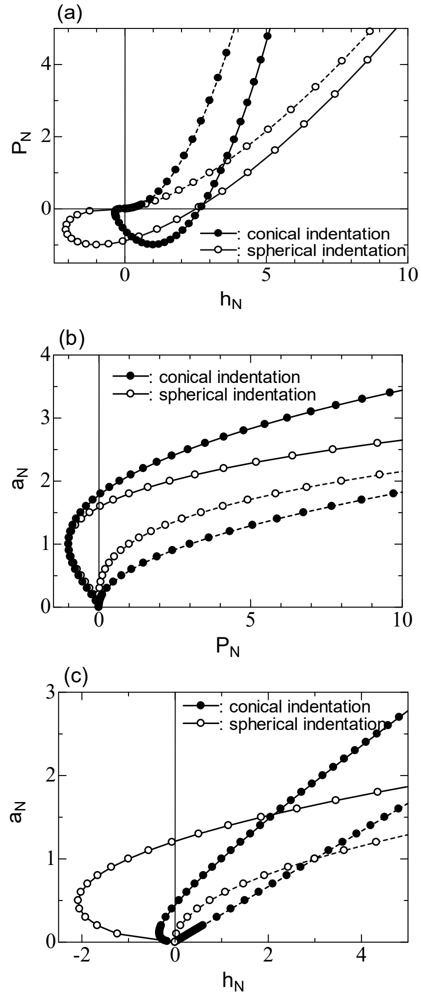

Figure 8.3 Normalized indentation contact diagrams; the solid lines indicate the adhesive contact (JKR theory), while the broken lines are those of the elastic body without surface adhesion

[FEA-Based Numerical Studies]

The numerical results of Finite Element Analysis (FEA) of the loading/unloading P - A relations for the perfectly elastic bodies are shown in Fig. 8.4 (Vickers/Berkovich-equivalent cone indentation for the penetration depth up to $h_{\max} = 30$ µm). Both the loading and the unloading P - A relations of the elastic body without surface adhesion ($E' = 20$ kPa, $\gamma = 0.0$ mJ/m^2; ● symbol) are linear and coincide with each other, where the dashed linear line is the analytical solution of $P = (E' \tan\beta/2) A$. On the other hand for the elastic body with surface adhesion ($E' = 20$ kPa, $\gamma = 5.0$ mJ/m^2; ○ symbol), however, a significant hysteresis is observed in its P - A loading/unloading relation, although the body is perfectly elastic. It must be noticed in their loading P - A relations that the indentation load of the elastic body with surface adhesion is always as well as significantly smaller than that without surface adhesion. This is resulted from the fact that the surface adhesion pulls the tip of indenter downward to the contact surface, i.e., a negative force is superimposed on the externally applied indentation load. It will be also worthy of note that the contact area at the maximum depth of indentation ($h_{\max} = 30$ µm) is about $A_{\max} \approx 100$ (x 100µm^2) for the elastic body without surface adhesion, while it is about $A_{\max} \approx 180$ (x100µm^2) for the elastic body with surface adhesion, i.e., about 1.8 times larger in its contact area under surface adhesion: The JKR-theory predicts this effect of surface adhesion on the contact radius as readily seen in Fig 8.3(c), although the JKR-theory cannot predict the unloading P - A path.

As readily seen in Fig. 8.4, the FEA-based numerical results (the symbols ○) well signify the JKR-theory (the dashed P - A path: Eq. (8.24'));

$$P = \left(\frac{E' \tan\beta}{2} \right) A - \lambda_E A^{3/4}, \tag{8.27}$$

where λ_E is defined with

$$\lambda_E = 4\sqrt{\frac{\gamma E'}{\pi^{1/2}}}, \tag{8.28}$$

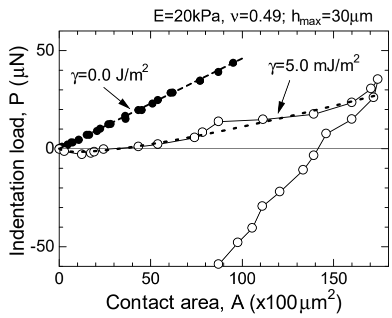

Figure 8.4 The effect of surface adhesion on the P - A loading/ unloading relations (FEA-based numerical results for the Vickers/ Berkovich equivalent cone). The symbols ○ and ● indicate the results of the elastic bodies ($E' = 20$ kPa) with ($\gamma = 5.0$ mJ/m^2) and without ($\gamma = 0.0$ m J/m^2) surface adhesion, respectively. The dashed lines indicate the JKR-theory (Eq. 8.24')

being referred to as the **adhesion toughness** (the subscript E indicates Elastic) that stands for the fracture toughness of interfacial delamination between the tip-of-indenter and the material indented. The physical dimension of λ_E is [Pa・m$^{1/2}$] that is the same as the mode-I fracture toughness, $K_{Ic}\left(\equiv\sqrt{2\gamma E'}\right)$.

8.2 ELASTOPLASTIC BODIES WITH SURFACE ADHESION - FEA-Based Numerical Analyses-

The plastic deformation and flow will lead to the mechanical processes that reduce the effect of surface adhesion on the elastoplastic contact mechanics. Suppose *an elastic body* with the elastic modulus E' and *an elastoplastic body* with the same elastic modulus E' along with the yield stress Y, and then inspect the effect of surface adhesion on the normalized indentation load $\left[\left|P(\gamma)-P(\gamma=0)\right|/P(\gamma)\right]_A$ of these two elastic and elastoplastic bodies; the normalized indentation load is defined by the indentation loads of $P(\gamma)$ and $P(\gamma=0)$ with and without surface adhesion at a given contact area A. Due to the reducing surface adhesion under plastic flow of the contact surface, the normalized indentation load $\left[\left|P(\gamma)-P(\gamma=0)\right|/P(\gamma)\right]_A$ of the elastoplastic body will always be smaller than that of the perfectly elastic body. To confirm this plastic effect on the adhesion toughness, the FEA-based numerical results are plotted in Fig. 8.5, indicating that the plastic flow reduces the effect of adhesion on the P - A loading/unloading relation.

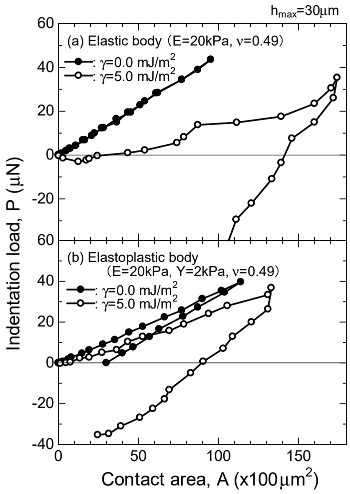

Figure 8.5
P - A loading/ unloading relations (FEA-based numerical results) of
(a) perfectly elastic bod
E' = 20.0 kPa, and
(b) elastoplastic body
E' = 20.0 kPa, Y = 2.0 kPa
The open circles (○) and the closed circles (●) indicate the P - A relations
with (γ = 5.0 mJ/m^2) and
without (γ = 0.0 mJ/m^2)
surface adhesion, respectively

Based on these FEA-based numerical studies, the JKR-theory (Eq. (8.27)) of perfectly elastic body can be modified into the following formula through including the plastic contribution to the indentation contact of elastoplastic body;

$$P = H_M A - \lambda_{EP} A^{3/4} \tag{8.29}$$

in which H_M stands for the Meyer hardness, and the **elastoplastic adhesion toughness** λ_{EP} is defined by

$$\lambda_{EP} = 4\sqrt{\frac{\gamma_{EP} E'}{\pi^{1/2}}} \tag{8.30}$$

In Eq. (8.30), γ_{EP} represents the elastoplastic surface adhesion (adhesion energy), although we have none of analytical formulas to corelate it to the yield stress Y. To circumvent this difficulty, therefore, we have to rely on the FEA-based approaches.

The FEA-based numerical results of elastoplastic bodies ($E = 20$ kPa; 1.0 kPa $\le Y \le$ 5.0 kPa) are shown in Fig. 8.6, indicating that the elastoplastic adhesion energy γ_{EP} monotonically decreases with the decrease in the yield stress Y, i.e., with enhancing plastic flow; γ_{EP} approaches to γ, i.e., $\gamma_{\mathrm{EP}} \to \gamma$ with the increase in Y, while it diminishes to zero, i.e., $\gamma_{\mathrm{EP}} \to 0$, with the decrease in Y. The correlations of the elastoplastic adhesion toughness $\lambda_{\mathrm{EP}}{}^2/E'\left(\equiv\left(16/\sqrt{\pi}\right)\gamma_{\mathrm{EP}}\right)$ and the surface energy γ of elastoplastic bodies with various value of E and Y are shown in Fig. 8.7. As readily seen in Figs. 8.6 and 8.7, the FEA-based numerical studies for the adhesive elastoplastic indentation contact problems lead to the following conclusions;

(i) both the elastoplastic adhesion toughness λ_{EP} and the adhesive surface energy γ_{EP} decrease with the decrease in the yield stress Y, i.e., with enhancing plastic flows,

(ii) these elastoplastic adhesion parameters increase to the values of perfectly elastic body, i.e., $\gamma_{\mathrm{EP}} \to \gamma$ and $\lambda_{\mathrm{EP}} \to \lambda_{\mathrm{E}}$, with the increase in the yield stress Y, leading to the perfectly elastic JKR-theory.

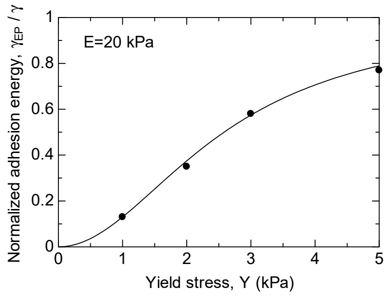

Figure 8.6 Correlation between the elastoplastic surface energy γ_{EP} and the yield stress Y of the elastoplastic bodies ($E = 20$ kPa) (FEA-based numerical results)

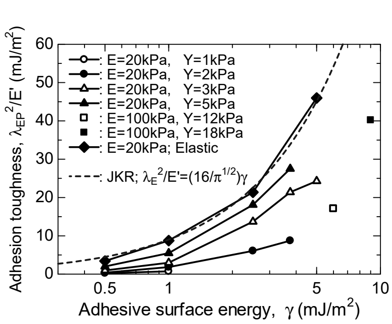

Figure 8.7 Correlations between the adhesion toughness $\lambda_{\mathrm{EP}}{}^2/E'$ and adhesive surface energy γ of elastoplastic bodies (FEA-based numerical results). The dashed line indicates the JKR-theory of perfectly elastic body

Figure 8.8 shows the ($\lambda_{\mathrm{EP}}{}^2/E'$ vs $a_\gamma \gamma$)-master curve that is made by horizontally shifting the respective $\lambda_{\mathrm{EP}}{}^2/E'$ vs γ curves having various values of E and Y in Fig. 8.7 along the $\log\gamma$-axis to superimpose on the perfectly elastic JKR-curve. The superposition is satisfactory as readily seen in Fig. 8.8, where the shift factor a_γ stands for the amount of horizontal shit in superposition, and is related to the elastoplastic adhesion energy γ_{EP} as follows;

$$a_\gamma = \gamma_{\mathrm{EP}}/\gamma \tag{8.31}$$

There may exist a well-defined relationship between the shift factor a_γ and the plastic index $PI\left(\equiv \varepsilon_{\mathrm{I}} E'/cY\right)$ (refer to Chap. 5), being expected that

$$a_\gamma \to 1 \quad (\gamma_{\mathrm{EP}} \to \gamma) \text{ for } PI \downarrow 0 \quad \text{(perfectly elastic)}$$

$$a_\gamma \to 0 \quad (\gamma_{\mathrm{EP}} \to 0) \text{ for } PI \uparrow \infty \quad \text{(fully plastic)}$$

The relationships between a_γ and $PI\left(\equiv \varepsilon_{\mathrm{I}} E'/cY\right)$ are shown in Fig. 8.9 (the FEA-based numerical results); the best-fitted empirical formula of this relation is given by

$$a_\gamma = 1/(3.5PI); \quad PI \geq 0.286 \tag{8.32}$$

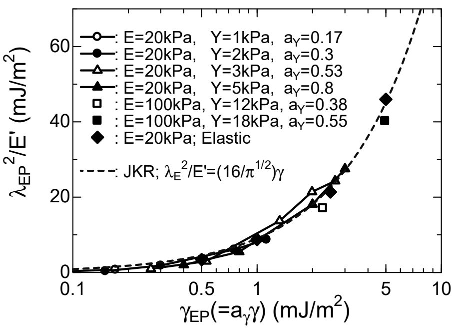

Figure 8.8 $\lambda_{\mathrm{EP}}{}^2/E'$ vs γ_{EP} master curve made by horizontally shifting the respective $\lambda_{\mathrm{EP}}{}^2/E'$ vs γ curves in Fig. 8.7 and superimposing onto the perfectly elastic JKR-curve (the dashed line)

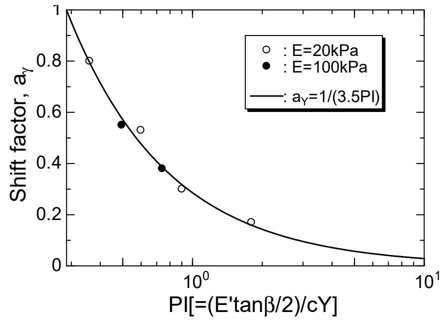

Figure 8.9 Correlation between the plastic index $PI\left(\equiv \varepsilon_{\mathrm{I}} E'/cY\right)$ and the shift factor $a_\gamma\left(\equiv \gamma_{\mathrm{EP}}/\gamma\right)$ utilized in Fig. 8.7 to make the master curve shown in Fig. 8.8 (FEA-based numerical result). The dashed line indicates the best-fitted empirical relation of $a_\gamma = 1/(3.5PI)$ (Eq. (8.32))

8.3 VISCOELASTIC BODIES WITH SURFACE ADHESION

(1) Load relaxation (cone/pyramid indentation)

Applying the "elastic-viscoelastic corresponding principle" to the JKR-theory leads to the following constitutive equation of viscoelastic bodies with surface adhesion *in Laplace-space*;

$$\bar{P}(p) = \left(\frac{E'^*(p)\tan\beta}{2}\right)\bar{A}(p) - \lambda_{\mathrm{VE}}{}^*(p)\bar{A}(p)^{3/4} \qquad (8.33)$$

where $\bar{P}(p)$, $\bar{A}(p)$, $E'^*(p)$, and $\lambda_{\mathrm{VE}}{}^*(p)$ are, respectively, defined with

$$\bar{P}(p) = \int_0^\infty P(t)e^{-pt}dt$$

$$\bar{A}(p) = \int_0^\infty A(t)e^{-pt}dt$$

$$E'^*(p) = p\int_0^\infty E_{\mathrm{relax}}'(t)e^{-pt}dt$$

$$\begin{aligned}\lambda_{\mathrm{VE}}{}^*(p) &= p\int_0^\infty \lambda_{\mathrm{VE}}(t)e^{-pt}dt \\ &= 4\sqrt{\frac{\gamma}{\pi^{1/2}}}\,p\int_0^\infty \sqrt{E'_{\mathrm{relax}}(t)}\,e^{-pt}dt\end{aligned}$$

The invers Laplace transform of Eq. (8.33) for viscoelastic bodies with surface adhesion, therefore, results in the following constitutive equation *in real space*;

$$\begin{aligned}P(t) = &\left(\frac{\tan\beta}{2}\right)\int_0^t E'_{\mathrm{relax}}(t-t')\frac{dA(t')}{dt'}dt' \\ &-4\sqrt{\frac{\gamma}{\pi^{1/2}}}\int_0^t \sqrt{E'_{\mathrm{relax}}(t-t')}\,\frac{dA(\mathrm{t'})^{3/4}}{dt'}dt'\end{aligned} \qquad (8.34)$$

Let us suppose, as an example, the indentation load relaxation test under the stepwise application of contact area to A_0;

$A(t) = u(t)A_0$, $u(t)$; Heaviside step-function $\qquad$ (8.35)

and then inspect the effect of surface adhesion on the load relaxation. Substituting Eq. (8.35) into Eq. (8.34) along with noticing the relation of $du(t)/dt = \delta(t)$ （$\delta(t)$: Dirac's delta function）, we finally have the following expression for the indentation load relaxation of cone/pyramid indentation;

$$P(t) = \left(\frac{\tan\beta}{2} A_0 \right) E'_{\text{relax}}(t) - 4\sqrt{\frac{\gamma}{\pi^{1/2}} A_0^{3/4}} \sqrt{E'_{\text{relax}}(t)} \tag{8.36}$$

In order to simply the subsequent numerical analyses, by way of example, the Maxwell viscoelastic *liquid*,

$$E'_{\text{relax}}(t) = E'_g \exp\left(-\frac{t}{\tau} \right) \tag{8.37}$$

and the Zener viscoelastic *solid*.

$$E'(t) = E'_{\text{e}} + \left(E'_{\text{g}} - E'_{\text{e}} \right) \exp\left(-\frac{t}{\tau} \right) \tag{8.38}$$

are applied to Eq. (8.36) for examining the effect of surface adhesion on the load relaxation behavior of $P(t)$ vs t; the results are demonstrated in Fig. 8.10 for the Maxwell liquids ($E'_{\text{g}} = 20$ kPa, $\tau = 50$ s) and in Fig. 8.11 for the Zener solid ($E'_{\text{g}} = 20$ kPa, $E'_{\text{e}} = 5$ kPa, $\tau = 50$ s) with and without surface adhesion for Vickers/Berkovich-equivalent cone indentation ($\beta = 19.7^\circ$, $A_0 = 2\times10^{-7}$ mm^2). It will be worthwhile noticing in Figs. 8.10 and 8.11 that the surface adhesion yields the negative indentation load, i.e., $P < 0$, due to the adhesive force at the contact interface, and the time to the complete load relaxation or to the steady-state , i.e., the time to $P \to 0$ or $dP/dt \to 0$, is shifted to longer side with the increase in the surface adhesion γ.

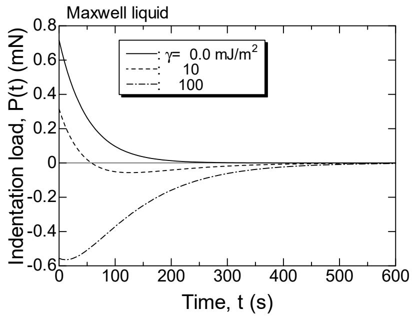

Figure 8.10 Effect of surface adhesion on the indentation load relaxation curve of the Maxwell viscoelastic liquid
(stepwise application of the contact area to $A_0 = 2\times10^{-7}$ m^2)

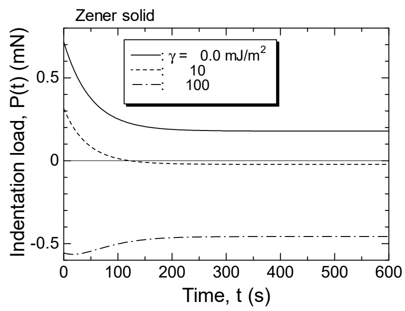

Figure 8.11 Effect of surface adhesion on the indentation load relaxation curve of the Zener viscoelastic solid
(stepwise application of the contact area to $A_0 = 2\times10^{-7}$ m^2)

(2) Creep deformation (spherical indentation)

The P vs a relation of perfectly elastic bodies for spherical indentation (JKR-theory; see Eq. (8.24))

$$P = \frac{4E'}{3R} a^3 - 4\sqrt{\pi\gamma E'} a^{3/2} \tag{8.42}$$

can be recast into the following quadratic equation in terms of the variable $x\left(\equiv a^{3/2}\right)$;

$$\frac{4E'}{3R} x^2 - 4\sqrt{\pi\gamma E'} x - P = 0 , \tag{8.43}$$

and then be solved as

$$\frac{4a^3}{3R} = C'P\left\{1 + 2\left(k + \sqrt{k + k^2}\right)\right\} \tag{8.44}$$

in which

$$\begin{aligned} C' &= 1/E' \\ k &= \Gamma/P \\ \Gamma &= 3\pi R \cdot \gamma \end{aligned} \tag{8.45}$$

* E' : elastic modulus, C' : compliance

Γ : adhesion force

γ : surface adhesion (adhesive energy)

R : radius of spherical indenter

The application of "elastic-viscoelastic correspondence principle" to Eq. (8.44) under stepwise indentation load $P(t) = P_0 u(t)$ ($u(t)$: Heaviside step-function) along with the Laplace transform and its inversion finally results in the following constitutive equation for creep deformation and flow;

$$\alpha_0(t)\left(\equiv \frac{4a_0(t)^3}{3RP_0}\right) = C'(t)\left\{1 + 2\left(k_0 + \sqrt{k_0 + k_0{}^2}\right)\right\} \tag{8.46}$$

where $C'(t)$ stands for the creep function and the subscript "0" indicates the stepwise indentation loading to P_0. Substituting $k_0 = 0$, i.e., $\gamma = 0$, in Eq. (8.46) yields

$$a_0(t)^3 = \frac{3R}{4} C'(t) \cdot P_0 \tag{8.47}$$

that describes the creep deformation and flow of *linear* viscoelastic bodies without surface adhesion; there exists a *linear* relation of $a^3(t) \propto P$ under stepwise spherical indentation. As readily seen in Eq. (8.46), however, the surface adhesion violates this linear relationship even if the indented body is *linear* viscoelastic. It must be also noticed that Eq. (8.46) can be rewritten with

$$a^3(t) = 3RC'(t) \cdot \Gamma \tag{8.48}$$

when the adhesion force Γ is large enough and/or the applied load P is small enough, i.e., $k \gg 1$. In other words, due to the surface adhesion that pulls the tip-of-indenter toward the material's surface, the finite creep deformation/flow will be observed even under the dead load of $P \equiv 0$.

In order for further examining the effect of surface adhesion, let make numerical considerations on the creep deformation and flow of the following Zener viscoelastic solid;

$$C'(t) = C'_{\mathrm{e}} + \left(C'_{\mathrm{g}} - C'_{\mathrm{e}}\right)\exp\left(-\frac{t}{\tau}\right) \tag{8.49}$$

with $C'_{\mathrm{g}} = 0.01$ mPa^{-1}, $C'_{\mathrm{e}} = 0.035$ mPa^{-1}, and $\tau = 200$ s. The numerical results of the creep curve $a^3(t)$ vs. t are shown in Figs. 8.12 and 8.13, leading to the following important conclusions as to the effect of surface adhesion on the creep deformation/flow;

(1) $a^3(t)$ -creep curve is not linearly proportional to the applied indentation load P

(2) creep deformation is enhanced with the increase in the surface adhesion

(3) significant creep is observed even under the dead-load of $P \equiv 0$

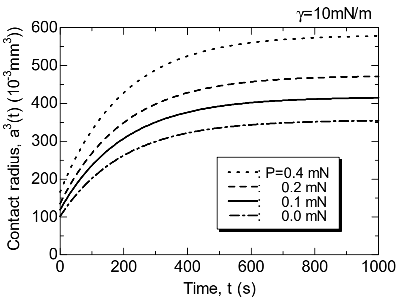

Figure 8.12 Creep curves of the viscoelastic Zener solid with surface adhesion ($\gamma = 10$ mN/m) under stepwise loading of spherical indentation (R =3.0mm). The curves are P =0.4, 0.2, 0.1, and 0.0mN from the top to the bottom. It must be noticed that creep deformation is induced even under the dead-load of $P \equiv 0$ (the dashed-dotted line)

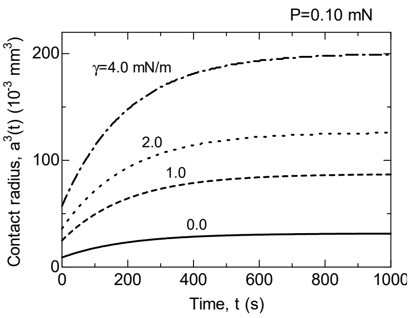

Figure 8.13 Creep curves of the viscoelastic Zener solid with surface adhesion under stepwise loading of spherical indentation (R =3.0mm; P =0.1mN). The curves are γ =4.0, 2.0, 1.0, and 0.0mN/m from the top to the bottom

INDENTATION CONTACT MECHANICS OF COATING/SUBSTRATE COMPOSITE

CHAPTER 9

Japanese craftworks "SHIKKI" (Japanese lacquered crafts), potteries (glazed ceramics), plated metals, etc. are all the typical examples of coated materials/arts that have long been making our daily lives enriching and comfortable. Painted walls and adhesive tapes, by way of example, are also classified as coating/substrate composites; the paint (coating) not only protects the walls (substrate) from hostile environments, but also make the wall more tactile; the adhesive coating makes the substrate more functional. The thickness of these coating films is in the range from nanometer to sub-millimeter. This fact makes the experimental determination of *film-only* mechanical characteristics critically difficult, thus remaining much works/problems/ issues for use to overcome.

On the other hand, as readily expected from the considerations we made in the preceding chapters, the science of indentation contact mechanics combined with the instrumented indentation apparatuses will provide a powerful tool for experimentally determining the mechanical characteristics of coating/substrate composites in their micro/ nano-regions. The theoretical formulation of the indentation contact mechanics of coating/substrate composites will be given in this chapter, though its present status is still immature **[9.1-9.5]**. The details of experimental techniques/analyses for determining mechanical properties of coating/substrate composite will be given in Chap. 11.

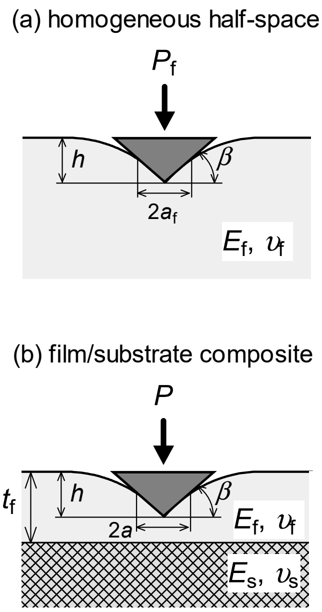

Figure 9.1 Geometrical details of a conical indenter pressed onto
(a) homogeneous half-space
(i.e., film-only half-space), and
(b) film/substrate composite

9.1 ELASTIC COMPOSITES

The mathematical formulation of indentation contact mechanics is fully established for the laminate of an *elastic* film coated on an *elastic* substrate. Figure 9.1 depicts the geometrical details of a conical indenter pressed onto (a) an elastic half-space (*file-only* half-space), and (b) a film having the thickness t_f coated on an elastic substrate extending to a half-space. The elastic moduli and the Poisson's ratios of the film and the substrate are denoted by (E_f, ν_f) and (E_s, ν_s), respectively. *At a given penetration depth* h, the induced indentation loads and the associated contact radii are described by (P_f, a_f) and (P, a) for the film-only half-space and for the laminate composite,

[9.1] C.H. Hsueh, P. Miranda, *J. Mater. Res.*, **19[1]**, 94 (2004)
[9.2] C.H. Hsueh, P. Miranda, *J. Mater. Res.*, **19[9]**, 2774 (2004)
[9.3] H.Y. Yu, S.C. Sanday, B.B. Rath, *J. Mech. Phys. Solids,* **38[6]**, 745 (1990)
[9.4] F. Yang, *Mater. Sci. Eng.*, **A358**, 226 (2003)
[9.5] M. Sakai, *J. Mater. Res.*, **24[3]**, 831 (2009)

respectively. When the thickness of the film is much larger than the penetration depth, i.e., $t_f >> h$, we can neglect the substrate effect on the contact behavior, leading to the perfectly elastic indentation contact mechanics of a homogeneous half-space of the film, the details of which are already given in Eqs. (3.33) and (3.34) (see Chapter 3, Tab. 3.1);

$$P_{\mathrm{f}} = k_h E_{\mathrm{f}}' h^n \tag{9.1}$$

$$\begin{aligned} a_{\mathrm{f}} (\equiv a_{\mathrm{H}}) &= B h^{n-1} \\ &= c P^{(n-1)/n} \end{aligned} \tag{9.2}$$

Due to the fact that the frontal factor B in Eq. (9.2) of a perfectly elastic half-space is *independent of the elastic modulus* (see Tab. 3.1), it must be noticed that the indentation contact radius a_{f} of the elastic film can be described in terms of the contact radius a_{H} of a *homogeneous elastic body having arbitrary elastic modulus* (the subscript H stands for "homogeneous").

On the other hand, in the cases of $t_{\mathrm{f}} \approx h$ and $t_{\mathrm{f}} < h$, as shown in Fig. 9.2, the indentation contact behavior is significantly affected by the substrate. Figure 9.2 demonstrates the substrate-effect on the indentation contact behavior for the coating/substrate composite with $E_{\mathrm{f}} << E_{\mathrm{s}}$, as an example. We must keep in mind the fact that there is a significant discrepancy in their contact behaviors of coating/substrate composite under *a fixed depth* h *of penetration* and under *a fixed load* P *of indentation*. As a matter of fact, as shown in Fig. 9.2, the substrate has an affect in an entirely different manner on the indentation contact behavior of $(P/P_{\mathrm{f}})_h$ and $(a/a_{\mathrm{f}})_h \left[\equiv (a/a_{\mathrm{H}})_h\right]$ observed under a *fixed depth* h of penetration, or of $(h/h_{\mathrm{f}})_P$ and $(a/a_{\mathrm{f}})_P \left[\equiv (a/a_{\mathrm{H}})_P\right]$ under a *fixed load* P of indentation. It should be noticed, in particular, $(a/a_{\mathrm{H}})_h \neq (a/a_{\mathrm{H}})_P$; this inequality will play an essential role in understanding the *effective elastic modulus of laminate composites* that we discuss in the following considerations.

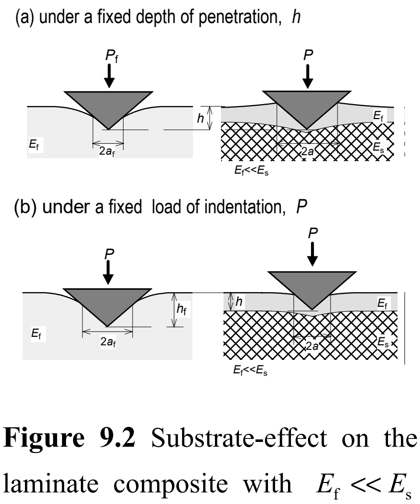

Figure 9.2 Substrate-effect on the laminate composite with $E_{\mathrm{f}} << E_{\mathrm{s}}$ for the indentations (a) under a fixed indentation depth h, and (b) under a fixed indentation load P

In order to discuss the indentation contact behavior of elastic coating/substrate composites in a phenomenological manner, let us now introduce the concept of *effective elastic modulus* $E'_{\mathrm{eff}}(t_{\mathrm{f}}/a)$ to

Eq. (9.1) as follows;

$$P = k_h E'_{\mathrm{eff}}\left(t_{\mathrm{f}}/a\right) h^n \tag{9.3}$$

where the effective elastic modulus $E'_{\mathrm{eff}}\left(t_{\mathrm{f}}/a\right)$ satisfies the following extremes;

$$\lim_{t_{\mathrm{f}}/a\to\infty} E'_{\mathrm{eff}}\left(t_{\mathrm{f}}/a\right) = E'_{\mathrm{f}}$$

$$\lim_{t_{\mathrm{f}}/a\to 0} E'_{\mathrm{eff}}\left(t_{\mathrm{f}}/a\right) = E'_{\mathrm{s}}$$

Accordingly, through Eqs. (9.1) and (9.3), the normalized values of indentation load $\left(P/P_{\mathrm{f}}\right)_h$ and penetration depth $\left(h/h_{\mathrm{f}}\right)_P$ are, respectively, given by

$$\left(P/P_{\mathrm{f}}\right)_h = E'_{\mathrm{eff}}/E'_{\mathrm{f}} \tag{9.4}$$

$$\left(h/h_{\mathrm{f}}\right)_P = 1\Big/\left(E'_{\mathrm{eff}}/E_{\mathrm{f}}\right)^{1/n} \tag{9.5}$$

In our next step of mathematical formulations through the Boussinesq Green function, we will make an analytical derivation of the effective modulus $E'_{\mathrm{eff}}\left(t_{\mathrm{f}}/a\right)$ that has been phenomenologically defined in Eq. (9.3). The contact problem of a concentrated point load P applied on an elastic half-space having the elastic modulus E and the Poisson's ratio ν was first solved by J. Boussinesq in 1885 **[1.1, 9.6]**. The problem is reduced to the elastic contact of a flat-ended cylindrical punch with radius a_0 (see Sec. 3.1) in its extreme of $a_0 \to 0$, leading to the following result of the displacement gradient $\partial u_z/\partial z$;

$$\frac{\partial u_z}{\partial z} = \frac{P(1+\nu)}{2\pi E}\left[\frac{3r^2 z}{\left(r^2+z^2\right)^{5/2}} - (3-2\nu)\frac{z}{\left(r^2+z^2\right)^{3/2}}\right] \tag{9.6}$$

Integrating both sides of Eq. (9.6) along the z-axis of the elastic composite shown in Fig. 9.3, we finally have the contact surface-displacement $u_z(r, z=0)$ induced by the concentrated force P **[9.1, 9.2]**;

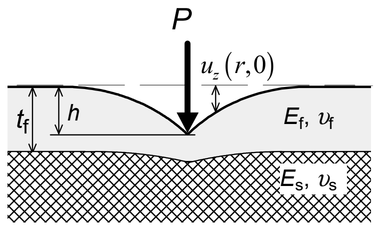

Figure 9.3 The Boussinesq problem of an elastic coating/substrate composite under a concentrated load P

[9.6] J. Boussinesq, "Application des potentials á l'etude de l'équilibre et du mouvement des solides élastiques", Gauthier-Villars (1885)

$$u_z(r,z=0)\left(\equiv G\left(r,z;E_i,\nu_i\right)\right)=\int_{\infty}^{t_\mathrm{f}}\left.\frac{\partial u_z}{\partial z}\right|_\mathrm{s}dz+\int_{t_\mathrm{f}}^{0}\left.\frac{\partial u_z}{\partial z}\right|_\mathrm{f}dz$$

$$=\frac{P\left(1-\nu_\mathrm{f}^2\right)}{\pi E_\mathrm{f}}\frac{1}{r}+\frac{P}{2\pi}\left\{\begin{aligned}&\frac{1+\nu_\mathrm{s}}{E_\mathrm{s}}\left[\frac{(3-2\nu_\mathrm{s})}{\left(r^2+t_\mathrm{f}^2\right)^{1/2}}-\frac{r^2}{\left(r^2+t_\mathrm{f}^2\right)^{3/2}}\right]\\&-\frac{1+\nu_\mathrm{f}}{E_\mathrm{f}}\left[\frac{(3-2\nu_\mathrm{f})}{\left(r^2+t_\mathrm{f}^2\right)^{1/2}}-\frac{r^2}{\left(r^2+t_\mathrm{f}^2\right)^{3/2}}\right]\end{aligned}\right\}\tag{9.7}$$

Equation (9.7) is the so-called Boussinesq Green function $G\left(r,z;E_i,\nu_i\right)$ of the coating/substrate composite, providing a basic equation in order to make the mathematical formulation of spherical/conical indentation contact mechanics, the details of which will be given in the following considerations.

Combining Eq. (9.7) with the indentation contact pressure distribution $p(r)\left(\equiv -\sigma_z(r,0)\right)$ ($r\le a$; contact radius a) (refer to Chap. 3 (Fig. 3.5, Tab. 3.1)) for the conventional axisymmetric indenter's geometry, the penetration depth h of the elastic laminate can be described in terms of $p(r)$ as the integration of the contact displacement $u_z(r,z=0)\left(\equiv G\left(r,z;E_i,\nu_i\right)\right)$ along the z-axis;

$$h=\int_0^a p(r)G\left(r,z;E_i,\nu_i\right)2\pi r dr\tag{9.8}$$

Accordingly, substituting Eq. (9.7) into Eq. (9.8), and furthermore using Eq. (9.4), we finally have the effective elastic modulus $E'_\mathrm{eff}\left(t_\mathrm{f}/a\right)$ as a function of the normalized film thickness ξ $(=t_\mathrm{f}/a)$ along with the material characteristics (E'_f, ν_f) of the film and (E'_s, ν_s) of the substrate;

$$\frac{E'_\mathrm{eff}}{E'_\mathrm{f}}\left[\equiv\left(\frac{P}{P_\mathrm{f}}\right)_h\right]=\left[1+\frac{E'_\mathrm{f}}{2I_0}\left\{\begin{aligned}&\frac{1+\nu_\mathrm{s}}{E_\mathrm{s}}\left[(3-2\nu_\mathrm{s})I_1(\xi)-I_2(\xi)\right]\\&-\frac{1+\nu_\mathrm{f}}{E_\mathrm{f}}\left\{(3-2\nu_\mathrm{f})I_1(\xi)-I_2(\xi)\right\}\end{aligned}\right\}\right]^{-1}\tag{9.9}$$

where I_0, $I_1(\xi)$, and $I_2(\xi)$ are respectively defined by

$$I_0 = \int_0^1 p_{\mathrm{N}}(\rho)\,d\rho$$
$$I_1(\xi) = \int_0^1 p_{\mathrm{N}}(\rho)\frac{\rho}{\left(\rho^2+\xi^2\right)^{1/2}}\,d\rho \qquad (9.10)$$
$$I_2(\xi) = \int_0^1 p_{\mathrm{N}}(\rho)\frac{\rho^3}{\left(\rho^2+\xi^2\right)^{3/2}}\,d\rho$$

in terms of the normalized contact pressure distribution $p_{\mathrm{N}}(\rho)$:

$$p_{\mathrm{N}}(\rho) = p(r)/p_m\,;$$
$$p_m = P/\pi a^2\,; \quad \rho = r/a$$

In the extreme of thick film, i.e., $t_{\mathrm{f}} \gg a\left(\xi \uparrow \infty\right)$, since there exists the relation of $I_1(\xi) = 0 = I_2(\xi)$, Eq. (9.9) naturally leads to $E'_{\mathrm{eff}} = E'_{\mathrm{f}}$, and the coating film dictates the indentation contact behavior of the laminate composite. On the other hand, in the extreme of thin film, i.e., $t_{\mathrm{f}} \ll a\left(\xi \downarrow 0\right)$, we have the relation of $I_1(\xi) = I_2(\xi) = I_0$, resulting in $E'_{\mathrm{eff}} = E'_{\mathrm{s}}$; the substrate characteristics dominate the contact behavior of the composite. The analytical formulas of the functions of $p_{\mathrm{N}}(\rho)$, $I_1(\xi)$, and $I_2(\xi)$ of the axisymmetric conventional indenters (flat-ended cylindrical punch, sphere, and cone) are listed in Tabs. 9.1 and 9.2.

The analytical expression for the contact pressure distribution $p_{\mathrm{N}}(\rho)$ is very essential prior to conducting the integral in Eq. (9.10), though we have no information on $p_{\mathrm{N}}(\rho)$ of the substrate-affected laminate composite in an analytical manner. Accordingly, in Tab. 9.1, $I_1(\xi)$ and $I_2(\xi)$ are approximately calculated by the use of $p_{\mathrm{N}}(\rho)$ for the *homogeneous half-space* (see Chap. 3; Tab. 3.1) *neglecting the substrate-effect*. Due to the fact of $I_0 = I_1(0) = I_2(0)$, the integral I_0 is readily obtained from $I_1(\xi)$ or $I_2(\xi)$ with $\xi = 0$. On the other hand, for a *thin-film* ($t_{\mathrm{f}}/a \ll 1$) coated on a *rigid substrate* ($E'_{\mathrm{s}} \uparrow \infty$) as a specific case of laminate composites, since there exists the analytical expression of $p_{\mathrm{N}}(\rho)$ **[9.4]**, the analytical solutions of $I_1(\xi)$ and $I_2(\xi)$ is readily obtained, the results of which are also listed in Tab. 9.2. In Fig. 9.4, the contact pressure distributions $p_{\mathrm{N}}(\rho)$ of the *homogeneous half-space* (the solid lines) and of the *thin-film coated on a rigid substrate* (the broken lines) are respectively plotted for comparison.

The elastic contact mechanics based on the preceding Boussinesq Green function $G(r,z;E_i,\nu_i)$ has the merit of providing the analytical

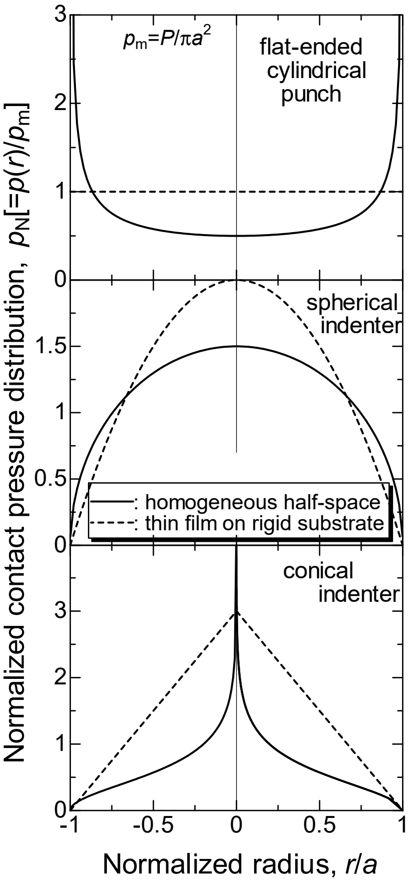

Figure 9.4 Contact pressure distributions $p_{\mathrm{N}}(\rho)$ of axi-symmetric indenters;
the solid line:
homogeneous half-space
the broken line:
a thin-film coated on a rigid substrate **[9.4]**

solution and its extension to the viscoelastic indentation contact mechanics via *the elastic-to-viscoelastic correspondence principle*. However, as mentioned above, there is a critical difficulty in obtaining the analytical solution for the contact pressure distribution $p_N(\rho)$ of substrate-affected laminate composite.

In contrast to the *analytical solution* based on the Boussinesq Green function given in the preceding considerations, on the other hand, we can get the *numerical solution* of the elastic contact mechanics of coating/substrate composites *in a quantitative manner* through the Fredholm integral equation; we first express the stresses/strains of the coating film and the substrate using the characteristic harmonic function (Papkovich-Neuber function) followed by the Hankel transform (refer to Chap. 3), and then we finally derive the following Fredholm integral equation of the second-kind **[9.3]**;

$$H(\rho)-\frac{1}{\pi}\int_0^1\left[K(y+\rho)+K(y-\rho)\right]H(y)dy=F(\rho) \qquad (9.11)$$

In Eq. (9.11), $H(\rho)$ stands for the non-dimensional function expressing the indentation contact pressure distribution. The kernel $K(y)$ of the integral includes the information of the material characteristics (E_f, ν_f), (E_s, ν_s), and the normalized film thickness $\xi(=t_f/a)$. The function $F(\rho)$ describes the geometry of the indenter;

$F(\rho)=1$; flat-ended cylinder

$F(\rho)=1-(\gamma\rho)^2$; sphere

$F(\rho)=1-\gamma\rho$; cone

in which γ stands for the relative contact radius $(a/a_H)_h$ at a given depth of penetration h as shown in Fig 9.2(a), i.e., $\gamma=(a/a_H)_h$ ($\equiv(a/a_f)_h$). The solution $H(\rho)$ of Eq. (9.11) is related to the normalized contact load $(P/P_f)_h$, as follows;

$$\left(\frac{P}{P_f}\right)_h\left(\equiv\frac{E'_{eff}}{E'_f}\right)=c\int_0^1 H(\rho)d\rho \qquad (9.12)$$

The frontal factor c in Eq. (9.12) is the indenter's tip-geometry dependent coefficient; $c=1$, 3/2, and 2 for the flat-ended cylindrical punch, spherical indenter, and the conical indenter, respectively. As readily seen in Eq. (9.11), the integral equation includes the unknown parameters of $\gamma = (a/a_{\mathrm{H}})_h$, $H(\rho)$, and $(P/P_{\mathrm{f}})_h$ of the film/ substrate composite that we are interested in.

In the first step of solving the integral equation (Eq. (9.11)), we transform the integral equation into the linear simultaneous algebraic equations by expressing the unknown function $H(\rho)$ in terms of the Chebyshev series expansion, and then we substitute $F(\rho)$ with $\gamma = 1$ as its initial value into this algebraic equations, leading to the zeroth-order-solution $H(\rho)$. In the next step, we repeat the preceding numerical procedures by systematically changing the γ-value until we finally get the solution $H(\rho)$ having the boundary value of $H(1) = 0$ (meaning that the contact pressure diminishes outside the contact area ($\rho \geq 1$)). The normalized elastic modulus of the laminate composite $E'_{\mathrm{eff}}/E'_{\mathrm{f}} \left[\equiv (P/P_{\mathrm{f}})_h \right]$ thus obtained by substituting the solution $H(\rho)$ into Eq. (9.12) is plotted in Fig. 9.5 against the normalized thickness t_{f}/a of the coating film for various values of the modulus-ratio $E'_{\mathrm{s}}/E'_{\mathrm{f}}$. We also plot in Fig. 9.5 the analytical solution (Eq. (9.9)) (the solid lines) derived from the Boussinesq Green function with the contact pressure distributions $p_{\mathrm{N}}(\rho)$ for the *homogeneous half-space* (see Tab. 9.1, Fig. 9.4), excepting the results of the composite $E'_{\mathrm{s}}/E'_{\mathrm{f}} = 100$ for which we utilize $p_{\mathrm{N}}(\rho)$ of the *thin-film coated on rigid substrate* (see Tab. 9.2, Fig. 9.4). As readily seen in Fig. 9.5, the analytical solution (Eq. (9.9); the solid lines) with the approximated $p_{\mathrm{N}}(\rho)$ rather faithfully realizes the precise numerical solution of the Fredholm integral equation (Eq. (9.11); the respective symbols with broken line). In particular for spherical indentation contact, the coincidence between both of the numerical and the analytical results is satisfactory. Figure 9.5 furthermore demonstrates that the effective elastic modulus E'_{eff} naturally converges to the modulus of the substrate E'_{s}, i.e., $E'_{\mathrm{eff}} \to E'_{\mathrm{s}}$, in the extreme of thin film or major penetration ($t_{\mathrm{f}}/a < 0.1$), while it converges to the modulus of the coating film E'_{f}, i.e., $E'_{\mathrm{eff}} \to E'_{\mathrm{f}}$, in the extreme of thick film or minor penetration ($t_{\mathrm{f}}/a > 50$). As has been given in Eq. (9.5), noticing the relation of $(h/h_{\mathrm{f}})_P = 1/(E'_{\mathrm{eff}}/E'_{\mathrm{f}})^{1/n}$, we can readily describe the normalized penetration depth $(h/h_{\mathrm{f}})_P$ under a fixed

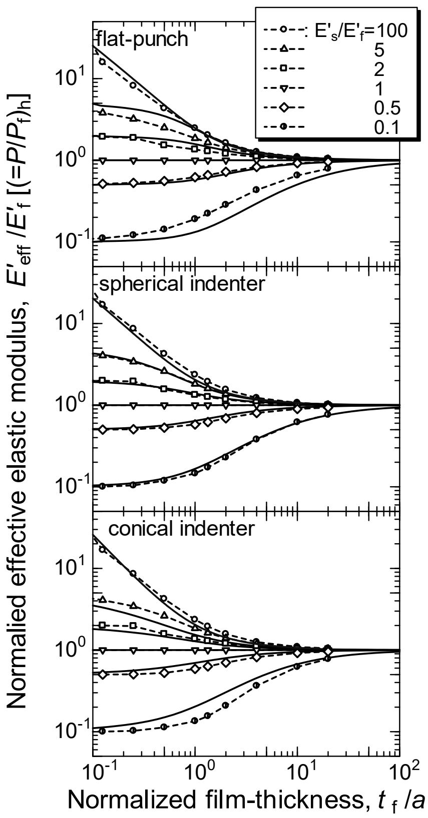

Figure 9.5 Normalized effective elastic modulus of coating/substrate composites plotted against the normalized film thickness. The symbols with broken line are the numerical results of the Fredholm integral equation (Eq. (9.11)), and the solid lines are the analytical results of the Boussinesq Green function (Eq. (9.9))

indentation load P in terms of the modulus ratio $E'_{\text{eff}}/E'_{\text{f}}$ via its numerical or analytical solution given in Eqs. (9.9) and (9.12), and in Fig. 9.5.

As mentioned in Chap. 3 for the elastic indentation contact mechanics of a homogeneous body, its free surface outside the indentation contact zone always exhibits *sinking-in* along with the penetration of the indenter, resulting in the relation of $h_c/h < 1$ (see Tab. 3.1) irrespective of the tip-geometry of the indenter we used. On the other hand, for coating/substrate composites, their surface profiles are significantly affected by the modulus ration E'_s/E'_f. Figure 9.6 shows the details of the contact profiles (sink-in/pile-up) of laminate composites having various values of E'_s/E'_f, in which the normalized contact radius $\gamma\left[\equiv (a/a_H)_h\right]$ is numerically determined through the iteration procedure in solving Eq. (9.11) as mentioned in the preceding considerations **[9.3]**.

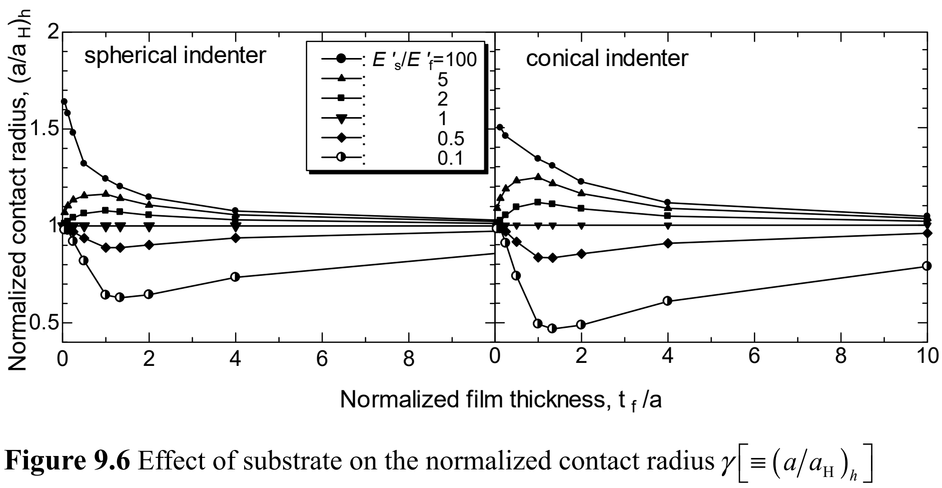

Figure 9.6 Effect of substrate on the normalized contact radius $\gamma\left[\equiv (a/a_H)_h\right]$ (numerical solutions of the Fredholm integral equation)

As shown in Fig. 9.6, the relation of $\left(a/a_{\mathrm{H}}\right)_h$ vs. t_{f}/a for the composites with $E'_{\mathrm{s}}/E'_{\mathrm{f}} > 1$ is convex upward, while it is concave downward for $E'_{\mathrm{s}}/E'_{\mathrm{f}} < 1$ at around $t_{\mathrm{f}}/a \approx 1$; in the former, the major of penetration-induced deformation at the fixed depth of penetration h is accommodated in the coating film due to the stiffer substrate, resulting in *suppressing the sink-in* or in *inducing the pile-up* of the free-surface outside the contact zone, while in the latter, due to the more compliant substrate, the major of penetration-induced deformation at the fixed depth of penetration h is accommodated in the substrate, resulting in *the enhanced sink-in* of the free-surface. In the conical indentation as an example, noticing the fact that the relative contact depth h_{c}/h of a homogeneous elastic half-space is given by $2/\pi$ (see Tab. 3.1), the preceding considerations lead to the following expression for the coating/substrate composite;

$$\frac{h_{\mathrm{c}}}{h} = \frac{2}{\pi}\left(\frac{a}{a_{\mathrm{H}}}\right)_h$$

Accordingly, using the results shown in Fig. 9.6 for the composite with $E'_{\mathrm{s}}/E'_{\mathrm{f}} = 5$, by way of example, the relative contact depth h_{c}/h at the penetration of $t_{\mathrm{f}}/a \approx 1$ is given by $h_{\mathrm{c}}/h \approx (2/\pi)\times 1.28 \approx 1.0$, implying none of sink-in nor pile up. Furthermore, for the composite having a nearly rigid substrate ($E'_{\mathrm{s}}/E'_{\mathrm{f}} = 100$ in Fig. 9.6), the relative contact depth becomes larger than 1.0, i.e., $h_{\mathrm{c}}/h > 1$, leading to *an enhanced pile-up* of the free-surface, like as the ductile plastic body that we have discussed in Chap.5 (see Figs. 5.6 and 5.7), although the composite is *perfectly elastic*. On the other hand for the laminate composite with very compliant substrate such as $E'_{\mathrm{s}}/E'_{\mathrm{f}} = 0.1$, the normalized contact radius at $t_{\mathrm{f}}/a \approx 1$ is $\left(a/a_{\mathrm{H}}\right)_h \approx 0.5$ (see Fig. 9.6), and then $h_{\mathrm{c}}/h \approx (2/\pi)\times 0.5 \approx 0.3$, meaning an *enhanced sink-in* more than that of a homogeneous elastic body ($h_{\mathrm{c}}/h = 2/\pi(=0.637)$).

Table 9.1 The contact pressure distributions $p_{\mathrm{N}}(\rho)$ of the axisymmetric indenters pressed onto a *homogeneous elastic half-space*, based on which the integrals $I_1(\xi)$ and $I_2(\xi)$ are determined (see Eq. (9.10))

	$p_N(r;a)$	$I_1(\xi)$	$I_2(\xi)$
Flat-ended cylinder	$\dfrac{1}{2\sqrt{1-(r/a)^2}}$	$\dfrac{1}{2}\left[\dfrac{\pi}{2}-\sin^{-1}\left(\dfrac{\xi}{\sqrt{1+\xi^2}}\right)\right]$	$\dfrac{1}{2}\left[\dfrac{\pi}{2}-\sin^{-1}\left(\dfrac{\xi}{\sqrt{1+\xi^2}}\right)-\dfrac{\xi}{1+\xi^2}\right]$
Sphere	$\dfrac{3}{2}\sqrt{1-(r/a)^2}$	$\dfrac{3}{2}\left[(1+\xi^2)\left\{\dfrac{\pi}{2}-\sin^{-1}\left(\dfrac{\xi}{\sqrt{1+\xi^2}}\right)\right\}-\xi\right]$	$\dfrac{3}{2}\left[(1+3\xi^2)\left\{\dfrac{\pi}{2}-\sin^{-1}\left(\dfrac{\xi}{\sqrt{1+\xi^2}}\right)\right\}-3\xi\right]$
Cone	$\cosh^{-1}(a/r)$	$\dfrac{\pi}{2}-\tan^{-1}\xi+\dfrac{\xi}{2}\ln\dfrac{\xi^2}{1+\xi^2}$	$\dfrac{\pi}{2}-\tan^{-1}\xi+\xi\ln\dfrac{\xi^2}{1+\xi^2}$

Table 9.2 The contact pressure distributions $p_{\mathrm{N}}(\rho)$ of the axisymmetric indenters pressed onto a *thin elastic film* ($t_f/a \ll 1$) *coated on a rigid substrate*, based on which the integrals $I_1(\xi)$ and $I_2(\xi)$ are determined (see Eq. (9.10))

	$p_N(r;a)$	$I_1(\xi)$	$I_2(\xi)$
Flat-ended cylinder	1	$\sqrt{1+\xi^2}-\xi$	$2(\sqrt{1+\xi^2}-\xi)-\dfrac{1}{\sqrt{1+\xi^2}}$
Sphere	$2\left[1-(r/a)^2\right]$	$2[(2/3)(1+\xi^2)\sqrt{1+\xi^2}$ $-\xi-(2/3)\xi^3]$	$4[(1/3)(1+4\xi^2)\sqrt{1+\xi^2}$ $-\xi-(4/3)\xi^3]$
Cone	$3[1-(r/a)]$	$3[(1/2)\sqrt{1+\xi^2}-\xi$ $-(1/2)\xi^2\ln\left\{\xi/(1+\sqrt{1+\xi^2})\right\}]$	$3[(1/2)\sqrt{1+\xi^2}-2\xi$ $-(3/2)\xi^2\ln\left\{\xi/(1+\sqrt{1+\xi^2})\right\}]$

9.2 VISCOELASTIC COMPOSITES

Based on the "elastic-to-viscoelastic correspondence principle" (refer to Chap. 7), i.e., the linear viscoelastic constitutive equations in the Laplace-space coincide with those of perfectly elastic body in the real-space, combined with the preceding considerations on the elastic laminate composites, we can rather easily extend the indentation contact mechanics of *elastic* laminate composites to that of *viscoelastic* composites **[9.7]**.

The indentation load relaxation of a viscoelastic laminate composite under a stepwise penetration to the contact area A_0, i.e., $A(t) = A_0 \cdot u(t)$, is given by

$$P(t) = \frac{\tan\beta}{2} A_0 \cdot E'(t) \tag{9.13}$$

like as Eq. (7.6). In Eq. (9.13), we denote the relaxation modulus $E'_{\mathrm{relax}}(t)$ by $E'(t)$ for simplicity. Once we apply the "elastic-to-viscoelastic correspondence principle" to Eq. (9.9), the relaxation modulus $E'(t)\left(\equiv E'_{\mathrm{eff}}(t)\right)$ of the viscoelastic laminate composite is described by

$$\frac{E'(t)}{E'_{\mathrm{f}}(t)}\left[\equiv\left(\frac{P(t)}{P_{\mathrm{f}}(t)}\right)_A\right] = \left[1 + \frac{E'_{\mathrm{f}}(t)}{2I_0}\left\{\begin{matrix} \dfrac{1+\nu_{\mathrm{s}}}{E_{\mathrm{s}}(t)}\left[\left(3-2\nu_{\mathrm{s}}\right)I_1(\xi) - I_2(\xi)\right] \\ -\dfrac{1+\nu_{\mathrm{f}}}{E_{\mathrm{f}}(t)}\left\{\left(3-2\nu_{\mathrm{f}}\right)I_1(\xi) - I_2(\xi)\right\} \end{matrix}\right\}\right]^{-1} \tag{9.14}$$

where $E'_{\mathrm{f}}(t)\left[\equiv E_{\mathrm{f}}(t)/\left(1-\nu_{\mathrm{f}}^2\right)\right]$ and $E'_{\mathrm{s}}(t)\left[\equiv E_{\mathrm{s}}(t)/\left(1-\nu_{\mathrm{s}}^2\right)\right]$ are the relaxation moduli of the coating film and of the substrate, respectively. Due to the assumption of stepwise penetration $A(t) = A_0 \cdot u(t)$, the normalized film thickness $\xi\left(\equiv t_{\mathrm{f}}/a_0\right)$ ($a_0 = \sqrt{A_0/\pi}$) is a time-independent constant. As emphasized in Sec. 6.4, the Poisson's ratio ν of viscoelastic body is time-dependent; by way of example for a *viscoelastic liquid* such as the Zener II model with $E_{\mathrm{e}} = 0$ in Eq. (6.8b), the Poisson's ratio $\nu(0)\left(\approx 0.1\right)$ at the onset of stress relaxation monotonically increases with time to the value of $\nu\left(\infty\right)\uparrow 0.5$ in its steady-state, while its time-dependence is very minor for a *viscoelastic solid* ($E_{\mathrm{e}} \neq 0$) (see Fig 6.10). In this chapter, therefore for simplicity, we assume that the Poisson's ratios of coating/substrate composites are

[9.7] M. Sakai, *Phil. Mag.*, **86[33-35]**, 5607 (2006) time-independent having the values of $\nu_{\mathrm{f}} = \nu_{\mathrm{s}} = 0.3$ in Eq. (9.14). This assumption by no means results in any critical issues in discussing the viscoelastic contact mechanics of laminate composites.

Let us suppose the Zener II model (refer to Chap. 6, Fig. 6.2, and Eq. (6.8b)) with a single relaxation time of $\tau = \eta / E'_{\mathrm{M}}$,

$$E'(t) = E'_{\mathrm{e}} + \left(E'_{\mathrm{g}} - E'_{\mathrm{e}}\right)\exp\left(\frac{-t}{\tau}\right) \qquad (9.15)$$
$$E'_{\mathrm{g}} = E'_{\mathrm{e}} + E'_{\mathrm{M}}$$

in order to describe the relaxation moduli of $E_{\mathrm{f}}(t)$ and $E_{\mathrm{s}}(t)$ in Eq. (9.14). The Zener II model with $E_{\mathrm{e}} = 0$ is readily reduced to the Maxwell model. We will discuss in what follows the viscoelastic contact mechanics of laminate composites subjected to a stepwise penetration to the contact area A_0 of a cone indentation, i.e., $A(t) = A_0 \cdot u(t)$, or to the contact radius $a(t) = a_0 \cdot u(t)$ with $a_0 = \sqrt{A_0/\pi}$.

(1) Stress relaxation behavior of an elastic film coated on a viscoelastic substrate

The indentation load relaxation $P(t)$ of a laminate for stepwise penetration of a cone indenter is well described in terms of the relaxation modulus $E'(t)$ through the relation given in Eq. (9.13). The relaxation modulus $E'(t)$ is shown in Fig. 9.7(a) for the laminate with $E'_{\mathrm{f}} = E'_{\mathrm{s}}(0) = 10$ GPa as an example, i.e., for the laminate composite with the elastic modulus E'_{f} of the coating film matching to the glassy modulus $E'_{\mathrm{s}}(0)$ of the viscoelastic substrate. On the other hand in Fig. 9.7(b), shown is the relaxation behavior of the laminate with the film modulus smaller than that of the glassy modulus and larger than the equilibrium modulus E'_{e} of the viscoelastic substrate, i.e., $E'_{\mathrm{s}}(0) > E'_{\mathrm{f}} > E'_{\mathrm{e}} \left(\equiv E_{\mathrm{s}}(\infty)\right)$ ($E'_{\mathrm{f}} = 5$ GPa; $E'_{\mathrm{s}}(0) = 10$ GPa、 $E'_{\mathrm{e}} = 1$ GPa). In Fig. 9.7, the relaxation moduli of the laminate composites are plotted for the various values of the normalized film thickness t_{f}/a in order to demonstrate how the film-thickness or the depth of penetration dictates the relaxation behavior.

(a)

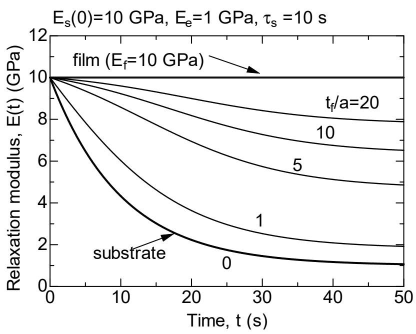

(b)

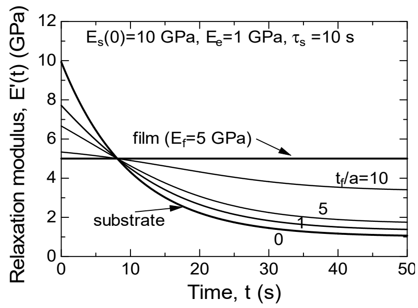

Figure 9.7 Relaxation moduli $E'(t)$ of the laminate composites with the viscoelastic substrate ($E'_{\mathrm{s}}(0) = 10$ GPa, $E'_{\mathrm{e}} = 1$ GPa, $\tau_{\mathrm{s}} = 10$ s) on which the elastic film ((a) $E'_{\mathrm{f}} = 10$ GPa; (b) $E'_{\mathrm{f}} = 5$ GPa) is coated

(2) Stress relaxation behavior of a viscoelastic film coated on an elastic substrate

The contact mechanics of the composite comprising a viscoelastic film coated on an elastic substrate is scrutinized for the stepwise penetration of conical indentation, in contrast to the composite with an elastic film coated on a viscoelastic substrate that we discussed above. We utilize the viscoelastic Zener II solid as the coating film;

$$E'_{\mathrm{f}}(t) = E'_{\mathrm{e}} + \left(E'_{\mathrm{g}} - E'_{\mathrm{e}}\right)\exp\left(\frac{-t}{\tau_{\mathrm{f}}}\right) ,$$

$$\tau_{\mathrm{f}} = 10\mathrm{s} \quad E'_{\mathrm{g}} = 10\mathrm{GPa} \quad E'_{\mathrm{e}} = 1\mathrm{GPa}$$

while we suppose the perfectly elastic substrates having various values of the elastic modulus E'_{s} in order to examine the effect of substrate modulus on the viscoelastic behavior of laminate composite.

Figure 9.8(a) demonstrates the effect of elastic modulus E'_{s} of the substrate on the relaxation behavior of the laminate composite for the conical indentation at a fixed depth of penetration, $t_{\mathrm{f}}/a = 1$. As readily seen in Fig. 9.8(a), the substrate-effect is predominant in the initial stage of stress relaxation. In order to further examine the substrate-effect, the relaxation modulus normalized by its initial value, i.e., $E'(t)/E'(0)$ is plotted against time in Fig. 9.8(b); the stress relaxation of the composites becomes progressively more sluggish along with the elastic substrate that becomes progressively more compliant, namely the elastic modulus of the substrate becomes progressively smaller. In other word, the relaxation time τ of the laminate composite shifts to the longer side by decreasing the elastic modulus of the substrate. It must be noticed that when the elastic modulus of the *elastic substrate* is larger than the initial modulus of the *viscoelastic film*, i.e., $E_{\mathrm{s}} > E_{\mathrm{f}}(0)$ (=10 GPa), the relaxation time of the *composite* shifts to the smaller side, and vice versa. In Fig. 9.8, we demonstrate the substrate-effect at the fixed stepwise penetration of $t_{\mathrm{f}}/a = 1$, although the substrate effect must be more enhanced with the decrease in t_{f}/a -value, or the increase in a/t_{f}. To confirm this substrate-effect in a quantitative manner, the relaxation time of the laminate composite is plotted against the normalized contact radius a/t_{f} in Fig. 9.9 for various values of the elastic modulus E'_{s} of the substrate. In Fig. 9.9, the relaxation time τ of the composite is defined as the time at which the normalized modulus $\left[E'(t) - E'(\infty)\right]/\left[E'(0) - E'(\infty)\right]$

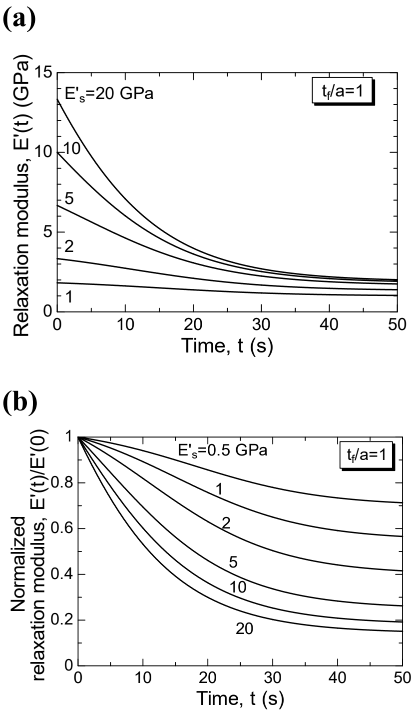

Figure 9.8 Effect of the elastic modulus E'_{s} of the substrate on the relaxation modulus $E'(t)$ of the laminate composites. All the relations are for the stepwise penetration ($t_{\mathrm{f}}/a = 1$) of conical indentation;

(a) viscoelastic film coated on elastic substrate, and

(b) the normalized moduli of the composites shown in (a).

relaxes to the value of $1/e$. In the region of smaller penetration $a/t_f \ll 1$, due to no substrate-effect, the relaxation time τ of the composite naturally coincides with that of the viscoelastic coating film τ_f ($\tau = \tau_f = 10$ s) itself. However, along with increasing the penetration, i.e., along with increasing a/t_f, the relaxation time τ progressively increases due to the enhanced substrate-effect. Furthermore, this substrate-effect is more significant for the substrate having a smaller value of the elastic modulus, as clearly seen in Fig. 9.8. The above considerations on the substrate effect thus lead to an important conclusion that *we can control the viscoelastic behavior of the laminate composite by only adjusting the elastic modulus of the substrate without any modification of the viscoelastic coating film*.

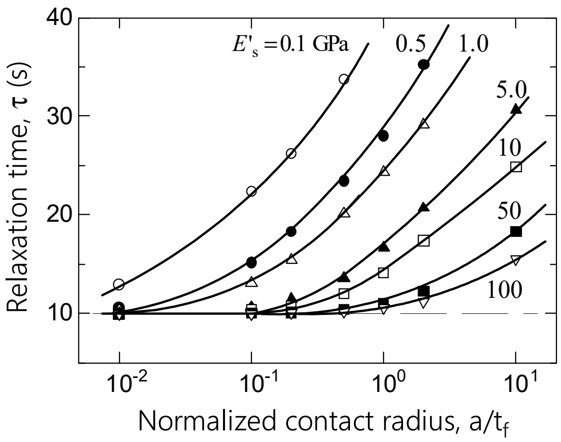

Figure 9.9 Effect of the elastic modulus E'_s of the substrate on the relaxation time of the laminate composite. The symbols in the figure indicate the elastic modulus E'_s of the respective substrates;

○(0.1 GPa) ●(0.5 GPa)
△(1 GPa) ▲(5.0 GPa),
□(10 GPa) ■(50 GPa),
▽(100 GPa)

9.3 ELASTOPLASTIC COMPOSITES

The elastoplastic Meyer hardness H_M of a homogeneous body is uniquely described in terms of the elastic modulus E' and the yield stress Y, the details of which have been well mentioned in Chap. 5. On the other hand for film/substrate composites, its mechanical field induced by indentation contact continuously changes from the field controlled by the coating film having the elastoplastic characteristic (E'_f、Y_f) to that of the substrate (E'_s、Y_s) along with the progressive increase in the penetration depth. In other words, as depicted in Fig. 9.10, *we can quantitatively make modeling the laminate composite as a homogeneous elastoplastic half-space with spatially graded mechanical characteristics* $E'(t_f/a)$ *and* $Y(t_f/a)$ *along the axis of indentation penetration*. **[9.5]**

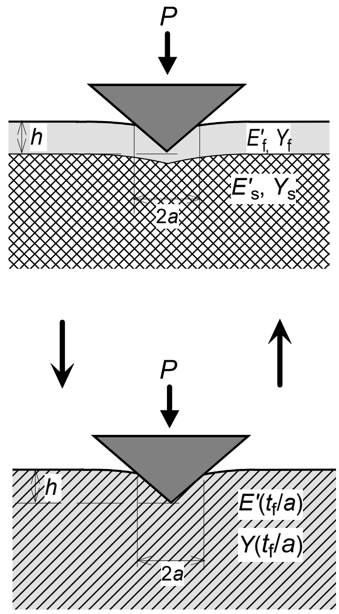

Figure 9.10 Mechanical equivalence between the elastoplastic laminate composite and the homogeneous elastoplastic body with spatially anisotropic mechanical characteristics of $E'(t_f/a)$ and $Y(t_f/a)$ (refer to Figs. 9.11 and 9.12)

We introduced in Chap. 5 *the additivity principle of the excluded volume of indentation* in order to quantitatively describe the Meyer hardness of a homogeneous elastoplastic body (see Eq. (5.14)). Accordingly, by simply replacing E' with $E'(t_f/a)$ and Y with $Y(t_f/a)$ in Eq. (5.14), we can readily extend this additivity principle to the elastoplastic homogeneous body having a spatially graded characteristics, resulting in the following analytical expression for the Meyer hardness $H_M(t_f/a)$:

$$\frac{H_M(t_f/a)}{cY(t_f/a)} = \left[\frac{\{\varepsilon_I E'(t_f/a)/cY(t_f/a)\}^m}{1+\{\varepsilon_I E'(t_f/a)/cY(t_f/a)\}^m}\right]^{1/m} \quad (9.16)$$

In the extreme of infinite yield stress, $Y(t_f/a)\uparrow\infty$, namely in the extreme of both of the coating film and the substrate exhibiting none of plastic yielding, the laminate composite is reduced to the perfectly elastic laminate that we discussed in Sec. 9.1, and then the Meyer hardness $H_M(t_f/a)$ in Eq. (9.16) is rewritten into the following simple formula (notice the similarity to the elastic Meyer hardness given in Eq. (3.32));

$$H_M(t_f/a) = \varepsilon_I E'(t_f/a) \quad (9.17)$$

where the details of indentation strain ε_I have already been given in Chaps. 3 and 5. *The indentation contact load* P of the present laminate model (i.e., a homogeneous body having spatially graded elastic modulus $E'(t_f/a)$), therefore, is readily related to *its contact area* A through the following relation;

$$P = \varepsilon_I E'(t_f/a)\cdot A \quad (9.18)$$

On the other hand, we defined *the effective elastic modulus* $E'_{\text{eff}}(t_{\text{f}}/a)$ *in Sec. 9.1 that relates the indentation load* P *to the penetration depth* h *as follows;*

$$P = k_h E'_{\text{eff}}(t_{\text{f}}/a)h^n \tag{9.3}$$

Since Eq. (9.18) in terms of the contact area A must be equivalent to Eq. (9.3) in terms of the penetration depth h, we finally relate $E'_{\text{eff}}(t_{\text{f}}/a)$ to $E'(t_{\text{f}}/a)$ through the following relation;

$$\begin{aligned} E'_{\text{eff}}(t_{\text{f}}/a) &= \left(\frac{A}{A_{\text{H}}}\right)_h E'(t_{\text{f}}/a) \\ &= \left(\frac{a}{a_{\text{H}}}\right)_h^2 E'(t_{\text{f}}/a) \end{aligned} \tag{9.19}$$

In Eq. (9.19), $(A_{\text{H}})_h$ and $(a_{\text{H}})_h$ are, respectively, the contact area and the contact radius of an axisymmetric indenter pressed onto a *homogeneous half-space* at a fixed depth of penetration h as defined in Sec. 9.1. Equation (9.19), therefore, means that the substrate-effect both on the contact area A (or on the contact radius a) and on the elastic modulus $E'(t_{\text{f}}/a)$ dictates the effective modulus $E'_{\text{eff}}(t_{\text{f}}/a)$ in a synergetic manner. The essential discrepancies of the substrate-effect on $E'_{\text{eff}}(t_{\text{f}}/a)$ and on $E'(t_{\text{f}}/a)$ are plotted in Fig 9.11 for conical indentation. As shown in Fig. 9.11(a), the substrate-effect on $E'_{\text{eff}}(t_{\text{f}}/a)$ becomes significant when the contact radius a exceeds $0.1t_{\text{f}}$, i.e., $a \geq 0.1t_{\text{f}}$ ($t_{\text{f}}/a \leq 10$), while it eventually becomes significant in the region of $a \geq 0.5t_{\text{f}}$ ($t_{\text{f}}/a \leq 2$) for $E'(t_{\text{f}}/a)$ as demonstrated in Fig. 9.11(b).

In contrast to the elastic extreme that we discussed above, suppose the plastic extreme with infinite elastic modulus $E'(t_{\text{f}}/a) \uparrow \infty$ in which both the coating film and the substrate are subjected to fully plastic yielding. For such a fully plastic laminate composite, the Meyer hardness $H_{\text{M}}(t_{\text{f}}/a)$ is given by substituting $E'(t_{\text{f}}/a) \uparrow \infty$ into Eq. (9.16), resulting in

$$H_{\text{M}}(t_{\text{f}}/a) = cY(t_{\text{f}}/a) \tag{9.20}$$

Equation (9.20) represents the Meyer hardness of *the fully plastic homogeneous model having spatially graded yield stress along the penetration axis*, corresponding to Eq. (5.7) for a fully plastic homogeneous body we discussed in Chap. 5. Unfortunately, however, we have so far no analytical theories for describing $Y(t_{\text{f}}/a)$ as a function of t_{f}/a, not like the case of $E'(t_{\text{f}}/a)$. To circumvent this

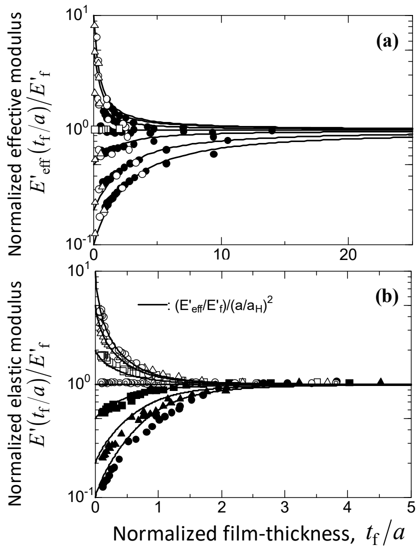

Figure 9.11 Substrate-effect on (a) $E'_{\text{eff}}(t_{\text{f}}/a)$ and on (b) $E'(t_{\text{f}}/a)$ for conical indentation. The symbols indicate the numerical results of the finite element analysis. The solid lines in (a) are the numerical solutions $E'_{\text{eff}}(t_{\text{f}}/a)$ of the Fredholm integral equation (Eq. (9.11); refer to Fig. 9.5). The solid lines in (b) are the numerical solution of $E'(t_{\text{f}}/a)$ in Eq. (9.19) combined with the $E'_{\text{eff}}(t_{\text{f}}/a)$-values given in (a). The solid lines and the symbols in (a) and (b) are the results for the modulus ratio $E'_{\text{s}}/E'_{\text{f}}$ of =10, 5, 2, 1, 0.5, 0.2, and 0.1 from the top to the bottom

difficulty, we can quantitatively/successfully describe the yield stress $Y(t_f/a)$ by mapping the FEA-derived Meyer hardness $H_M(t_f/a)$ as a function of t_f/a for laminate composites having various combinations of elastoplastic characteristics of the coating film and of the substrate; we first determine the Meyer hardness $H_M(t_f/a)$ by the use of FEA-based numerical results, and then substitute this $H_M(t_f/a)$-value along with the $E'(t_f/a)$-value into Eq. (9.16) to calculate $Y(t_f/a)$ as a function of t_f/a, some of the examples thus obtained are shown in Fig. 9.12.

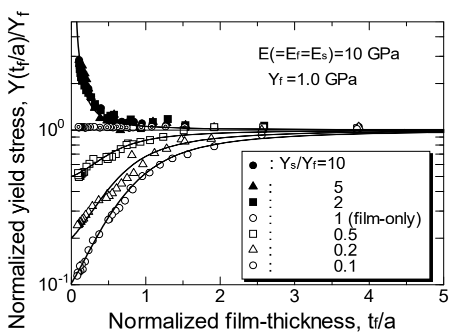

Figure 9.12 Normalized yield stress $Y(t_f/a)/Y_f$ of the homogeneous anisotropic elastoplastic bodies having various Y_s/Y_f-values (FEA-based numerical results)

Once we get the detailed information on $E'(t_f/a)$ (Fig. 9.11) and on $Y(t_f/a)$ (Fig. 9.12) as the functions of t_f/a *in a numerical manner* via FEA, we inversely predict *in an analytical manner* the Meyer hardness $H_M(t_f/a)$ of the elastoplastic laminate composite using Eq. (9.16). In Figs. 9.13-9.15, shown are the Meyer hardness $H_M(t_f/a)$ of various types of laminate composites (elastoplastic film coated on elastic substrate, elastoplastic film coated on ductile substrate, and ductile film on elastic substrate). In these figures, the symbols are the *FEA-based numerical results*, and the solid/broken lines are the *analytical predictions* via Eq. (9.16). As clearly seen in these figures, the analytical predictions of Eq. (9.16) faithfully realize the elastoplastic behaviors of laminate composites having wide varieties of their elastoplastic characteristics. This fact implies that we can quantitatively determine in experiments the elastic modulus (E_f, E_s) and the yield stress (Y_f, Y_s) from the FEM-based numerical analysis combined with the Meyer hardness $H_M(t_f/a)$ observed on *the instrumented indentation microscope*; the details of experimental procedures will be given in Sec. 11.3.

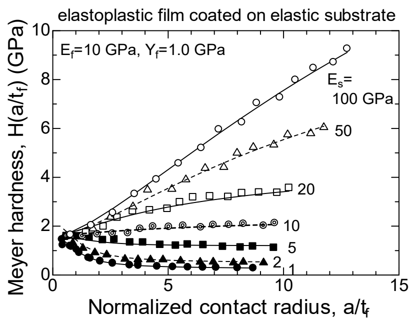

Figure 9.13 Meyer hardness of an elastoplastic film coated on elastic substrates ($2 \le E_s \le 100$ GPa). The symbols are the results of FEA, and the solid/broken lines are the analytical predictions (Eq. (9.16))

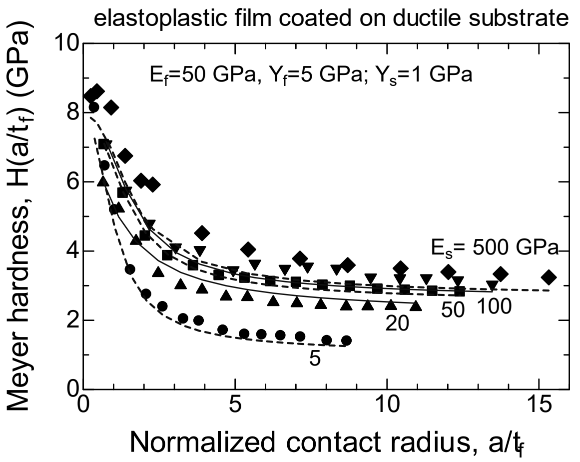

Figure 9.14 Meyer hardness of an elastoplastic film coated on ductile substrates. The symbols are the results of FEA, and the solid/broken lines are the analytical predictions (Eq. (9.16))

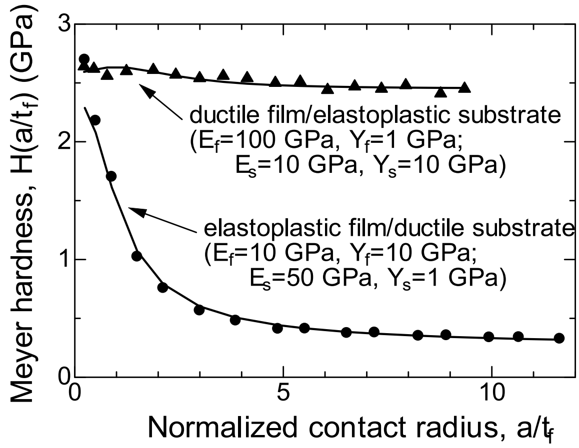

Figure 9.15 Meyer hardness of an elastoplastic film coated on a ductile substrate, and a ductile film on an elastoplastic substrate. The symbols are the results of FEA, and the solid lines are the analytical predictions (Eq. (9.16))

NUMERICAL INDENTATION CONTACT MECHANICS

CHAPTER 10

None of *analytical theories* have been established for the indentation contact mechanics except the elastic contact due to the extremely complicated mechanical processes induced beneath the tip of indenter, as repeatedly emphasized in the preceding chapters. When we overview the long history of the indentation contact mechanics since the end of the 18th century, we readily notice that we will not be able to overcome these difficulties within the present century. On the other hand, in order to *numerically* solve the problems of deformation and fracture of mechanically complicated structures, *the Finite Element Method (FEM)* has been proposed over the period 1950-1962 by the pioneers of The Boeing Co. Ltd and The University of Washington. The prominent development of electronics-based computer science and engineering since the mid-20th century along with the mathematical contributions of numerical analyses has enhanced and boosted the application of FEM to the *numerical* analyses for solving the problems of structural engineering. The FEM, therefore, has long been provided powerful tools to the specific engineering fields of the contact mechanics, nonlinear fracture mechanics, and the hydrodynamic science/engineering, etc., in which we cannot *analytically* solve their problems **[10.1]**. Currently available commercial FEM software packages include (1) NASTRAN developed in 1968 by NASA (United States **N**ational **A**eronautics and **S**pace **A**dministration), (2) ABAQUS that has been intensively applied to the field of numerical indentation contact mechanics since 1980s, and (3) ANSYS that has been designed and developed for the users of interactive personal computer (PC) through Graphical User Interface (GUI). In this chapter, based on the Finite Element Analysis (FEA), we will extensively discuss the reliability and the usefulness of the numerical indentation contact mechanics applied to the axisymmetric indentation contacts problems (spherical and conical indentation).

[10.1] O.C. Zienkiewicz and R.L. Taylor, and J.Z. Zhu, *The finite element method: its basis and fundamentals*, Seventh Ed., Elsevier, 2013; David V. Hutton, *Fundamentals of finite element analysis*, McGraw-Hill, 2004; J.N. Reddy, *An introduction to the finite element method*, third Ed., McGraw-Hill, 2006.

10.1 OUTLINE OF FINITE ELEMENT ANALYSIS IN INDENTATION CONTACT MECHANICS

In this section, we will focus on the FEM applied to the indentation contact mechanics (the mathematical theory, concept of finite elements, modeling the mechanical structures, boundary and initial conditions, etc. of FEM are published in the literatures **[10.1]**). Most of the commercially available FEM-packages equip an interactive user interface, through which we readily make modeling the geometry of the solid structures we are interested in, defining the element type and the material characteristics/boundary conditions, meshing to create the finite element model, solving the problems, and then plotting/viewing the solution.

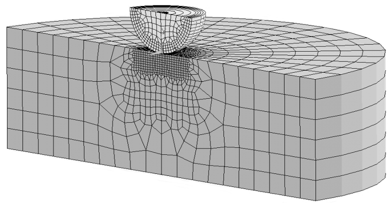

Figure 10.1 An example of the axisymmetric finite element model for a spherical indenter pressed onto a homogeneous half-space

An example of the axisymmetric finite element model is demonstrated in Fig. 10.1 of a spherical indentation on an infinite half-space. We need to make finer meshing beneath the contact area that is requisite for improving the reliability/accuracy of the numerical solution due to the very steep spatial gradient of stresses/strains. Figure 10.2 shows an example of FEA for the surface-profile (sink-in profile) and the distribution of indentation-induced in-surface displacements along the axis of penetration at $h = 3$ μm (Vickers/ Berkovich-equivalent cone) for a perfectly elastic body. As clearly seen in Fig. 10.2, one of the advantages of FEA is the visualization of in-surface mechanical information (stress-strain details) that is very essential for us to get the intuitive as well as deep insight into the *physics of indentation contact* (some FEA-based numerical results have already been given in Figs. 4.4, 5.3, 5.5, 5.7, 5.11, 8.4-8.9, and 9.11-9.15).

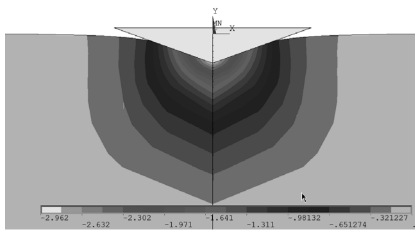

Figure 10.2 The surface-profile and the in-surface distribution of deformation at the penetration depth $h = 3$ μm for the Vickers/Berkovich equivalent cone pressed onto a perfectly elastic body

10.2 ELASTIC ANALYSIS

As well described in Chap. 3, there exist the analytical solutions in a closed form for the axisymmetric indentation contact onto a homogeneous elastic half-space. We will scrutinize in this section the reliability and the accuracy of the numerical FEA-results for the spherical/conical indentation contact by comparing them with the analytical solutions. Furthermore, we will make the FEA-based numerical approach to the Poisson's effect on the indentation contact behavior since the analytical theories have been implicitly based on an assumption of incompressible elastic body, i.e. $\nu = 0.5$.

As discussed in Chap. 3, the indentation contact load P is related to the induced penetration depth h through the following relation;

$$P = \frac{4}{3} E' \sqrt{R} h^{3/2} \tag{3.18}$$

for spherical indentation (the Hertzian theory), and

$$P = \frac{2 \cot \beta}{\pi} E' h^2 \tag{3.25}$$

for conical indentation (the Sneddon's theory). These analytical formulae implicitly assume the Poisson's ratio of $\nu = 0.5$, though the Poisson's ratio of most of engineering materials is $\nu \approx 0.3$, suggesting the difficulty in applying the above analytical formulae to the indentation contact behavior of engineering materials. Equations (3.18) and (3.25) are described in terms of the plane-strain elastic modulus E' ($= E/1-\nu^2$) that includes the Poisson's ratio, suggesting that the theoretical framework of the above equations seems to include the Poisson's effect. However, it must be noticed the fact that these theories make a priori assumption of incompressible elastic body. On the other hand, we can introduce any value of the Poisson's ratio ν to the FEA-based model material, leading to the resultant numerical solution that is applicable to any of engineering materials. The FEA-results with the Poisson's effect on the P - h loading relations (the plots with the symbols of ○ and ●) are shown in Figs. 10.3 and 10.4, where the solid lines and the broken lines indicate the analytical results with E' ($= E/1-\nu^2$) for $\nu = 0.5$ and $\nu = 0.3$. As clearly seen in these figures, the analytical solutions for $\nu = 0.5$ (the solid lines) well realize the FEA-numerical results, while the analytical solutions for $\nu = 0.3$ (the broken lines) always underestimate the FEA-numerical results due to the a priori assumption of the incompressible elastic body included in the Hertz/Sneddon theories.

The profile of the free-surface outside the contact region ($r > a$) of a perfectly elastic body is described by

$$\begin{aligned} u_z(\rho, 0) &= \frac{a^2}{\pi R}\left[\left(2-\rho^2\right)\sin^{-1}\frac{1}{\rho} + \sqrt{\rho^2 - 1}\right] \\ &= \frac{h}{\pi \rho^2}\left[\left(2-\rho^2\right)\sin^{-1}\frac{1}{\rho} + \sqrt{\rho^2 - 1}\right]; \quad \rho \geq 1 \end{aligned} \tag{3.20}$$

that is indented by a sphere with the radius R, and

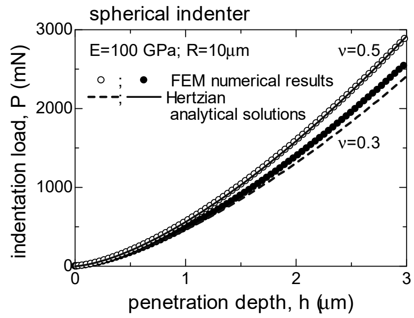

Figure 10.3 The P - h loading curves of spherical indentation (the tip-radius $R = 10$ μm). The solid line ($\nu = 0.5$) and the broken line ($\nu = 0.3$) indicate the Hertzian analytical solutions. The symbols ○ ($\nu = 0.5$) and ● ($\nu = 0.3$)) are the FEM-numerical results

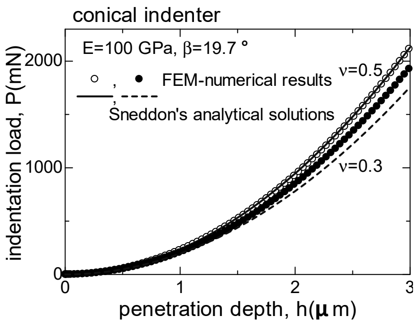

Figure 10.4 The P - h loading curves of conical indentation (the inclined face-angle $\beta = 19.7°$). The solid line ($\nu = 0.5$) and the broken line ($\nu = 0.3$) indicate the Sneddon's analytical solutions. The symbols ○ ($\nu = 0.5$) and ● ($\nu = 0.3$) are the FEM-numerical results

$$u_z(\rho,0)=\frac{2h}{\pi}\left[\sin^{-1}\frac{1}{\rho}-\rho+\sqrt{\rho^2-1}\right];\quad \rho\ge 1 \tag{3.27}$$

for conical indentation (refer to Chap.3). The comparison of these analytical solutions with the FEA-based numerical results ($\nu=0.5$) is shown in Fig. 10.5; the excellent agreement between the analytical and the numerical results ensures the accuracy/reliability of the FEA.

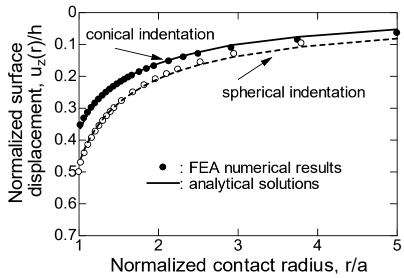

Figure 10.5 The elastic contact profiles ($\nu=0.5$) of the free-surface outside the contact zone of spherical or conical indentation contact: the symbols (●, ○) are the FEA-based numerical results and the solid/broken lines are the analytical solutions (Eqs. (3.20) and (3.27)) (refer to Fig. 3.6)

10.3 ELASTOPLASTIC ANALYSIS

(1) P - h Hysteresis Curve

As emphasized in Chap.5, we have no analytical solutions for the elastoplastic indentation contact mechanics, excepting the unified theory based on the additivity principle of excluded volume of indentation (see Sec. 5.1(2)). The FEM-based numerical analysis, therefore, exclusively plays an essential role in the elastoplastic indentation contact mechanics.

Due to the irreversible plastic flow, we observe a hysteresis in the indentation loading-unloading P - h curve (see Figs. 5.5, 5.8 - 5.10, and 5.12). This fact implies that the observed P - h hysteresis curve combined with FEA makes it possible for us to quantitatively determine the elastoplastic characteristics, i.e., the elastic modulus E' and the yield stress Y of the material tested. Figure 10.6 depicts the loading/unloading P - h^2 linear plot along with the contact geometries of an elastoplastic half-space for pyramid/cone indentation. As emphasized in the following considerations, the contact depth h_c is essential for calculating the contact area A, and the residual depth h_r plays an important role in determining the plastic flow; both are the key parameters for determining the elastoplastic characteristics. The geometrical similarity of the pyramid indenter (Vickers/Berkovich indenter) leads to the *penetration-depth-independent indentation strain* $\varepsilon_I (=\tan\beta/2)$, depending only on the inclined face-angle β (refer to Chaps. 3 and 5, and Tab. 3.1). This fact of penetration-depth- independent strain is very essential for quantitatively determining the elastoplastic characteristics through P - h hysteresis curve. The linear plots both for the loading and the unloading $P-h^2$ relations shown in Fig. 5.5 for the wide range of plastic index ($0.05\le PI\le 20$) are actually resulted from the penetration-depth-independent ε_I. In Fig. 10.6, we define the contact depth h_c at the applied load P as well as the depth h_r and the

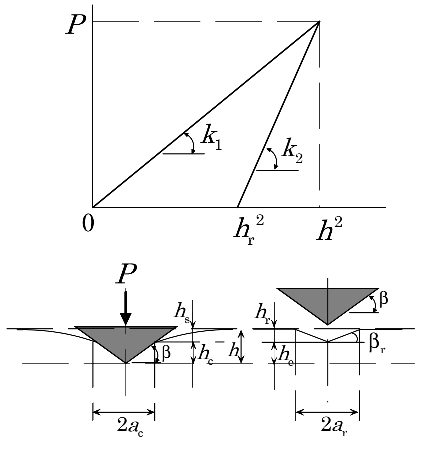

Figure 10.6 Loading/unloading $P-h^2$ linear plot and the pyramid/ cone indentation contact geometries of an elastoplastic body

inclined face-angle β_r of residual impression after unload. Since there exist the linear P - h^2 relations both in loading/unloading processes for pyramid/cone indentation, we can describe the loading/unloading process in terms of the loading coefficient k_1 and the unloading coefficient k_2;

$$P = k_1 h^2 \tag{10.1}$$

$$P = k_2 (h^2 - h_r^2) \tag{10.2}$$

Furthermore, due to the fact that the loading line crosses the unloading line at the maximum penetration depth h, there is the interrelation between k_1 and k_2;

$$k_1 = k_2 \left(1 - \xi_r^2\right) \tag{10.3}$$

in which ξ_r is the normalized residual depth h_r/h. Accordingly, the loading coefficient k_1 is related to the unloading coefficient k_2 via ξ_r. On the other hand, as given in the following considerations, both the loading coefficient k_1 and the normalized residual depth ξ_r are intimately related to the plastic index *PI*, while the unloading coefficient k_2 is closely related to the elastic modulus E'. The FEA-based numerical results of the normalized elastoplastic characteristics, k_1/Y, k_2/E', and h_r/h are, respectively, plotted against the plastic index *PI* ($=\varepsilon_I E'/cY$) in Figs. 10.7 – 10.9. These figures show that the normalized parameters of k_1/Y, k_2/E', and h_r/h are quantitatively related in a unique manner to the plastic index $PI\left(=\varepsilon_I E'/cY\right)$ in the wide ranges of 0.5 GPa $\leq E' \leq$ 500 GPa and 0.5 GPa $\leq Y \leq$ 100 GPa. The preceding considerations imply that we can quantitatively determine the elastic modulus E' and the yield stress Y through Figs. 10.7 – 10.9 after we determine in experiment the loading coefficient k_1, unloading coefficient k_2, and/or the residual depth of impression h_r by the use of the conventional instrumented indentation apparatus; the detailed experimental procedures are given as follows;

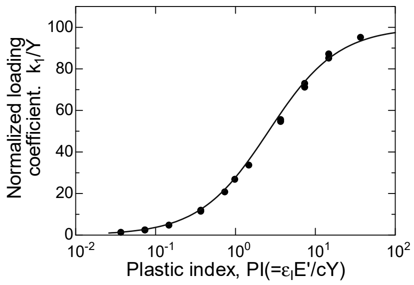

Figure 10.7 Normalized loading coefficient k_1/Y vs. plastic index *PI* (FEA-based numerical results for the Vickers/Berkovich equivalent cone)

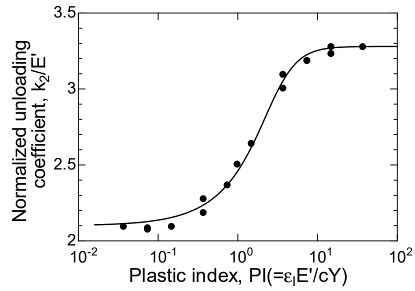

Figure 10.8 Normalized unloading coefficient k_2/E' vs. plastic index *PI* (FEA-based numerical results for the Vickers/Berkovich equivalent cone)

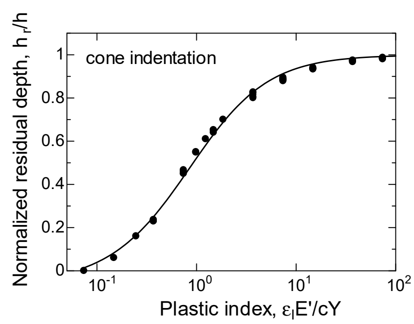

Figure 10.9 Normalized residual depth $h_r/h(\equiv \xi_r)$ vs. plastic index *PI* (FEA-based numerical results for the Vickers/Berkovich equivalent cone)

(i) Apply the experimentally observed h_r/h-value to the ordinate of Fig. 10.9 to estimate the plastic index $PI(=\varepsilon_I E'/cY)$ from the corresponding abscissa, followed by the application of this *PI*-value to the abscissa of Fig. 10.7 in order to determine the k_1/Y-value from the corresponding ordinate. This k_1/Y-value combined with the experimentally observed loading coefficient k_1 and the *PI*-value are then utilized to determine the elastoplastic characteristics of the elastic modulus E' and the yield stress Y, or

(ii) Assume the initial value Y_0 of the yield stress, and then calculate k_1/Y_0 using the experimentally observed k_1. Apply this k_1/Y_0-value to the ordinate of Fig. 10.7 to estimate the corresponding plastic index $\varepsilon_I E'/cY_0$ from the abscissa, leading to the initial estimate of the elastic modulus E_0'. Substitute these initial values of Y_0 and E_0' into the abscissa (the plastic index) of Fig. 10.8 to make the first-order approximation of the elastic modulus E_1 from the ordinate combined with the experimentally observed k_2-value. And then apply the $\varepsilon_I E_1'/cY_0$-value to the abscissa of Fig. 10.7 for determining the first-order approximation of the yield stress Y_1 from the ordinate. Repeat these procedures until the convergences of E_n and Y_n are obtained, finally resulting in the elastoplastic characteristics of E' and Y.

Among these elastoplastic parameters, the most essential one is the contact depth h_c at the indentation load P (see Fig. 10.6), though *it cannot be determined in experiment on the conventional instrumented indentation apparatus*. On the other hand, as shown in Fig. 5.6 in Chap. 5, using the FEA-based numerical results, the normalized contact depth h_c/h is intimately related to the plastic index $\varepsilon_I E'/cY$. As a matter of fat, combining Fig. 5.6 and Fig. 10.9 results in Fig. 10.10. By the use of Fig. 10.10, therefore, *we can readily estimate the contact depth* h_c *from the experimentally observable residual depth* h_r. Once we determine the contact depth h_c, we can successfully calculate the contact radius a_c, and then the contact area A that is requisite for determining the elastoplastic characteristics, the details of which have already been given in Chaps. 3 and 5.

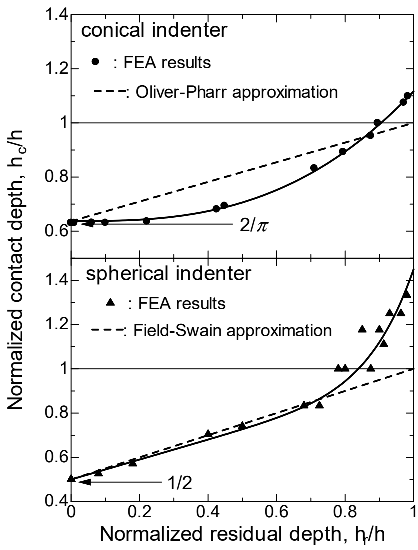

Figure 10.10 Correlation between the normalized contact depth h_c/h and the normalized residual depth h_r/h. The broken lines are, respectively, the Oliver-Pharr (conical indenter) and the Field-Swain (spherical indenter) approximations. The symbols (●, ▲) indicate the FEA-based numerical results

The considerations on the conical indentation in Fig. 10.10, by way of example, make clear that (1) the normalized contact depth h_c/h converges to the Sneddon's solution of $2/\pi$ in the perfectly elastic extreme of $h_r/h \to 0$, (2) the normalized contact depth h_c/h monotonically increases with the increase in the residual depth h_r/h due to the enhanced plastic flow-out to the free-surface outside the contact zone, implying the depression of the sink-in profile of the surface, (3) none of sink-in nor pile-up of the free-surface, i.e., $h_c/h = 1$, is observed at $h_r/h \approx 0.85$, (4) a significant pile-up of the free-surface is induced in the perfectly plastic extreme of $h_r/h \to 1$, resulting in the increase of the contact depth up to $h_c/h \approx 1.1$. The FEA-visualized contact profiles of the free-surface have already been given in Figs. 5.6 and 5.7 in relation to the plastic index $PI\left(= \varepsilon_1 E'/cY\right)$. Figure 10.10 also suggests that the elastoplastic contact behavior of spherical indentation is similar to that of conical indentation; the normalized contact depth h_c/h converges to the Hertzian value of 1/2 in the elastic extreme of $h_r/h \to 0$, and goes up to about 1.4 in the plastic extreme of $h_r/h \to 1$.

(2) The Oliver-Pharr/Field-Swain Approximation [10.2-10.4]

In the preceding section, using the FEA-based numerical results, we correlate the normalized residual depth h_r/h to the normalized contact depth h_c/h in a quantitative manner. In this section, we will discuss the Oliver-Pharr approximation for conical indentation and the Field-Swain approximation for spherical indentation; both of the approximations stand on the same *elastic assumption prior to analytically corelating* h_r/h to h_c/h. In *elastoplastic* indentation contact, however, this elastic assumption is very critical in estimating the contact penetration depth h_c, and then for determining the elastoplastic characteristics in the conventional instrumented indentation apparatus. There exist the following geometrical relations in the elastoplastic indentation contact (see the details in Fig. 10.6);

$$h = h_s + h_c = h_r + h_e \tag{10.4}$$

The Oliver-Pharr/Field-Swain approximation *assumes* that the sink-in depth h_s and the depth of elastic recovery h_e of *the elastoplastic body* with the elastic modulus E' are the same as those of *the perfectly elastic body* with the same elastic modulus E' when both of the bodies are

[10.2] W.C. Oliver, G.M. Pharr, J. Mater. Res., **7**, 1567 (1992)
[10.3] J.S. Field, M.V. Swain, J. Mater. Res., **8**, 297 (1993)
[10.4] M. Sakai, "Principle and Application of Indentation", in *Micro and Nano Mechanical Testing of Materials and Devices*, Edited by F. Yang, J.C.M. Li, 1-47, Springer (2008)

indented at the same load of P. The elastic indentation contact mechanics (refer to Eqs. (3.21) and (3.28)) leads to the following relations between h_e and h_s;

$$\frac{h_s}{h_e} = \frac{1}{2} \quad \text{(spherical indentation)} \qquad (10.5)$$

$$\frac{h_s}{h_e} = 1 - \frac{2}{\pi} \quad \text{(conical indentation)} \qquad (10.6)$$

Substituting these elastic relations into the elastoplastic relations of Eq. (10.4), we finally have the following approximations that relate h_r/h to h_c/h;

Field-Swain approximation:

$$\frac{h_c}{h} = \frac{1}{2}\left(1 + \frac{h_r}{h}\right) \quad \text{(spherical indentation)} \qquad (10.7)$$

Oliver-Pharr approximation:

$$\frac{h_c}{h} = \frac{2}{\pi}\left[1 - \left(1 - \frac{\pi}{2}\right)\frac{h_r}{h}\right] \quad \text{(conical indentation)} \qquad (10.8)$$

The broken lines in Fig. 10.10 represent the Oliver-Pharr/Field-Swain approximations. Since both of Eqs. (10.7) and (10.8) assume the elastic relations of Eqs. (10.5) and (10.6), these approximations converge to $h_c/h \to 1$ in the plastic extreme of $h_r/h \to 1$, being impossible to describe the plastic-flow-induced surface pile-up ($h_c/h > 1.0$), as well recognized in Fig. 10.10.

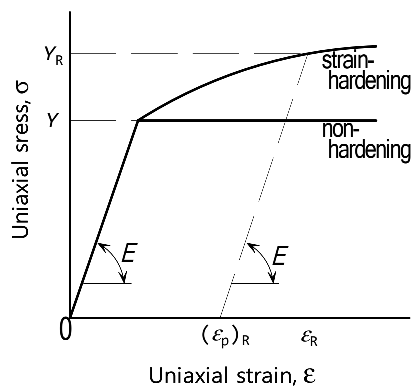

Figure 10.11

Stress σ vs. strain ε curve (S-S curve) of elastoplastic material. The S-S curve of strain hardening material increases with strain exceeding the elastic limit. The representative flow stress Y_R is defined as the value at the representative plastic strain $(\varepsilon_p)_R$ or at the representative total strain ε_R

(3) Strain Hardening and the Representative Stress/Strain

The discussions in Chap.5 and the preceding considerations have only been applicable to *elastic-perfectly-plastic solids* having a constant yield stress Y in the region exceeding the elastic limit at which the plasticity index $PI(\equiv \varepsilon_I E'/cY)$ is about 0.2. However, in most of engineering materials, such as mild steel, aluminum, copper, etc., ever-increasing actual stress is required for continued deformation beyond the yield point, i.e., strain hardening (work hardening), as shown in Fig. 10.11. The experimental results of D. Tabor as well as the FEA-based numerical studies have shown that the conclusions obtained in the indentation contact mechanics of *non-hardening elastoplastic solids* may be applied with a good approximation to *strain hardening solids* if Y is simply replaced with the *representative flow stress* Y_{R}. This fact indicates that the preceding elastoplastic analyses in terms of PI that we made, by way of examples, in Figs. 10.7–10.9 still survive by simply replacing PI with $(PI)_{\mathrm{R}}\left(=\varepsilon_{\mathrm{I}}E'/cY_{\mathrm{R}}\right)$ **[4.1, 10.5, 10.6]**. The representative flow stress Y_{R} is defined by the representative plastic strain $\left(\varepsilon_{\mathrm{p}}\right)_{\mathrm{R}}$ or the representative total strain ε_{R} as sown in Fig. 10.11. The FEM-based numerical result, on the other hand, indicates that $\left(\varepsilon_{\mathrm{p}}\right)_{\mathrm{R}}$ is related to the indentation strain ε_{I} as follows **[10.6]**;

$$\left(\varepsilon_{\mathrm{p}}\right)_{\mathrm{R}}=0.44\varepsilon_{\mathrm{I}} \tag{10.9}$$

Accordingly, substituting the indentation strain ε_{I} (see Eqs. (3.30) and (3.31)) into Eq. (10.9), the representative plastic strain of conical indenter with the inclined face-angel β is written by

$$\left(\varepsilon_{\mathrm{p}}\right)_{\mathrm{R}}=0.22\tan\beta, \tag{10.10}$$

and of spherical indenter with the radius R is given by

$$\left(\varepsilon_{\mathrm{p}}\right)_{\mathrm{R}}=0.19\frac{a}{R}, \tag{10.11}$$

We can, therefore, readily determine the respective flow stresses Y_{R} in Fig. 10.11 by the use of these $\left(\varepsilon_{\mathrm{p}}\right)_{\mathrm{R}}$-values.

(4) The Effects of Indenter's Tip Geometry and of Contact Friction on the Constraint Factor c

The role of contact friction at the interface between the indenter and the material tested is not well understood even for the perfectly elastic contact mechanics. Furthermore, the indenter-tip geometry and the contact friction will have a significant effect on the sink-in/pile-up of an elastoplastic body (see Figs. 5.6 and 5.7), as well as on the constraint factor c (refer to Chap. 5 and Eq. (5.7)), since the constraint factor dictates the in-surface plastic flow out to the free surface outside the contact region. The contact friction may resist this plastic flow-out along the indenter's face, leading to a larger c-value. Furthermore, when the inclined face-angle of conical/pyramidal indenter becomes larger, i.e., the tip of indenter becomes sharper, it will be expected that the plastic flow

[10.5] D. Tabor, "Hardness of Metals", Clarendon (1951)
[10.6] M. Sakai, T. Akatsu, S. Numata, K. Matsuda, *J. Mater. Res.*, **18[9]**, 2087 (2003)

out to the free surface will be enhanced, leading to progressively smaller c -value.

As discussed in Chap.5, the experimental results indicate that the constraint factor of ductile metals falls in the range of $2.5 \le c \le 3.5$ depending on the contact friction and the indenter's geometry. On the other hand, the FEM-based numerical analyses enable us to determine in a quantitative manner the constraint factor of an arbitrary tip-geometry of indenter in a wide range of its contact friction.

The FEA-based numerical results of the constraint factor c are plotted against the contact friction μ in Fig. 10.12 (for Vickers/ Berkovich-equivalent cone), and against the inclined face angle β (for conical indenters) in Fig. 10.13. The constraint factor of the equivalent cone significantly increases from the initial value of $c \approx 2.65$ to the plateau of $c \approx 3.2$ with the increase in the contact friction ($0 \le \mu \le 0.5$), as shown in Fig. 10.12. Since the contact friction of most of engineering materials against diamond falls in the range of $0.1 \le \mu \le 0.5$, the FEA-based preceding conclusions quite well satisfy the experimentally observed c -values of $3.0 \le c \le 3.2$ for Vickers diamond indentation (**[10.5]**, **[10.6]**). As well seen in Fig. 10.13, the constraint factor c decreases with the increase in the inclined face-angle β . This fact implies the enhanced in-surface plastic flow out to the free surface when the conical indenter becomes sharper, i.e., the inclined face-angle β becomes larger.

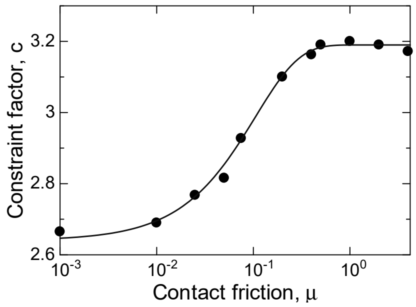

Figure 10.12 Effect of contact friction on the constraint factor for Vickers/Berkovich equivalent cone indentation (FEA-based numerical results)

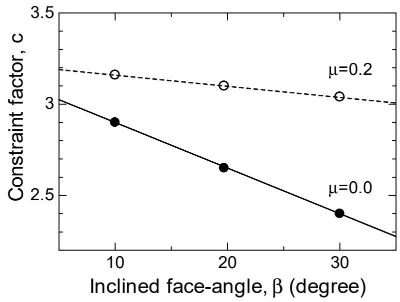

Figure 10.13 Effect of the inclined face-angle of conical indentation on the constraint factor (FEA-based numerical results; the contact frictions of $\mu = 0.0$ and $\mu = 0.2$)

10.4 VISCOELASTIC ANALYSIS

In contrast to the preceding *elastoplastic analysis*, *we can readily extend the elastic contact mechanics to the viscoelastic contact mechanics by the use of* "*the elastic-to-viscoelastic corresponding principle*" (refer to Chaps. 6 and 7). However, the time-dependent Poisson's effect (see Figs. 6.7 - 6.10) associated with indentation contact makes the analysis rather difficult. As a matter of fact, when we indent a Vickers/Berkovich equivalent cone onto a viscoelastic body in *a stepwise manner to a constant penetration depth of* h_0 , due to the increase in the Poisson's ratio associated with stress relaxation, we observe *the progressively increasing contact area induced by creeping-up of the free-surface along the face of indenter*. An example of the FEA-based numerical result is shown in Fig. 10.14 for the *creeping-up of indentation contact area under a stepwise penetration* onto a Maxwell liquid (the relaxation shear modulus $G(t) = G_g \exp(-t/\tau)$ with the glassy modulus $G_g = 36.4$ GPa, relaxation time $\tau = 200$ s, and the glassy Poisson's ratio $\nu_g = 0.1$). This result indicates that we cannot determine the stress relaxation modulus $E'_{\mathrm{relax}}(t)$ from the observed load relaxation $P(t)$ using Eq. (7.6) because of the time-dependent contact area $A(t)$. We, therefore, need to use the following integral equation

$$P(t) = \frac{\tan\beta}{2} \int_0^t E'_{\mathrm{relax}}(t-t') \frac{dA(t')}{dt'} dt' \qquad (7.3)$$

in order to determine the relaxation modulus $E'_{\mathrm{relax}}(t)$. We have to, therefore, measure in experiment the time-dependent contact area $A(t)$ along with the indentation load relaxation $P(t)$, though it is impossible for us to measure the time-dependent contact area $A(t)$ in the conventional instrumented indentation apparatus (the details will be given in Sec. 11.3 of *the instrumented indentation microscope* that enables to measure $A(t)$ as a function of time). In the FEM-based numerical analyses, on the other hand, it is easy for us to numerically determine the plane-strain relaxation modulus $E'_{\mathrm{relax}}(t)$, since we can easily determine the time-dependent contact area $A(t)$ in a quantitative manner.

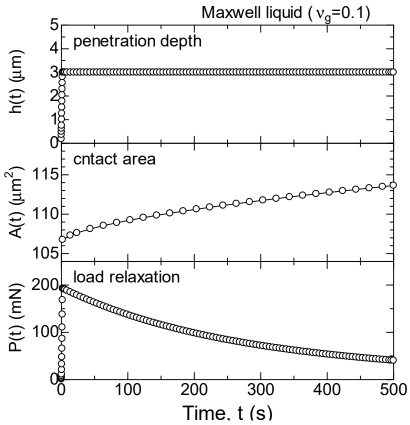

Figure 10.14 Load relaxation and contact-area creep under a *stepwise* penetration of a conical indenter (FEA-based numerical results of a Maxwell liquid)

Comparison between the FEA-based numerical result and the analytical solution of a viscoelastic liquid having a time-dependent Poisson's effect with shingle relaxation time (Eq. (6.26));

$G_g = 3.85$ GPa, $G_e = 0$ GPa, $\tau_0 = 200$ s, and $\nu_g = 0.3$,

is shown in Fig. 10.15, where the relaxation modulus $E'_{\mathrm{relax}}(t)$ obtained by substituting the FEA-derived $P(t)$ and $A(t)$ into Eq. (7.3) is plotted along with the analytical solution (Eq. (6.29)), demonstrating that the FEA-based numerical result faithfully realizes the analytical solution. This excellent agreement between the analytical solution and the FEA-based numerical result indicates the usefulness of the FEA–based numerical indentation contact mechanics in the studies of engineering materials having rather complicated mechanical characteristics such as the viscoelastic laminate composite discussed in the following section.

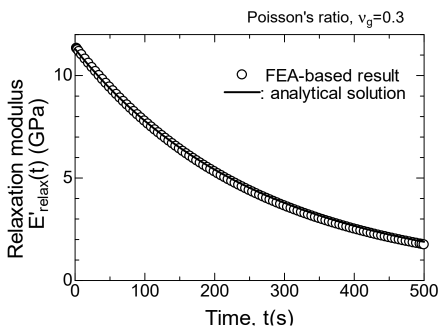

Figure 10.15 Relaxation modulus of a viscoelastic liquid; the numerical result (○) via Eq. (7.3) with FEA-derived $P(t)$ - $A(t)$ relation, and the analytical solution (Eq. (6.29); the solid line)

10.5 APPLICATION TO LAMINATE COMPOSITES

As mentioned in Secs. 9.1 and 9.2, there exist the analytical solutions for the indentation contact mechanics of coating/substrate composites in elastic as well as viscoelastic regimes, though we inevitably face the extremely complicated mathematical procedures such as solving the Fredholm integral equation (Eq. (9.11)) and/or integrating the Boussinesq Green function (Eqs. (9.7) and (9.8)). Even in these analytical approaches, however, we cannot control the mechanical consistency at the interface between the coating film and the substrate. To circumvent this difficulty, the FEA-based numerical indentation contact mechanics plays an essential role; we can take into account the *mechanical consistency* at the interface in a quantitative manner, as well as deal with the indentation contact mechanics of *multi-laminar composites*.

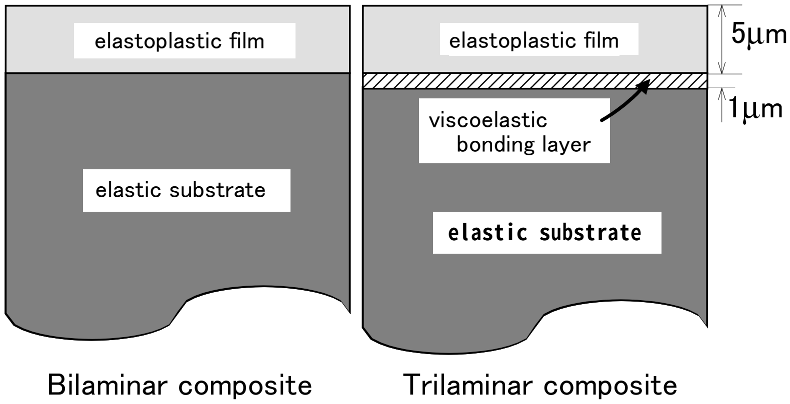

Figure 10.16 Bilaminar and trilaminar composites used in the FEA

As an example, let us make the FEA-based numerical analysis of a trilaminar composite depicted in Fig. 10.16; an elastoplastic coating film ($E_{\mathrm{f}} = 100$ GPa, $Y_{\mathrm{f}} = 10$ GPa, $\nu_{\mathrm{f}} = 0.3$) with the thickness of 5 μm is bonded to an elastic substrate ($E_{\mathrm{s}} = 100$ GPa, $\nu_{\mathrm{s}} = 0.3$) through an interfacial viscoelastic bonding layer (Maxwell liquid; $E_{\mathrm{relax}}(t) = E_g \exp(-t/\tau)$, E_{g}=10GPa, τ=200s) having the thickness of 1 μm. In order to scrutinize the role of this viscoelastic interface in the indentation contact behavior, the bilaminar composite without viscoelastic bonding layer is also examined for comparison (see Fig. 10.16).

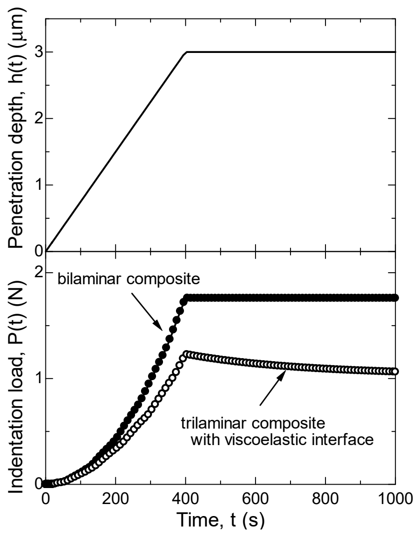

Figure 10.17 Time-dependent loads for the bilaminar and the trilaminar composites indented by a Vickers-equivalent cone under a constant-rate of penetration to the depth of $h = 3.0$ μm in 400s, and then the depth is kept to $t = 1000$ s (FEA-based numerical results)

Figure 10.17 shows the FEA-based numerical results of the load $P(t)$ plotted against time t for the bilaminar and the trilaminar composites indented by a Vickers-equivalent cone under a constant-rate of penetration to the depth of $h = 3.0$ μm in 400s, and then the depth is kept to $t = 1000$ s (see the top view of Fig. 10.17). The indentation load relaxation is observed for the trilaminar composite due to the presence of viscoelastic interface. It must be noticed the fact that this load relaxation is very sluggish while the relaxation time of the viscoelastic interface is τ =200s, being resulted from the geometrical constraints of the time-independent elastoplastic coating film as well as of the elastic substrate.

In Sec. 9.2, we emphasized in the indentation contact mechanics of bilaminar composites that we can control and design the viscoelastic behavior of the laminate composite by only adjusting the elastic modulus of the elastic substrate without any modification of the viscoelastic coating film (refer to Fig. 9.9). We can also control the viscoelastic behavior of the trilaminar composites by only adjusting the elastic modulus of the substrate. In Fig. 10.18 plotted are the FEA-based numerical results of the trilaminar composites shown in Fig. 10.16 with the substrate having its elastic modulus ranging $10\text{GPa} \le E_s \le 500\text{GPa}$. In Fig. 10.18, the normalized load relaxation $P(t)/P(400)$ is plotted against the time $t(\ge 400\text{s})$, where the penetration depth is kept constant at $h = 3.0$ μm (see the top view of Fig. 10.17). As shown in Fig. 10.18, the load relaxation becomes progressively significant, i.e., the relaxation time of the laminate shifts to the shorter side, with the increase in the elastic modulus E_s of the substrate.

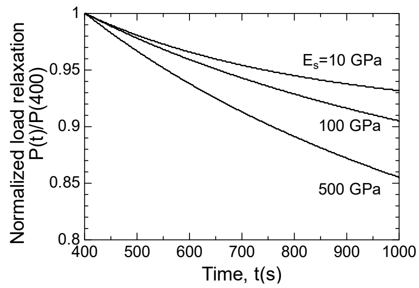

Figure 10.18 Effect of the elastic modulus E_s of the substrate on the relaxation behavior of the trilaminar composite with a viscoelastic bonding layer (the right-hand view in Fig 10.16). A Vickers-equivalent cone under a constant-rate of penetration to the depth of $h = 3.0$ μm in 400s, and then the depth is kept constant to $t = 1000$ s (see the top view of Fig. 10.17).

The normalized load relaxation $P(t)/P(400)$ is plotted against the time $t(\ge 400\text{s})$

(FEA-based numerical results)

EXPERIMENTAL APPARATUS AND DATA ANALYSIS

CHAPTER 11

11.1 TIP-GEOMETRY OF THE CONVENTIONAL INDENTERS

Figure 11.1 depicts the tip-geometries of the conventional Vickers and the Berkovich indenters. In order to add the geometrical consistency to the Brinell hardness test, the inclined face-angle β of the Vickers tetrahedral pyramid is 22.0°, and thus the apex angle, i.e., the diagonal face-to-face angle 2θ is designed to be 136°, since this is the angle subtended by the tangent of a Brinell sphere when the ratio of the contact diameter $2a$ to the diameter $2R$ of Brinell sphere is 0.375, being the most recommended ratio in the Brinell hardness test (refer to Fig. 5.4 in Chap. 5). The diagonal edge-to-edge angle 2ψ is, therefore, 148.1°. On the other hand, the tip-geometry of the Berkovich trihedral pyramid indenter is designed in order that its excluded volume of the material beneath the indenter at a penetration depth of h is the same as that of the Vickers pyramid, resulting in $\beta = 24.7^\circ$ and $\psi = 77.1^\circ$. The projected contact area A of *cone/pyramid indenter* is, due to its geometrical similarity, described by $A = gh^2$ using the index of projected area g ($g = 4\cot^2\beta$ for the Vickers indenter, and $g = 3\sqrt{3}\cot^2\beta$ for the Berkovich indenter). Accordingly, the g-value of the Vickers coincides with that of the Berkovich, resulting in $g = 24.5$, and then giving the same projected contact area $A = gh^2$, as well as the same excluded volume of $V\left(\equiv gh^3/3\right) = 8.17h^3$ at a given penetration depth h.

Upon machining a pyramidal tip on a tiny diamond single crystal, it is impossible to make an ideally sharp-tip, i.e., an atomic tip, always resulting in a rounded or a truncated tip. Due to the trihedral tip-geometry, machining a sharp tip on the Berkovich indenter is rather easier than the tetrahedral Vickers indenter. This is the reason why the Berkovich indenter is rather preferable than the Vickers indenter in nanoindentation testing. Commercially available Berkovich indenter, in general, has the

(a) Vickers tetrahedral indenter

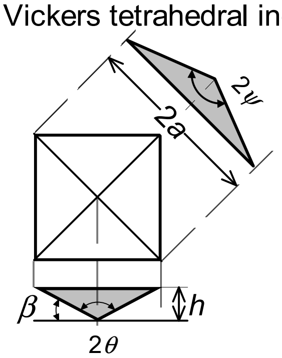

	β	ψ	2θ
Vickers	22.0°	74.05°	136.0°

(b) Berkovich trihedral indenter

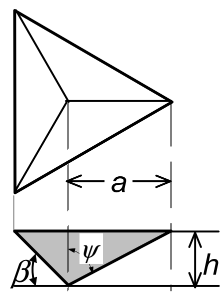

	β	ψ
Berkovich	24.7°	77.1°

Figure 11.1 Tip-geometries of the conventional pyramid indenters:
(a) Vickers indenter,
(b) Berkovich indenter

rounded tip-radius of about 100 nm. This rounded tip may yield crucial difficulties in *nano*indentation testing when the penetration depth is several tenth of nanometers or less. The effect of a rounded tip on the indentation contact behavior will be discussed in what follows for the Vickers/Berkovich equivalent conical indenter ($\beta = 19.7^\circ$) via the FEA-based numerical results.

The tip-geometry of Vickers/Berkovich equivalent cone with a rounded tip (radius of curvature, R_t) is shown in Fig. 11.2. Suppose the apex radius of $R_t = 100$ nm, by way of example, then the lost-tip-depth is to be $\Delta h_t \left(= R_t(\sin\beta\tan\beta + \cos\beta - 1)\right) = 6.22$ nm, the spherical depth is $h_{sphere} \left(= R_t(1-\cos\beta)\right) = 5.85$ nm, and the region of conical depth is given by $h_{cone} \geq 5.85$ nm. Once we press this indenter onto a flat half-space, we will observe the spherical contact response in the initial stage of penetration followed by the conical indentation contact.

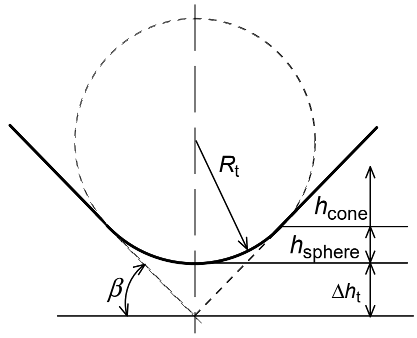

Figure 11.2 Tip-geometry of the Vickers/Berkovich equivalent cone ($\beta = 19.7^\circ$) having a rounded tip with the radius of curvature, R_t

Figure 11.3 shows the FEA-based numerical result of the P - h plot for this rounded-tip cone indented on a perfectly elastic body with the elastic modulus $E = 100$ GPa and the Poisson's ratio $\nu = 0.5$. As clearly seen in Fig. 11.3, it must be noticed in the region of $h \leq 150$ nm that there exists a finite deviation from the conical indentation in its P - h relation. This numerical study suggests that we have to pay an attention in *nanoindentation tests* upon using the conventional Vickers/Berkovich pyramid. In other word, we have to make an experimental examination/correction of the tip-radius in a quantitative manner prior to nanoindentation testing. However, on the conventional instrumented indentation apparatuses unlike the *indentation microscope* (refer to the subsequent Sec. 11.3 for the details), we can neither measure the contact depth h_c nor determine the contact area A_c in experiment; it is only possible for us to determine the indentation load P and the associated penetration depth h. This fact implies that, even after we completed the quantitative correction for the tip-radius, we have to make approximations/assumptions to estimate h_c and/or A_c, before we experimentally determine the material characteristics such as the elastic modulus and the yield stress of the material tested.

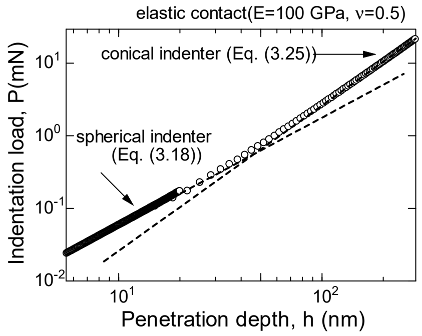

Figure 11.3 P - h plot of a perfectly elastic body (elastic modulus $E = 100$ GPa, Poisson's ratio $\nu = 0.5$) indented by a Vickers/Berkovich equivalent cone with a rounded tip (radius; $R_t = 100$ nm). The broken lines indicate the analytical relations, and the symbol (○) are the FEA-based numerical results

11.2 INSTRUMENTED INDENTATION TEST SYSTEM

The studies on instrumented indentation testing have been started in 1980s in order to make a quantitative measurement/determination of the material characteristics in micro/nano region **[11.1-11.3].** The schematic of instrumented micro/nano indentation test system is given in Fig. 11.4. A piezo or an electromagnetic actuator is widely utilized as the load/displacement driving unit. Load sensor with the precision of about ±0.5μN and displacement sensor with the precision of ±0.1nm are commercially available. As shown in Fig. 11.4, depending on the spatial configuration between the displacement sensor and the test specimen, the test system is grouped into (a) the apparatus-frame-referenced and (b) the specimen-holder-referenced test systems **[9.4, 11.4-11.6]**. In the former test system (a), since the displacement sensor can be fixed away from the specimen tested, we can easily make indentation testing at elevated temperatures, in a hostile environment, etc. by setting a specimen chamber, while the elastic deformations of the frame, load-train, and of the specimen-holder are inevitably included as the *frame compliance* in the penetration depth observed, leading to *the fatal defect* of this test system. The frame-compliance-associated problem becomes more significant in micro/nano indentation testing. Accordingly, we have to a priori determine the frame compliance of the test system in a quantitative manner (refer to the details in the subsequent section). In the latter test system (b), on the other hand, due to detecting the displacement of the indenter-tip relative to the specimen-surface, the undesirable effect of frame compliance is insignificant. Accordingly, we can determine the mechanical characteristics such as the Meyer hardness, elastic modulus, and the yield stress in a quantitative manner without any corrections of the frame compliance, while it is rather difficult for us to conduct indentation testing at elevated temperatures that is contrary to the former test system (a). In both of the test systems, we must pay attention to tightly fixing the test specimen on the holder in order to eliminate undesirable errors in measuring the penetration depth.

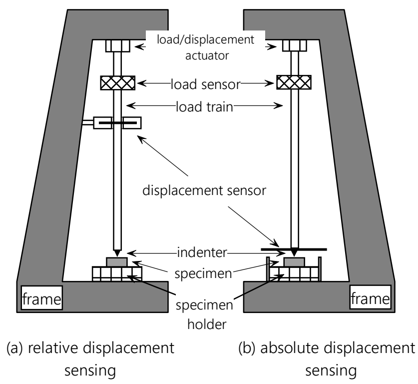

Figure 11.4 Instrumented micro/ nano indentation test systems:
(a) sensing the *relative depth* of penetration, and
(b) sensing the *absolute depth* of penetration

[11.1] M.K. Shorshorov, S.I. Bulychev, V.A. Alekhim, *Sov. Phys. Doki.*, **26**, 769 (1981)
[11.2] D. Newey, M.A. Wilkins, H.M. Pollock, *J. Phys.* **E15**, 119 (1982)
[11.3] J.B. Pethica, R. Hutchings, W.C. Oliver, *Phil. Mag.*, **A48**, 593 (1983)
[11.4] G.M. Pharr, R.F. Cook, *J. Mater. Res.*, **5**, 847 (1990)
[11.5] M. Sakai, *Acta. Metall. Mater.*, **41**, 1751 (1993)
[11.6] M. Sakai, S. Shimizu, T. Ishikawa, *J. Mater. Res.*, **14[4],** 1471 (1999)

(1) Experimental determination of the frame compliance

Aw well discussed in the preceding section, the elastic deformation of the frame, i.e., the frame compliance, has always undesirable effect on determining the mechanical characteristics such as the elastic modulus, viscoelastic functions, etc. in micro/nano indentation testing.

Suppose a perfectly elastic indentation contact and define the *observed* penetration depth as h_{obs}, the *actual* depth of penetration as h, and the indentation load as P, then the following relations are given;

$$\begin{aligned} h_{\mathrm{obs}} &= C_{\mathrm{obs}} P \\ h_{\mathrm{obs}} &= h + h_{\mathrm{f}} \end{aligned} \tag{11.1}$$

where h_{f} represents the frame-deformation-induced penetration, and C_{obs} is defined as the elastic compliance observed. Once we define the elastic compliance of *test specimen* C by $h = CP$, and the frame compliance C_{f} by $h_{\mathrm{f}} = C_{\mathrm{f}} P$, then the observed compliance C_{obs} is related to the specimen's compliance C as follows;

$$C_{\mathrm{obs}} = C + C_{\mathrm{f}} \tag{11.2}$$

via the frame compliance C_{f}. In most of the commercially available conventional instrumented indentation test systems, their frame compliance is to be $C_{\mathrm{f}} \approx 200\,\mathrm{nm/N}$.

The load vs. penetration depth hysteresis curve (*P–h* loading/ unloading curve) of an elastoplastic body is depicted in Fig. 11.5. Since the unloading curve is resulted from the *elastic recoveries* of the test specimen and of the apparatus frame, the initial slope of the unloading *P–h* curve at the maximum penetration depth h_{max}, being referred to as the unloading stiffness $S_{\mathrm{obs}} \left(\equiv \left(dP/dh \right)_{h_{\mathrm{max}}} \right)$, is related to the observed elastic compliance C_{obs} through the inverse relation of $S_{\mathrm{obs}} = 1/C_{\mathrm{obs}}$. On the other hand, when we substitute the relation of $C = dh/dP$ into Eqs. (3.33) and (3.34), for arbitrary *axisymmetric* indenters including spherical, conical, and pyramidal indenters, the unloading compliance is related to the elastic modulus E' of the specimen tested **[9.4]**;

$$C_{\mathrm{obs}} \left(\equiv 1/S_{\mathrm{obs}} \right) = C_{\mathrm{f}} + \frac{\sqrt{\pi}}{2E'} \frac{1}{\sqrt{A_{\mathrm{c}}}}, \tag{11.3}$$

where A_{c} stands for the contact area at the maximum indentation load P_{max}. The contact area A_{c} is related to the contact depth of penetration

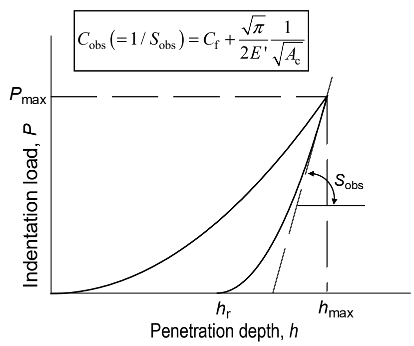

Figure 11.5 Loading/unloading *P-h* hysteresis curve of an elastoplastic body. The initial slope S_{obs} of the unloading curve is referred to as the unloading stiffness; there is an inverse relation between the observed compliance C_{obs} and the unloading stiffness S_{obs}, i.e., $S_{\mathrm{obs}} = 1/C_{\mathrm{obs}}$

h_c via the formula of $A_c = gh_c^2$ in terms of the area index g (the Vickers/Berkovich indenters; $g = 24.5$) *for deep penetration*, where we can neglect the effect of indenter's rounded-tip on the indentation contact behavior. Furthermore, there exists a quantitative correlation of $h_c = \eta_c h_{max}$ between the contact depth h_c and the penetration depth h_{max} at the maximum indentation load, where the relative penetration depth η_c is given by the function of plastic index $\varepsilon_I E'/cY$ (refer to Fig. 5.6). Substituting the preceding formulas into Eq. (11.3), both of the experimentally observable parameters $C_{obs}\left(\equiv 1/S_{obs}\right)$ and h_{max} are correlated in the following equation via the frame compliance C_f ;

$$C_{obs}\left(\equiv 1/S_{obs}\right) = C_f + \frac{\sqrt{\pi}}{2E'}\frac{1}{\sqrt{g\eta_c}}\frac{1}{h_{max}} \tag{11.4}$$

An example of the C_{obs} - $1/h_{max}$ plot is shown in Fig. 11.6 in order to scrutinize the preceding procedure for determining the frame compliance C_f, where all the data are of the FEA-created model elastoplastic body (the elastic modulus $E = 100$ GPa, yield stress $Y = 10$ GPa, and the Poisson's ratio $\nu = 0.3$) indented by a Vickers/Berkovich equivalent cone with the truncated tip-radius $R_t = 100$ nm (see Fig. 11.2). The frame compliance is a priori set to be $C_f = 200$ nm/N in this FEA-based modeling. In Fig. 11.6, we can readily confirm that the frame compliance C_f determined from the intercept of the *y*-axis (the axis of ordinate), and the elastic modulus E' calculated from the slope of C_{obs} - $1/h_{max}$ linear plot *coincide well* with those a priori fixed in the FEA-model. In other words, Fig. 11.6 indicates that we can successfully determine *in experiment* the frame compliance C_f from the C_{obs} - $1/h_{max}$ linear plot obtained in the conventional instrumented indentation apparatus.

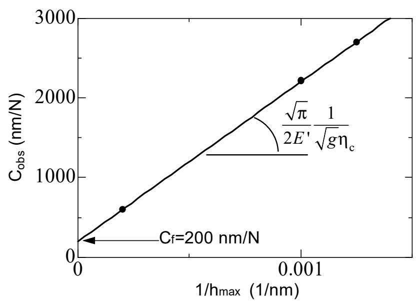

Figure 11.6 C_{obs} vs. $1/h_{max}$ plot for determining the frame compliance C_f in experiment

(FEA-based numerical results)

Experimental procedure for determining the frame compliance of instrumented indentation apparatus

(1) Experimental determination of $C_{obs}\left(\equiv 1/S_{obs}\right)$ vs. h_{max} relations at several discrete values of $h_{max}\left(\geq 500\text{nm}\right)$ by the use of *a higher-modulus material such as a brittle ceramic*; a higher-modulus material enhances the deformation of the frame, thus leading to determining the frame-compliance C_f with a higher precision.

(2) Determination of C_f from the intercept of the C_{obs} vs. $1/h_{max}$ linear plot (see Fig. 11.6) obtained in the procedure **(1)**.

* Once we use a test material *having the known elastic modulus* E' such as a fused silica, we can readily determine η_c from the slope $\left(=\sqrt{\pi}/\left(2E'\sqrt{g}\eta_c\right)\right)$ of the linear C_{obs} vs. $1/h_{max}$ plot, then we can correlate h_{max} to the contact depth $h_c = \eta_c h_{max}$ as well as to the contact area $A_c\left(= g{h_c}^2\right)$

The unloading compliance $C\left(\equiv C_{obs} - C_f\right)$ of these FEA-based numerical results is plotted in Fig. 11.7 against the penetration depth h_{max} in a double-logarithmic way in order to evaluate the tip-radius R_t of the indenter used, since there exist the relations of

$$C \equiv \left(dh/dP\right) \propto 1/{h_{max}}^{1/2}\left[\rightarrow -\left(1/2\right)\log h_{max}\right]$$

for spherical, and

$$C \propto 1/h_{max}\left(\rightarrow -\log h_{max}\right)$$

for conical indentation (refer to Eqs. (3.18) and (3.25)). As a matter of fact, Fig. 11.7 demonstrates the linear log-log plots with the slope of -1 in the region of conical indentation and with the slope of -1/2 in the region of spherical indentation. There exists, therefore, the spherical-to-conical transition in the region of $10\text{nm} \leq h_{max} \leq 60\text{nm}$ that is marked by the hatched zone in Fig. 11.7. This transition is actually resulted from the tip-geometry of the indenter (Fig. 11.2) modeled in the present FEA

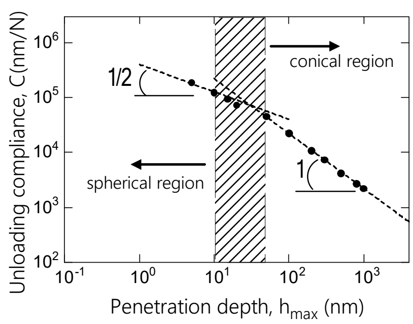

Figure 11.7 Double-logarithmic plot of the unloading compliance $C\left(\equiv C_{obs} - C_f\right)$ vs. the penetration depth h_{max} (FEA-results for an elastoplastic body with the elastic modulus $E = 100$ GPa, Poisson's ratio $\nu = 0.3$ and the yield stress $Y = 10$ GPa)

having the tip-radius $R_t = 100$ nm and $h_{\text{sphere}} [= R_t(1-\cos\beta)] = 5.85$ nm.

As well demonstrated in the preceding FEA-results, once we determine the frame compliance C_f in experiment, we can readily determine the tip-radius of the commercially available pyramidal indenter through the double-logarithmic plot of the unloading compliance $C(\equiv C_{\text{obs}} - C_f)$ vs. $h_{\max}$ as shown in Fig. 11.7. Along with this compliance method, making direct observation for the tip of indenter through a scanning probe microscope refines the experimental determination of the indenter's tip-radius R_t.

(2) Experimental determination of elastoplastic characteristics

The mechanical characteristics such as the elastic modulus and the yield stress can, therefore, be determined in indentation tests through analyzing the indentation load P vs. the penetration depth h hysteresis, i.e., the loading/unloading P - h hysteresis relation, once we have completed an a priori evaluation of the frame compliance and the tip-geometry of the indenter used. As mentioned in the preceding sections, however, *due to the incapability of determining the indentation contact area A in the conventional instrumented indentation test systems*, we have to reckon the approximation and assumption and/or the FEA-based calibration to estimate the contact area, leading always to somewhat uncertainty and inaccuracy in experimentally determining the mechanical characteristics from the P - h hysteresis relation observed.

【Procedure for determining the elastoplastic characteristics from the P - h hysteresis observed in experiment】

The flow chart for determining the elastoplastic characteristics from the observed P - h hysteresis of *pyramidal indentation* is given in Fig. 11.8: Figures 1 and 2 in the flow chart exhibit the key parameters; the maximum penetration depth h_{max}, depth of residual impression h_{r} that is attributed to the plastic deformation, loading coefficient k_1 including the elastoplastic information, and the unloading coefficient k_2 that is resulted from the elastic recovery of indentation-induced impression.

(1) Apply the observed dimensionless residual depth $h_{\mathrm{r}}/h_{\mathrm{max}}$ to the *y*-axis of Fig. 3 (FEA-derived plot; see Fig. 10.9), and then determine the plastic index $PI\left(=\varepsilon_{\mathrm{I}}E'/cY\right)$ from the *x*-axis

(2) In a similar way, apply the observed $h_{\mathrm{r}}/h_{\mathrm{max}}$ to the *x*-axis of Fig 4 (see Fig. 10.10) in order to determine the dimensionless contact depth $h_{\mathrm{c}}/h_{\mathrm{max}}$ from the *y*-axis. Instead of using this graphical procedure, the Oliver-Pharr elastic approximation (Eq. (10.8)) is also applicable to determining $h_{\mathrm{c}}/h_{\mathrm{max}}$

(3) Determine the contact radius a_{c} through the relation $a_{\mathrm{c}}=h_{\mathrm{c}}\cot\beta$ by the use of h_{c} obtained in the preceding procedure **(2)**, then calculate the contact area using the relation of $A_{\mathrm{c}}\left(=\pi a_{\mathrm{c}}^2\right)=\left(\pi\cot^2\beta\right)h_{\mathrm{c}}^2$, leading to the determination of the Meyer hardness H_{M} from A_{c} combined with the maximum indentation load P_{max};

$$H_{\mathrm{M}}\left(\equiv P_{\mathrm{max}}/A_{\mathrm{c}}\right)=\left(P_{\mathrm{max}}\tan^2\beta\right)\Big/\pi h_{\mathrm{c}}^2 \qquad (11.5)$$

(4) Apply the plastic index *PI* determined in the preceding procedure **(1)** to the *x*-axis of Fig. 5 (see Fig. 10.7) and of Fig. 6 (see Fig. 10.8), then determine k_1/Y and k_2/E' from the respective y-axes. Since the values of k_1 and k_2 have already been known in the observed P - h^2 plot in Fig. 2, we are ready to determine the elastic modulus E' and the yield stress Y of the elastoplastic body

(5) Apply the plastic index *PI* obtained in Fig. 3 to the *x*-axis of the FEA-derived Fig. 5.3, then determine the constraint factor c from the corresponding *y*-axis of the normalized hardness of H_{M}/cY, because the values of H_{M} and Y have already been determined in the preceding procedures of **(3)** and **(4)**

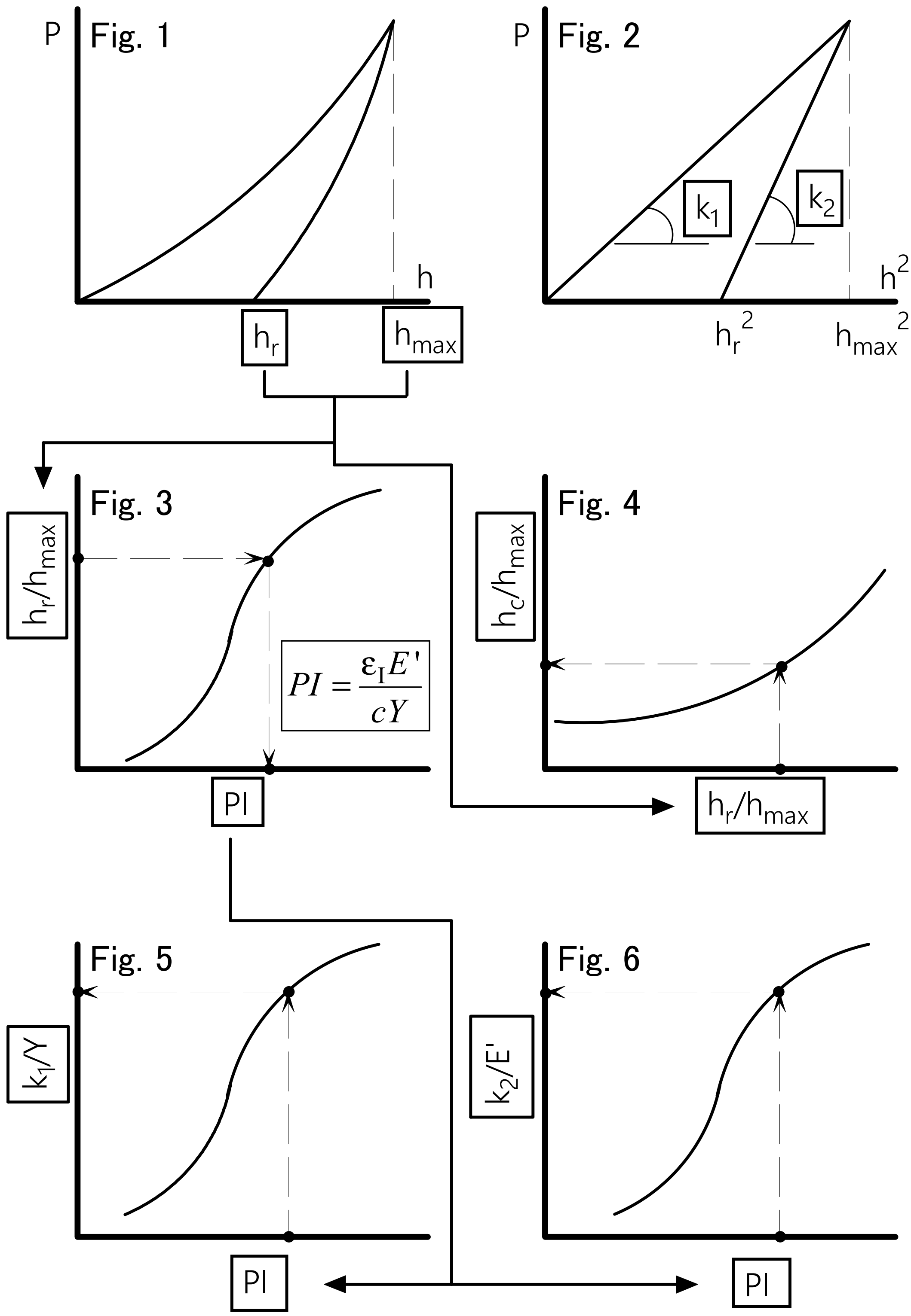

Figure 11.8 Flow chart for determining the elastoplastic characteristics from the P - h hysteresis obtained in experiment

(3) Experimental determination of viscoelastic functions

As discussed in Chap. 7, without measuring the indentation contact area $A(t)$ in a quantitative manner, it is impossible for us to obtain any of viscoelastic functions such as the stress relaxation modulus $E'_{\text{relax}}(t)$ and the creep compliance function $C'_{\text{creep}}(t)$. In the conventional instrumented indenters, however, we have to *estimate* the time-dependent contact area $A(t)$ from the penetration depth $h(t)$ observed in experiment through the assumption/approximation, resulting in the very *qualitative* viscoelastic functions, not the *quantitative* material characteristics.

As emphasized in the preceding sections, due to the luck of geometrical similarity, the indentation strain ε_{I} of spherical or flat-ended cylindrical indenter is dependent on the penetration depth or the contact area. This fact results in undesirable complexity for analyzing the time-dependent viscoelastic characteristics. To circumvent this difficulty, we make the viscoelastic analysis only for *conical/pyramidal indentation contact* in this section like as the considerations we made in Chap. 7; the viscoelastic constitutive equations for conical indentation given in Chap. 7 (see Eq. (7.3)) are

$$
\begin{aligned}
P(t) &= \frac{\tan\beta}{2}\int_0^t E'_{\text{relax}}(t-t')\frac{dA(t')}{dt'}dt' \\
A(t) &= 2\cot\beta\int_0^t C'_{\text{creep}}(t-t')\frac{dP(t')}{dt'}dt'
\end{aligned}
\tag{11.6}
$$

Equation (11.6) alternatively represented in terms of the penetration depth $h(t)$ is given as follows;

$$
\begin{aligned}
P(t) &= \frac{\pi\cot\beta}{2}\int_0^t E'_{\text{relax}}(t-t')\frac{d\left\{\eta_{\text{c}}^2(t')h^2(t')\right\}}{dt'}dt' \\
\eta_{\text{c}}^2(t)h^2(t) &= \frac{2\tan\beta}{\pi}\int_0^t C'_{\text{creep}}(t-t')\frac{dP(t')}{dt'}dt'
\end{aligned}
\tag{11.7}
$$

in which the relative contact depth of penetration $\eta_{\text{c}}(t)$ is defined by $\eta_{\text{c}}(t) = h_{\text{c}}(t)/h(t)$. The $\eta_{\text{c}}(t)$ -value of a *perfectly elastic* body is always time-independent having the value of $\eta_{\text{c}} = 2/\pi$ (refer to Eq. (3.28)). Furthermore, η_{c} for *elastoplastic* indentation is also time-independent material characteristic as shown in Eq. (10.8) and in Fig. 10.10. On the other hand, as seen in Eq. (11.7) even for conical indentation contact, we have to take into account *the time-dependent nature of $\eta_c(t)$ for viscoelastic indentation contact*. The time-dependent $\eta_c(t)$-values are shown in Fig. 11.9, by way of example, under the step-wise penetration of $h(t) \equiv 3$ μm ($t \ge 0$) for the Vickers/Berkovich-equivalent cone indented on the viscoelastic Maxwell liquids having various values of their Poisson's ratios ($\nu(0) =$ 0.1, 0.3, and 0.5) (FEA-based numerical results). The $\eta_c(t)$-value of the incompressible viscoelastic body with $\nu(0) = 0.5$ is always time-independent ($\eta_c = 2/\pi$) like as a perfectly elastic body, while for the viscoelastic liquids with $\nu(0) < 0.5$, $\eta_c(t)$ monotonically increases along with the load relaxation, though the applied penetration is kept constant of $h(t) \equiv 3$ μm in a step-wise manner. This fact implies that *the free-surface outside the contact area creeps-up during load relaxation*.

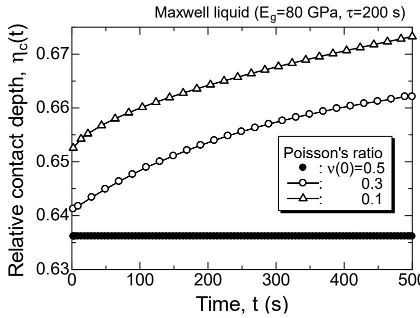

Figure 11.9 Poisson effect on the time-dependent relative contact depth $\eta_c(t)$ for the Maxwell liquid with the relaxation modulus:

$$E_{\mathrm{relx}}(t) = E_g \exp(-t/\tau)$$

(E_g =80GPa, τ =200s) *under a step-wise penetration* (numerical FEA-results)

We can neither measure the time-dependent $h_c(t)$ nor determine $\eta_c(t)$ in experiments on the conventional instrumented indenter. We have therefore no choice but to simply assume the *time-independent elastic value* of $\eta_c(t) \equiv 2/\pi$ in Eq. (11.7), leading to the following *approximated* viscoelastic constitutive equations;

$$\begin{aligned} P(t) &= \frac{2\cot\beta}{\pi}\int_0^t E'_{\mathrm{relax}}(t-t')\frac{d\{h^2(t')\}}{dt'}dt' \\ h^2(t) &= \frac{\pi\tan\beta}{2}\int_0^t C'_{\mathrm{creep}}(t-t')\frac{dP(t')}{dt'}dt' \end{aligned} \tag{11.8}$$

(i) Step-wise penetration test

In Eq. (11.8), the indentation load relaxation $P(t)$ observed under the step-wise penetration to h_0

$$h(t) = h_0 u(t), \tag{11.9}$$

is related to the relaxation modulus $E'_{\mathrm{relax}}(t)$ as follows,

$$P(t) = \frac{2h_0^2\cot\beta}{\pi}E'_{\mathrm{relax}}(t), \tag{11.10}$$

while under the step-wise loading to P_0

$$P(t) = P_0 u(t), \tag{11.11}$$

the resultant creeping penetration depth $h(t)$ is related to the creep compliance function $C'_{\mathrm{creep}}(t)$ in the following equation;

$$h^2(t) = \frac{\pi P_0 \tan\beta}{2} C'_{\mathrm{creep}}(t) \tag{11.12}$$

We can, therefore, determine the relaxation modulus $E'_{\mathrm{relax}}(t)$ from the relaxation load $P(t)$ and the creep function $C'_{\mathrm{creep}}(t)$ from the creeping penetration $h^2(t)$ in these step-wise penetration tests. In addition to neglecting the time-dependent nature of $\eta_{\mathrm{c}}(t)$ in deriving Eq. (11.8), it must be noticed in this context that the frame compliance C_{f} of the instrumented apparatus inevitably induces the creeping penetration $h(t)$ during the load relaxation $P(t)$ *even for the stepwise penetration to* h_0;

$$h(t) = h_0 - C_{\mathrm{f}} P(t) \tag{11.13}$$

This frame-compliance effect implies that *the relaxation time* τ *is always significantly overestimated*, resulting in an undesirable *estimate of the relaxation modulus* $E'_{\mathrm{relax}}(t)$ in Eq. (11.10). On the other hand, for step-wise loading of $P(t) = P_0 u(t)$ as well as for constant-rate of penetration $h(t) = k_h \cdot t$ or $P(t) = k_P \cdot t$, as will be discussed in the subsequent section, we do not need to take care of the complexity and the difficulty associated with the frame compliance due to *their indentation tests without load relaxation*, *i.e.*, $P(t) \geq P(0)$. Even for the viscoelastic deformations without load relaxation, however, it must be noticed the fact that *there exist crucial difficulties in the reliability and the accuracy of the viscoelastic functions estimated through using Eq. (11.8), because it has been derived by making a fatal assumption of the time-independent* $\eta_{\mathrm{c}}(t)(\equiv 2/\pi)$.

(ii) Constant-rate of penetration test

The application of Eq. (11.8), i.e., Eq. (11.7) with $\eta_{\mathrm{c}}(t)(\equiv 2/\pi)$, to the constant-rate of penetration test

$$h(t') = k_h t' \tag{11.14}$$

and to the constant loading test

$$P(t') = k_P t' \tag{11.15}$$

leads to the following viscoelastic constitutive equations, respectively;

$$\begin{aligned} P(t) &= \frac{4k_h^2 \cot\beta}{\pi} \int_0^t E'_{\mathrm{relax}}(t-t')t'dt' \\ h^2(t) &= \frac{\pi k_P \tan\beta}{2} \int_0^t C'_{\mathrm{creep}}(t-t')dt' \end{aligned} \tag{11.16}$$

Once we apply the Laplace transform and its inversion to Eq. (11.16), we finally have the following formulae of the relaxation modulus and the creep compliance function;

$$
\begin{aligned}
E'_{\mathrm{relax}}(t) &= \frac{\pi \tan\beta}{4{k_h}^2}\frac{d^2P(t)}{dt^2} \\
C'_{\mathrm{creep}}(t) &= \frac{2\cot\beta}{\pi k_P}\frac{d\left\{h^2(t)\right\}}{dt}
\end{aligned}
\qquad (11.17)
$$

We can, therefore, readily determine these viscoelastic functions in terms of the time-dependent indentation load $P(t)$ and the penetration depth $h^2(t)$ observed in experiments.

11.3 INSTRUMENTED INDENTATION MICROSCOPE

We have repeatedly emphasized the key roles of the indentation contact mechanics in the micro/nano materials science for studying the materials characteristics (elastic, elastoplastic, viscoelastic characteristics). We have also emphasized the importance of *the indentation contact area* A induced by the applied indentation load P, or the interrelation of *the applied contact area* A to the resultant indentation load P (see in Chaps. 4 ~ 9). As described in Sec. 11.2, however, it is impossible for us to measure the contact area A in the conventional instrumented indentation apparatuses, although we can measure the penetration depth h in a quantitative manner. In these conventional test apparatuses, therefore, we have to determine the mechanical characteristics through making appropriate assumptions/approximations to estimate the contact area A from the penetration depth h observed in experiments. On the other hand, upon *using the instrumented indentation microscope, we can easily measure the contact area* A *as a function of the indentation load* P *and/or of the penetration depth* h, then *readily determine the mechanical characteristics without relying on any of undesirable assumptions/approximations*.

(1) Basic configuration of the apparatus and the principle of measuring the contact area [11.7 - 11.9]

The basic configuration of the instrumented indentation microscope is depicted in Fig. 11.10. The optical image of the contact area A measured at the contact interface is stored into a personal computer as the digital data through an optical microscope combined to a CCD camera. In Fig. 11.11, shown are the schematic details of (a) the dark field and (b) the bright field microscopies that are utilized in the indentation microscope. As shown in these figures, not only the inlet but also the outlet beams must be transferred through the indenter, indicating that the indenter must be transparent for the beams. In this context, the conventional *diamond indenter* is always applicable to the indentation test in air, i.e., in oxidative environments under 300°C, while an indenter made of *sapphire* is the most appropriate at temperatures in 300°C~1200°C. The test specimen shown in Fig. 11.10 is lifted up to the indenter fixed to the test frame. The indentation load P is measured by the load cell that is arranged in series beneath the specimen, and the penetration depth h is monitored by a displacement sensor (a linear transducer or a capacitance sensor). All of the mechanical characteristics can be readily determined in a quantitative manner once we get the contact area A as a function of the applied load P on this instrumented indentation microscope, implying no need of monitoring the penetration depth h, the details of which will be discussed in the following section. The penetration depth sensor equipped in the indentation microscope, however, is required in order to confirm the consistency of the P - h relation to that of the conventional instrumented indentation apparatuses. It must be noticed furthermore that we do not need to take into account the effect of the frame compliance C_f (refer to Sec. 11.2(1)), since all the mechanical characteristics are quantitatively determined from the P - A relation directly observed on the instrumented indentation microscope.

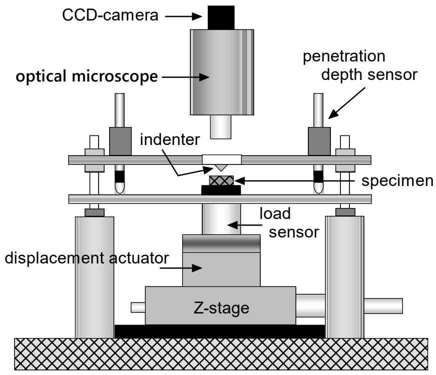

Figure 11.10 Basic configuration of the instrumented indentation microscope

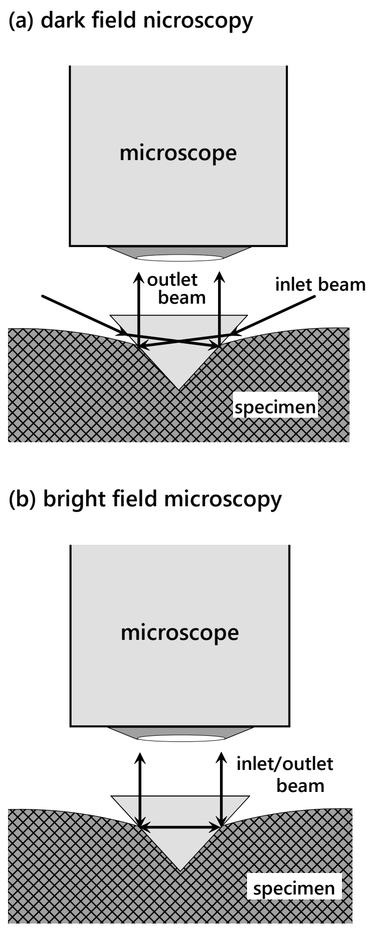

Figure 11.11 The inlet/outlet beams to monitor the indentation contact images: (a) dark field microscopy, (b) bright field microscopy

＊＊＊＊＊＊＊＊＊＊＊＊＊＊＊＊＊＊＊＊＊

[11.7] T. Miyajima, M. Sakai, *Phil. Mag*, **86[33-35]**, 5729 (2006)
[11.8] M. Sakai, N. Hakiri, T. Miyajima, *J. Mater. Res*., **21[9]**, 2298 (2006)
[11.9] N. Hakiri, A. Matsuda, M. Sakai, J. Mater. Res., **24[6]**, 1950(2009)

The optical image of contact area A is digitized and stored in a personal computer as the binary image in relations to the scanning time, indentation load and the penetration depth. An example of the optical image (bright-field image) and its digitized binary image is shown in Fig. 11.12 for Berkovich indentation onto a polycarbonate resin. In the instrumented indentation microscope, it is also possible for us to control the contact area A applied to the test specimen as a function of scanning time by feeding these digital date back to the displacement actuator; in time-dependent viscoelastic indentation tests, by way of example, we can conduct the indentation tests not only for applying a constant-rate contact area to the specimen ($A(t) = k_A \cdot t$), but also for a step-wise penetration to a constant contact area ($A(t) = A_0 u(t)$), leading to the quantitative determination of the stress relaxation modulus and the creep compliance function, the details of which have already been given in Chap. 7 .

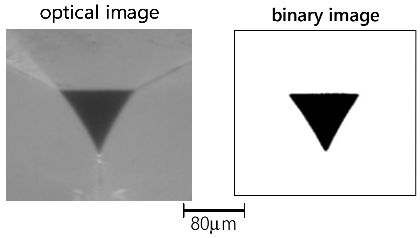

Figure 11.12 Optical and its binary images of the contact area of a Berkovich indenter pressed onto a polycarbonate resin

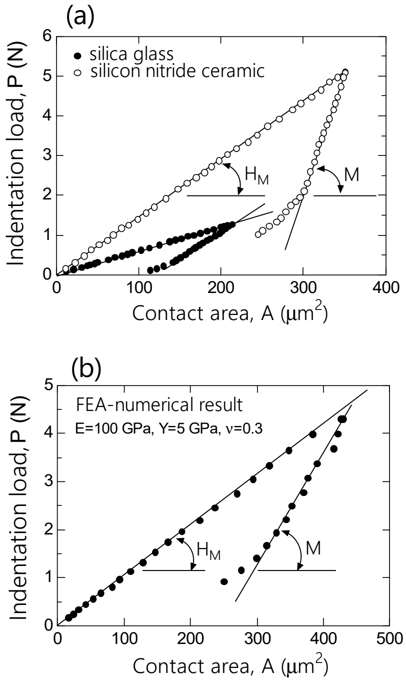

Figure 11.13

(a) Loading-unloading P - A linear relations of silica glass and silicon nitride ceramic observed on the instrumented indentation microscope (Vickers indentation)

(b) FEA-based numerical result of an elastoplastic body ($E' = 100$ GPa, $Y = 5$ GPa) for Vickers/ Berkovich equivalent con indentation

(2) Determination of elastoplastic characteristics

We can *quantitatively* determine the elastoplastic characteristics such as the Meyer hardness H_M, elastic modulus E' and the yield stress Y in the instrumented indentation microscope through analyzing the loading-unloading hysteresis relation of the indentation load P and the contact area A, i.e., the P - A hysteresis relation *without making any assumptions and approximations.* The loading-unloading P - A hysteresis relations are shown in Fig 11.13(a) for the Vickers indentation test results of silica glass and silicon nitride ceramic, and in Fig. 11.13(b) for the FEA-based numerical result of an elastoplastic body indented by the Vickers/Berkovich-equivalent cone. As clearly shown in these figures, not only the loading but also the unloading P - A relations are linear. The slope of the loading line gives the Meyer hardness itself (see Eq. (5.1b)), while the unloading slope $M\left(\equiv \varepsilon_I E'\right)$ (the unloading modulus) is directly related to the elastic modulus E';

$$M = \frac{\tan\beta}{2} E' \tag{11.18}$$

where use has been made of the indentation strain of $\varepsilon_I = \tan\beta/2$ for pyramid/cone indentation. We can, therefore, readily determine the elastic modulus E' from the unloading modulus M observed on the indentation microscope. Furthermore, "*the additivity principle of the excluded volume of indentation*" (see Eqs. (5.13a) and (5.14) in Chap. 5), leads to the following formula of cone/pyramid indentation;

$$\frac{1}{(cY)^{3/2}} = \frac{1}{{H_{\mathrm{M}}}^{3/2}} - \frac{1}{M^{3/2}} \tag{11.19}$$

Substituting the Meyer hardness H_{M} and the unloading modulus M thus directly determined from the loading/unloading slopes of the linear P - A relations into the right-hand side of Eq. (11.19), we finally obtain the yield stress cY, and then the plastic index PI as a measure of plasticity (refer to Chap. 5)

$$PI\left(\equiv \varepsilon_I E'/cY\right) = M/cY \tag{11.20}$$

is readily fixed in terms of M and cY in experiment by the use of the instrumented indentation microscope.

(3) Determination of viscoelastic functions [7.5]

The viscoelastic constitutive equation in terms of the contact area for cone/pyramid indentation is described by

$$A_{\mathrm{ve}}(t)^{3/2} = A(t)^{3/2} - A_{\mathrm{p}}(t)^{3/2} \tag{11.21}$$

through applying *the elastic-to-viscoelastic corresponding principle* (see Chap. 6) to Eq. (5.13a). Equation (11.21) implies, therefore, that we have to eliminate the plastic contribution of A_{p} from the contact area $A(t)$ observed on the instrumented indentation microscope prior to determining the viscoelastic contact area $A_{\mathrm{ve}}(t)$, and then the viscoelastic functions, as follows:

(1) Experimental determination of cY through the procedures given in the preceding section (2) using the *elastoplastic* P - A loading/unloading linear relations in the *higher-rate penetration test* (i.e., the time/rate-independent indentation test with invisible viscoelastic flow) , followed by

(2) Determination of the plastic contact area $A_{\mathrm{p}}(t)$ by substituting this cY -value into $A_{\mathrm{p}}(t) = P(t)/cY$, and then

(3) Determination of the viscoelastic contact area $A_{\mathrm{ve}}(t)$ by the uses of $P(t)$ and $A(t)$ both observed on the instrumented indentation microscope via the following relation derived from Eq. (11.21);

$$A_{\mathrm{ve}}(t) = \left\{ A(t)^{3/2} - \left[P(t)/cY\right]^{3/2} \right\}^{2/3} \tag{11.22}$$

(i) Step-wise penetration tests

Using the function of feed-back controlling of the instrumented indentation microscope, we can conduct the test of step-wise penetration to a constant contact area A_0, i.e., $A(t) = A_0 u(t)$, and then measure the resultant indentation load relaxation $P(t)$. The viscoelastic indentation contact area $A_{ve}(t)$ in this test is, therefore, given by

$$A_{ve}(t)(\equiv A_{ve}) = \left\{ A_0^{3/2} - \left[P(0)/cY \right]^{3/2} \right\}^{2/3} \qquad (11.23)$$

via Eq. (11.22). It must be noticed in Eq. (11.23) that $A_{ve}(t)(\equiv A_{ve})$ is time-independent, because the plastic contact area

$$A_p(t)\left[\left(\equiv A_p(0) \right) = P(0)/cY \right]$$

induced at the onset of the load relaxation $P(0)$ is time-independent constant due to the *irreversible nature of plastic flow*, although the viscose flow still results in the load relaxation under this step-wise penetration of $A(t) = A_0 u(t)$. Accordingly, substituting the $A_{ve}(t)$-value calculated in Eq. (11.23) combined with the observed load relaxation $P(t)$ into Eq. (7.6), we readily determined the stress relaxation modulus, as follows;

$$E'_{relax}(t) = 2\cot\beta \frac{P(t)}{A_{ve}} \qquad (11.24)$$

In step-wise loading to a constant indentation load P_0, i.e., $P(t) = P_0 u(t)$, the indentation contact area $A(t)$ observed on the indentation microscope increases with time in a monotonic manner resulting in a creep deformation. Accordingly, the creep compliance function $C'_{creep}(t)$ is determined in experiment by substituting the viscoelastic contact area $A_{ve}(t) = \left\{ A(t)^{3/2} - \left[P_0/cY \right]^{3/2} \right\}^{2/3}$ into Eq. (7.6);

$$C'_{creep}(t) = \frac{\tan\beta}{2} \frac{A_{ve}(t)}{P_0} \qquad (11.25)$$

The creep compliance $C'_{creep}(t)$ of an amorphous selenium (Se) at its glass-transition temperature ($T_g = 30.0^\circ$ C)) determined on the indentation microscope is plotted against time in Fig. 11.14 for a Berkovich indentation, where demonstrated are both the compliance

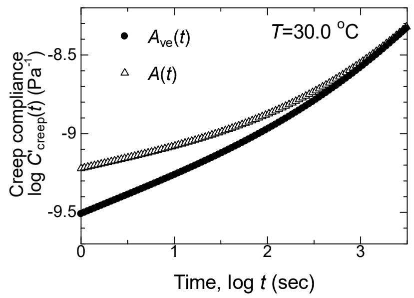

Figure 11.14 Creep compliance function of an amorphous selenium at $T = 30.0^\circ$ C for Berkovich indentation in step-wise loading to a constant load P_0, i.e., $P(t) = P_0 u(t)$.

To demonstrate the effect of the plastic deformation, the creep compliance functions determined from the viscoelastic contact area $A_{ve}(t)$ with plastic correction ($A_p(t) = P_0/cY$) (the closed circles, ●) and from the observed contact area $A(t)$ without plastic correction (the open triangles, △) are plotted against time. Both of the creep functions represent an asymptotic coincidence in the long-time region since the plastic deformation induced at the onset of the step-wise loading becomes relatively insignificant with the increase in the viscoelastic creep under viscus flow functions determined from the viscoelastic contact area $A_{\mathrm{ve}}(t)$ with plastic correction (the closed circles) and from the observed contact area $A(t)$ without plastic correction (the open triangles) for comparison.

(ii) Constant-rate of loading test

In constant-rate of loading test, the contact area $A(t)$ combined with the applied indentation load $P(t) = k_P \cdot t$ gives the viscoelastic contact area $A_{\mathrm{ve}}(t)$ via the relation of

$$A_{\mathrm{ve}}(t) = \left\{ A(t)^{3/2} - \left(k_P \cdot t / cY\right)^{3/2} \right\}^{2/3}$$

for cone/pyramid indentation. Substituting this viscoelastic contact area into the second formula of Eq. (11.6) leads to the creep compliance function, as follows;

$$C'_{\mathrm{creep}}(t) = \frac{\tan\beta}{2k_P} \frac{dA_{\mathrm{ve}}(t)}{dt} \tag{11.26}$$

Equation (11.26) indicates that we can readily determine the creep compliance function through the time-derivative of the viscoelastic contact area $A_{\mathrm{ve}}(t)$ that has been determined by eliminating the plastic contribution from the contact area $A(t)$ observed on the indentation microscope.

(iii) General-purpose indentation tests

The “step-wise penetration to a constant contact area” and/or the “constant-rate of loading” are the most appropriate and well recommended in the conventional viscoelastic indentation tests, since we can quantitatively eliminate the undesirable plastic contribution to the viscoelastic deformation and flow, leading to readily determine the viscoelastic functions without any approximations/assumptions, as mentioned in the preceding sections **(i)** and **(ii)**. On the other hand, in more general-purpose indentation test, we face on several mathematical difficulties in applying the observed data to Eq. (11.6) for determining the viscoelastic functions in an *analytical manner*. However, we can circumvent these difficulties through the *numerical approach* via using personal computers (PCs) that have made a remarkable breakthrough since the end of 20$^{\text{th}}$ century. We can easily determine the viscoelastic functions *in numerical manners* by the use of PCs even for rather complicated viscoelastic/viscoplastic stimulus-response phenomena in indentation contact problems.

The basic protocols for determining the viscoelastic functions are given as follows through the numerical analyses of the observed $P(t)$ vs. $A(t)$ relation:

First of all, the application of Laplace transform to the viscoelastic constitutive equation (7.3) leads to the following viscoelastic functions in the Laplace space

$$\begin{aligned} \bar{E}'_{\mathrm{relax}}(p) &= 2\cot\beta \frac{\bar{P}(p)}{p\bar{A}_{\mathrm{ve}}(p)} \\ \bar{C}'_{\mathrm{creep}}(p) &= \frac{\tan\beta}{2}\frac{\bar{A}_{\mathrm{ve}}(p)}{p\bar{P}(p)} \end{aligned} \tag{11.27}$$

In advance of conducting these Laplace transforms, we have to calculate the viscoelastic contact area $A_{\mathrm{ve}}(t)$ by applying the observed $P(t)$ and $A(t)$ into Eq. (11.22), and then represent these $P(t)$ and $A_{\mathrm{ve}}(t)$ in their Prony series expansions (refer to the table given below) respectively, followed by their Laplace transforms of $\bar{P}(p)$ and $\bar{A}_{\mathrm{ve}}(p)$, leading to $\bar{E}'_{\mathrm{relax}}(p)$ and $\bar{C}'_{\mathrm{creep}}(p)$ in Eq. (11.27). The viscoelastic functions $\bar{E}'_{\mathrm{relax}}(p)$ and $\bar{C}'_{\mathrm{creep}}(p)$ are, therefore, finally given by making their Laplace transform inversions. These numerical procedures for determining the viscoelastic functions are summarized in the following table, where we focus only on the stress relaxation modulus $E'_{\mathrm{relax}}(t)$, as an example. Similar procedures are also applicable to deriving the creep compliance function $C'_{\mathrm{creep}}(t)$. It must be noticed, furthermore, that we can also derive the creep function from the stress relaxation modulus by the use of the convolution integral (Eq. (7.2)) in its Laplace space;

$$p\bar{C}'_{\mathrm{creep}}(p) = 1/p\bar{E}'_{\mathrm{relax}}(p) \tag{11.28}$$

【Numerical analyses for determining the viscoelastic functions】

(1) Determination of the yield stress cY in Eq. (11.19) in terms of the Meyer hardness H_{M} and the unloading modulus M using the slopes of the loading/unloading P - A linear plot (see Fig. 11.13) in the *time-independent elastoplastic regime* through conducting a higher-rate indentation test.

(2) Determination of $A_{\mathrm{ve}}(t)$ by substituting the observed $P(t)$ - $A(t)$ relation combined with the cY - value into Eq. (11.22), where $P(t)$ must be fixed to $P(0)$ in the *load-relaxation test* whenever the load $P(t)$ at time t is smaller than that at the onset of the relaxation, *i.e.,* $P(t) \le P(0)$ (refer to the details given in Sec. **(i)**).

(3) Description of $P(t)$ and $A_{\mathrm{ve}}(t)$ in their Prony series expansions using the collocation method;

$$\begin{aligned} P(t) &= P_{\mathrm{e}} + \sum_{i=1}^{n} P_i \exp\left(-t / \lambda_{1i}\right) \\ A_{\mathrm{ve}}(t) &= A_{\mathrm{e}} + \sum_{i=1}^{n} A_i \exp\left(-t / \lambda_{2i}\right) \end{aligned} \qquad (11.29)$$

(4) Substitution of the Laplace transform of Eq. (11.29),

$$\begin{aligned} \overline{P}(p) &= \frac{P_{\mathrm{e}}}{p} + \sum_{i=1}^{n} \frac{P_i}{p + 1/\lambda_{1i}} \\ \overline{A}_{\mathrm{ve}}(p) &= \frac{A_{\mathrm{e}}}{p} + \sum_{i=1}^{n} \frac{A_i}{p + 1/\lambda_{2i}} \end{aligned} , \qquad (11.30)$$

into Eq. (11.27) in order to describe $\overline{E}'_{\mathrm{relax}}(p)$ in the following formula by the use of collocation method;

$$\overline{E}'_{\mathrm{relax}}(p) = \frac{E_{\mathrm{e}}}{p} + \sum_{i=1}^{n} \frac{E_i}{p + 1/\tau_i} \qquad (11.31)$$

(5) Laplace transform inversion of Eq. (11.31) finally results in the stress relaxation modulus;

$$E'_{\mathrm{relax}}(t) = E_{\mathrm{e}} + \sum_{i=1}^{n} E_i \exp\left(-t / \tau_i\right) \qquad (11.32)$$

MATERIALS PHYSICS BASED ON THE EXPERIMENTAL DATA OF INSTRUMENTED INDENTATION TESTING

CHAPTER 12

12.1 THE EFFECT OF TIP-GEOMETRY OF PYRAMIDAL INDENTATION ON THE CONTACT BEHAVIOR [12.1]

The most favorable feature of pyramidal/conical indentation is in its geometrical similarity, resulting in the penetration-depth-independent mechanical characteristics such as the Meyer hardness, elastic modulus, and the viscoelastic functions observed in instrumented indentation testing, unlike the penetration-depth-dependent characteristics of spherical indentation. On the other hand, however, there exists a minor demerit resulted from the geometrical discontinuity at the pyramidal edges that leads to the mathematical complexity in analyzing the indentation contact mechanics. This is the reason why we have exclusively adopted in the preceding chapters the *Vickers/Berkovich equivalent cone indenter* in order to circumvent the pyramidal edge-related difficulties.

In this section, based on the experimental examinations, we discuss the effect of the tip-geometry of *the conventional pyramidal indenters* on the indentation contact behavior of the several engineering materials; the indenters examined include the conventional pyramid indenters (the tetrahedral Vickers, trihedral Berkovich (see Fig. 11.1), tetrahedral pyramid indenters with various values of the inclined face angle β, and the Knoop indenter shown in Fig. 12.1. The Knoop indenter has widely been utilized in the fields of crystallography and mineralogy since its anisotropic tip-geometry is appropriate for examining the crystallographic orientation.

Figure 12.2 shows the $P-h$ loading/unloading hysteresis curves of a silicon nitride ceramic for the Vickers/Berkovich/Knoop indentations. As readily seen in Fig. 12.2, the loading/unloading hysteresis curve of the Berkovich indentation coincides well with that of the Vickers indentation, because the index of projected area g of the Berkovich indenter

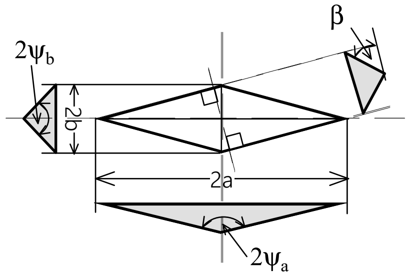

Figure 12.1 Tip-geometry of the Knoop indenter:

- Ratio of major/minor axes; $a/b = 7.11$
- Inclined face-angle; $\beta = 25.2^{\circ}$
- Diagonal apex angles; $2\psi_a = 172.5^{\circ}$ and $2\psi_b = 130^{\circ}$ for major/minor axes

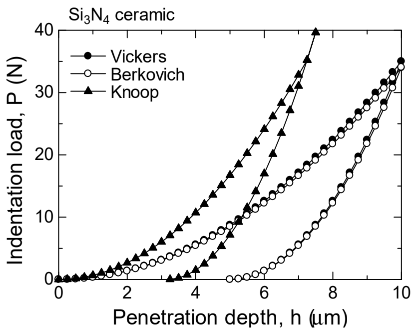

Figure 12.2 Effect of the tip-geometry of the conventional pyramidal indenters on the $P-h$ loading/unloading hysteresis of silicon nitride ceramic;

● : Vickers indenter
○ : Berkovich indenter
▲ : Knoop indenter

[12.1] J. Zhang, M. Sakai, *Mater. Sci. Eng. A*:**381**, 62 (2004)

($g = 3\sqrt{3}\cot^2\beta = 24.5$) is design to coincide with the value of the Vickers indenter ($g = 4\cot^2\beta$ =24.5), resulting in the same values of their induced contact area ($A = gh^2$) and the excluded volume ($V = gh^3/3$) for a given penetration depth h , the details of which have already been mentioned in Sec. 11.1. The good coincidence of the Vickers/Berkovich indentations shown in Fig. 12.2 means that the indentation contact responses are equivalent both for the Vickers/Berkovich indentations, implying the insignificant "*edge-effect*" of the trigonal and the tetragonal pyramids. On the other hand for Knoop indentation, its g -value $(= 2\tan\psi_a \cdot \tan\psi_b = 65.4)$ is 2.7 times larger than the value of the Vickers/Berkovich indentation, resulting in its $P-h$ loading/unloading hysteresis curve much steeper than that of Vickers/ Berkovich indentation, as demonstrated in Fig. 12.2. Furthermore, the loop energy U_r (refer to Sec. 5.2) of the $P-h$ loading/unloading hysteresis curve of the Knoop indentation and its normalized residual depth $\xi_r \,(= h_r/h_{max})$ are significantly smaller than those of Vickers/ Berkovich indentations, indicating that the elastoplastic response of Knoop indentation is *more elastic* than those of Vickers/ Berkovich indentations.

Since the inclined face-angel β_c of the Vickers/Berkovich *equivalent cone* is 19.7° (see Chap. 5), while the face-angle of the *equivalent cone* of Knoop indenter is $\beta_c = 12.4^{\circ}$ (the subscript c of the face-angle β in these context indicates the *equivalent cone*). This fact leads to more elastic Knoop contact than that of Vickers/Berkovich, the details of which is given in the following considerations.

The face-angle-dependence of the elastoplastic responses (the $P-h$ loading/unloading hysteresis curves) of a silicon nitride ceramic is shown in Fig. 12.3 for the tetragonal indenters with various values of their face-angle ($\beta = 10^{\circ}$, $\beta = 22^{\circ}$ (Vickers indenter), and $\beta = 40^{\circ}$); the g -values ($= 4\cot^2\beta$) of these indenters are, respectively, 129, 24.5 (Vickers indenter), and 5.68, and then the corresponding face-angles of their *equivalent cone* are, respectively, β_c = 8.87°, 19.7°, and 36.6°. As well recognized in Fig. 12.3, the indentation contact responses *become more plastic along with the increase in the inclined-face angle*, i.e., *along with the pyramid-tip becoming shaper*. This fact is resulted from the increase in the plastic index ($PI = \varepsilon_I E'/cY$; $\varepsilon_I = \tan\beta/2$) with the

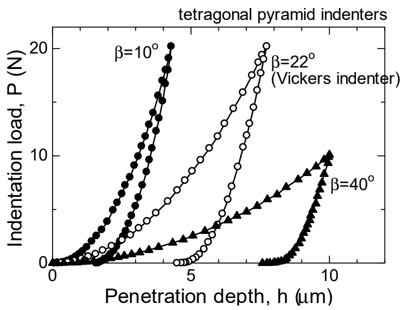

Figure 12.3 Loading/unloading $P-h$ hysteresis curves of a silicon nitride ceramic for the tetragonal pyramid indenters with their inclined face-angles; $\beta = 10^{\circ}$ (●), $\beta = 22^{\circ}$ (Vickers)(○), and $\beta = 40^{\circ}$ (▲)

increase in the face angle β (refer to Sec. 5.1).

The Meyer hardness H_M of a silicon nitride ceramic determined in experiments for the pyramid indenters with various values of their incline-face angle is plotted in Fig. 12.4 against their equivalent cone angle β_c (these indenters have their tip geometry of *regular* tetrahedral pyramid except the Knoop indenter). As shown in Fig. 12.4, the Meyer hardness is uniquely represented by the use of the equivalent-cone angle β_c even for *the Knoop indenter having its highly anisotropic tip-geometry*.

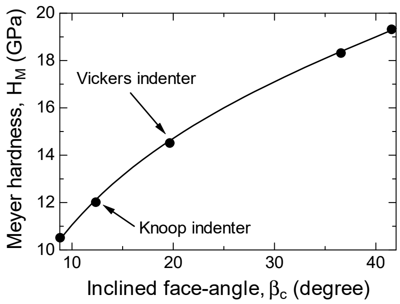

Figure 12.4 Meyer hardness of a silicon nitride ceramic determined in experiments for tetrahedral pyramid indenters. The solid line is the analytical prediction (Eq. (5.14) with m=3/2)

12.2 INDENTATION CONTACT MECHANICS OF ENGINEERING MATERIALS

In this section, we discuss the instrumented indentation testing and the indentation contact mechanics/physics of engineering materials ranging from ductile metals to brittle ceramics by the uses of the test results obtained on the conventional instrumented indenter and/or the instrumented indentation microscope. The mechanical characteristics of the engineering materials demonstrated in this section will play important roles not only in designing the microstructures of materials, but also in scrutinizing the reliability/accuracy of the instrumented indentation apparatuses.

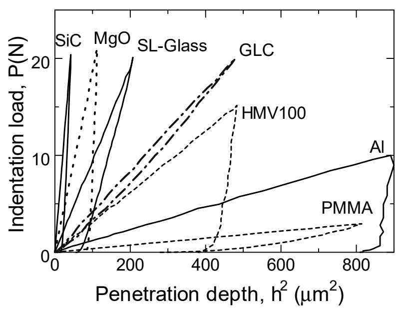

Figure 12.5 $P-h^2$ hysteresis curves for the Vickers loading/unloading indentation:

SiC: silicon carbide
MgO: magnesia
SL-Glass: soda-lime glass
GLC: glassy carbon (GL-200H)
HMV100: copper/zinc alloy (Vickers hardness standard; HV=1GPa)
Al: metallic aluminum (99% pure)
PMMA: methyl methacrylate resin

(1) Loading/unloading $P-h$ hysteresis curve and the elastoplastic characteristics [12.2]

The loading/unloading $P-h$ hysteresis curves of the engineering materials indented by Vickers pyramid are plotted in Fig. 12.5 (the $P-h^2$ plots discussed in Secs. 5.2, 10.3, and 11.2). It is readily seen that the hysteresis loop energy U_r of the ductile metal (aluminum, Al) is very significant comparing to that of the brittle ceramic such as silicon nitride ceramic (SiC). Since the loop energy U_r stands for the energy dissipation associated with indentation-induced plastic flow (refer to Sec. 5.2), it plays an important role in characterizing the elasticity/plasticity of engineering materials, as clearly seen in Fig. 12.5.

The normalized residual depth of indentation-induced impression $\xi_r\left(=h_r/h_{max}\right)$ is also an important elastoplastic characteristic (there exists one-to-one correlation between ξ_r and the loop energy U_r;

[12.2] M. Sakai, Y. Nakano, *J. Mater. Res.*, **17[8]**, 2161 (2002) refer to Secs. 5.2 and 10.3), and easy to be determined in experiment without any undesirable complications that are required in calculating the area integral for determining U_r. The ξ_r-values are shown in Fig. 12.6 for the various types of engineering materials. Table 12.1 summarizes the elastoplastic characteristics of the engineering materials, in which the materials demonstrated in Figs. 12.5 and 12.6 are also included.

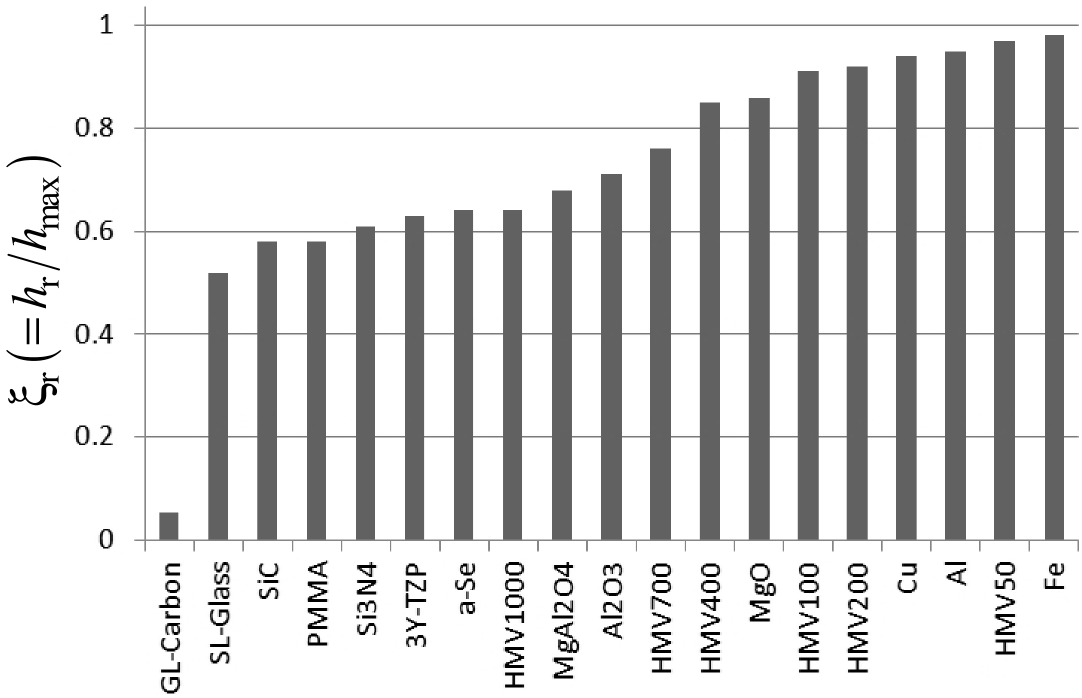

Figure 12.6 Normalized residual depth $\xi_r\left(=h_r/h_{max}\right)$ of indentation-induced impression of engineering materials; the loading and the unloading paths of a *perfectly elastic* material coincide with each other, resulting in $\xi_r = 0$, while the *perfectly plastic* body yields $\xi_r = 1$ due to none of elastic recovery in its unloading process. The details of the elastoplastic characteristics of these engineering materials are summarized in Table 12.1.

Table 12.1 Material characteristics of engineering materials

material	density d (g/cm^3)	Young's modulus E (GPa)	Poisson's ratio (-)	Meyer hardness H_M (GPa)	k_1 * (100 GPa)	ξ_r (h_r/h_{max})
alumina (Al2O3)	3.94	410	0.24	15.5	3	0.71
spinel (MgAl2O4)	3.54	289	0.28	13.4	2.53	0.68
magnesia (MgO)	3.56	310	0.2	5.95	1.75	0.86
partially stabilized zirconia (3Y-TZP)	6.05	212	0.32	14.8	3.13	0.63
silicon carbide (SiC)	3.22	420	0.18	16.3	4.58	0.58
silicon nitride (Si3N4)	3.22	310	0.23	11.8	3.28	0.61
soda-lime glass (SL=Glass)	2.51	74.5	0.23	4.34	0.94	0.52
glassy carbon (GL-Carbon) (GL200H)	1.5	28.7	0.15	1.94	0.42	0.053
amorphous selenium (a-Se)	4.26	9.5	0.33	0.43	0.11	0.64
metallic aluminum (Al) (99% pure)	2.69	71.1	0.34	0.4	0.11	0.95
metallic copper (Cu) (99.9% pure)	8.88	124	0.35	1.02	0.26	0.94
metallic iron (Fe) (99.5%pure)	7.82	222	0.25	1.13	0.27	0.98
copper zinc alloy, HMV50 (hardness standard; HV=0.5GPa)	8.96	128	0.35	0.51	0.11	0.97
copper zinc alloy, HMV100 (HV=1GPa)	8.54	118	0.33	1.14	0.3	0.91
high-carbon chromium steel, HMV200 (hardness standard, HV=2GPa)	7.84	215	0.29	2.22	0.61	0.92
high-carbon chromium steel, HMV400 (HV=4GPa)	7.84	214	0.29	4.17	1.23	0.85
high-carbon chromium steel, HMV700 (HV=7GPa)	7.8	209	0.3	7.04	1.86	0.76
high-carbon chromium steel, HMV1000 (HV=10GPa)	7.82	208	0.29	9.93	2.23	0.64
methyl methacrylate resin (PMMA)	1.41	4.45	0.38	0.16	0.034	0.58

* k_1 : loading coefficient of pyramid indentation; $P = k_1 h^2$

k_2 : uloading coefficient of pyramid indentation; $P = k_2 (h - h_r)^2$

$\boxed{k_2 = k_1/(1-\xi_r)^2}$

It must be noticed in Figs. 12.5, 12.6, and Tab. 12.1 that the mechanical characteristics of the glassy carbon and the magnesia are very unique. The glassy carbon looks like a perfectly elastic body; the elastic recovery is very significant in its unloading process, leading to none of residual impression, $\xi_r \approx 0$. This very unique indentation contact behavior is resulted from its microstructure, the details of which will be discussed in the subsequent section. On the other hand, the contact behavior of magnesia is very ductile with $\xi_r = 0.86$ like a ductile metal as demonstrated in Fig. 12.6, although it is a ceramic. The *isotropic cubic crystallography* of magnesia results in such a very ductile nature. In general, however, the very *anisotropic crystallography* of most of ceramic materials leads to their brittleness, resulting in their ξ_r-values less than 0.7.

(2) Indentation-induced elastoplastic behavior of carbon materials

Most of organic materials are carbonized by heat-treatment at elevated temperatures, yielding various types of carbons with their unique microstructures depending on the chemical structures of these organic precursors. Carbon materials are categorized into the graphitizable carbon and the non-graphitizable carbon: The former is easily graphitized at the heat-treatment-temperatures (HTT) exceeding 1500°C, yielding *extensively developed graphite crystals* that lead to *significant plastic deformation* resulted from the prominent slippages along the graphite basal planes, while the latter is *rather brittle* even heat-treated at temperatures exceeding 2000°C due to the *spatially suppressed growth of graphite crystals in nano-regions*.

(a) Glassy carbon [12.3]

The significant brittleness of glassy carbon (Glass-Like Carbon; GLC) leads to engineering difficulties in its machining such as cutting/grinding. Due to the conchoidal appearance of its fracture surface like that of inorganic glasses, it is also referred to as "glassy" carbon, although the indentation contact behavior of GLC is totally different from that of inorganic glasses. Details of the indentation contact mechanics of GLC will be given in this section along with its nano-structure.

The specific brittleness of GLC is resulted from the *crystallographically disordered carbons* that are made by the pyrolysis of thermosetting polymers (phenol/ epoxy/cellulose resins) heat-treated at elevated temperatures (1000°C~2500°C). The microstructure of GLC contains a significant amount of "closed nano pores"; the porosity is 25~30 vol%, the pore diameter ranges from 0.5 to 5 nm, and the specific surface area of the nanopores is of the order of several hundred m^2/cm^3. All of the nanopores are essentially inaccessible to nitrogen gas; the respective nanopores are surrounded by the partition walls of hexagonal networks of carbon atoms.

In Fig. 12.7, the $P-h$ loading/unloading hysteresis curve of a GLC is given in comparison to that of a soda-lime glass (SLG); it should be noticed for the GLC that the unloading path goes closely back along its loading path to the origin of the $P-h$ curve with insignificant amount of energy dissipation (i.e., very small hysteresis loop energy, U_r) and without any residual indentation impression after complete unloading, unlike the SLG that leaves behind a well-defined residual indentation impression. The purely elastic deformation of nano-size partition walls surrounding the nanopores of GLC results in such a unique $P-h$

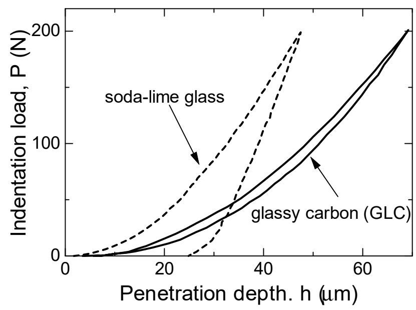

Figure 12.7
$P-h$ loading/unloading hysteresis curves of soda-lime glass (SLG) and glassy carbon (GLC)

[12.3] M. Sakai, H. Hanyu, M. Inagaki, *J. Am. Ceram. Soc.,* **78[4]**, 1006 (1995) loading/unloading hysteresis.

Scanning electron micrographs (SEM) of the residual indentation impressions for GLC and SLG made by Vickers indentation (P=98.1N) are shown in Fig. 12.8. As well illustrated in Fig 12.8 (c) of the SLG, the Vickers indentation usually results in two sets of median/radial cracks in the form of mutually perpendicular cracks in directions parallel to the pyramidal indentation diagonals. On the other hand, the most important feature of the indentation-induced surface damage patterns of the GLC is its *concentric ring cracks* (Fig. 12.8 (a)), which are very anomalous in brittle materials under a *sharp indenter* like the Vickers pyramid indenter. Furthermore, as clearly seen in Fig. 12.8 (b), a *well-defined cone crack* develops from one of the surface ring cracks. Such a well-developed cone crack induced by a sharp indenter has never been reported in other brittle ceramics, although a partially developed cone crack by Vickers indentation in fused silica glass has only been reported. These anomalous cone cracks of GLC and fused silica make an angle of about 30^o with the specimen surface, being significantly different from the Hertzian cone angle (about 22^o) usually made by a spherical indenter on brittle materials. These anomalous ring/cone cracks induced by a pyramid indenter are resulted from *the microscopically open structures* of GLC and fused silica; the nano-porous structure in the former and the three-dimensionally developed silica (SiO_2) chain networks in the latter.

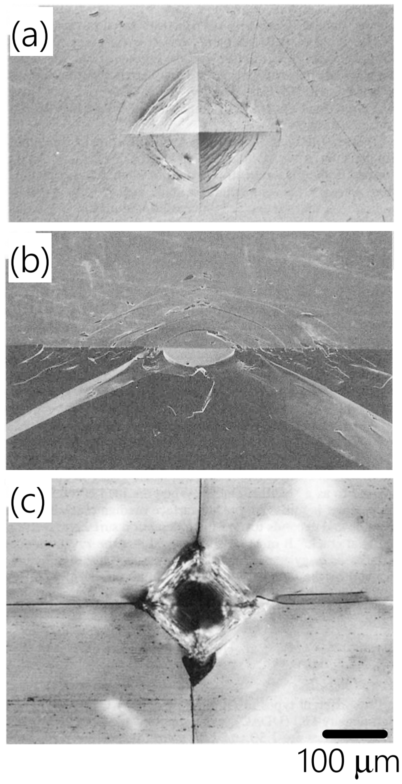

Figure 12.8 Scanning electron micrographs of the residual indentation impressions of GLC and SLG induced by a Vickers indentation (P=98.1N); (a) glassy carbon (GLC), (b) the in-surface ring/cone cracks of GLC, and (c) soda-lime glass (SLG)

(b) Polycrystalline graphite [12.4]

As mentioned above, due to its *non-graphitizable nature*, GLC is very brittle and hardly machining. On the other hand, polycrystalline graphites, that are referred to as the *graphitizable carbon*, are highly plastic/ductile and easily machining with high precision. They are extensively utilized not only as the graphite blocks of nuclear power reactors, but also as various types of engineering tools in semiconductor industries. Most of polycrystalline graphites are produced by baking molded green bodies [coal/petroleum-derived coke grains (several microns or less) bonded by pitch binder] at about 1000^{o}C, and then followed by graphitization at temperatures of 2000^{o}C~3000^{o}C.

Figure 12.9 shows the $P-h$ loading/unloading hysteresis curves of the isotropic carbon/graphite materials heat-treated at three different

[12.4] M. Sakai, Y. Nakano, S. Shimizu, *J. Am. Ceram. Soc.*, 86[6], 1522 (2002) temperatures. The carbon with HTT880 (Heat-Treatment-Temperature of 880°C) has its $P-h$ hysteresis curve similar to that of brittle ceramic, while the $P-h$ hysteresis is progressively enhanced with the increase in HTT, resulting in highly significant loop energy U_r, i.e., leading to significant amount of plastic energy dissipation in the loading/unloading processes. Since the HTTs exceeding 2000°C make highly developed graphite crystals, the very unique as well as the significant elastic recovery is observed in their indentation unloading paths due to the microscopic slippages along the hexagonal graphite basal planes. As actually demonstrated in Figs. 12.9 and 12.10, the residual depth of indentation impression $\xi_r\left(=h_r/h_{max}\right)$ progressively reduces to zero with the increase in HTT; *the carbon material with well-developed graphite structure leaves no residual indentation impression after complete unloading although the prominent* $P-h$ *hysteresis* is observed *in its indentation loading/unloading process*. As shown in Fig. 12.10, furthermore, the Meyer hardness H_M progressively decreases with HTT that is resulted from the enhanced plastic deformation associated with the development of graphite structures.

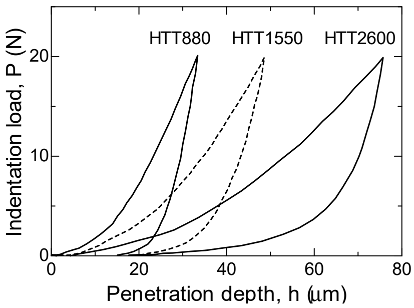

Figure 12.9 $P-h$ loading/unloading hysteresis curves of the isotropic carbons: their HTTs are 880°C, 1550°C, and 2600°C, respectively

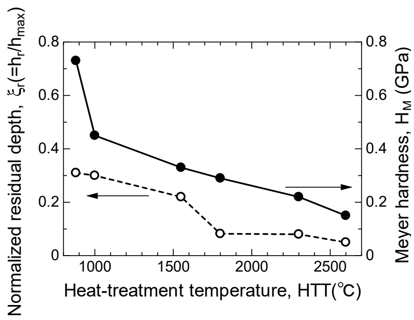

Figure 12.10 Normalized residual depth $\xi_r\left(=h_r/h_{max}\right)$ and Meyer hardness H_M of the polycrystalline carbon and graphite materials plotted against the heat-treatment temperature (HTT)

The well-defined residual indentation impression left behind on an ordinary elastoplastic body means that the dislocation-derived plastic flow is *irreversible*. In other words, the forwarded slip of dislocation in the indentation loading process is not fully recovered or only partially recovered in its unloading process, i.e., the slip of dislocation networks is always *irreversible* in the ordinary elastoplastic bodies. For the well-graphitized carbons as demonstrated in Figs. 12.9 and 12.10, on the other hand, the slip of dislocation networks on graphitic basal planes is *partially or fully reversible*, resulting in the disappearance of residual impression, i.e., $\xi_r \downarrow 0$ after complete unloading, though the significant plastic energy dissipation U_r is observed in its loading/unloading process. It may be easy for us to understand this reversible dislocation slippages once we notice the van der Waals forces acting on graphite basal planes. In order to further appreciate these reversible dislocation slippages observed in the well-graphitized carbon material, its $P-h^2$ hysteresis curves observed in the sequential "loading → unloading → reloading" indentation processes are shown in Fig. 12.11 along with those of a silicon nitride ceramic for comparison. It is worthwhile noticing for the silicon nitride ceramic that the reloading path coincides with its preceding unloading path, implying that the unloading and the subsequent loading behaviors is elastic, being a typical indentation unloading/reloading behavior of the ordinary elastoplastic materials. On the other hand, however, for the well graphitized carbon (HTT2300), there exists *a well-recognized as well as a very unique hysteresis loop along the unloading-to-reloading paths*. It must be also noticed that the significant *concaving* unloading $P-h^2$ path of the graphite material is very unique, by no means observed in the ordinary elastoplastic materials that have *linear unloading* $P-h^2$ paths like as that of the silicon nitride ceramic demonstrated in Fig. 12.11. These very unique indentation contact behaviors of well graphitized carbons are resulted from the *reversible dislocation slippages* along the basal planes of graphite crystals.

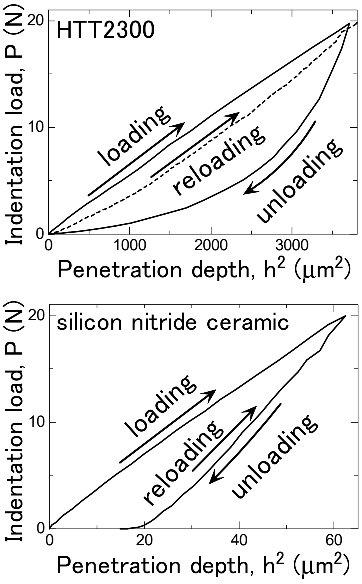

Figure 12.11 $P-h^2$ hysteresis curves (Vickers indentation) observed in the sequential "loading→unloading→reloading" indentation processes of the well-graphitized carbon (HTT2300) and of a silicon nitride ceramic

(3) Viscoelastic indentation contact mechanics of inorganic glasses [7.4]

The detailed considerations on the glass transition behavior, viscoelastic theories and the indentation contact mechanic of amorphous bodies have already been made in Chaps. 6 and 7. In this section, the viscoelastic indentation contact mechanics at elevated temperatures will be given of the inorganic glasses including silica glass.

Silica glass (vitreous pure silica; SG) is a covalent-bonded amorphous material comprising three-dimensionally extended continuous random silica networks, resulting in rather open microstructures as inferred from its density (d=2.200 g/cm^3) and molar volume (27.3 cm^3/mol); the former is the smallest and the latter is the largest among other silicate glasses including soda-lime-silicate glass (SLG). The glass-transition temperature T_g of SG is extremely high (T_g =1050°C). Three-dimensionally extended silica networks can be modified by adding low-molecular-weight oxides (the network modifiers) such as Na_2O, CaO, and B_2O_3; these modifiers fragment the three-dimensional silica networks leading to densification of the microstructures and then controlling/designing the material characteristics. By way of example, SLG (so called soda-lime float glass or window glass) is manufactured by adding a given amount of Na_2O, CaO, and MgO into SG. The glass-transition temperature is T_g=540 °C and the density is d=2.500 g/cm^3;

this significant decrease in T_g with an amount of about 500 °C is attained by adding these network modifiers to SG, resulting in very significant influences on its *viscoelastic characteristics*, the details of which will be given in what follows.

The softening curves of SLG and SG are shown in Fig. 12.12 measured by a Berkovich indenter made of sapphire, since it is incapable of using the conventional diamond indenter due to the oxidation in ambient air at temperatures exceeding 400 °C. The softening behavior is represented as the penetration depth $h_s(T)$ vs. the scanning temperature T relationship, in which a constant indentation load $P_0 = 0.98\,\mathrm{N}$ is applied to the specimen at a temperature beneath the glass-transition point, and then the monotonically increasing penetration is measured that is associated with a constant-rate of rising temperature ($T = qt$; $q = 5.0^\circ\,\mathrm{C/min}$). Due to the time/rate-dependent viscoelastic nature, the softening temperature T_s of glassy material is always affected by the scanning rate q, resulting in the lager T_s for the higher scanning rate of q . The softening temperatures T_s for the scanning rate of $q = 5.0^\circ\,\mathrm{C/min}$ demonstrated in Fig. 12.12 nearly coincide with the glass transition temperatures T_s of SLG and of SG, respectively. It is worthy of note in Fig. 12.12 that SLG exhibits a sharply rising penetration depth curve against the scanning temperature. In fact, the scanning temperature of about 60°C (corresponding to the scanning time of about 12min) is enough for SLG to result in the penetration of 60μm, while SG requires about 250°C (the scanning time of about 50min) to attain the same penetration depth. This significant difference in the softening behavior is directly resulted from their time/rate-dependent viscoelastic characteristics (i.e., relaxation-time spectrum, retardation-time spectrum; refer to APPENDIX D for the details) of these glasses having significantly different their three-dimensional silica network structures; the spatially fragmented rather small silica-network clusters of SLG and the spatially well-extended large clusters of SG.

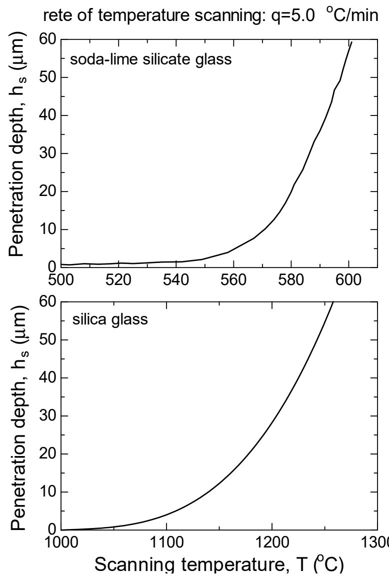

Figure 12.12 Softening curves of soda-lime silicate glass (SLG) and silica glass (SG); penetration depth $h_s(T)$ vs. scanning temperature T curves for temperature scanning with the rate of $q = 5.0^\circ\,\mathrm{C/min}$ under a constant load ($P_0 = 0.98\,\mathrm{N}$) of Berkovich indentation

Figure 12.13 shows the experimental results of SLG in the constant-rate penetration test ($h(t) = k_h \cdot t$; $k_h = 0.045$ μm/s), where the indentation load $P(t)$ is plotted against the penetration depth $h(t)$. The plot of SLG at 570 °C combined with Eq. (11.17) leads to the stress

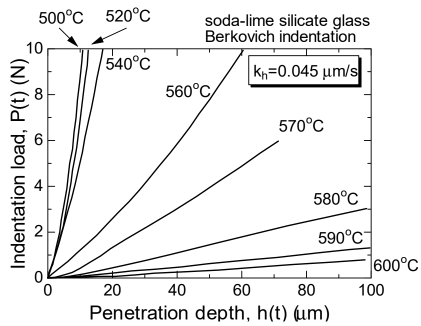

Figure 12.13 Constant-rate of penetration test results of SLG ($k_h = 0.045$ μm/s; Berkovich indentation)

relaxation modulus $E'_{\mathrm{relax}}(t)$ and the creep compliance function $C'_{\mathrm{creep}}(t)$ shown in Fig. 12.14 and in Fig. 12.15, respectively. Furthermore in Fig. 12.16, the retardation time spectrum $L(\tau)$ of SLG derived from $C'_{\mathrm{creep}}(t)$ is given in comparison to that of SG.

As emphasized in Chap. 11, *the accuracy and the reliability of these viscoelastic functions given in Figs. 12.14 to 12.16 are by no means satisfactory, since all of the experimental data are obtained on the conventional instrumented indentation apparatus that is incapable of measuring the indentation contact area*. The details of more accurate/reliable determination for the viscoelastic functions will be given in the subsequent section on the basis of the *indentation contact area* directly observed via the instrumented indentation microscope.

The detailed considerations on the concept, rheological meanings and the experimental determination of relaxation-time/retardation-time spectra are given in Appendix D.

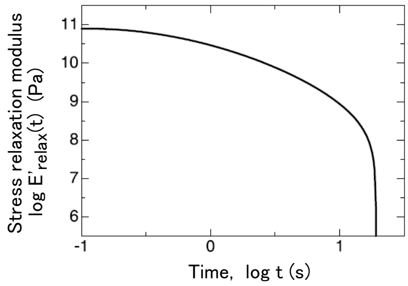

Figure 12.14 Stress relaxation modulus $E'_{\mathrm{relax}}(t)$ of SLG at 570°C

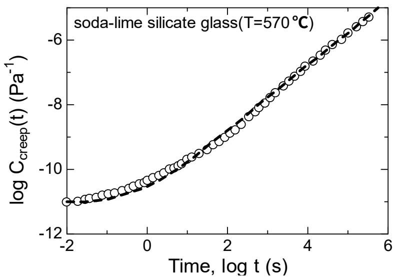

Figure 12.15 Creep compliance function of SLG at 570 °C. The dashed line is the numerical conversion from the relaxation modulus $E'_{\mathrm{relax}}(t)$ shown in Fig. 12.14 (refer to Eqs. (6.18) and (6.19))

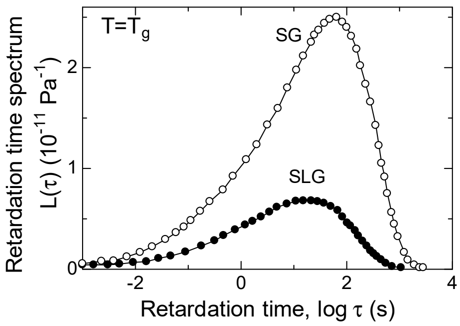

Figure 12.16 Retardation-time spectra of SLG and SG at the respective glass-transition temperatures; $T_g = 1050$ °C: silica glass (SG), $T_g = 540$ °C: soda-lime silicate glass (SLG)

(4) Instrumented indentation microscope applied to the viscoelastic studies of amorphous selenium (a-Se) [7.5]

In Chap. 11 briefly mentioned was the creep compliance of a-Se as an example for the application of instrumented indentation microscope to viscoelastic studies (refer to Fig. 11.14). We will make a detailed consideration on the stress relaxation function of a-Se in this section. Selenium (Se) is a non-metallic element classified in the 16th group (the oxygen group; chalcogens) of the periodic table. Se forms a hexagonal or a monoclinic crystal as well as an amorphous state like as those of sulfur that belongs in the same periodic group. Amorphous selenium (a-Se) comprises entangled random chain networks resulting in viscoelastic behavior at temperatures (25ºC~40ºC) around its glass-transition point of $T_g = 30.0$ ºC.

The instrumented indentation microscope is capable of not only measuring indentation load and penetration depth, but also programming/determining the in-situ indentation contact area as a function of time. By way of example, it is possible to measure the indentation load relaxation $P(t)$ under a stepwise application of a fixed contact area of $A(t) = A_0 \cdot u(t)$ ($u(t)$: Heaviside step function) to the test specimen, readily leading to the stress relaxation modulus $E'_{\text{relax}}(t)$ by substituting the observed $P(t)$ into Eq. (11.24). The stress relaxation moduli $E'_{\text{relax}}(t)$ of a-Se thus determined on the instrumented indentation microscope (Berkovich indentation) are plotted against time in Fig. 12.17 for various temperatures of measurement including the glass-transition point. In the subsequent considerations, it will be demonstrated that the respective relaxation curves shown in Fig. 12.17 satisfy the so-called "*time-temperature superposition principle*".

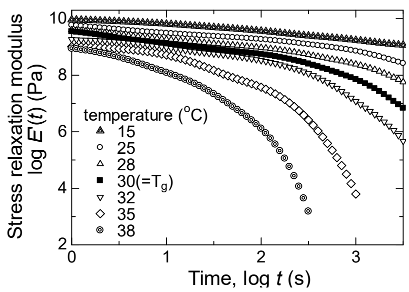

Figure 12.17 Stress relaxation moduli of a-Se at various temperatures of measurement

First of all in the procedure of time-temperature superposition, the relaxation curve is chosen at a specific temperature, i.e., at *the standard temperature* T_0, and then the other relaxation curves beside the standard relaxation curve at T_0 are shifted along the logarithmic time axis in order to superimpose to this standard curve for making a single master curve; the curves at temperatures exceeding the standard temperature are shifted to the longer-time region, and vice versa for the curves at the lower temperatures. Figure 12.18 shows the master curve thus obtained by applying this superposition procedure to the relaxation curves given in Fig. 12.7 (the standard temperature $T_0\left(=T_g\right)=30.0$ °C)). In Fig. 12.18, the solid line is the master curve of a-Se obtained in the uniaxial compression test (the macro test) of a rectangle test specimen with the dimensions of 1 x 1 x 3 mm^3 for comparison. As well recognized in Fig. 12.8, *the stress relaxation of the indentation test (the micro test) is more significant in the shorter time region of* $0.1\text{s} \le t \le 100\text{s}$ *than the relaxation of the macro test. This is resulted from the two-dimensional unconstrained molecular motions on the free surface beneath the indenter, whereas the stress relaxation proceeds with three-dimensionally constrained molecular motions in the macro test*. The shift factor a_T utilized in the time-temperature superposition procedure (see Fig 12.18) is related to the shear viscosity η through the relation of $a_T=\eta(T)/\eta(T_0)$ ($\eta(T)$: the viscosity at temperature T, $\eta(T_0)$: the viscosity at the standard temperature). The temperature dependence of the shift factor a_T utilized in Fig. 12.18 is shown in Fig. 12.19, indicating that the shift factor a_T of a-Se is well described with the Arrhenius plot, $a_T=A\exp(\Delta H/T)$. It is worthwhile noticing in Fig. 12.19 that there exists a finite difference in the activation enthalpy ΔH at the temperatures bounded above/below the glass-transition point T_g. This fact indicates that the rheological deformation/flow processes of the viscoelastic *liquid* ($T>T_g$) are somewhat different from those of the viscoelastic *solid* ($T<T_g$).

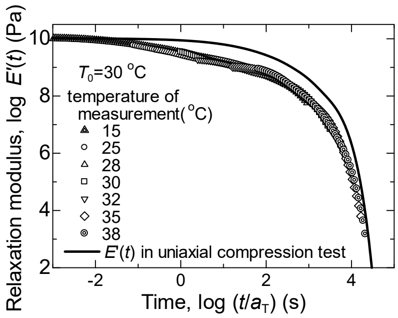

Figure 12.18 Master curves of the stress relaxation modulus of a-Se at $T_0\left(=T_g\right)$ =30.0 °C in terms of the shift factor a_T. The solid line is the relaxation master curve observed in the uniaxial compression test (macro test)

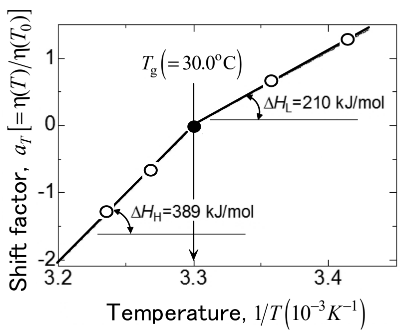

Figure 12.19 Arrhenius plot of the shift factor a_T utilized in Fig. 11.18

(5) Instrumented indentation microscope applied to the viscoelastic/plastic studies of polycarbonate resin in the glassy state [12.5]

The glass-transition temperature T_g of polycarbonate resin (PCR) is about 145 °C, meaning that it is *a glassy solid* at room temperature, the mechanical characteristics of which are, therefore, *time/rate- independent* at room temperature *in the conventional macro tests*. Due to the unconstrained molecular motions at the free-surface of glassy solids including most of organic polymers as well as a-Se mentioned above, on

[12.5] C.G.N. Pelletier, J.M.J. Den Toonder, L.E. Govaert, N. Hakiri, and M. Sakai, *Phil. Mag*. **88[9]**, 1291 (2008) the other hand, their rheological characteristics are *time/rate-dependent in the indentation contact tests (micro/nano tests) even at temperatures well below the glass-transition point*.

The indentation loading/unloading hysteresis curve of PCR *at room temperature* is shown in Fig. 12.20; a spherical diamond indenter (tip-radius 100μm) is penetrated with the rate of 1μm/s to the depth of 13μm (i.e., to the peak indentation load of 1.0N), and then held for 100s at this peak load followed by unloading with the rate of 1μm/s. As readily seen in Fig. 12.20, the well-defined load relaxation is observed during the holding time of 100s at the peak depth of penetration. This fact implies that PCR behaves as a *viscoelastic solid in the indentation test (i.e., in the micro test) even at room temperature*, *whereas PCR is a glassy solid at room temperature*. The dashed line in Fig. 12.20 indicates the elastic P - h analytical relation of the Hertzian contact, $P = (4/3)E'\sqrt{R}h^{3/2}$ (refer to Eq. (3.18)); the purely elastic response dominates the initial stage of indentation loading, followed by the viscoelastic/plastic deformation/flow that becomes significant with the increase in the penetration. The indentation load relaxation and the associated creep of the contact area A_c proceeding at the *fixed depth* of $h(=h_0)=13$ μm are plotted in Fig. 12.21 against the holding time. It is interesting to note that the contact area A_c monotonically increases with time under the fixed penetration depth. This fact indicates the *viscoelastic creeping-up of the free-surface* of PCR along the spherical indenter's side-surface due to the time-dependent Poisson's effect, the details of which have already been discussed in Sec. 10.4 through the FEA-based numerical results (see Fig. 10.14).

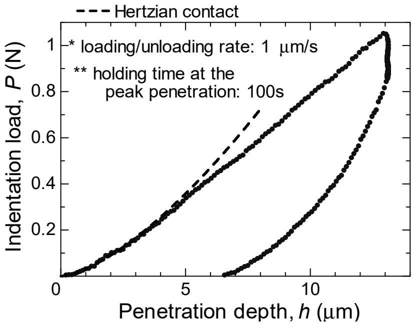

Figure 12.20

P-h loading/unloading hysteresis curve of polycarbonate resin under spherical indentation *at room temperature*. The dashed line is the analytical solution of Hertzian contact

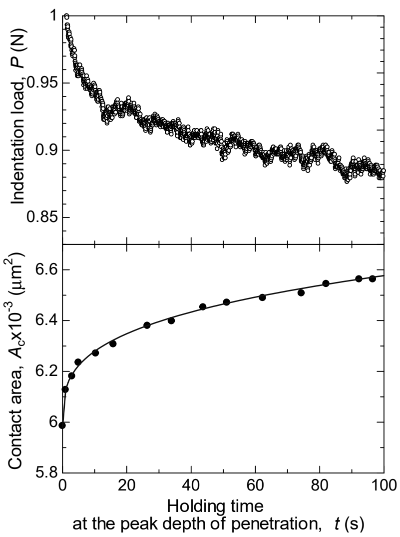

Figure 12.21 Indentation load relaxation and the associated creep of the contact area of polycarbonate resin observed at room temperature under the fixed penetration depth of $h_0 = 13$ μm (the test result given in Fig. 12.20)

(6) Instrumented indentation microscope applied to the elastoplastic studies of coating/substrate composite [12.6]

The elastoplastic indentation contact mechanics will be given in this section of the sol-gel-derived film/substrate laminates (methyl-silsesquioxian ($MeSiO_{3/2}$) film coated on various types of engineering materials). *In the conventional instrumented indentation testing* for laminate composites, due to the incremental increase of the *substrate-effect* with the increase in the indentation penetration, it has been well

[12.6] H. Hakiri, A. Matsuda, and M.Sakai *J. Mater. Res.*, **24[6]**, 1950 (2009) known that there exist crucial difficulties not only in estimating the mechanical characteristics of the coating film and of the substrate respectively, but also in measuring the elastic modulus and the Meyer hardness of *the composites* as a function of the penetration depth (refer to the details in Chap. 9). On the other hand, once we use *the instrumented indentation microscope*, we can determine in experiments the respective mechanical characteristics (elastic modulus, yield stress, viscoelastic functions, etc.) of the film and of the substrate in a precise manner (refer to Chaps. 9 and 10).

$MeSiO_{3/2}$ films (elastic modulus; $E'_f = 3.9$ GPa) with various thicknesses ($t_f = 3 \sim 15\mu m$) are coated on the five engineering substrates; poly carbonate resin PCR (E'_s=3.5GPa ; E'_s/E'_f =0.95), polyacrylate resin PAR (4.5GPa ; 1.2) , polyphenol resin PPR (7.1GPa ; 1.9), glass-like carbon GLC (28.7GPa ; 7.7), and soda-lime silicate glass SLG (80.5GPa ; 22). Using these laminate composites having a rather wide range of film/substrate modulus ratio $0.95 \le E'_s/E'_f \le 22$, let us examine the substrate-effect on the indentation contact mechanics. The indentation load P vs. contact area A hysteresis curves in the loading/unloading processes of Berkovich indentation are plotted in Fig. 12.22 for $MeSiO_{3/2}$/PCR and $MeSiO_{3/2}$/SLG laminate composites by way of example. As clearly demonstrated in Fig. 11.13 for *semi-infinite homogeneous bodies*, the elastoplastic loading/unloading P - A relations are both linear for cone/pyramid indentation; the slope of the loading linear line gives the Meyer hardness H_M and that of the unloading line, i.e., the unloading modulus M provides the elastic modulus E' through the relation of $M = (\tan\beta/2)E'$. In contrast to semi-infinite homogeneous body, on the other hand, the loading/unloading P - A hysteresis relations of the laminate composites are not linear due to the substrate-effect, as shown in Fig. 12.22, where the P - A hysteresis of $MeSiO_{3/2}$/PCR laminate is somewhat linear due to its film/substrate modulus ratio ($E'_s/E'_f = 0.95$) being nearly 1.0, i.e., film/substrate modulus matching. On the other hand, the nonlinear P - A hysteresis of the $MeSiO_{3/2}$/SLG laminate composite is very

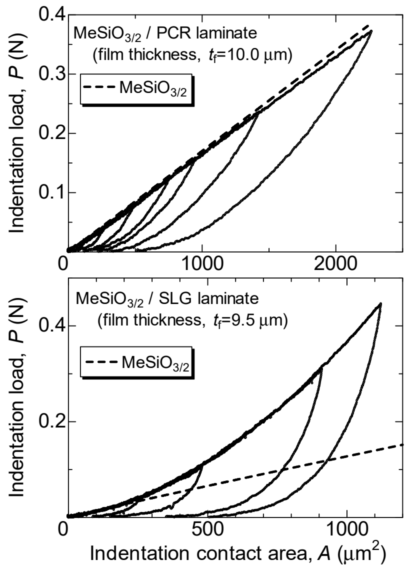

Figure 12.22 Indentation load P vs. contact area A hysteresis relations of $MeSiO_{3/2}$/PCR and $MeSiO_{3/2}$/SLG laminate composites in the multi-step loading/unloading cycle tests (Berkovich indentation). The dashed line is the P - A loading linear relation of the semi-infinite homogeneous $MeSiO_{3/2}$

significant that is resulted from the modulus mismatching ($E'_s/E'_f = 22$). The slope of the P - A loading path of $MeSiO_{3/2}$/PCR laminate slightly decreases with the increase in the indentation penetration due to the little bit lower modulus of the substrate, i.e., $E'_s/E'_f = 0.95$. On the other hand, for $MeSiO_{3/2}$/SLG laminate, reflecting its larger modulus mismatching ($E'_s/E'_f \gg 1$), the slope of the P - A loading line progressively and significantly increases with penetration, approaching to the slope of semi-infinite homogeneous SLG.

Based on the detailed considerations made in Sec. 11.3 for the instrumented indentation microscope, we can make the quantitative assessment of the elastoplastic characteristics of *laminate composites*. As mentioned above, the P - A relation of laminate composite is not linear due to the substrate-effect, whereas it is possible for us to estimate the Meyer hardness $H_M(A)$ from the tangential slope of the P - A loading line at a given value of the contact area A:

$$H_M(A) = dP/dA \tag{12.1}$$

In other words, due to the substrate-effect, the Meyer hardness of laminate composite is dependent on the contact area A: the Meyer hardness is approaching to the value of the coating film by extrapolating $A \downarrow 0$, and to the value of the substrate in the extreme of $A \uparrow \infty$. On the other hand, as shown in Fig. 12.22, the unloading modulus $M(A)(\equiv (dP/dA))$ (the initial slope of the unloading curve at the peak indentation load for the respective multi-step loading/unloading cycles) combined with the following relation (see Eq. (11.18))

$$E'(A) = 2\cot\beta \cdot M(A) \tag{12.2}$$

gives the elastic modulus $E'(A)$ of the laminate at a given value of the contact area A. Like as the Meyer hardness, the elastic modulus $E'(A)$ approaches to E'_f for $A \downarrow 0$, and is extrapolated to E'_s with $A \uparrow \infty$. We can also determine the yield stress $Y(A)$ of the laminate by substituting the values of $H_M(A)$ and $M(A)$ thus determined in the above procedures into Eq. (11.19).

The Meyer hardness $H_M(a/t_f)$ and the effective elastic modulus $E'_{eff}(a/t_f)$ of the MeSiO3/2-coated laminates are plotted in Figs. 12.23 and 12.24, respectively, against the normalized contact radius a/t_f. Notice that the interrelation between $E'(A)$ and $E'_{eff}(A)$ has already been given in Sec. 9.3 with Eq. (9.19).

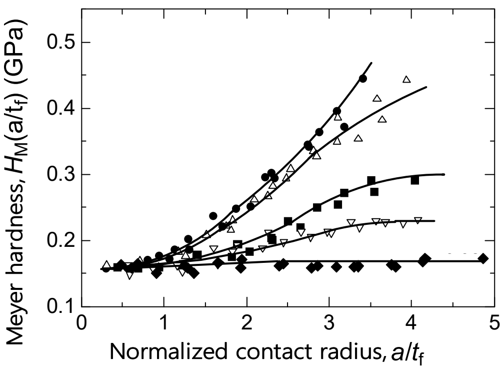

Figure 12.23 Meyer hardness is plotted against the normalized contact radius a/t_f of the MeSiO3/2-coated laminate composites determined on the indentation microscope. The symbols from the top to the bottom indicate the materials used for the respective substrates;

●: soda-lime silicate glass (SLG)

△ : glass-like carbon (GLC)

■: polyphenol resin (PPR)

▽ : polyacrylate resin (PAR)

◆ : polycarbonate resin (PCR)

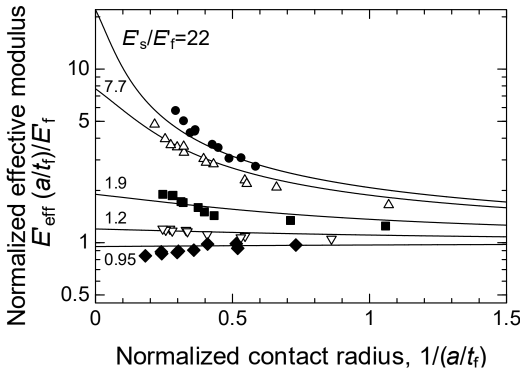

Figure 12.24 Normalized effective modulus $E'_{eff}(a/t_f)/E'_f$ vs. normalized contact radius $1/(a/t_f)$ relations of the MeSiO3/2- coated laminate composites (refer to Fig. 12.23 for the respective symbols) determined on the indentation microscope. The solid lines are the numerical solution of the Fredholm integral equation given in Eq. (9.11)

(7) Instrumented indentation microscope applied to the soft matters with surface adhesion

The technology of cell culture media has been advancing in these few decades. It is critically essential in the studies of cell culture to find a good medium, since the optimized mechanical characteristics of the gel-medium such as the contact hardness, elastic modulus and the surface adhesion (surface energy) play essentially important roles in the studies of stem cell such as the induced pluripotent stem cell (iPS cell).

(i) Elastoplastic indentation contact characteristics of aloe-gel

The contact test results of an aloe-gel as a model bio medium are given in this section through utilizing the indentation microscope for determining the adhesive surface energy γ along with the elastoplastic characteristics of E' and Y).

An example of the P - A loading-unloading hysteresis (Berkovich indentation) is shown in Fig. 12.25. In general, both the P - A loading and the unloading relations of cone/pyramid indentation are *linear* as well demonstrated in Fig. 11.13 for elastoplastic bodies **without surface adhesion**. However, as readily seen in Fig. 12.25, the surface adhesion of the tested aloe-gel leads to a significant *nonlinear* P - A hysteresis. Furthermore, it must be noticed the fact that the *observed indentation load always turns to negative*, implying that the tip-of-indenter is pulled to the contact surface due to surface adhesion (refer to Eq. (8.29) in Chap. 8 for the modified JKR-theory);

$$P = H_{\mathrm{M}} A - \lambda_{\mathrm{EP}} A^{3/4} \tag{8.29}$$

The non-linear P - A *loading* relation shown in Fig. 12.25, therefore, stems from the elastoplastic adhesion toughness λ_{EP} . The linear P vs. A loading line, i.e., $P = H_{\mathrm{M}} A$ of the aloe-gel is plotted in Fig. 12.26 that is derived by applying Eq. (8.29) to the observed P - A *non-linear loading* line in Fig. 12.25 and then making the numerical correction for the non-linear adhesion term, $\lambda_{\mathrm{EP}} A^{3/4}$. The Meyer hardness H_{M} and the adhesion toughness as well as the surface energy γ can thus be successfully determined in experiments through these linearization procedures.

One can determine in experiments the elastic modulus

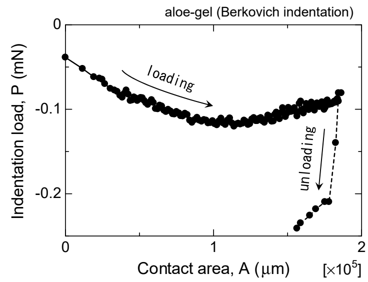

Figure 12.25 P - A loading-unloading hysteresis (Berkovich indentation) of aloe-gel. The indentation load is always negative ($P < 0$) due to surface adhesion

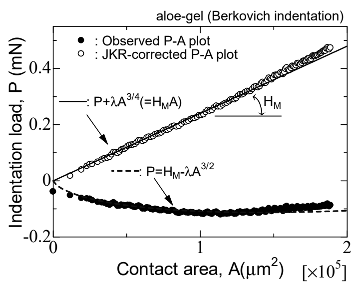

Figure 12.26 P - A loading relations of aloe-gel (Berkovich indentation). The closed symbols (●) and the dashed curve indicate the experimental observation obtained on the indentation microscope. The open symbols (○) and the solid linear line stand for the relation with the JKR-correction for the adhesion toughness λ ;

$$P + \lambda_{\mathrm{EP}} A^{3/4} = H_{\mathrm{M}} A$$

$E'\left[=\left(\tan\beta/2\right)M\right]$ in a quantitative manner via the unloading modulus M as the slope of unloading linear P - A line (refer to Fig. 11.13) whenever the surface adhesion of the specimen is negligibly small enough. However, as shown in Fig. 12.25, the surface adhesion not only leads to the nonlinear loading P - A relation, but also results in a very steep unloading slope that leads to a significant overestimate of the modulus M, yielding the fatal error in determining the elastic modulus E'. As a matter of fact, the unloading modulus estimated from the M -value turns to infinity when the surface adhesion of the specimen tested is large enough, since the tip-of-indenter sticks to the contact surface and the contact area A keeps its maximum value $A \equiv A_{max}$ during unloading. In such a specific unloading contact process proceeding with a constant contact area, the unloading stiffness S defined by the unloading slope of the indentation load P vs. the penetration depth h is quantitatively related to the elastic modulus E' as follows (refer to Chap. 11 and Eq. (11.3)) for the axisymmetric indenter with any geometry including flat-ended cylinder, sphere, cone/pyramid, etc.;

$$E' = \frac{\sqrt{\pi}}{2\sqrt{A_{max}}} S \qquad (12.3)$$

The P - h loading/unloading hysteresis of the aloe-gel is shown in Fig. 12.27, indicating the unloading stiffness S as the initial slope of the unloading path. Since one can measure the contact area A_{max}, penetration depth h as well as the unloading stiffness S through utilizing the instrumented indentation microscope, the application of these experimental data to Eqs. (8.29) and (12.3) yields the Meyer hardness H_M, elastic modulus E', yield stress Y (refer to the details of the additivity principle of the excluded volume of indentation given in Chap. 5) as well as the adhesive surface energy γ of the test specimen, i.e., aloe-gel;

Elastic modulus	E'=25.5kPa
Meyer hardness	H_M=2.40kPa
Yield stress	Y=1.25kPa
Adhesive surface energy	γ=15.6mJ/m^2

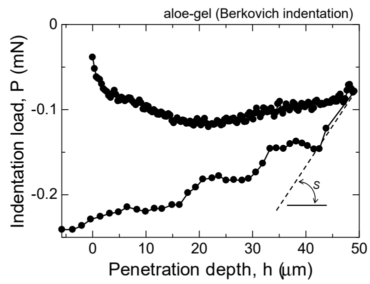

Figure12.27

Loading /unloading P - h hysteresis of aloe-gel (Berkovich indentation). The unloading stiffness S combined with Eq. (12.3) yields the elastic modulus E'

(ii) Viscoelastic indentation contact characteristics of polyurethane-gel

The creep test results (spherical indentation) on the instrumented indentation microscope are given in this section of a commercially available sticky polyurethane gel mat that is to be utilized as vibration dumping mediums.

The creeping contact radius $a_0(t)^3$ of a spherical indenter combined with Eq. (8.46) in Chap.8 is capable of determining in experiment not only the creep function $C'(t)$ but also the surface energy γ (and/or the adhesive surface force Γ) ; these material characteristics can be obtained by solving the simultaneous equations of $a_0(t)^3$ and $a_1(t)^3$ in Eq. (8.46) for the stepwise indentation loads of P_0 and of P_1, respectively. An example of the creep curve $a_0(t)$ under the indentation load $P_0 = 0.11$ mN of the spherical indenter (tip-radius, $R = 3$ mm) is shown in Fig. 12.28 with the indentation contact images in time. Figure 12.29 shows the creep curves of $a_0(t)^3$ and $a_1(t)^3$ for $P_0 = 0.11$ mN and $P_1 = 0.05$ mN, respectively. It must be noticed in Fig. 12.29 that the $a(t)^3$-creep curve is not linearly proportional to the

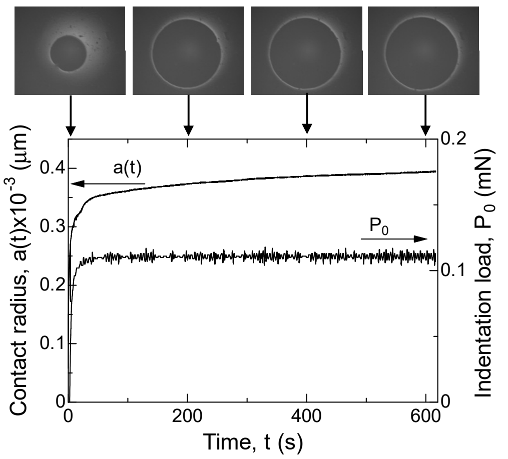

Figure 12.28 Creep curve of the contact radius $a(t)$ of polyurethane-gel for stepwise loading ($P_0 = 0.11$ mN) (spherical indentation with the tip-radius of $R = 3$ mm). The contact images at the respective creeping times of $t =$ 0, 200, 400, and 600s are shown on top of the graph

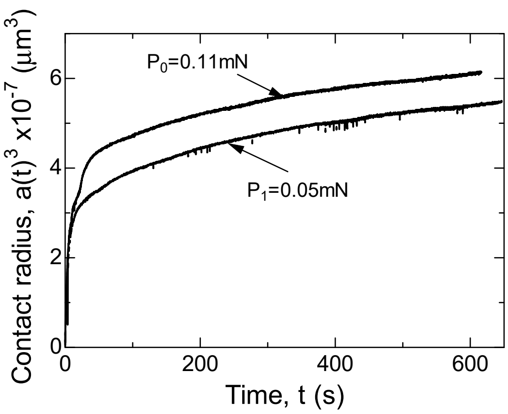

Figure 12.29 Creep curves of the contact radius $a(t)^3$ of polyurethane-gel for stepwise loading of P_0 =0.11mN and P_1 =0.050mN (spherical indentation with the tip-radius of $R = 3$ mm)

applied load due to the significant effect of surface adhesion on the creep deformation, the details of which have already been discussed in Chap. 8.

In this creep test, a significant increase in the contact radius $a(t \approx 0)$ is observed even right after the tip-of-indenter contacts to the specimen's surface and just before the load is applied to the indenter ($P \approx 0$). This observation confirms that the adhesion force of the polyurethane gel mat plays an essential role in its creeping behavior.

The creep function $C'(t)$ thus obtained by applying Eq. (8.46) to the observed creep curves shown in Fig. 12.29 is plotted in Fig. 12.30 along with the relaxation modulus $E'(t)$ in Fig, 12.31 that is converted from $C'(t)$ through Laplace transform and its inversion (refer to Eqs. (6.18) and (6.19) in Chap. 6 for the details). Once we determine the creep function $C'(t)$ in the preceding procedures, by applying it to Eq. (8.46), we successfully estimate the surface energy (adhesive energy) of the polyurethane gel mat as γ=6.61mN/m (=6.61mJ/m^2).

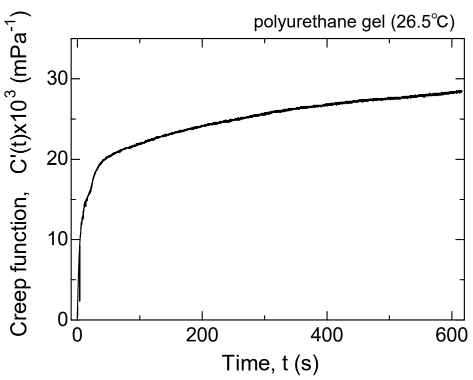

Figure 12.30 Creep function $C'(t)$ of polyurethane-gel
(the temperature of measurement: 26.5°C)

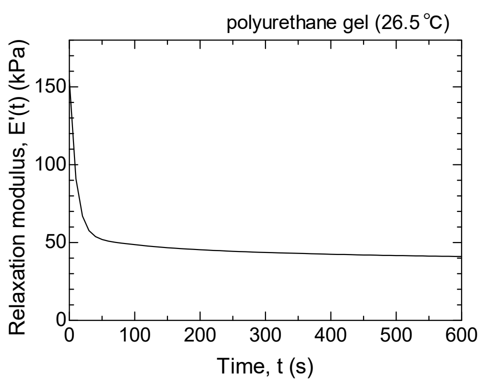

Figure 12.31 Relaxation modulus $E'(t)$ converted from the creep function $C'(t)$ shown in Fig. 12.30 through Laplace transform and its inversion (the temperature of measurement: 26.5°C)

KINEMATIC EQUATIONS IN CYLINDRICAL COOEDINATE

APPENDIX A

(1) Displacement and Strain

Suppose a point A is displaced to the point A' in a continuum body by stretching and torsion, as shown in Fig. A1. This displacement (u, v) in the Cartesian coordinate is related to that in the cylindrical coordinate (u_r, u_θ);

$$\begin{aligned} u &= u_r \cos\theta - u_\theta \sin\theta \\ v &= u_r \sin\theta + u_\theta \cos\theta \end{aligned} \tag{A1}$$

On the other hand, there exist the following interrelations between the Cartesian and the cylindrical coordinates;

$$\begin{aligned} & r^2 = x^2 + y^2 \\ & x = r\cos\theta \qquad y = r\sin\theta \\ & \tan\theta = y/x \end{aligned} \tag{A2}$$

Substituting Eq. (A1) into Eqs. (1.2) ~ (1.5), the strains in the Cartesian coordinate, ε_x, ε_y, ε_z, γ_{xy}, γ_{yz}, and γ_{zx} can be described in terms of u_r, u_θ, and θ through the following mathematical operations.

For the normal strain in the *x*-direction, as an example, is represented by

$$\varepsilon_x = \frac{\partial u}{\partial x} = \frac{\partial u}{\partial \theta}\frac{\partial \theta}{\partial x} + \frac{\partial u}{\partial r}\frac{\partial r}{\partial x} \tag{A3}$$

Furthermore, Eq. (A1) combined with Eq. (A2) gives the following expressions;

$$\begin{aligned} \frac{\partial u}{\partial \theta} &= \frac{\partial u_r}{\partial \theta}\cos\theta - u_r \sin\theta - \frac{\partial u_\theta}{\partial \theta}\sin\theta - u_\theta\cos\theta \\ \frac{\partial u}{\partial r} &= \frac{\partial u_r}{\partial r}\cos\theta - \frac{\partial u_\theta}{\partial r}\sin\theta \\ \frac{\partial \theta}{\partial x} &= -\frac{\sin\theta}{r} \\ \frac{\partial r}{\partial x} &= \cos\theta \end{aligned} \tag{A4}$$

Substituting Eq. (A4) into Eq. (A3), therefore, we finally have

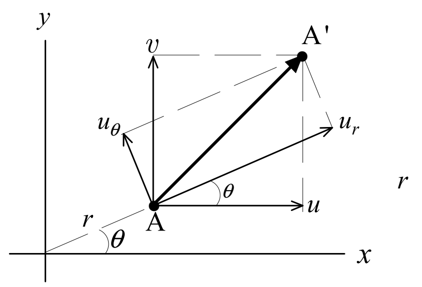

Figure A1 Displacement of a point A to the point A' in a continuum body by stretching/torsion in Cartesian (x, y) and cylindrical (r, θ) coordinates

$$\varepsilon_x = -\left(\frac{\partial u_r}{\partial \theta}\cos\theta - u_r\sin\theta - \frac{\partial u_\theta}{\partial \theta}\sin\theta - u_\theta\cos\theta\right)\frac{\sin\theta}{r} + \left(\frac{\partial u_r}{\partial r}\cos\theta - \frac{\partial u_\theta}{\partial r}\sin\theta\right)\cos\theta \tag{A5}$$

Once we notice $\varepsilon_x \to \varepsilon_r$ as $\theta \to 0$ in Fig. A1, we obtain

$$\varepsilon_r \left(= \varepsilon_x\big|_{\theta\to 0}\right) = \frac{\partial u_r}{\partial r} \tag{A6}$$

via $\theta \to 0$ in Eq. (A5). Analogously, noticing $\varepsilon_x \to \varepsilon_\theta$ as $\theta \to \pi/2$,

we have

$$\varepsilon_\theta \left(= \varepsilon_x\big|_{\theta\to \pi/2}\right) = \frac{1}{r}\frac{\partial u_\theta}{\partial \theta} + \frac{u_r}{r} \tag{A7}$$

After applying a similar procedure conducted above to the shear strain $\gamma_{xy}\left(= \partial u/\partial y + \partial v/\partial x\right)$ in the xy-plane (see Eq. (1.3)), we have the following expression;

$$\begin{aligned}\gamma_{xy} = &\left(\frac{\partial u_r}{\partial \theta}\cos\theta - u_r\sin\theta - \frac{\partial u_\theta}{\partial \theta}\sin\theta - u_\theta\cos\theta\right)\frac{\cos\theta}{r} \\ &+ \left(\frac{\partial u_r}{\partial r}\cos\theta - \frac{\partial u_\theta}{\partial r}\sin\theta\right)\sin\theta \\ &+ \left(\frac{\partial u_r}{\partial \theta}\sin\theta + u_r\cos\theta + \frac{\partial u_\theta}{\partial \theta}\cos\theta - u_\theta\cos\theta\right)\left(-\frac{\sin\theta}{r}\right) \\ &+ \left(\frac{\partial u_r}{\partial r}\sin\theta + \frac{\partial u_\theta}{\partial r}\cos\theta\right)\cos\theta\end{aligned} \tag{A8}$$

and then noticing $\gamma_{xy} \to \gamma_{r\theta}$ as $\theta \to 0$, Eq. (A8) leads to

$$\gamma_{r\theta}\left(\equiv \gamma_{xy}\big|_{\theta\to 0}\right) = \frac{\partial u_\theta}{\partial r} + \frac{1}{r}\frac{\partial u_r}{\partial \theta} - \frac{u_\theta}{r} \tag{A9}$$

that has already been given in Chap. 1 (Eq. (1.9)).

The expressions given in Eqs. (A6), (A7), and (A9) for the strains in the cylindrical coordinate are derived from the strains in the Cartesian coordinate by *the use of coordinate-conversion from the* (x, y) *-space to the* (r, θ) *-space* (*Eqs.* (*A1*) *and* (*A2*))*, in mathematical manner*, not derived from *the actual displacements and deformations of continuum body*. In order to make clear *the physics of these strains* of ε_r, ε_θ, and

$\gamma_{r\theta}$ associated with the deformation of continuum body, therefore, let us derive again these strains ε_r, ε_θ, and $\gamma_{r\theta}$ through using the displacements/deformations depicted in Figs. A2 ~ A5.

The normal deformations are depicted in Figs. A2 and A3; the quadrangle abcd in Fig. A2 is deformed to the quadrangle a'b'c'd' through the normal displacement u_r from bc (length dr) to b'c' (length δ_r) along the radial direction, and from ab (length $rd\theta$) to a'b' (length $\left(r+u_r\right)d\theta$) along the azimuthal direction. Accordingly, the radial strain ε_r is given by

$$\varepsilon_r = \frac{\delta_r}{dr} = \frac{\left(\partial u_r / \partial r\right)dr}{dr} = \frac{\partial u_r}{\partial r} \tag{A6}$$

and the azimuthal strain $\varepsilon_{\theta 1}$ is described by

$$\varepsilon_{\theta 1} = \frac{\left(r+u_r\right)d\theta - rd\theta}{rd\theta} = \frac{u_r}{r} \tag{A10}$$

that is associated with the *radial displacement of* u_r. In addition to the azimuthal strain $\varepsilon_{\theta 1}$ induced by u_r, there also exists the strain $\varepsilon_{\theta 2}$ induced by the *azimuthal displacement of* u_θ as shown in Fig. A3;

$$\varepsilon_{\theta 2} = \frac{\left(\partial u_\theta / \partial \theta\right)d\theta}{rd\theta} = \frac{1}{r}\frac{\partial u_\theta}{\partial \theta} \tag{A11}$$

The azimuthal strain ε_θ is, therefore, given by the sum of $\varepsilon_{\theta 1}$ and $\varepsilon_{\theta 2}$, as follows;

$$\varepsilon_\theta \left(= \varepsilon_{\theta 1} + \varepsilon_{\theta 2}\right) = \frac{1}{r}\frac{\partial u_\theta}{\partial \theta} + \frac{u_r}{r} \tag{A7}$$

The shear deformations are depicted in Figs. A4 and A5; the quadrangle abcd in Fig. A4 is deformed to the quadrangle a'bcd' through the shear displacement du_r along the radial direction, and the same quadrangle abcd in Fig. A5 to the quadrangle a'b'c'd' through the shear displacement u_θ along the azimuthal direction. As shown in Fig. A4, the shear strain γ_r associated with the displacement du_r along the radial direction is given by

$$\gamma_r = \frac{1}{r}\left(\frac{\partial u_r}{\partial \theta}\right), \tag{A12}$$

On the other hand, as shown in Fig. A5, the shear strain γ_θ through the azimuthal displacement u_θ is described with

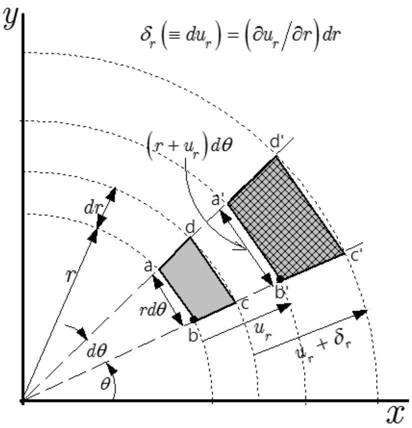

Figure A2 Normal deformation of the quadrangle abcd to the quadrangle a'b'c'd' through the radial displacement u_r

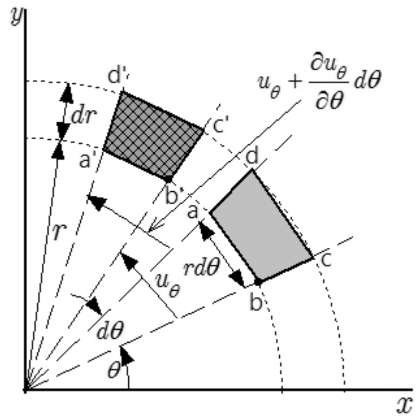

Figure A3 Normal deformation of the quadrangle abcd to the quadrangle a'b'c'd' through the azimuthal displacement u_θ

$$\gamma_\theta = \beta - \alpha = \frac{\partial u_\theta}{\partial r} - \frac{u_\theta}{r} \qquad \text{(A13)}$$

where β indicates the relative shear angle between the lines cd and ab of the quadrangle abcd that is induced by the azimuthal displacement u_θ, while α is the angle of rigid rotation of the quadrangle abcd associated with the azimuthal displacement u_θ, leading to the resultant shear angle $\gamma_\theta\,(\equiv \beta - \alpha)$ as given in Eq. (A13). Accordingly, the total shear strain $\gamma_{r\theta}$ in the (r,θ)-plane associated with the displacements along the r- and θ- directions is finally given by

$\gamma_{r\theta} =$ (A9)

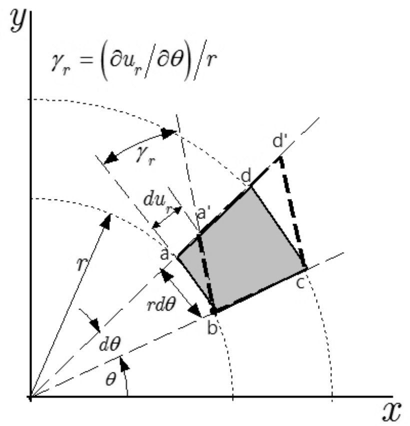

Figure A4 Shear deformation of the quadrangle abcd (the solid lines) to the quadrangle a'bcd' (the broken lines) associated with the radial displacement du_r

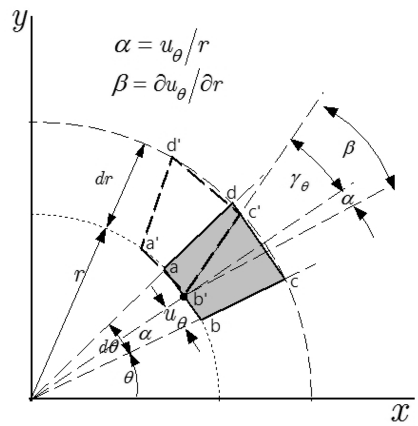

Figure A5 Shear deformation of the quadrangle abcd (the solid lines) to the quadrangle a'b'c'd' (the broken lines) associated with the azimuthal displacement u_θ

(2) Equilibrium Equations

The mechanical equilibrium shown in Fig. A6 along the radial direction results in

$$\left[\left(\sigma_r + \frac{\partial \sigma_r}{\partial r}dr\right)(r+dr)d\theta - \sigma_r r d\theta\right]$$
$$-\left[\left(\sigma_\theta + \frac{\partial \sigma_\theta}{\partial \theta}d\theta\right)\sin\frac{d\theta}{2}dr + \sigma_\theta \sin\frac{d\theta}{2}dr\right] \qquad \text{(A14)}$$
$$+\left[\left(\tau_{\theta r} + \frac{\partial \tau_{\theta r}}{\partial \theta}d\theta\right)\cos\frac{d\theta}{2}dr - \tau_{\theta r}\cos\frac{d\theta}{2}dr\right]$$
$$+Rrd\theta dr = 0$$

and then,

$$\frac{\sigma_r - \sigma_\theta}{r} + \frac{\partial \sigma_r}{\partial r} + \frac{1}{r}\frac{\partial \tau_{\theta r}}{\partial \theta} + \frac{\partial \tau_{zr}}{\partial z} + R = 0 \qquad \text{(A15)}$$

by noticing $d\theta \ll 1$, $\sin(d\theta/2) \approx d\theta/2$, $\cos(d\theta/2) \approx 1$, and by letting the higher-order variables ($(dr)^2, drd\theta$) to be negligible, although the shear stress τ_{zr} on the *z*-plane (the plane with its normal vector directed to *z*-axis) is not depicted in Fig. A6 for simplicity (Eq. (A15) has already been given in Chap. 1 (see Eq. (1.11)).

The equilibrium equation for azimuthal direction (θ-direction) is also given by

$$\left[\left(\sigma_\theta + \frac{\partial \sigma_\theta}{\partial \theta}d\theta\right)dr - \sigma_\theta dr\right]\cos\frac{\theta}{2}$$
$$+\left[\left(\tau_{r\theta} + \frac{\partial \tau_{r\theta}}{\partial r}d\theta\right)(r+dr)d\theta - \tau_{r\theta} r d\theta\right] \qquad \text{(A16)}$$
$$+\left[\left(\tau_{\theta r} + \frac{\partial \tau_{\theta r}}{\partial \theta}d\theta\right)dr + \tau_{\theta r}dr\right]\sin\frac{d\theta}{2}$$
$$+\Theta r d\theta dr = 0$$

After a similar consideration we made above on the radial direction, we finally have the following equilibrium equation for azimuthal direction;

$$\frac{2\tau_{\theta r}}{r} + \frac{\partial \tau_{\theta r}}{\partial r} + \frac{1}{r}\frac{\partial \sigma_\theta}{\partial \theta} + \frac{\partial \tau_{z\theta}}{\partial z} + \Theta = 0 \qquad \text{(A17)}$$

through taking into account of $d\theta \ll 1$, $\sin(d\theta/2) \approx d\theta/2$, $\cos(d\theta/2) \approx 1$, the contribution of shear stress $\tau_{z\theta}$ on the z-plane, as

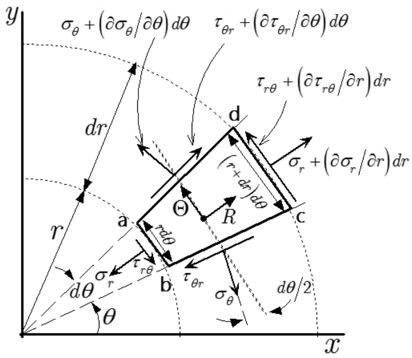

Figure A6 Stress components (σ_r, σ_θ, $\tau_{\theta r}$, $\tau_{r\theta}$) acting on the infinitesimal quadrangle abcd with unit thickness under the external body forces (R, Θ)

well as the symmetric nature of the stress tensor, $\tau_{r\theta} = \tau_{\theta r}$. Equation (A17) has already been given in Chap. 1 (see Eq. (1.11))

BESSEL FUNCTION

APPENDIX B

Daniel Bernoulli first introduced the concept of Bessel functions in 1732 to solve the problem of an oscillating chain suspended at one end, although Bessel functions are named for Friedrich W. Bessel (1784-1846). In 1824, F.W. Bessel incorporated Bessel functions in the Kepler's perturbation problems for determining the motion of three planets moving under mutual gravitation. In 1878, Lord Rayleigh (John W. Strutt) employed Bessel functions in the analysis of a membrane stretched within a cylinder, that has been the historical origin of the application of Bessel functions to solving the bi-harmonic equation through Hankel transformation as demonstrated in Chap. 2 of this textbook.

Bessel equation (see Eq. (2.22)) is defined by the second order differential equation given as

$$\frac{d^2y}{dx^2}+\frac{1}{x}\frac{y}{dx}+\left(1-\frac{n^2}{x^2}\right)y=0 \qquad \text{(B1)}$$

The solution of Eq. (B1) is described in terms of Bessel functions of the first and the second kind, $J_n(x)$ and $Y_n(x)$ of the n-th order, as follows;

$$y=AJ_n(x)+BY_n(x) \qquad \text{(B2)}$$

with arbitrary integral constant A and B. The second kind Bessel function $Y_n(x)$ is sometimes referred to as the Weber function or the Neumann function, and related to the first kind Bessel function in the following formula;

$$Y_n(x)=\frac{J_n(x)\cos(nx)-J_{-n}(x)}{\sin(nx)} \qquad \text{(B3)}$$

The function $J_n(x)$ is *always finite* for all values of n, while the function $Y_n(x)$ becomes singular, i.e., *becomes infinite* at $x=0$, as readily seen in Eq. (B3). In order to describe the problems of physics/mechanics, therefore, we need to set the integral constant B as $B=0$ in Eq. (B2). In other words, only the first kind Bessel function $J_n(x)$ is essential in analyzing any of physical/mechanical phenomena and problems without singularity.

The Bessel function of the first kind of order n can be determined using an infinite power series expansion as follows;

$$J_n(x) = \sum_{k=0}^{\infty} \frac{(-1)^k \left(x/2\right)^{n+2k}}{k!(n+k)!} \tag{B4}$$

Equation (B4) leads to the following recurrence formulas, i.e., Bessel functions of higher order are expressed by Bessel function of lower order for all real values of *n*;

$$\begin{aligned} \frac{d}{dx}\left[x^n J_n(x)\right] &= x^n J_{n-1}(x) \\ \frac{d}{dx}\left[x^{-n} J_n(x)\right] &= -x^{-n} J_{n+1}(x) \end{aligned} \tag{B5}$$

The equivalent alternatives of Eq. (B5) are

$$\begin{aligned} J_{n+1}(x) &= \frac{2n}{x} J_n(x) - J_{n-1}(x) \\ \frac{dJ_{n+1}(x)}{dx} &= \frac{1}{2}\left[J_{n-1}(x) - J_{n+1}(x)\right] \end{aligned} \tag{B6}$$

or

$$\begin{aligned} \frac{dJ_n(x)}{dx} &= J_{n-1}(x) - \frac{n}{x} J_n(x) \\ \frac{dJ_n(x)}{dx} &= \frac{n}{x} J_n(x) - J_{n+1}(x) \end{aligned} \tag{B7}$$

Using these recurrence formulas, it will be easy to prove that the first-order Hankel transform of the derivative $d\varphi / dr$, i.e., $\int_0^\infty r\left(d\varphi / dr\right) J_1\left(\xi r\right) dr$, is expressible in terms of the zeroth-order Hankel transform $\int_0^\infty r\varphi J_0\left(\xi r\right) dr$ of the function φ, as follows

$$\int_0^\infty r\left(d\varphi / dr\right) J_1\left(\xi r\right) dr = -\xi \int_0^\infty r\varphi J_0(\xi r) dr$$

This formula has already been utilized in Chap. 2 for describing the displacements, u_r and u_z, in cylindrical coordinate. As emphasized in Chapt.2, Hankel transform plays an important role in solving the harmonic/bi-harmonic equations *in cylindrical coordinate*.

LAPLACE TRANSFORMS

APPENDIX C

The Laplace transform, like the Fourier series, give us a method of tackling differential/integral equation problems we couldn't otherwise solve. In the linear response theory such as the linear viscoelastic theory, the Laplace transform is a very powerful tool that enables us to solve complicated viscoelastic problems, as demonstrated in Chap. 6.

Linear differential/integral equations *in real space* are transformed to the algebraic equations *in Laplace space*, and then the solutions of these algebraic equations are inversely transformed to the real space resulting in the solutions of these original differential/integral equations.

(1) Definition of Laplace Transform

An arbitrary function $f(t)$ with the variable t in real space is transformed to $\bar{f}(p)$ with the variable p in Laplace space through using the Laplace operator $\mathcal{L}$ as follows;

$$\mathcal{L} f(t) = \bar{f}(p) = \int_0^{\infty} f(t) e^{-pt} dt \tag{C1}$$

The variable p in Laplace space has the inverse physical dimension of the variable t in real space; p has its physical dimension of [1/s], provided that t is referred to as time [s]. The variable pt in the integrand in Eq. (C1) is therefore dimensionless.

(2) Fundamental Properties

The most fundamental properties of Laplace transform are listed below;

(i) $$\mathcal{L}\left[c_1 f_1(t) + c_2 f_2(t)\right] = c_1 \bar{f}_1(p) + c_2 \bar{f}_2(p) \tag{C2}$$

where c_1 and c_2 are constant

(ii) $$\mathcal{L}\left[\frac{df(t)}{dt}\right] = p\bar{f}(p) - f\left(0^-\right) \tag{C3}$$

with $f\left(0^-\right) = \lim_{\varepsilon \to 0} f(0 - \varepsilon)$

$$\mathcal{L}\left[\frac{d^2 f(t)}{dt^2}\right] = p^2 \bar{f}(p) - pf\left(0^-\right) - \left.\frac{df(t)}{dt}\right|_{t=0^-} \tag{C4}$$

(iii) $$\mathcal{L}\left[\int_0^t f(t-t') g(t') dt'\right] = \bar{f}(p) \cdot \bar{g}(p) \tag{C5}$$

in which the integral $\int_0^t f(t-t')g(t')dt'$ is the so-called convolution integral; the Boltzmann's hereditary integral (Eqs. (6.15) and (6.20) in Chap. 6.3) typifies the convolution integral.

(3) Some Useful Transform Pairs

Table C1 Laplace Transform Pairs useful in The Linear Response Theory

	$f(t)$	$\bar{f}(p)$
1	$u(t-a)$; Heaviside step function	e^{-ap}/p
2	$\delta(t)(\equiv du(t)/dt)$; Dirac function	1
3	1	$1/p$
4	t^n; $n=1,2,3\cdots$	$n!/p^{n+1}$
5	e^{at}	$1/(p-a)$
6	$(e^{bt}-e^{at})/(b-a)$; $a\neq b$	$1/[(p-a)(p-b)]$
7	$(be^{bt}-ae^{at})/(b-a)$; $a\neq b$	$p/[(p-a)(p-b)]$
8	$\sin at$	$a/(p^2+a^2)$
9	$\cos at$	$p/(p^2+a^2)$
10	$J_0(at)$; zeroth-order Bessel function	$1/\sqrt{p^2+a^2}$

(4) An Example of the Application of Laplace Transform to Linear Differential Equation

Let us solve the following linear differential equation (see Eq. (6.1)) as an example:

$$a_0\varepsilon(t)+a_1\frac{d\varepsilon(t)}{dt}=b_0\sigma(t)+b_1\frac{d\sigma(t)}{dt} \qquad \text{(C6)}$$

Laplace transform of Eq. (C6) results in the following algebraic equation;

$$a_0\bar{\varepsilon}(p)+a_1\left[p\bar{\varepsilon}(p)-\varepsilon\left(0^-\right)\right]$$
$$=b_0\bar{\sigma}(p)+b_1\left[p\bar{\sigma}(p)-\sigma\left(0^-\right)\right] \tag{C7}$$

Since none of external loads and displacements are applied to the body in the past ($t<0$), Eq. (C7) with the initial condition of $\varepsilon\left(0^-\right)=0=\sigma\left(0^-\right)$ leads to the following algebraic equation in the Laplace space;

$$\bar{\sigma}(p)=E^*(p)\bar{\varepsilon}(p)$$
$$E^*(p)=\frac{a_0+a_1p}{b_0+b_1p} \tag{C8}$$

In Eq. (C8), $E^*(p)$ stands for the *pseudo elastic modulus* (refer to Eq. (6.4)), and the constants a_0 , a_1 , b_0 , and b_1 are related to the viscoelastic characteristics such as the elastic modulus, viscosity and the relaxation time (see Eqs. (6.2a) ~ (6.2c)) of the viscoelastic model (Maxwell/Zener models; refer to Eqs. (6.5a) ~ (6.5c)).

Suppose a step-wise strain $\varepsilon(t)=\varepsilon_0u(t)$ in Eq. (C6), and then notice its Laplace transform $\bar{\varepsilon}(p)=\varepsilon_0/p$ via Table C1#1. Equation (C8) is therefore rewritten by

$$\frac{\bar{\sigma}(p)}{\varepsilon_0}=\frac{a_1}{b_0+b_1p}+\frac{a_0}{p\left(b_0+b_1p\right)} \tag{C9}$$

The inverse Laplace transform of Eq. (C9) via Table C1 finally results in the solution of the linear differential equation (Eq. (C6)) as follows;

$$\frac{\sigma(t)}{\varepsilon_0}=\frac{a_0}{b_0}+\left(\frac{a_1}{b_1}-\frac{a_0}{b_0}\right)\exp\left(-\frac{t}{\tau}\right)$$
$$\tau=\frac{b_1}{b_0} \tag{C10}$$

Equations (6.2a) ~ (6.2c) applied to the constants a_0 , a_1 , b_0 , and b_1 in Eq. (C10), therefore, finally give the constitutive expressions for the stress relaxation behaviors of the respective viscoelastic models we discussed in Chap. 6.

RELAXATION TIME SPECTRUM AND RETARDATION TIME SPECTRUM

APPENDIX D

It is incapable of quantitatively describing the viscoelastic behaviors of engineering materials in terms of a simple viscoelastic model like as the Maxwell/Zener model discussed in Chaps. 6 and 7. We need, therefore, to adopt a more general viscoelastic model such as the Wiechert model (see Fig. 6.5 in Chap. 6) with multiple relaxation time through introducing the concept of "*time spectrum*" to the constitutive equations, Eqs. (6.8) ~ (6.13) in Chap. 6, for expressing the relaxation modulus and the creep compliance **[A1]**.

The Wiechert model (refer to Chap. 6) well describes the generalized relaxation modulus $E_{\mathrm{relax}}(t)$ in terms of a *discrete distribution of relaxation times*;

$$E_{\mathrm{relax}}(t) = E_{\mathrm{e}} + \sum_i E_i e^{-t/\tau_i} , \qquad (6.13)$$

while its corresponding expression with a *continuous time distribution* is given by

$$E_{\mathrm{relax}}(t) = E_{\mathrm{e}} + \int_0^{\infty} M(\tau) e^{-t/\tau} d\tau \qquad (\mathrm{D1})$$

in Eq. (D1), the function $M(\tau)$ is referred to as the "*relaxation time distribution*" that stands for the elastic modulus $E_i \left(\equiv \eta_i / \tau_i\right)$ with the relaxation time τ_i in the discrete model (Eq. (6.13)). The distribution function $M(\tau)$ is a kind of the memory function *having the physical dimension of* [Pa/s], *being not the dimension of elastic modulus* [Pa], though the function $M(\tau)$ in its physical meaning stands for the elastic modulus itself. To circumvent such a confusing physical meaning, Eq. (D1) is rewritten to

$$E_{\mathrm{relax}}(t) = E_{\mathrm{e}} + \int_{-\infty}^{\infty} H(\tau) e^{-t/\tau} d \ln \tau \qquad (\mathrm{D2})$$

by introducing the *relaxation time spectrum* $H(\tau)\left[\equiv \tau M(\tau)\right]$ *with the physical dimension of* [Pa]. By the use of the relaxation time spectrum $H(\tau)$ instead of using the time distribution $M(\tau)$, we can, therefore, successfully express the elastic modulus of the springs having their relaxation times ranging from $\ln \tau$ to $\ln \tau + d \ln \tau$.

In a similar manner to the relaxation modulus, we can describe the creep compliance as follows,

[A1] J.D. Ferry, *Viscoelastic Properties of Polymers*, 3rd Ed. Wiley (1980)

$$C_{\mathrm{creep}}(t) = C_{\mathrm{g}} + \frac{t}{2(1+\nu)\eta} + \int_{-\infty}^{+\infty}\left(1-e^{-t/\tau}\right)L(\tau)d\ln\tau \qquad \text{(D3)}$$

in terms of the *retardation time spectrum* $L(\tau)$ for the springs having the retardation times ranging from $\ln\tau$ to $\ln\tau + d\ln\tau$. In Eq. (D3), C_{g} is the glass compliance, and η is the steady-state viscosity. The relaxation modulus $E_{\mathrm{relax}}(t)$ is related to the creep compliance $C_{\mathrm{creep}}(t)$ via the convolution integral (refer to Chap. 6);

$$\int_0^t E_{\mathrm{relax}}(t-t')C_{\mathrm{creep}}(t')dt' = t \qquad \text{(6.19)}$$

In this context, therefore, the relaxation time spectrum $H(\tau)$ is correlated to the retardation time spectrum $L(\tau)$ as follows **[A2-A4]**;

$$\begin{aligned} L(\tau) &= \frac{H(\tau)}{\left[\pi H(\tau)\right]^2 + \left[E_{\mathrm{g}} - \int_0^\infty \frac{H(1/s)}{s-1/\tau}ds\right]^2} \\ H(\tau) &= \frac{L(\tau)}{\left[\pi L(\tau)\right]^2 + \left[C_{\mathrm{g}} + \frac{\tau}{\eta} + \int_0^\infty \frac{L(1/s)}{s-1/\tau}ds\right]^2} \end{aligned} \qquad \text{(D4)}$$

The retardation time spectra $L(\tau)$ in Fig. 12.16 are determined via the Schwarzl-Staverman approximation **[A3-A4]**

$$L(\tau) = \left[\frac{dC_{\mathrm{creep}}(t)}{d\ln t} - \frac{d^2C_{\mathrm{creep}}(t)}{d(\ln t)^2}\right]_{t=2\tau} \qquad \text{(D5)}$$

applied to the experimental data of creep compliance curves $C_{\mathrm{creep}}(t)$ in Fig. 12.15. In a similar way, the relaxation time spectrum $H(\tau)$ is also determined from the experimentally observed relaxation modulus $E_{\mathrm{relax}}(t)$ by the use of the following relation;

$$H(\tau) = \left[-\frac{dE_{\mathrm{relax}}(t)}{d\ln t} + \frac{d^2E_{\mathrm{relax}}(t)}{d(\ln t)^2}\right]_{t=2\tau} \qquad \text{(D6)}$$

[A2] B. Gross, *Mathematical Structure of the Theories of Viscoelasticity*, Hermann (1953)

[A3] F. Schwarzl, A.J. Staverman, *Physica*, **18**, 791 (1952)

[A4] F. Schwarzl, A.J. Staverman, *Appl. Sci. Res.,* **A4**, 127 (1953)

HYSTORY OF INDENTATION CONTACT MECHANICS

APPENDIX E

(1) Thermodynamics and Continuum Mechanics in The Era of Industrial Revolution

Thomas Young (1773-1829)

In the early 19th century in Great Britain, the industrial revolution began in earnest with the technological innovations associated with textile industry, development of steam locomotives/ships, etc., followed by the development of iron/steel industry with the engineering innovation of coal-to-coke producing processes. The transportation of coal in South Wales to Glasgow/Manchester, the center of the industrial revolution, significantly improved Britain's transport infrastructure with railway networks, canal/waterway networks, etc.

It was the historical necessities in the era of the industrial revolution that there were numbers of the "superbrains" for making great contributions to founding the thermodynamics [N.L.S. Carnot (1796-1832), B.P.E. Clapeyron (1799-1864), J.P. Joule (1818-1889), H.L.F. von Helmholtz (1821-1894), R.J.E. Clausius (1822-1888), W. Thomson (Load Kelvin) (1824-1907), J. W. Gibbs (1839-1903), L.E. Boltzmann (1844-1906), W.H. Nernst (1864-1941)], and to founding the continuum mechanics [T. Young (1773-1829), S.D. Poisson (1781-1840), C-L. Navier (1785-1836), A. Caucy (1789-1857), G. Green (1793-1841), G. Lame (1795-1870), B.S. Saint-Venant (1797-1886), F. Neumann (1798-1895), G.G. Stokes (1819-1903), J.C. Maxwell (1831-1879), J. Bauschinger (1834-1893), J.V. Boussinesq (1842-1929), W. Voigt (1850-1919), H. Hertz (1857-1894)].

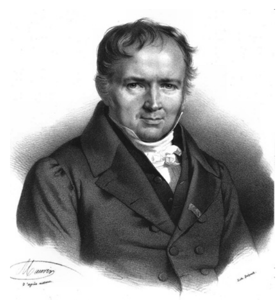

Simeon Denis Poisson (1781-1840)

(2) The Role of Measuring the Indentation Hardness in The Era of Industrial Revolution

James Clerk Maxwell (1831-1879)

Establishment of the test methods for determining the mechanical characteristics (elasticity, strength, plasticity, etc.) of iron/steel-products were the fatal issues in The Industrial Revolution. The test methods for characterizing "*elasticity*" have already been established in the Era with the pioneering works made by R. Hook (1635-1703) and T. Young. On the other hand, as to the test method and the physics of "*strength*" in The Mid-Term Industrial Revolution (the mid-19th century), there were none of systematic studies until the Weibull statistics (W. Weibull (1887-

1979)) in the end of 19th century and the Griffith's deterministic strength theory (A.A. Griffith (1893-1963)) in the beginning of 20th century. The science and engineering for the study of "*plasticity*" of iron/steel was in the most earnest with the practical issues of rolling/sliding problems of wheel/rail contact along with the developments of steam locomotives, although the concept, physics, as well as the testing techniques of plasticity were still in predawn darkness. In 1886, however, J. Bauschinger examined the *elastic limit* and the plasticity-related *irreversible deformation* that has been widely recognized as the "Bauschinger effect" in the 20th century. In these historical ambience, *indentation hardness testing* played an important role in *practically characterizing the plasticity* of iron/steel products, though it was required one more century for us to get a deeper understanding of *the physics of indentation hardness*.

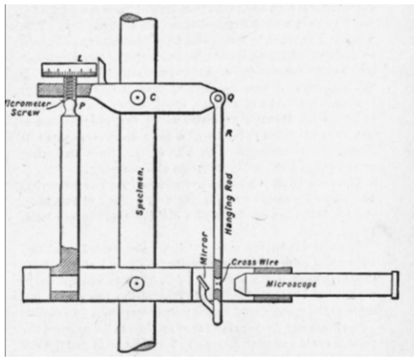

Bauschinger-Ewing extensometer (precision of strain measurement: $\varepsilon \approx 2.5\times10^{-6}$)

(3) Test Techniques for Measuring Indentation Hardness and the History of Elastoplastic Contact Mechanics

F. Mohs (1773-1839) introduced the "Mohs hardness" in order to rank the hardness (scratch resistance) of minerals. The Mohs hardness is the so-called "*scratch hardness*", not the *indentation hardness*. It is based on the relative scratch resistance; talc ($Mg_3Si_4O_{10}(OH)_2$) as the softest mineral is assigned a value of 1, and diamond (C) as the hardest mineral is assigned a value of 10. Most of minerals are *relatively ranked* between 1 and 10. There is a tight correlation between the Mohs hardness and the indentation hardness, while we cannot use the Mohs hardness as a *quantitative* material characteristic, not like the indentation hardness. The Brinell indentation test was proposed by J.A. Brinell (1849-1925) in 1890 to quantitatively characterize the hardness of steel. In its standard test procedure, the Brinell hardness HB is defined as the indentation load P (=3ton) divided by the total surface area A of the residual impression, i.e., $HB = P/A$, by the use a spherical steel indenter with the diameter of 10mm, having been widely utilized up to the present date. In 1898, A. Martens developed a breakthrough indenter that may be a pioneering instrument of the present instrumented indentation apparatus. The Martens indenter is capable of measuring not only the indentation load P, but also the penetration depth h, namely measuring the P - h

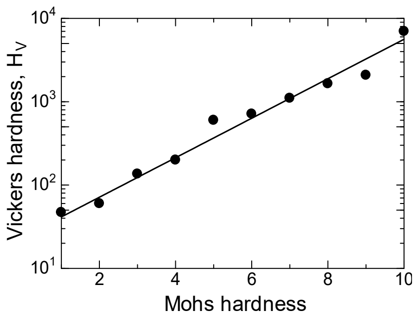

Correlation between the Vickers hardness and the Mohs hardness loading curve. He proposed the Martens hardness HM in terms of *the maximum indentation load* $P_{\max}$ and *the in-situ penetration depth* $h_{\max}$ at the maximum load. The Martens hardness is widely in use nowadays as the Universal Hardness HU. The concept of hardness via *in-situ determination under load* was actually very pioneering in the end of 19th to the beginning of 20th centuries because it has been usual to determine the indentation hardness such as the Brinell hardness and the Vickers hardness by the use of *the residual indentation impression*.

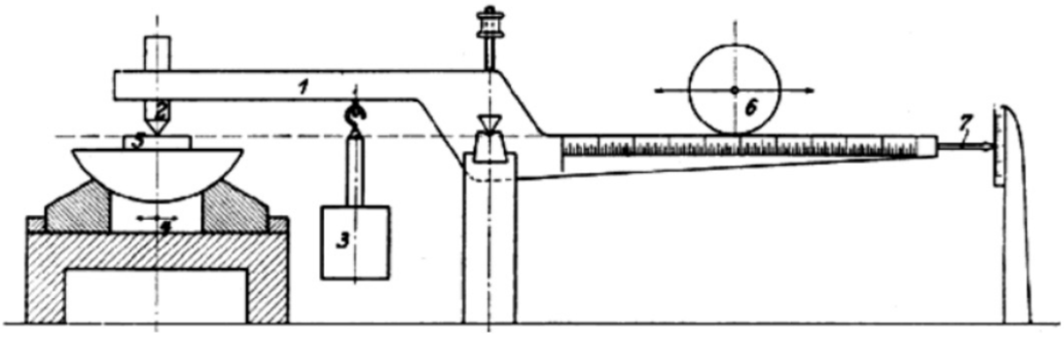

Martens indenter

The indentation test techniques with a spherical-tip indenter such as the Brinell hardness test became inappropriate for characterizing the contact hardness of *high-tech hard materials* developed in 20th century, leading to the diamond conical/pyramidal-tip indenters. R. Smith and G. Sandland at Vickers Ltd. proposed in 1923 the indentation test technique using a diamond tetrahedral pyramid, and then commercialized in 1925 the "Vickers hardness tester". As we made detailed considerations in Chap. 5, the Vickers indenter has a specific inclined face-angle (refer to Fig. 5.4) in order to keep a consistency with the Brinell hardness testing. This design concept has then been transferred to the trigonal pyramid indenter proposed by E.S. Berkovich in 1950.

The Brinell hardness HB and the Vickers hardness HV are defined as the indentation load divided by the *total contact area* of the resultant residual impression. On the other had in Martens hardness testing, the *projected contact area* under load is utilized in order to calculate the Martens hardness HM that means the *mean contact pressure under load*. The significance of the indentation hardness defined as the mean contact pressure was first emphasized by E. Meyer in 1908 on the basis of materials physics. He demonstrated that the indentation-induced normal stresses on the contact surface solely as well as exclusively contribute to the applied indentation load, and then concluded the importance of *the projected contact area not the total contact area* in calculating the indentation hardness. The indentation contact hardness in terms of the indentation load divided by the projected contact area is now referred to as the Meyer hardness H_{M}.

The Meyer hardness H_{M} of spherical indentation is dependent on the penetration depth, i.e., H_{M} increases with the increase in penetration depth due to the geometrically non-similar tip-configuration unlike the cone/pyramid indenters with geometrical self-similarity (see the details given in Chap. 5). On the basis of experimental observations, Meyer proposed the Meyer's law; the Meyer hardness of spherical indentation is expressed with $H_{\mathrm{M}} = f\left(d/D\right)$ in terms of the diameter D of the spherical indenter and the diameter d of the projected circle of residual impression (refer to Eqs. (3.30), (5.4) and (5.9)). In other words, the Meyer hardness is independent of the diameter D of the spherical indenter once we control the penetration depth in order to make the ratio of d/D constant (the Meyer's law of geometrical similarity).

In the beginning of the 20th century, it has been well recognized that the contact hardness H_{M} is a "*measure of plasticity*", although there existed none of materials physics to correlate the contact hardness to the yield stress Y. In the 1920s, R. Hill and then C. Prandtle derived the formula of $H_{\mathrm{M}} = c \cdot Y$ (the constraint factor $c = 2.57$) by applying the two-dimensional slip-line field theory to a *perfectly plastic body* indented by a flat punch. The extensive as well as the intensive indentation testing and the finite-element-based numerical analyses were conducted in the decade from 1960 to 1970 by D. Tabor, et al. for evaluating the constraint factor c. They proved that the constraint factor ranges in $2.5 \leq c \leq 3.2$ depending on the tip-geometry of the indenter used as well as the contact friction of the material indented.

In 1961, N.A. Stilwell and D. Tabor emphasized the importance of measuring the indentation loading/unloading $P-h$ hysteresis curve and then demonstrated that it is capable of determining the elastic modulus from the slope of the unloading $P-h$ line. Based on these

Fig. 15.

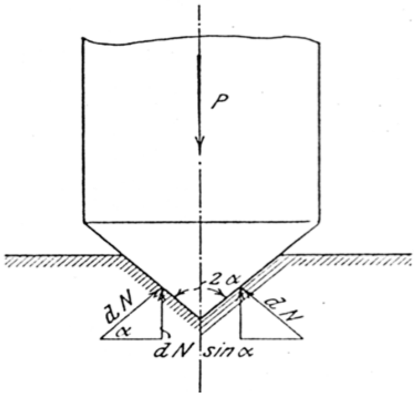

E. Meyer, *Zeit. Verein. Deutsch. Ing.* **52**,740(1908) experimental results and analyses, D. Newey, M.A. Wilkins, and H.M. Pollock designed a pioneering instrumented indentation apparatus in 1982, having been the historical origin of the present conventional micro/nano instrumented indentation apparatus.

The Meyer hardness H_M of a *fully plastic body* is a quantitative measure for the yield stress Y as mentioned above. On the other hand, not only the plastic flow but also the elastic deformation significantly affects the Meyer hardness of *elastoplastic body*. R. Hill (1950) first applied the cavity model to describe the Meyer hardness in terms of the elastic modulus E' and the yield stress Y of an elastoplastic body indented by a sphere, and then followed by K.L. Johnson (1970) for conical indentation. Based on these pioneering works, we can now fully understand the contact physics of the Meyer hardness of elastoplastic body as a function of the plastic index $PI\left(=\varepsilon_I E'/cY\right)$ in a unified manner based on the *additivity principle of the excluded volume of indentation*, the details of which have already been given in Sec. 5.1(2) of this textbook.

Heinrich Rudolf Hertz (1857-1894)

(3) Theoretical Foundation of Elastic/Viscoelastic Contact Mechanics

The classic paper of H.R. Hertz (1882),

" Über die Berührung fester elastischer Körper (On the contact of elastic solids)", J. reine und angewandte Mathematik, 92, 156-171,

is the historical origin of the indentation contact mechanics. He successfully solved an elastic contact problem; the analytical derivation of the contact pressure distribution $p(r)$ as a function of the contact displacement $u_z(r)$ for an elastic sphere (radius R_1, elastic modulus E_1) pressed into contact with another sphere (R_2, E_2) by an external force P. Only three years afterward from the Hertz theory, J.V. Boussinesq (1885) published a paper based on the potential theory for the more generalized elastic contact problems including the Herzian contact problem. Due to the mathematical difficulties in applying the Boussinesq theory to various types of axisymmetric contact problems, its analytical solution was first made by A.E.H. Love in the 1930s, and then by I.N. Sneddon in the 1960s through using the Hankel transformation, the

Joseph Valentin Boussinesq (1842-1929)

details of which have already been demonstrated in Chap.3.

We have had a significant upsurge of the science and engineering of organic polymers and plastic materials since 1940s. In these periods, the great scientists including P.J. Flory, J.D. Ferry, et al. made a sound basis of the theoretical as well as experimental frameworks of the polymer rheology and the molecular theories of viscoelastic deformation and flow. The theoretical extension of indentation contact mechanics to the time-dependent viscoelastic studies was first made by J.R.M. Radock(1957) through applying the “elastic-to-viscoelastic correspondence principle” to the elastic Hertz theory, and then followed by S.C. Hunter, M. Sakai, W.H. Yang, et al. through extending the Radock’s study for spherical indentation to the various types of axisymmetric indentation contact problems and experiments.

#【INDEX】